On the Numerical Modelling of Machining Processes via the Particle Finite Element Method (PFEM)

J. M. Rodríguez
J. C. Cante
X. Oliver

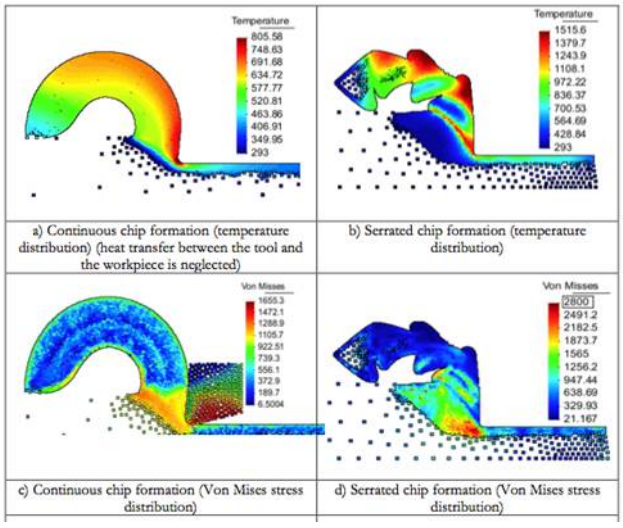

a) Continuous chip formation (temperature distribution) (heat transfer between the tool and the workpiece is neglected)

b) Serrated chip formation (temperature distribution)

c) Continuous chip formation (Von Mises stress distribution)

d) Serrated chip formation (Von Mises stress distribution)

Monograph CIMNE Nº-156, June 2015

On the Numerical Modelling of Machining Processes via the Particle Finite Element Method (PFEM)

J. M. Rodríguez
J. C. Cante
X. Oliver

Monograph CIMNE Nº-156, June 2015

International Center for Numerical Methods in Engineering
Gran Capitán s/n, 08034 Barcelona, Spain

INTERNATIONAL CENTER FOR NUMERICAL METHODS IN ENGINEERING
Edificio C1, Campus Norte UPC
Gran Capitán s/n
08034 Barcelona, Spain
www.cimne.com

First edition: June 2015

ON THE NUMERICAL MODELLING OF MACHINING PROCESSES VIA THE PARTICLE FINITE ELEMENT METHOD (PFEM)
Monograph CIMNE M156

ISBN: 978-84-944244-1-0
Depósito legal: B-19108-2015

Abstract

Metal cutting or machining is a process in which a thin layer or metal, the chip, is removed by a wedge-shaped tool from a large body. Metal cutting processes are present in big industries (automotive, aerospace, home appliance, etc.) that manufacture big products, but also high tech industries where small piece but high precision is needed. The importance of machining is such that, it is the most common manufacturing processes for producing parts and obtaining specified geometrical dimensions and surface finish, its cost represent 15% of the value of all manufactured products in all industrialized countries.

Cutting is a complex physical phenomena in which friction, adiabatic shear bands, excessive heating, large strains and high rate strains are present. Tool geometry, rake angle and cutting speed play an important role in chip morphology, cutting forces, energy consumption and tool wear.

The study of metal cutting is difficult from an experimental point of view, because of the high speed at which it takes place under industrial machining conditions (experiments are difficult to carry out), the small scale of the phenomena which are to be observed, the continuous development of tool and workpiece materials and the continuous development of tool geometries, among others reasons.

Simulation of machining processes in which the workpiece material is highly deformed on metal cutting is a major challenge of the finite element method (FEM). The principal problem in using a conventional FE model with langrangian mesh is mesh distortion in the high deformation. Traditional Langrangian approaches such as FEM cannot resolve the large deformations very well. Element distortion has been always matter of concern which limited the analysis to incipient chip formation in some studies. Instead, FEM with an Eulerian formulation require the knowledge of the chip geometry in advance, which, undoubtedly, restricts the range of cutting conditions capable of being analyzed. Furthermore serrated and discontinuous chip formation cannot be simulated.

The main objective of this work is precisely to contribute to solve some of the problems described above through the extension of the Particle Finite Element Method (PFEM) to thermo-mechanical problems in solid mechanics which involve large strains and rotations, multiple contacts and generation of new surfaces, with the main focus in the numerical simulation of metal cutting process. In this work, we exploit the particle and lagrangian nature of PFEM and the advantages of finite element discretization to simulate the different chip shapes (continuous and serrated) that appear when cutting materials like steel and titanium at different cutting speeds. The new ingredients of PFEM are focused on the insertion and remotion of particles, the use of constrained Delaunay triangulation and a novel transfer operator of the internal variables.

The remotion and insertion of particles circumvents the difficulties associated to element distortion, allowing the separation of chip and workpiece without using a physical or geometrical criterion. The constrained Delaunay improves mass conservation and the chip shape through the simulation, and the transfer allows us to minimize the error due to numerical diffusion.

The thermo-mechanical problem, formulated in the framework of continuum mechanics, is integrated using an isothermal split in conjunction with implicit, semi-explicit and IMPLEX schemes. The tool has been discretized using a standard three-node triangle finite element. The workpiece has been discretized using a mixed displacement-pressure finite element to deal with the incompressibility constraint imposed by plasticity. The mixed finite element has been stabilized using the Polynomial Pressure Projection (PPP), initially applied in the literature to the Stokes equation in the field of fluid mechanics.

The behavior of the tool is described using a Neo-Hookean Hyperelastic constitutive model. The behavior of the workpiece is described using a rate dependent, isotropic, finite strain j2 elastoplasticity with three different yields functions used to describe the strain hardening, the strain rate hardening and the thermal softening (Simo, Johnson Cook, Baker) of different materials under a wide variety of cutting conditions. The friction at the tool chip interface is modeled using the Norton-Hoff friction law. The heat transfer at the tool chip interface includes heat transfer due to conduction and friction.

To validate the proposed mixed displacement-pressure formulation, we present three benchmark problems which validate the approach, namely, plain strain Cook´s membrane, the Taylor impact test and a thermo-mechanical traction test. The isothermal-IMPLEX split presented in this work has been validated using a thermo-mechanical traction test.

Besides, in order to explore the possibilities of the numerical model as a tool for assisting in the design and analysis of metal cutting processes a set of representative numerical simulations are presented in this work, among them: cutting using a rate independent yield function, cutting using different rake angles, cutting with a deformable tool and a frictionless approach, cutting with a deformable tool including friction and heat transfer, the transition from continuous to serrated chip formation increasing the cutting speed. We have assembled several numerical techniques which enable the simulation of orthogonal cutting processes. Our simulations demonstrate the ability of the PFEM to predict chip morphologies consistent with experimental observations. Also, our results show that the suitable selection of the global time integration scheme may involve savings in computation time up to 9 times.

Furthermore, this work present a sensibility analysis to cutting conditions by means of a Design of Experiments (DoE). The Design of Experiments carried out with PFEM has been compared with DoE carried out with AdvantaEdge, Deform, Abaqus and Experiments. The results obtained with PFEM and other numerical simulations are very similar, while, a comparison of numerical simulations and experiments show some differences in the output variables that

depend on the friction phenomena. The results suggest that is necessary to improve the modelization of the friction at the tool-chip interface.

Table of contents

Nomenclature

$\mathbf{X}^{(i)}$	Material particles
$\mathbf{u}^{(i)}$	Material displacement
$\mathbf{x}^{(i)} = \boldsymbol{\varphi}^{(i)}(\mathbf{X}^{(i)}, t)$	the deformation map of the body $\beta^{(i)}$
$\mathbf{V}^{(i)} := \partial_t \boldsymbol{\varphi}^{(i)}(\mathbf{X}^{(i)}, t)$	material velocity
$\mathbf{A}^{(i)} := \partial_t \mathbf{V}^{(i)}(\mathbf{X}^{(i)}, t),$	Material acceleration
$\mathbf{F}^{(i)} = D\boldsymbol{\varphi}^{(i)}(\mathbf{X}^{(i)}, t)$	Deformation gradient
$\boldsymbol{\theta}^{(i)}$	Absolute temperature
$\rho_0^{(i)}$	the reference density
$\mathbf{B}^{(i)}$	prescribed forces per unit of reference volume
DIV	reference divergence operator
$\mathbf{P}^{(i)}$	first Piola-Kirchhoff stress tensors
$\mathbf{S}^{(i)}$	second Piola-Kirchhoff stress tensors
$E^{(i)}$	the internal energy
$\mathbf{Q}^{(i)}$	the nominal heat flux
$R^{(i)}$	the prescribed reference heat source
$D_{\text{int}}^{(i)}$	the internal dissipation per unite reference volume
$N^{(i)}$	the entropy
Ψ	free energy
α	rake angle
β	flank angle
R	Tool radius
$\phi^{(i)}$	the Mises yield function

$\lambda^{(i)}$	the consistency parameter
J	the Jacobian of the deformation gradient
$\mathbf{b}^e$	elastic left Cauchy-Green tensor
μ	the shear modulus
κ	the bulk modulus
c	the heat capacity
β	the thermal expansión coeficient
B	the constant strength coefficient
θ_0	the reference temperature
θ_{melt}	the reference melt temperature
m	a power coefficient of the thermal softening term
A	the initial yield stress
$\overline{e}^p$	Plastic strain
$\dot{\overline{e}}^p$	strain rate
C	dimensionless strain rate hardening coefficient
g_N	the gap, separating a material point $\mathbf{X}^{(1)}$ on $\Gamma^{(1)}$ from the tool boundary, is defined in the spatial description
P_N	the normal contact force
g_T	The tangential gap
$P_T = \kappa_T g_T$	Tangential contact force
κ_T	the tangential penalty factor
h	the thermal conductance coefficient
D_{fric}	Heat generation at the tool chip interface
t	time

Chapter 1

1 Introduction

1.1 Motivation

The steam engine is considered to be driving force and the most important technology of the Industrial Revolution .Watt steam engine (1760), with its large metal cylinders and other parts of unprecedented dimensional accuracy, it led to the first major developments in metal cutting. Rapid failures of the tools could be avoided only by cutting very slowly, as a consequence 27 working days to bore and face one of Watt's large cylinders were required.

From 1760 to 1860 the knowledge of how to machine different shapes in materials like cast iron, wrought iron and few copper allows using high carbon steel tools was acquired. During this century, the research focus was based on the improvement of the quality and consistency of tool steels using a trial and error approach.

With the invention of the Bessemer (1855) and Siemens-Martin (1865) steel making processes, steel rapidly replace wrought iron as the workhorse of construction materials, because these processes allow the rapid production of large quantities of basic steel during a short period of time. Due to the high strength and stiffness of steel, it is much more difficult than wrought iron to machine, and cutting speeds has to be lowered even further to maintain reasonable tool life.

During the last century, the incentive to reduce the cost by accelerating and automating the cutting process has been the major driving force behind the technological developments in metal cutting. Mainly, productivity has been increased with the higher cutting speeds achievable using high speed steel and cemented carbide tool, both representing an advantage over traditional carbon steel technology. Also, designers and manufactures have optimized the shape of the tools to lengthen tool life at high cutting speeds, while lubricants manufactures have developed new coolants and lubricants to improve surface finish and permit increased rates of removal.

The study of metal cutting is difficult from an experimental point of view, because of the high speed at which it takes place under industrial machining conditions (experiments are difficult to carry out), the small scale of the phenomena which are to be observed, the continuous development of tool and workpiece materials and the continuous development of tool geometries, among others reasons.

In the last 100 years there have been many attempts to developed mathematical models which will predict quantitatively the behaviour of work material during cutting from knowledge of their properties. From the mechanistic point of view, Taylor (1907), Ernst and Merchant (1945), Oxley (1959) and Rowe and Spick

(1967), and De Vor et al. (1980). More complex mathematical models were developed using Finite Element Analysis. The first numerical simulation of metal cutting was carried out by Tay el al. (1974).
As reported in [2], a mathematical model of metal cutting should be able to give the following information:

1. prediction of tool life
2. prediction of the accuracy of the components being machined
3. prediction of the surface finish on the component being machined
4. prediction of chip control
5. prediction of the loads on the tool, the workpiece and the fixtures

The analytical and empirical models have contributed a great deal to the field providing information about chip formation processes in the average sense. Instead, numerical simulation of metal cutting processes has become increasingly more popular due to its ability to provide detailed insight the process. Such simulations have the prospect to replace the difficult and costly experiments used for tool and process design. Most of the times, the analytical or empirical models are the preferred options at industry due to its simplicity.
For two reasons, the empirical, mechanistic and FEA models are prone to be criticized. First, if the chosen inputs to the model do not match the conditions in practice, the forecast will be an uncertainty. Second, if the internals of the model do not embody the correct material constitutive equation, or have no way of accounting for the friction phenomena through the secondary shear zone, then again the forecast will be uncertain. Furthermore, FEA is also criticized due to its large computational cost needed to carry out a numerical simulation.
More than 300 years of study of metal cutting reflect the complexity of the process. The long path started with the tool and process design in 1760 using a trial an error approach and continues, today, with the tool and process design using mechanistic and numerical models of metal cutting. Nevertheless, is necessary to improve the experimental devices and the mechanistic and numerical models to increase our understanding about metal cutting.
The above considerations constitute solid and compelling reasons to pursue a line or research in the field of numerical simulations of metal cutting processes.

1.2 Objective and Scope of the present research

The central goal of this work is to extend the Particle Finite Element Method (PFEM) to thermo-mechanical problems in solid mechanics which involve large strains and rotations, multiple contacts and generation of new surfaces, with the main focus in the numerical simulation of metal cutting process. In this work, we exploit the particle and lagrangian nature of PFEM and the advantages of finite element discretization to simulate the different chip shapes (continuous and serrated) that appear when cutting materials like steel and titanium at different cutting speeds. Also, in this work, we developed a mixed (displacement/pressure) stabilized linear triangle finite element based in the

work of Dohrmann and Bochev [13, 14], able to deal with the incompressibility constraint due to plastic phenomena.

1.3 Metal cutting mechanics

Metal cutting or machining is a process in which a thin layer or metal, the chip, is removed by a wedge-shaped tool from a large body. Metal cutting processes are present in big industries (automotive, aerospace, home appliance, etc.) that manufacture big products, but also high tech industries where small piece but high precision is needed. The importance of machining is such that, it is the most common manufacturing processes for producing parts and obtaining specified geometrical dimensions and surface finish, its cost represent 15% of the value of all manufactured products in all industrialized countries.
Cutting is a complex physical phenomena in which friction, adiabatic shear bands, excessive heating, large strains and high rate strains are present.
Tool geometry, rake angle and cutting speed play an important role in chip morphology, cutting forces, energy consumption and tool wear.
Due to the complex physical process that takes place in cutting, machining processes is one of the most interesting industrial problems to be analysed from the numerical point of view.

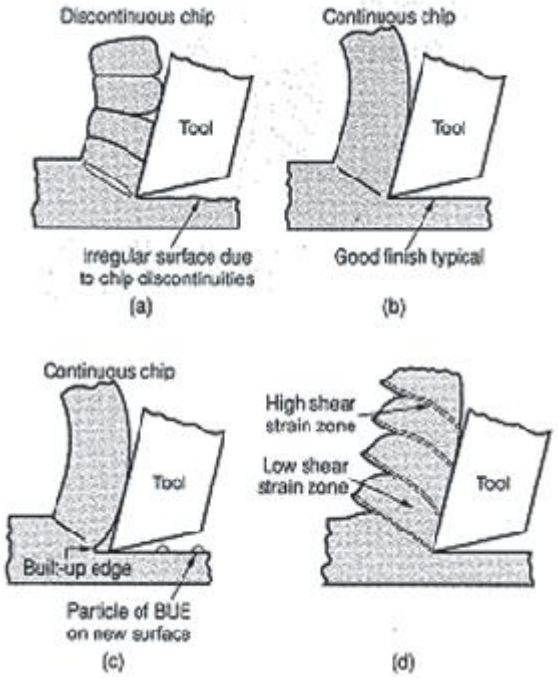

Figure 1. Four types of chip deformation in metal cutting.[1]

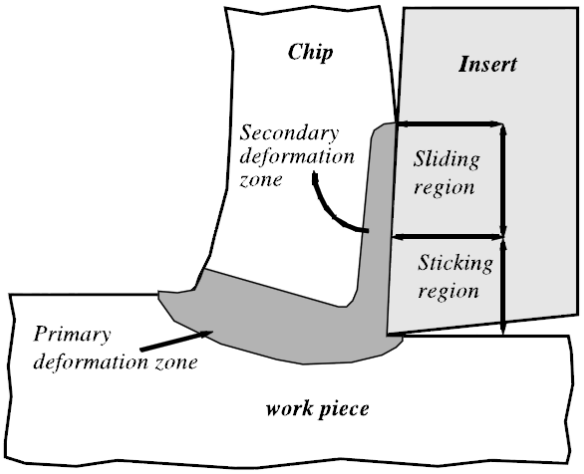

Figure 2. Localization of the primary and the secondary shear zones.[7]

This section introduces the main concepts related to cutting mechanics. Among them, the types of chips that can be formed depending on material and cutting conditions, the two regions where plastic flow takes place and as a consequence an increase of temperature due to plastic work, the cutting forces acting on the tool, and the main vocabulary associated to angles and dimensions in which cutting forces depends on, and finally, the mechanical and thermal contact in the chip-tool interface.

1.3.1 Chip shapes

Figure 1 shows the wide range of chip flows that are free to be formed, depending on the material and cutting conditions. The formation of all types of chips involves a shearing of the work material in the region of a plane extending from the tool edge to the position where the upper surface of the chip leaves the work surface. A very large amount of strain takes place in this region in a very short interval of time, and not all metals and alloys can withstand this strain without fracture. The vast majority of chip available, can be classified as follows: discontinuous, continuous, continuous with build-up-edge and serrated chip.

Discontinuous chip (Figure *1*(a)): This type of chip is typically obtained when machining brittle materials at low cutting speeds, sometimes the chip is formed in separate segments or sometimes in segments with very thin material junctions. With this type of chip is typical to obtain high surface roughness. Other factors that influence the formation of discontinuous chips are a high friction between the work piece and the chip, high feed rate and cutting depths.

Continuous chip (Figure 1(b)): when machining ductile materials at high cutting speeds and low feed rates and depths of cut. A good surface finish is obtained

when this type of chip is formed. A low friction coefficient between the tool and the chip encourage the formation of this kind chip.
Continuous chip with build-up-edge (Figure 1(c)): when machining ductile materials at low to medium cutting speeds, the friction between the chip and the rake face is high and the chip may weld onto the tool face. This formation is called a build-up-edge.
Serrated chip (Figure 1(d)): These chips are semi-continuous in the sense that they possess a saw-tooth appearance that is produced by a cyclical chip formation of alternating high shear strain followed by low shear strain. This type of chip is related with materials like titanium alloys, nickel alloys and super austenitic stainless steels.

1.3.2 Processes zones

During machining processes, the major deformations are concentrated in two

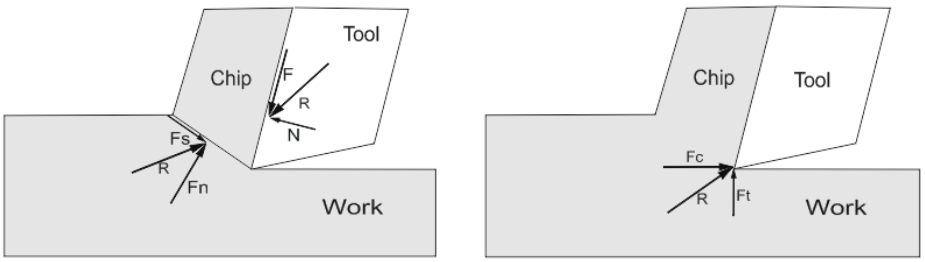

Figure 3. Forces in metal cutting: (a) forces acting on the chip in orthogonal cutting and (b) forces acting on the tool that can be measured.

regions close to the cutting tool edge. These regions are usually called primary and secondary deformation zones. (Figure 2)
The primary deformation zone extends from the tip of the cutting tool to the junction between the undeformed work material and the deformed chip. The workpiece is subjected to large deformation at a high strain rate in this region. The heating is due to energy dissipation from plastic deformation. Metal cutting experiments have indicated that the thickness of the primary shear zone is only a few thousandths of a centimetre. The primary shear zone is inclined at angle ϕ (shear angle) with the plane of work.
Secondary shear zone results from the friction between the tool and the chip as the chip slides along the rake face of the tool. At the secondary shear zone, heat is generated due to plastic deformation and friction between the tool and the chip. This region is usually divided in two regions, the sticking and the sliding.

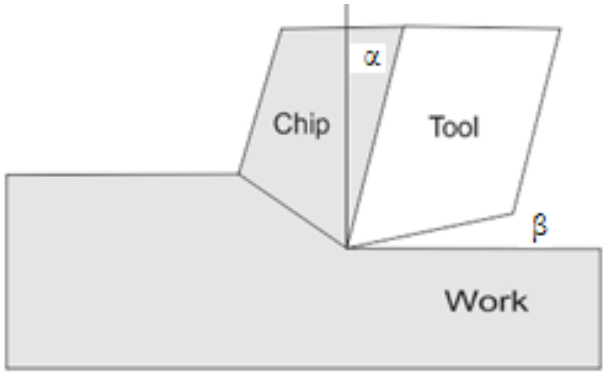

Figure 4. Orthogonal cutting geometrical parameters.

1.3.3 Forces in metal cutting

The forces applied against the chip by the tool can be separated into two mutually perpendicular components (Figure 3 (a)): friction force and the normal force to friction. The friction force F is the frictional force resisting the flow of the chip along the rake face. The normal force N to friction is perpendicular to the friction force.

In addition to the tool forces acting on the chip, there are two force components applied by the workpiece on the chip: shear force and normal force to shear. The shear force F_S is the force that causes shear deformation to occur in the shear plane, and the normal force to shear F_N is the perpendicular to the shear force.

None of these forces F, N, F_S, F_N can be measured in the machining operations, because the directions in which they act vary with different tool geometries and cutting conditions. However, it is possible to measure the cutting force and the thrust force. The cutting force F_C is in the direction of cutting, and the thrust force F_T is perpendicular to the cutting force (Figure 3(b)). Mathematical equations to relate the four components that cannot be measured to the two forces that can be measured are present by Groover in [1].

The tool in orthogonal cutting has only two elements of geometry (Figure 4): (1) rake angle α and (2) clearance angle β . The rake angle determines the direction that the chips flows as it is formed from the workpiece; and the clearance angle provides a small clearance between the tool flank and the newly generated machined surface.

1.3.4 Mechanical and thermal contact at the tool-chip interface

To improve the machinability and the performance of cutting tools is mandatory to understand the movement of the chip and of the work material across the faces and around the edge of the tool.
In most studies this has been treated as a classical friction situation, in which frictional forces tend to restrain movement across the tool surface, and the forces have been considered in terms of a coefficient of friction μ between the tool and work materials (Coulomb friction law). However, detailed studies of the tool/work interface have shown that this approach is inappropriate to most metal cutting conditions [15-18]. At this stage, it is necessary, to explain why

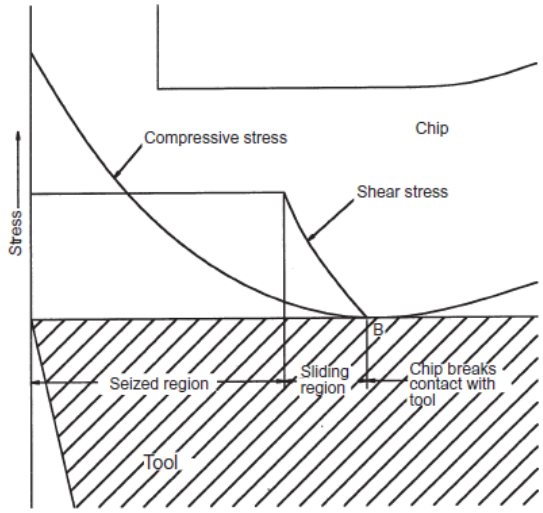

Figure 5. Normal and frictional stress distributions on the tool rake face.[2]

classical friction concepts do not apply and to suggest a more suitable model for analyzing this situation.
Coulomb based in many common examples of the sliding of one solid surface over another, proposes that the force F required to initiate or continue sliding is proportional to the force N normal to the interface at which sliding is taking place

$$F = \mu N \tag{0.1}$$

The friction coefficient μ is dependent only on these forces and is independent of the sliding area of the two surfaces. Bowden and Tabor [19], Archard [20] demonstrated that this proportionality results from the fact that real solid

surfaces are never completely flat on a molecular scale, and therefore make contact only at the tops of the hills, while the valleys are separated by a gap.
When the normal force is increased to such an extent that the real area of contact is a large proportion of the apparent contact area, a typical case in machining, it is no longer possible for the real contact area to increase proportionately to the load. In the extreme case, where the two surfaces are completely in contact, the real area of contact becomes independent of the normal force, and the frictional force becomes that required to shear the material across the whole interface. When two materials of different strengths are in contact, as in metal cutting, the force required to move one body over the other becomes that required to shear the weaker of the two materials across the whole area.
This force is almost independent of the normal force, but is directly proportional to apparent area of contact - a relationship directly opposed to that of classical friction concepts.
Due to the inadequacy of Coulomb friction law to study the complex phenomena that takes place at the tool chip interface, several constitutive models have been proposed which try to explain the complex phenomena which takes place at the tool chip interface. A summary about some of the new developed friction models is presented in the following lines:
Arrazola et al. (2010)[17] present a friction law which consider the stick and the slip phenomena at the chip-tool interface (Figure 5).
In the former zone the shear stresses are defines as follows:

$$\tau(x) = k \quad \text{when} \quad \mu\sigma_n \geq mk \quad \text{and } 0<\text{x} \leq \text{l}_p \tag{0.2}$$

While in the latter the shear is given by:

$$\tau(x) = \mu\sigma_n(\text{x}) \quad \text{when} \quad \mu\sigma_n < mk \quad \text{and } \text{l}_p<\text{x} \leq \text{l}_c \tag{0.3}$$

Where k is the shear flow stress of the workpiece material, μ is the friction coefficient, σ_n is the normal compressive stress acting at the tool face, l_p is the size of the seizure region, l_c is the contact length between the tool and the workpiece and m is a constant that takes a value of $0 < m \leq 1$.
Usui and Shirakashi derived an empirical equation as a friction model, which relates the frictional stress τ to the normal stress σ_n

$$\tau = k\left[1 - e^{-\left(\frac{\mu\sigma_n}{k}\right)}\right] \tag{0.4}$$

Where k is the shear flow stress of the workpiece material and μ is a friction coefficient experimentally obtained for different workpiece–tool material combinations.
Childs et al. [21] modified this model by multiplying k with a friction factor m, where $0 < m \leq 1$:

$$\tau = mk\left[1 - e^{-\left(\frac{\mu\sigma_n}{k}\right)}\right]$$

Dirikolu et al. [22] made a further modifications to this model by multiplying k with a friction m , where $0 < m \leq 1$ and introducing an exponent n :

$$\tau = mk\left[1 - e^{-\left(\frac{\mu\sigma_n}{k}\right)^n}\right]^{\frac{1}{n}} \tag{0.6}$$

More information about the friction model at the tool-chip interface is given in [15-18, 21-23]

1.4 Numerical Simulation of Metal Machining. (Finite Element): State of the Art

The set of numerical tools used in the numerical simulation of metal cutting should be able to represent the complex thermo-mechanical phenomena taking place inside the tool and the workpiece. At the same time, the set of numerical ingredients should be as simple as possible in order to decrease the computing time to get accurate results. As results, the following question arises:

What are the set of numerical tools that allow simulating metal cutting processes with high accuracy, but with a low computational cost?

In order to answer this question, first of all, the following lines present a summary about the state of the art in the numerical simulation of metal cutting processes. This summary includes mesh and meshless strategies, different formulations (lagragian, eulerian, ALE), strategies to deal with the incompressibility constraint imposed due to the plastic behavior of the workpiece, time integration schemes, contact algorithms to represent the contact between the tool and the workpiece, that have been used or can be used in the numerical simulations of metal cutting processes. This summary includes advantages and drawbacks according to the point of view of the author of this work, about the different numerical strategies capable to represent the complex phenomena taking place in machining.

1.4.1 Problem Formulation

A Finite Element Lagrangian calculation embeds a computational mesh in the material domain and solves for the position of the mesh at discrete points in time. As a consequence the Finite Element Lagrangian formulation is related to the problem of mesh distortion. The calculation process can even be impossible to continue when the Jacobian determinants become negative at some integrations points. At times, Finite Element Lagrangian formulations use a criterion to separate the chip from the workpiece. Those criteria included

element deleting based on a geometrical distance of the tool tip to closest workpiece element, plastic strain and strain energy density. Other times, Finite Element Lagrangian formulations are used with mesh adaptivity and automatic remeshing, and as a consequence this strategy does not require a chip separation criterion. Using remeshing means that the fields of state variables have to be mapped from to old mesh to the new one. This mapping is not a straight forward task and introduces some numerical diffusion to the state variables. This technique has been successfully applied in simulations of continuous and serrated chip formation. A lagrangian description of motion and adaptive remeshing was used to simulate orthogonal cutting in [24, 25] and [26]. Instead, a Lagrangian formulation plus a node separation as a criterion to predict chip piece separation was used in [27], [28] and [29].

Finite Element Eulerian formulations have been used by many authors to simulate continuous chip formation at steady state. Finite Element Eulerian formulation avoid the problem of mesh distortion but needs a predefined chip shape to develop the numerical simulation, while Finite Element lagrangian formulation is able to predict chip formation from incipient to steady state. A proper assumption of the chip shape is very difficult to obtain since it depends on many factors. In the Finite Element Eulerian formulation the material flows through the fixed mesh. The main disadvantage of Eulerian formulations is that is no easily adaptable for modeling the unconstrained flow of the material as the chip evolves during the process. As a consequence Finite Element Eulerian formulations cannot simulate serrated and discontinuous chip formation. An example of a Finite Element Eulerian formulation applied to the numerical simulation of metal cutting is presented in [30].

In order to avoid the disadvantages of Finite Element Lagrangian and Eulerian formulations, other computational techniques have been investigated. One of them is the Finite Element Arbitrary Lagrangian Eulerian (ALE) formulation in conjunction with adaptive mesh techniques [31-33]. The ALE formulation combines the best features of pure Lagrangian analysis (in which the mesh follows the material) and Eulerian analysis (in which the mesh is fixed and the material flows through the mesh). In ALE framework mesh motion is independent of material motion, for that reason high quality finite element meshes are preserved during the numerical simulation of machining process. ALE formulation does not need a criterion to separate the chip and the workpiece. Generally, ALE formulation is computationally cheaper than a Lagrangian formulation, but needs a preformed chip, which puts some restriction to an ALE formulation to predict different chip shapes (serrated, discontinuous). ALE formulation can be used to simulate chip formation from incipient to steady state, but the problem is to define a mesh motion scheme in order to preserve a high quality finite element mesh during the simulation. Numerical simulations in 3D using ALE are difficult to carry out, because the mesh motion in order to preserve a high quality mesh is more difficult in 3D

than in 2D. A detailed information on use of ALE formulations in modeling metal machining are presented by [33, 34], and [31].

1.4.2 Numerical treatment of the incompressibility constraint due to plasticity

The most common finite elements used in the numerical simulations of metal cutting are the following: a plane strain quadrilateral isoparametric finite element used in [24, 27, 35], a 6 noded isoparametric triangular elements used in [24] and [25], an enhanced four node quadrilateral with 1-point quadrature used in [26] and a 3 noded linear triangle plus the Average Nodal Pressure formulation to deal with the incompressibility constraint used in [36]. The 6 noded isoparametric triangular element presented in [25], is now used in the commercial software AdvantEdge and the 4 noded quadrilateral with reduced integration is used in Deform. Those softwares are the most common numerical tools used in industry in the numerical simulation of metal cutting processes.
Also, a number of different finite elements have been developed to improve the poor performance of linear triangles and tetrahedral under incompressible and nearly incompressibility conditions. These finite elements can be classified in four groups mainly: 1) Mixed Enhanced Element, 2) Pressure stabilized finite elements, 3) Composite pressure fields and 4) Average Nodal Pressure/Deformation Gradient. The following lines present a summary about the advantages and the disadvantages of each of the improved linear triangle and tetrahedral, and in case it is available a reference which apply the improved triangle in the numerical simulations of metal cutting processes.

1.4.2.1 Mixed enhanced elements

Enhanced Strain Technique, essentially consists in augmenting the space of discrete strains with local functions, which may not derive from admissible displacements. A suitable choice of these additional modes can improve the numerical performance of low-order elements and, more importantly, it can greatly alleviate the well-known volumetric locking phenomenon in the nearly-incompressible regime.
Most of the schemes taking advantage of the Enhanced Strain technique have been designed in connection with quadrilateral elements, because linear displacement finite elements enriched with an enhanced strain locks. Instead, the mixed linear displacement linear pressure finite element enriched with enhanced strains is able to deal with the incompressibility constraint. Literature review [37], remarks that the straightforward extension of the Enhanced Strain approach to large deformation problems generally leads to unstable methods, representing a disadvantage of Enhanced Strain Technique. As the author knowledge, Mixed enhanced finite elements have not been applied in the numerical simulations of metal cutting.

1.4.2.2 Pressure stabilization

The pressure field in mixed linear displacement linear pressure finite elements when used in the numerical simulations of incompressible or nearly incompressible materials presents unphysical oscillations. Mathematically, it means that equal order interpolation for displacement and pressure does not satisfy Babuska-Brezzy condition. In order to remove these undesirable oscillations, a literature overview shows four different strategies mainly: characteristic based split (***CBS***)[38], Finite Calculus (***FIC***) [39], Orthogonal Subgrid Scales (***OSS***) [40-42] and the Polynomial Pressure Projection (***PPP***) [13, 14]

The characteristic based split (***CBS***) was originally developed in the field of fluid mechanics [38]. This method is based on the introduction of an artificial compressibility into the mass conservation equation, in such a way that the final results do not depend on the artificial compressibility. The other main ingredient of *CBS* is the fractional step method used in the time integration of momentum balance. This fractional step proposes a split of momentum equation in two equations such that its sum is equal to the balance of momentum equation. The equation split is equivalent to split the velocity update in a time step into deviatoric and hydrostatic components. In summary, *CBS* algorithm uses four main steps: 1) Compute the velocity update using an explicit time integration scheme of the equation of balance of momentum; in this time integration schemes hydrostatic forces are not taken into account; 2) Using the balance on mass, calculates the nodal pressure and 3) Using the velocity obtained in (1) and the gradient of the pressure field obtained at (2) update the velocity field. 4) Given the updated velocity using an explicit integration scheme get the value of nodal displacements and update nodal positions. After this four steps, the next time step start. One advantage of *CBS* algorithm is the possibility to evaluate the pressure in a complete explicit way, but at the same time *CBS* allows to solve the pressure using an implicit scheme, in case it is needed. As the author knowledge, there is no a complete *CBS* implicit scheme for velocity and pressure, so does not matter if the pressure is integrated implicitly *CBS* algorithm is conditionally stable, and as a consequence there is a restriction in the maximum allowed time steps.

The Finite Calculus (***FIC***) [39] method is the based on the satisfaction of the balance of momentum and mass conservation in a domain of finite size and retaining higher order terms in the Taylor expansions used to express the different terms of the differential equations over the balance domain. The modified differential equations contain additional terms which main function is to suppress the unphysical oscillations of the pressure field. The mixed linear displacement/linear pressure tetrahedral could be used with implicit, explicit and semi-implicit time integration schemes. This represents an advantage in comparison with other modified tetrahedral finite elements. Also, *FIC* method needs 5 degrees of freedom per node (2 displacement, 1 pressure, 2 projected pressure gradients) in case of linear triangle and 7 (3 displacement, 1 pressure, 3

projected pressure gradients) in case of tetrahedral. The number of degrees of freedom per node represents a disadvantage of *FIC*, in terms of computing time, required memory and an extra nodal variable to transfer between remeshings. Another disadvantage of *FIC* is that, the term added to the mass conservation equation depends on the shear modulus, the mesh size and a constant that is problem depend,

Orthogonal Subgrid scales ***(OSS)*** was applied in the field of solid mechanics in [40-43]. Orthogonal Subgrid scales approach is based on two main ingredients: 1) a mixed equal order interpolation of the pressure and displacement fields and 2) a decomposition of the unknowns into resolvable and sub grid scales orthogonal to the finite element space. The idea behind Orthogonal Subgrid scales is to approximate the effect of the continuous solution which cannot be captured by the finite element solution which is the cause of volumetric locking. The main purpose of Orthogonal Subgrid Scales is to define a strategy to overcome the requirements of Babuska-Bressi conditions and in consequence make possible the use of equal order continuous interpolation for displacement and pressure. As a consequence of adding a subgrid scale displacement, extra degrees of freedom are added to a node. Furthermore, a term that depends on mesh size, shear modulus, and a constant that is problem depend is added to the mass conservation equation. Then, subgrid scales needs 5 degrees of freedom per node (2 displacement, 1 pressure, 2 projected pressure gradients) in case of linear triangle and 7 (3 displacement, 1 pressure, 3 projected pressure gradients) in case of tetrahedral.. In the framework of implicit dynamics, a staggered scheme in which the displacement and pressure are solved implicitly, while the pressure gradient is solved explicitly is usually used as proposed in [42]. As a consequence the pressure gradients degrees of freedom added represent a minor cost in terms of computing time.

It is important to remark that the terms added to the balance equations using *FIC* and subgrid scales to overcome Babuska-Brezzi conditions are exactly the same. Being the difference between *FIC* and subgrid scales the idea to get the terms that stabilize the finite element solution.

Polynomial Pressure Projection ***(PPP)*** was initially formulated and applied to stabilize stokes equations in [13, 14]. PPP is based on two ingredients. First, use a mixed equal order the pressure and velocity fields and second, and L_2 pressure projection. *FIC* and *OSS* introduce the projection of the pressure gradient onto the displacement space as a new dependent variable, and use the difference between these two fields to relax the continuity equation, while *PPP* uses a projection on a discontinuous space and as a consequence can be implemented in an elementary level. *FIC* and *OSS* use mesh dependent and problems dependent parameters while *PPP* does not need. *PPP* has not been applied in the numerical simulations of metal cutting processes. More detail about the

extension of *PPP* to solid mechanics problems will be presented in the next chapter.

1.4.2.3 Composite pressure fields

These finite elements enforce a constant pressure field over a group of triangles or tetrahedrals to reduce pressure constraints. The most representative finite elements are F-Bar[44, 45] and Composite Triangles [46, 47].

The ***F-bar*** is another strategy to deal with the incompressibility constrains using linear triangles. F-bar formulation was proposed in [45] in the framework of implicit dynamics and in [44] in the framework of explicit dynamics. It relies essentially on the relaxation of the excessive volumetric constraint typical of low order elements through the enforcement of the incompressibility constraint over a patch of simplex elements. An important aspect of the present method is that it preserves the displacement-based format of the corresponding finite element equations. At the same time, this method presents an unconventional stiffness format that stem from the fact that the internal force vector of a particular element depends on the nodal displacements of all elements of its patch, breaking the typical elementary assembly of the internal force vector and the stiffness matrix.

A triangular element in which a six-node triangle is constructed from four 3-node triangles with linear displacement fields in each subtriangle and a continuous linear strain field over the assemblage is presented in [46]. They have called this finite element a "composite triangles ***(CT)***". This element presents some advantages in terms of contact search and imposition in comparison with 6-node-triangle and furthermore this element is locking free in comparison with three node triangle. Furthermore, this element does not satisfy BB condition. An improved *CT* triangle in order to satisfy BB conditions using a constant volumetric strain and a linear deviatoric strain over the six-node finite element is presented in [47].

1.4.2.4 Average Nodal strains / Average Nodal stresses

Computes the average volumetric strain/ volumetric stress or strains/stresses at nodes based on surrounding triangles or tetrahedrals. Then, the elementary volumetric strain/ volumetric stress or strains/stresses are equal to the average of the nodal values that belongs to the element.

Average Nodal Pressure ***(ANP)*** was presented in [48] and [49] in the framework of explicit dynamics and by [50] in the framework of implicit dynamics. *ANP* is a simple linear tetrahedron element that can be used in applications involving nearly incompressible materials or incompressible materials modelled using a

penalty formulation. The element prevents volumetric locking by defining nodal volumes and evaluating average nodal pressures in terms of these volumes.
Average Nodal Pressure (ANP) defines the nodal volume as follows:

$$V^a = \sum_{e \in a} \frac{1}{\text{ndim} + 1} V^{(e)} \tag{0.7}$$

Where $V^{(e)}$ is the element volume, ndim is the dimension of the problem to solve and V^a is the nodal volume. This definition of nodal volume, allows to define a nodal volume change ratio and as a result a nodal pressure. The average of nodal pressures is used as the modified elementary pressure. This definition of nodal volume reduces the volumetric locking tendency of linear triangles and tetrahedral and allows an accurate prediction of deformed shapes and forces. But, *ANP* formulation is found to produce considerable checkerboard-type hydrostatic pressure fluctuations, which limits the range of applicability of *ANP* pressure formulations. It is important to remark that *ANP* work well for volumetric locking but present locking due to bending.[51]. *ANP* has been applied in the numerical simulation of high speed cutting in [52]. The critical time step of *ANP* formulations imposed by stability is more or less 7 times greater in comparison with *CBS* formulations [49]. In terms of computing time it represents a great advantage of *ANP* formulations.
Node Based Uniform Strain Elements ***(NBUSE)*** [53] and Average Nodal Deformation Gradient ***(ANDG)*** [54] present a formulation using linear triangle and tetrahedral that is free of volumetric and shear locking. These formulations are based on the definition of the nodal displacement gradient (*NBUSE*) and Average nodal deformation gradient (*ANDG*). These average gradients are defined as follows:

$$\bar{\nabla}\mathbf{u}^a = \frac{\sum_{e \in a} V^{(e)} \nabla \mathbf{u}^{(e)}}{\sum_{e \in a} V^{(e)}} \tag{0.8}$$

$$\bar{\mathbf{F}}^a = \frac{\sum_{e \in a} V^{(e)} \mathbf{F}^{(e)}}{\sum_{e \in a} V^{(e)}} \tag{0.9}$$

Where $V^{(e)}$ is the element volume, $\nabla \mathbf{u}^{(e)}$ is the element displacement gradient, $\bar{\nabla}\mathbf{u}^a$ is the nodal displacement gradient, $\mathbf{F}^{(e)}$ element deformation gradient and $\bar{\mathbf{F}}^a$ is the nodal deformation gradient. Then using $\bar{\nabla}\mathbf{u}^a$ / $\bar{\mathbf{F}}^a$ and the constitutive equation, nodal stresses are calculated and finally, modified elementary stresses are calculated as the average of nodal stresses. As reported in [53] and [54] these formulation can lead to the presence of non-physical low-energy modes. An improved nodal deformation gradient based on Streamline upwind Petrov-

Galerkin ***(SUPG)*** which remove the non-physical energy modes was proposed in [54]. A stabilization strategy to remove the unphysical energy modes in the frameworks of implicit dynamics was proposed in [51], even so, the pressure field in some examples presents unphysical oscillations. The great advantage of average nodal formulations is that are locking free without increasing the number of degrees of freedom per node. ***NBUSE*** has been applied in the numerical simulation of metal cutting processes in [55].

A Mixed Discretization Technique ***(MD)*** [56] which is based on the following ingredients. 1) Mesh the solid body in quadrilateral or hexahedral zones; then divide each quadrilateral or hedrahedral into triangles or tetrahedrons. 2) The deviatoric behavior is defined on an elementary basis (triangle/tetrahedral), while the volumetric is averaged over a zone (quadrilateral/hexahedral). Then, an improvement of **(*MD*)** is presented in [57], the authors of that work call their formulation Nodal Mixed discretization **(*NMD*).** The main advantage of **(*NMD*)** is that the average of the volumetric behavior is carried out in a nodal basis rather than in a zone basis (quadrilateral/hexahedral), it implies that only a mesh of triangles or tetrahedral is needed. NMD uses a nodal volumetric strain rates, defined as weighted average of the elementary surrounding values. Then, a modified elementary volumetric strain rate is defined as the average of the nodal values. The difference between *NMD* and *ANP* is that in *NMD* the constitutive model is called on an element basis, while in *ANP* the constitutive model is called in a nodal basis for the volumetric behavior. Due to the similarities between *ANP* and *NMD*, is expected that *NMD* presents checkerboard-type hydrostatic pressure fluctuations, being a disadvantage of both formulations. In case the hydrostatic part of the stress tensor depends linearly on the determinant of the deformation gradient, *ANP* and *NMD* are exactly the same.

1.4.3 Time integration schemes (implicit, explicit, semi-explicit)

The Finite Element Method allows different time discretization schemes. The most common are the implicit and explicit time integration schemes. Each of them has its advantages or disadvantages.
The implicit scheme is unconditionally stable; it means that there is no restriction on the time step used in the numerical simulation. In implicit formulations, mechanical problem can be solved in a static o dynamic way. Furthermore, implicit formulations can be used with standard and mixed (displacement/pressure) finite elements. However, implicit schemes needs the solution of a linear system certain number of times each time step. Usually, the solution of the linear system represent most of the computing time. Implementation of a new constitutive equation is a long task, due to the requirement to implement the algorithmic constitutive tensor. Moreover, in some cases an implicit scheme does not converge, due to the high nonlinearities involved in the problem.

Finally, contact conditions decrease the size of the time step used in the numerical simulation and as a consequence increase the computing time of an implicit scheme.

Explicit formulation solves the mechanical problem in a dynamical way. The solution of each time step in an explicit scheme is simple and computationally efficient, provided use a lumped mass matrix in the simulation. Explicit scheme does not need the solution of a linear system; this topic is an advantage if the numerical solution is done using parallel computing. Implementation of a new constitutive equation is an easy task; it allows implement simple or complex constitutive equation without a big effort. Explicit scheme are conditionally stable, it means that the time step used in the simulations should be less or equal than a given critical time step, the critical time step correspond to the time that take to an wave to travel through the small finite element of the mesh. In case of an elastic material, the critical time step depends on the mesh size, elastic modulus, Poisson ratio, density of the material and γ a constant that depends on the finite element used.

$$\Delta t_c = \gamma \frac{\Delta x}{\sqrt{\frac{3\kappa\ (1-\nu)}{\rho\ (1+\nu)}}} = \gamma \frac{\Delta x}{\sqrt{\frac{2G\ (1-\nu)}{\rho\ (1-2\nu)}}} \tag{0.10}$$

The restriction imposed on the time step by the explicit schemes, allows concluding that for numerical simulation which involves long period of computing time or low speeds, implicit schemes are more favorable in comparison with explicit schemes. On the contrary, when velocities are high and the contact conditions are complex, is necessary to decrease the time step used in implicit formulations, so in this case explicit formulations appear as an effective and an efficient tool, with a really interesting computing time. One example in cutting mechanics in which explicit scheme are more efficient that implicit scheme is high speed cutting. Now, the question is:

At what cutting speed, explicit schemes are more computationally efficient than implicit schemes?

It is important to mention that in the literature there is no a comparison between explicit and implicit time integration schemes, which shows under what condition one scheme is better than the other.

In the literature, implicit schemes have been used in [24, 27, 29, 58] and explicit schemes in [25, 26] and [52].

Also, there are some mixed schemes in which the hydrostatic part of the balance of momentum is integrated implicitly and the deviatoric part is integrated explicitly. Some examples of mixed time integration schemes are: Characteristic Based Split [59] and Finite Calculus [39]. These strategies have not been applied in the numerical simulations of metal cutting.

The commercial software AdvantEdge uses an explicit time integration schemes, while the software Deform uses an implicit time integration scheme.

1.4.4 Contact algorithms

Modeling the complex thermo-mechanical phenomena that takes place at the tool chip interface is of paramount importance, because numerical results like feed force and contact depends strongly on an accurate modeling of the thermo-mechanical contact at the tool-chip interface . For that reason, in the numerical simulation of metal cutting processes is necessary to use accurate, robust and computational efficient contact algorithms. Contact problems using Finite Elements implies two basic problems: First, the way in which the contact constraint is imposed and second, the contact detection strategy. Contact constrains are imposed using the penalty approach [60-66] and the Lagrangian multipliers [63, 65], A mixed penalty-lagrangian formulation which uses the advantages of penalty and lagrangian formulations is presented in [67]. Several contact formulations developed up to now, enforce the contact constraints at specific collocation points (contact detection strategy). The most common strategy is the node-to-segment approach developed by Hallquist et al. [61] Its main idea is that a node located on the slave surface must not penetrate the opposing master side segment. This approach can be applied in a single and two pass algorithm. In a single pass algorithm only nodes on the slave side are checked against penetration into the master segment, and the nodes on the master side are free to penetrate the slave segments, while in the two pass algorithm, the nodes on the slave surface are checked against penetration into the master segment and the nodes on the master surface are checked against penetration into the slave segment. Both searching strategies have disadvantages because one pass algorithm allows penetration of master nodes into slave segments and do not pass the patch test and the two pass is prone to lock due to overconstraining of the displacements on the contact surface, but it pass the patch test. The node to segment approach has been extended to thermo-mechanical contact by Wriggers, Zavarise, and Miehe in [68-70]

Recently, a contact algorithm strategy based on following ingredients [71, 72]: The continuity constraints imposition along the entire coupling boundary in a weak integral sense and the use of segment-to-segment discretization strategies based on the so-called mortar method was presented. In contrast to classical node-to-segment formulations, in the segment to segment discretization the contact constraints are not imposed pointwise at a finite number of slave nodes but are defined along the entire contact boundary and therefore a more complete coupling between the degrees of freedom of the contact surfaces is obtained. The extension of the mortar method to thermo-mechanical dynamic contact problems including frictional heating and thermal softening effects at the contact interface was present by Hüeber and Wohlmuth in [73]

Oliver et al. [74, 75] propose the Contact Domain Method (***CDM***). In this method, contact constraints are enforced using a stabilized Lagrange multiplier formulation based on an interior penalty method (this allows the condensation of the introduced Lagrange multipliers and leads to a purely displacement driven problem) and contact detection strategy is done with a fictive intermediate

region connecting the potential contact surfaces of the deformable bodies (this fictive intermediate region is built using Delaunay triangulation). Oliver identifies the following advantages of *CDM* in comparison with other contact algorithms: 1) The solution does not dependent on the choice of slave and master sides, as the contact pairing is uniquely defined via a constraint Delaunay triangulation 2) the performance of the contact domain method (CDM) is superior to classical node-to-segment formulations and comparable to mortar based contact algorithms. Up to now, the Contact Domain Method (*CDM*) has not been applied in the simulations of thermo-mechanicals problems.

The summary present above about contact imposition and contact search is focused on implicit dynamics. In case of explicit dynamics special procedures have been developed [61, 76], such as the momentum related techniques in which modifications are made to acceleration, velocities and displacements. The main goal of these modifications is to avoid the penalizing effect of the time step introduced by the high stiffness, associated with penalty approaches. Precisely, this strategy has been used in the numerical simulation of metal cutting processes by Marusich and Ortiz [25].

Bruchon et al. [77], propose the use the metric properties of the distance (or gap) function between two bodies in the formulation of contact problems. In this formulation, the vectors normal to the contact surfaces are defined through the gradient of this distance function. This contact strategy can be applied with in explicit and implicit frameworks. The contact strategy presented by Bruchon has been applied in the numerical simulation of high speed metal cutting processes by De Micheli and Mocelin in [52].

Sekhon and Chenot [24] present a very simple contact strategy applied to the numerical simulation of metal cutting processes using a flow formulation, such that if a boundary node is found lie inside the tool the length of time step is decreased in such a way that the node would lie on the tool face. Then, if the node at the start of the time step is in a compressive stress state, then the node is restricted to move along the tool face.

An overview about the contact algorithms available in the literature, shows that contact modeling using finite elements is not a simple a task, a more research is need in other to develop a robust, efficient and general contact algorithm. However, the best algorithm able to predict the contact phenomena at the tool chip interface can be chosen based on the following parameters: 1) computationally efficient, 2) exact satisfaction of contact constraints, 3) decrease matrix ill-conditioning and 4) no extra degrees of freedom due to contact constraints. The set of parameters presented above, will allows us in the next chapter to choose the most appropriate contact algorithm with its respective improvements to model the contact at the tool chip interface.

1.4.5 Adaptive remeshing, Error estimators, Transfer operators

In the numerical simulations of metal cutting processes large deformation, material and geometrical nonlinearities are present. Due to this reason, mesh

degeneration through the numerical simulation is present, the first approach to tackle this problem was using predistorted finite element meshes [29, 35, 78], some of these references mention the limitations of predistorted meshes in the numerical simulation of metal cutting processes. Another approach to deal with this problem is adaptive remeshing. In this kind of numerical simulations the magnitude and distribution of error estimators evolve during the incremental solution, showing that is necessary to refine the mesh where high gradients are taking place or de-refine the mesh where errors estimators are small in order to preserve a bounded computational cost. Furthermore, remeshing is used to preserve an adequate element shape and to predict cracking in the numerical simulation of serrated and discontinuous chip formation. Moreover, the boundary elements in contact with the tool are prone to distort and interfere with the tool, such an interference can lead to losses of volume of the workpiece and the undesirable effect of enlarging the tool radius, for that reason contact boundary conditions is one important remesh indicator. Generally, three steps are needed to remesh the workpiece:

1) Calculate error estimators and distortion metrics. If these values are greater than a given tolerance, go to 2.
2) Create a new finite element mesh
3) Data transfer from the old to new mesh

Recently, several **error estimators** have been proposed for elasto-plastic problems based on mathematical foundations and physical considerations. Zienkiewicz-Zhu [78, 79] error estimator, calculates for each node an improved stress and defines the error as the difference between this stress and the one calculated by the standard finite element procedure. Ortiz and Quigley [80] propose an adaptation strategy based on equi-distributing the variation of the velocity field over the elements of the mesh. Marusich and Ortiz [25] used an adaptation criterion based on the equi-distribution of plastic power, the plastic work criteria has been applied in [25] to the numerical simulation of metal cutting processes. Lee and Bathe [81] propose a point wise indicator for error in stresses and plastic strain increments, based on the difference between smoothed (stress/plastic strain) and the (stress/plastic strain) at gauss points. Peric et al. [82] present an error estimator based on the projection and smoothing of plastic power rate and the rate of fracture, as a consequence, it is not only able to capture the progression of plastic deformation, but also provide refined meshes at regions of possible material failure. This error estimator has been applied in the numerical simulation of high speed machining in [26, 82]. Micheli and Mocelin [52] presented an adaptive remesher coupled with mesh boxes used to mesh very precisely the area where adiabatic shear bands.

After error estimation and distortion metrics are calculated, the next step is **mesh generation**. Structured and unstructured meshes can be used in the discretization of the domain. Also, in the literature three different refinement approaches have been proposed and used: h-version, in which the density of the finite elements is increased using the same interpolation order in the elements,

the p-version, in which the finite element is fixed and the interpolation order of the elements is increased; and the hp-version, which is an hybrid of the two approaches. Marusich and Ortiz [25] present an h refinement scheme plus continuous Delaunay triangulation at the nodes in their spatial position. Sekhon and Chenot [24] create a completely new finite element mesh based on a Delaunay-Voronoi type algorithm each time one or more elements of the mesh have got overly distorted. Peric et al. [82] present a remeshing scheme using quadrilaterals (constructed using Delaunay triangulation). The remeshing schemes presented above were applied to the numerical simulation of metal cutting in [24-26].

After creating a new mesh, the transfer of displacement, temperatures, pressure as nodal variables and history-dependent variables as Gauss point variables from the old mesh to a new mesh is required. The main goal of a transfer operator is the minimization of the numerical diffusion of the state variables. Ortiz and Quigley [80], proposed a transfer operator based on the weak form of the equilibrium equations in conjunction with the interpolation of nodal variables and apply it in the context of strain localization problems. That transfer operator has been applied in the numerical simulation of metal cutting by Marusich and Ortiz [25]. Lee and Bathe [81], Peric et al. [82, 83] present an adaptive mesh strategy for large deformation problems, which uses a different transfer operator for nodal variables and gauss point variables. The nodal variables use the inverse isoparametric mapping. The gauss point variables are smoothed to the nodes of the old mesh followed by transfer to the nodes of the new mesh and, finally interpolated to the Gauss points. This error estimator has been applied in the numerical simulation of high speed machining in [26, 82].

1.4.6 Workpiece-chip separation criteria

Material separation is a complex phenomenon involving many physical processes occurring at the micromechanical level. Fracture begins at the micromechanical scale and eventually macroscopic fracture is observed. As a consequence, the chip separation is one of the stumbling blocks in the numerical simulation of metal cutting process. The methodologies used in the literature to model chip separation can be classified as follows: continuous chip separation along a predefined cutting plane or chip separation using element deleting or killing elements based on some element deleting indicator, and the last option is based on large plastic deformations and continuous remeshing.

There are basically two types of indicators: those based on geometrical and physical considerations. Some examples of the most common indicators used in the numerical simulations with FEM are listed below: (a) a chip separation criterion based on the distance between the tool tip and the nearest node along a predefined cutting direction, (b) constant equivalent strain criterion, (c) maximum shear stress criterion, (d) Johnson–Cook fracture model and (d) Cockroft–Latham criterion.

The equivalent strain criterion has been a popular failure criterion for metal cutting simulations [27]. In this approach fracture is assumed to occur when plastic strain calculated at the nearest node to the cutting edge, reaches a critical value. The drawback of this method is, if uncontrolled, node separation propagates faster than the cutting speed, as a result forming a large crack ahead the tool tip.
Similarly a critical stress criterion has also been suggested where node separation is activated once the material reaches a critical stress value [84].
The Johnson–Cook failure criterion is based on the postulation that the critical equivalent fracture strain is a function of stress triaxiality, strain rate and temperature. The Johnson–Cook fracture model is semi-empirical in nature and necessitates the determination of constants from tensile tests with high triaxiality, shear tests and Hopkinson bar torsion tests at varying temperatures and strain rates. Jcohson-Cook fracture model has been used to model machining of titanium alloy (Ti-6Al-4V) in [85].
Another fracture model implemented in machining simulation is the Cockcroft–Latham fracture criterion [86, 87].
Adaptive remeshing has been used in 1[24-26, 52] as a strategy to separate the chip form the workpiece.

1.4.7 Chip segmentation and breakage

The process of segmented and discontinuous chip formation involves the propagation of fractures through the deforming chip. Chip segmentation by shear localization is an important characteristic which can be observed in a certain range of cutting speeds when machining materials like titanium. Experimental studies have shown that shear localization in machining titanium alloys is due to the occurrence of thermo-plastic instability and ductile fracture. Instead, structural steels can fracture in a ductile or a brittle manner depending on cutting conditions.
Marusich and Ortiz [25] present a brittle fracture criteria formulated in terms of the toughness, K_{IC}, used in conjunction with a multi-fracturing algorithm and a ductile fracture expressed in terms of the fracture strain, derived from Rice and Tracey`s void growth criterion. The brittle or ductile fracture criterions are used depending on the machining conditions.
Owen and Vaz [26] present a fracture criteria based on the equivalent plastic strain and the uncoupled integration of Lemaitre`s damage model. These fracture criteria are able to model the material failure (thermal softening/failure softening) in problems involving adiabatic strains localization, where high speed cutting is a representative example. Boroushaki et al. [88] and Umbrello [86, 89] also included damage mechanics in the simulation of crack propagation based on Lemaitre's model.
Umbrello et al. [90] is employed Brozzo`s criterion to predict the effect of hydrostatic stress on the chip segmentation during orthogonal cutting.

Ceretti et al. [87] combined the Cockroft and Latham criterion with a criterion based on the effective stress in order to optimize the material fracture in cutting operations.
Chen et al. [85] use the Johnson–Cook fracture model to simulate serrated chip formation in titanium alloy (Ti-6Al-4V) high speed machining.

1.5 Numerical simulation of Metal Machining (Meshless Methods): State of the Art

1.5.1 Smooth Particles Hydrodynamics (*SPH*)

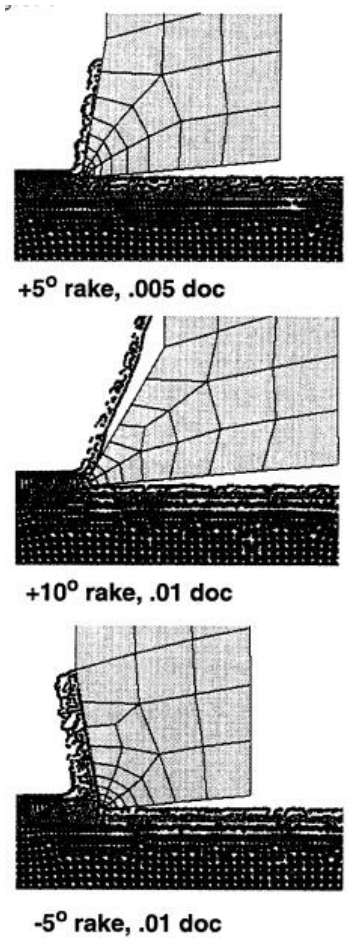

SPH simulation of cutting Aluminium 6061-T6 at different rake angles and feeds [3]

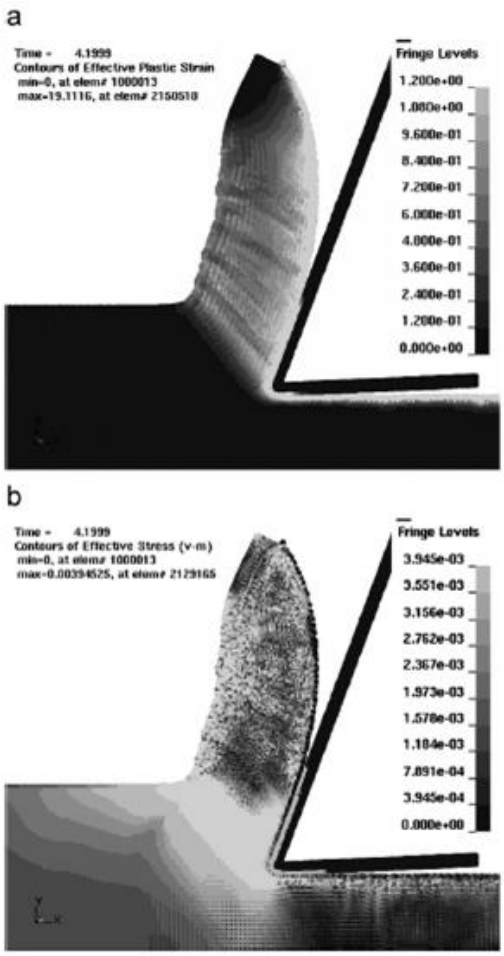

SPH simulation of cutting Aluminium 6061-T6 [12]

Figure 6. Numerical simulation of metal cutting processes using SPH

The first element free Lagrangian technique applied to cutting process is *SPH* (Smoothed Particle Hydrodynamics).First, Heinstein et al. [3] applied the *SPH* method for orthogonal cutting process simulations. Then, Limido et al. [12] apply *SPH* to high speed numerical cutting of an Al6061 Aluminum alloy using the commercial software Ls-Dyna. Authors reports that *SPH* results are in good

agreement with the experimental observations and numerical simulations carried out with AdvantEdge. The main advantage of *SPH* is that it does not need a finite element mesh to calculate derivatives. Material properties and state variables are available at a set of points, called particles. This avoids severe problems associated with mesh tangling and distortion which usually occur in Finite Element Lagrangian formulations involving large deformation and strain rates. In *SPH* the value of a function, or its derivative can be estimated at any particle *i* based in the set of particles that are within a given distance h from *i* particle. One of the advantages of *SPH* is the natural workpiece-tool separation; the workpiece matter flows naturally around the tip tool. An additional advantage of *SPH* is contact handling, because contact is modeled as a particle interaction and friction parameters (like Coulomb friction parameter) do not have to be defined. The main disadvantage of *SPH* in comparison with *FEM* is the neighbours search, because updating the data base of neighbor particles takes usually a long time in comparison with other calculations needed during each time step. One example of the numerical simulation of metal cutting processes using *SPH* is shown in Figure 6.

1.5.2 Finite Point Set Method (*FPM*)

Uhlmann et al. [9, 91] apply the Finite Point Set Method (*FPM*) to model cutting of Inconel 718. *FPM* is an implicit scheme which is based on the differential form of the conservation laws of mass, momentum and energy. In detail, *FPM* is a generalized Finite Difference scheme based on Moving Least Square Method (*MLS*). The main advantages of *FPM* are: 1) Remeshing is avoided by the mesh free approach, 2) Numerical losses due to remeshing does not occur, 3) Because

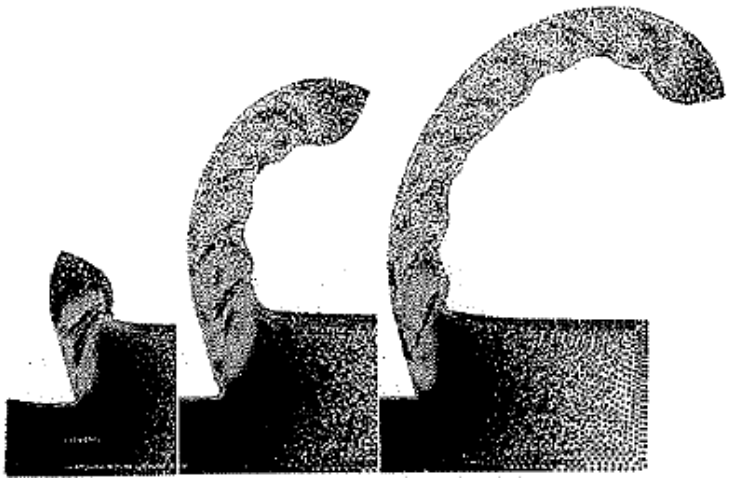

Figure 7. Numerical simulation of metal cutting processes using Finite Point Set Method.[9]

FPM is a lagrangian formulation allows for an easy way to represent free and dynamics boundaries. Some disadvantages of the *FPM* are: 1) Relatively high computational cost in comparison to *FEM*, due to the high number of neighbours that each node has in *FPM* compared to *FEM*. In the referenced work, the authors consider the tool as rigid, and no heat transfer between the tool and the piece. Moreover, authors say that *FPM* needs further development to simulate a more realistic chip formation process. There are some similarities between *SPH* and *FPM*, because both use a sphere of influence to study particles interaction, but *SPH* uses for field function approximation the kernel approximation while *FPM* uses Moving Least Squares. One example of the numerical simulation of metal cutting processes using Finite Point Set Method (*FPM*) is shown in Figure 7.

1.5.3 Constrained Natural Element Method (CNEM)

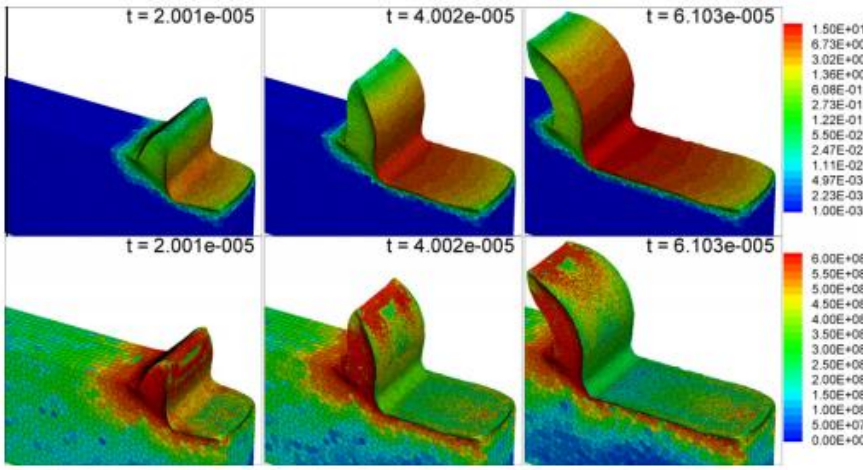

Figure 8. Numerical simulation of metal cutting processes using CNEM.[6]

Illoul et al. [6] applied *CNEM* to 3D numerical simulation of orthogonal and oblique cutting of a Ti-6A-4V alloy. The *CNEM*'s shape functions are built using the constrained Voronoi diagram. *CNEM* involves three main steps. First, the constrained Voronoi diagram is built. Thus, for each node, a Voronoi cell is geometrical defined. Then, *CNEM* shape functions are computed. Finally, using a variational formulation, internal and external forces, acceleration, velocities and displacements are calculated. In *CNEM*, state variables are available on particles, so there is no numerical diffusion due to an update of the Voronoi diagram. Furthermore, *CNEM* does not need chip-workpiece separation criteria. The main disadvantage of *CNEM* is the computer time need to calculate shape functions. Another disadvantage is the necessity to remesh surfaces, due to surfaces folds, excessive elongations or where nodes become too close. The numerical results presented by Illoul and Lorong have not been validated against

experiments. Figure 8 shows an example of a numerical simulation of metal cutting using *CNEM*.

1.5.4 Discrete Element Method (*DEM*)

Fleissner et al. [4] applied *DEM* method to orthogonal cutting process simulations. The authors represented the workpiece as a bulk of identical spheres arranged in a face centered cubic lattice. Particles interact by a visco-elasto-plastic law neglecting thermal effects. The numerical model of metal cutting presented in that work was not validated against experimental results. In contrast to other meshless methods, which are mainly designed to solve partial differential equations that describe the physical phenomena, *DEM* accounts for the simulations of particle interactions. *DEM* developers recommend this technology to problems which involves breakage, rupture and large deformations, and together with contact of multiple bodies. Precisely, the numerical ingredients needed for simulation of orthogonal cutting. However, at the same time, *DEM* developers recognize that *FEM* is superior to *DEM* for problems where small elastic strain are of interest or for the investigation on mode shape of structural oscillations. *DEM* needs to be further developed to predict accurate chip formation. One example of the numerical simulation of metal cutting processes using Discrete Element Method (*DEM*) is shown in Figure 9.

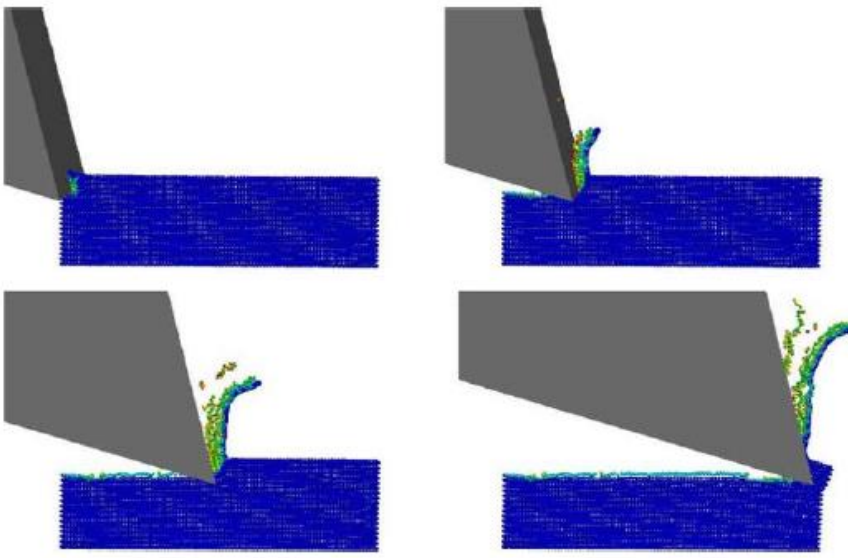

Figure 9. Numerical simulation of metal cutting processes using DEM.[4]

Eberhard and Gaugele [92] show the applicability of the *DEM* for modeling of an orthogonal cutting process of steel and aluminum. In that work, particles interact by a visco-elasto-plastic law including thermal effects. The numerical results are examined by comparing the simulated forces acting on the tool with experimentally obtained forces. Results presented in [92] shown that using a workpiece with a regular lattice the cutting force component can be reproduced very nicely whereas the passive force shows considerable deviation. Instead, modeling a cutting process with a random lattice workpiece fails to reproduce basic qualitative characteristics of metal cutting. Furthermore, Eberhard and Gaugele [92] identifies that the main challenge of *DEM* is to find appropriate force laws and parameters in order to synthesize the solid with correct physical properties whereas the difficulty with *FEM* is found with regard to separation of material and remeshing. Eberhard and Gaugele [92] suggest that some ingredients of *SPH* can be added to *DEM* to overcome its drawbacks.

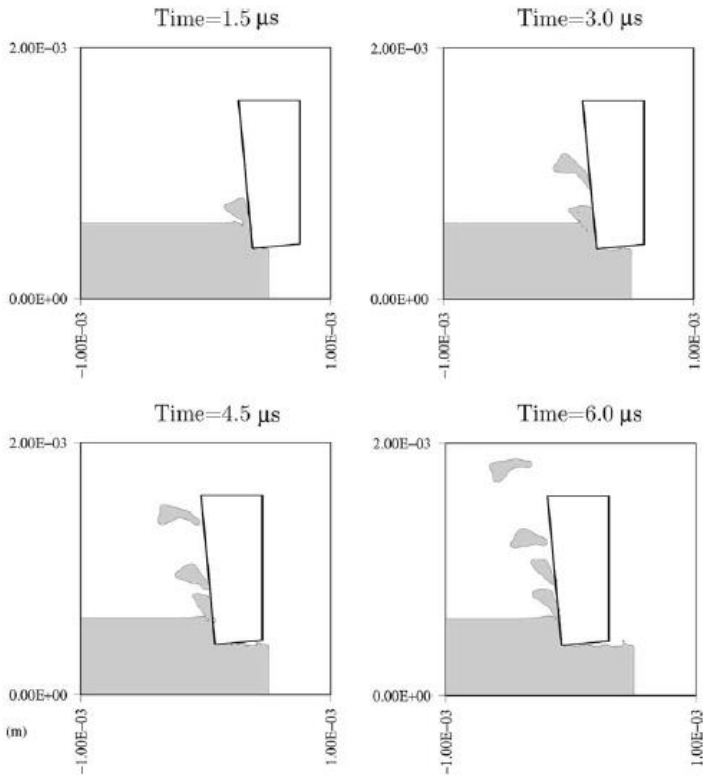

Figure 10. Numerical simulation of metal cutting processes using Multi Material Eulerian Formulation.[10]

1.6 Improved Eulerian Formulation: State of the Art

1.6.1 Multi material Eulerian Method (*MMEM*)

Eulerian formulations can be improved using a Multi-material Eulerian (*MMEM*) method [10, 93] based on finite elements. The Multi-material Eulerian strategy is able to deal with large deformations and free surface generation, which usually take place in the numerical simulation of machining processes. *MMEM* overcomes the main disadvantage of standard Eulerian Formulation. Typically, the contact in *MMEM* is based on mixtures theory. The main disadvantage of Multi material Eulerian formulation is the contact strategy between the chip and the work piece, because mixtures theory does not predict

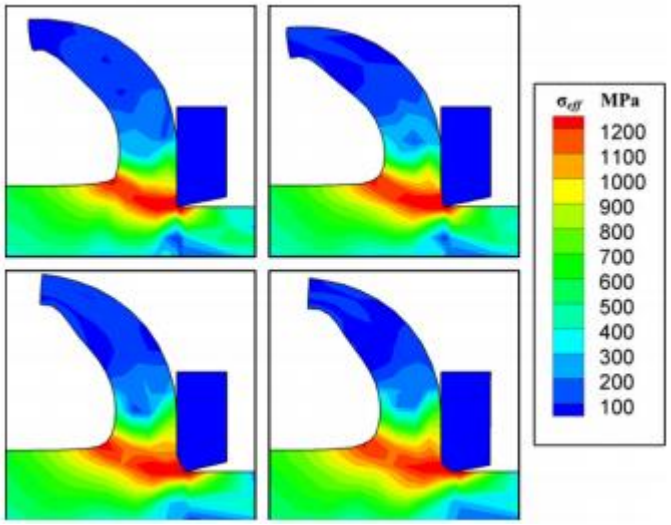

Figure 11. Numerical simulation of metal cutting processes using an Eulerian Formulation and a Volume of Solid Approach. [8]

well the friction phenomena at the tool-chip interface. Recently, Vitali et al. [94] improve *MMEM* using *X-FEM* at the interface where two materials come in contact, getting as a result a discontinuity in the velocity field at interfaces and as a consequence predicting well the friction phenomena. *MMEM* has been applied to the numerical simulation of AISI 4340 steel under orthogonal cutting conditions in [10], getting results that agree well with experimental results. The numerical simulation presented in that work used a rigid tool; friction is neglected and does not take into account heat transfer between the tool and the workpiece. One example of the numerical simulation of metal cutting processes using the Multi Material Element Method is shown in Figure 10.

1.6.2 Volume of Solid *(VOS)*

Al-Athel et al. [8] propose a new strategy to simulate orthogonal cutting based on a modified Finite Element Eulerian formulation and a Volume of Solid (*VOS*) Approach. Finite Element Eulerian *VOS* formulation uses the advantages of an Eulerian formulation plus a numerical scheme (*VOS*) that can track the free surface of the material and model the unconstrained flow of the chip without being limited to only steady state scenarios with an assumed shape for the deformed chip. The results from numerical simulations showed good agreement in values and behavior with the ones obtained from ALE and experiments. Authors remarks that Eulerian *VOS* formulation is only able to

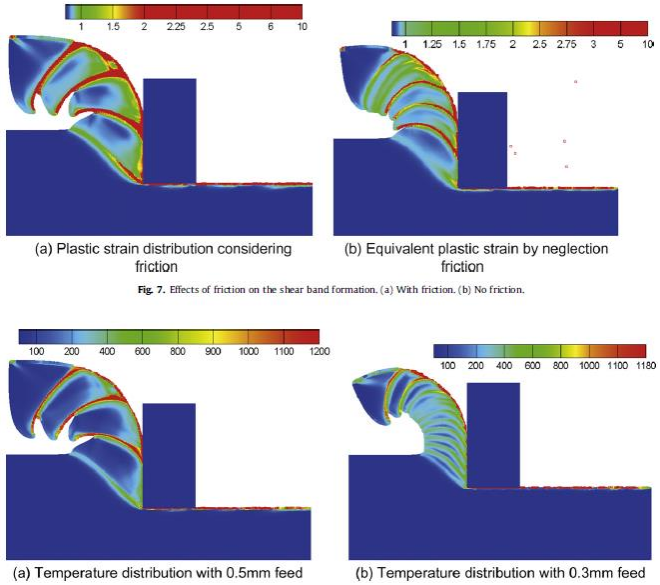

Fig. 7. Effects of friction on the shear band formation. (a) With friction. (b) No friction.

Figure 12. Numerical modeling of metal cutting processes using Material Point Method (MPM).[5]

predict continuous chip formation and cannot handle segment chip. Then main advantage of Eulerian *VOS* formulation is that does not require any mesh motion scheme or remeshing strategy.

1.6.3 Material Point Method (*MPM*) or Point in Cell (*PIC*)

The material point method (*MPM*), introduced initially in fluid dynamics by [95] and applied to orthogonal cutting simulations by [96] and [5]. In the material point method, state variables are traced at a set of points (materials points) defined independently of an Eulerian mesh on which the equations of motions are formulated and solved. More in detail, the weak form is solved on a background mesh at each time step and the computed acceleration is used to

update the particle positions. Later the updated particle data is used to reinstate the position and coordinates of the background mesh nodes. As the mesh is defined in an arbitrary way, the problem of mesh distortion, which leads to difficulties in Lagrangian *FEM*, is avoided. Another advantage of *MPM* is the easy way to solve free surface problems. The main drawback of the material point method is related to the condition of stability for the procedure of time integration of dynamics equations. Because for a given inter particle distance equivalent to a certain mesh size, the critical time step used in *MPM* is many times smaller than in case of standard *FEM*. Furthermore, strain localization in *MPM* is very sensitive to the density of materials points used in the calculation. Also, MPM needs more memory in comparison with standard *FEM*, because it is necessary to save information of the Eulerian mesh and Lagrangian particles. Ambati and co-workers [5] compared *MPM* and *FEM* in terms of the plastic strain field and temperature field, finding a good agreement between the numerical simulations. Also, the comparison shows that MPM provides a smoother chip formation and less strain localization than FEM.

1.7 Particle Finite Element Method (*PFEM*)

The initial developments of the Particle Finite Element Method (*PFEM*) took place in the field of fluid mechanics [97], because PFEM facilitates tracking and modeling of free surfaces. Later on, the Particle Finite Element (*PFEM*) was applied in a variety of simulation problems: fluid structure interaction with rigid bodies, erosion processes, mixing processes, coupled thermo-viscous processes and thermal diffusion problems [98, 99]. First applications of *PFEM* to solid mechanics were done in problems involving large strains and rotations, multi body contacts and creation of new surfaces (riveting, powder filling and machining) [100]. In this work we extended the Particle Finite Element Method to the numerical simulation of metal cutting processes.

In the *PFEM*, the continuum medium, considered as an infinite pack of particles each of them of infinitesimal size, is represented by *a finite set (or a cloud)* of infinitesimal-sized particles. The particles of the cloud describe and contain the properties of the continuum medium (displacement, pressure, temperatures, strains, stresses, internal variables, etc.) at their instantaneous locations, and, when necessary, the properties of the other particles of the continuum are obtained by interpolation from those in the cloud.

The *PFEM* is characterized by two basic ingredients:

1) A Delaunay triangulation is generated at each time step connecting the particles of the cloud on the basis of their updated positions (see [101]): this triangulation is used as the finite element mesh during the time step, and, when necessary for computational purposes, the properties of the particles (e.g. at the nodes of the mesh) are interpolated to the Gauss points. Due to the optimal properties of Delaunay triangulations for minimizing angle distortions, *this continuous re-meshing minimizes the element distortions making the method suitable and advantageous, in terms of reliability and robustness*, in front of

more classical finite element methods. Specifically the method becomes suitable for simulation of those industrial problems displaying "material flow" (cutting processes, granular material flow, metal forming processes, etc.).

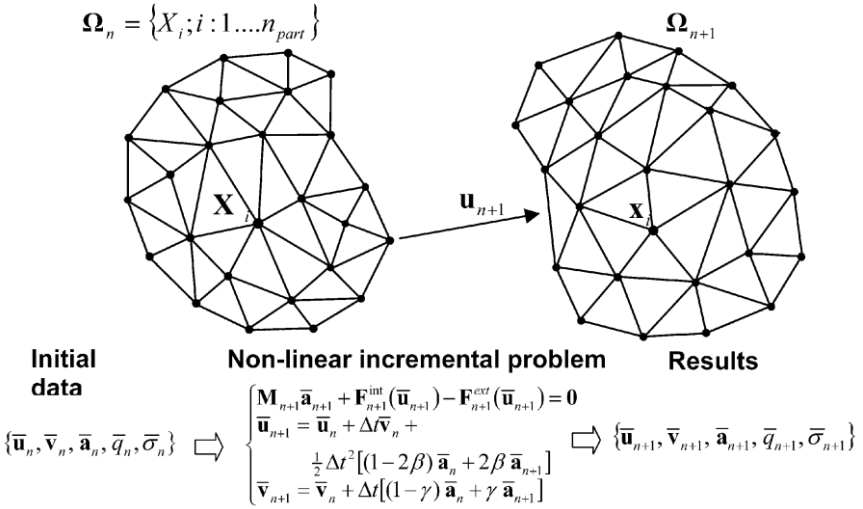

Figure 13. Sketched Particle Finite Element Method (PFEM) at time-step $[t_n, t_{n+1}]$

2) Boundary recognition techniques can be naturally used in the *PFEM* (e.g. alpha-shape techniques). This facilitates modeling those complex mechanical processes in which new boundaries, different from the initial ones, appear.

Figure 14 shows a numerical simulation using *PFEM* of *continuous chip formation*, but also the more complex *serrated chip formation*. Details about material properties, tool velocity, and tool shape used in the numerical simulations will

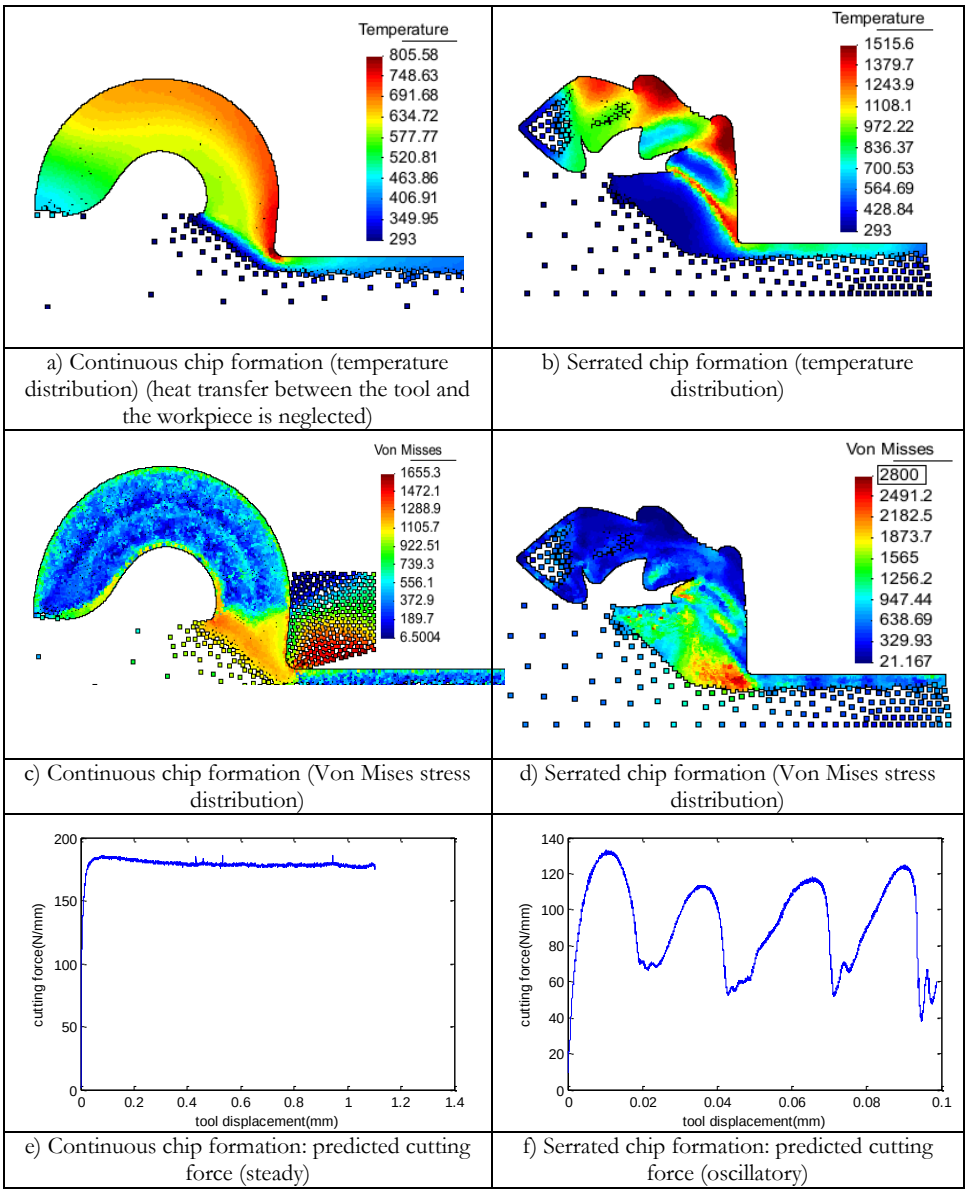

a) Continuous chip formation (temperature distribution) (heat transfer between the tool and the workpiece is neglected)

b) Serrated chip formation (temperature distribution)

c) Continuous chip formation (Von Mises stress distribution)

d) Serrated chip formation (Von Mises stress distribution)

e) Continuous chip formation: predicted cutting force (steady)

f) Serrated chip formation: predicted cutting force (oscillatory)

Figure 14. Numerical simulation of continuous and serrated chip formation using PFEM

be given in the following chapters.

1.8 Work Outline

The remainder of this work is organized as follows.

Chapter 2 explains the numerical scheme developed to model metal cutting process using *PFEM*. Details are given about the finite element discretization of the governing equations using mixed finite elements, the remeshing procedure, the contact modeling at the tool chip interface, the time integration equation of balance equations and integration of the thermo-elastoplastic constitutive equations. Some examples are presented which validated the set of numerical tools developed in this work.

In chapter 3 some examples are presented which validated the set of numerical tools developed in this work, ans then a set of numerical simulations of metal cutting processes using *PFEM* is presented. This chapter presents a comparison of explicit, IMPLEX and implicit time integrations schemes in terms of computing time at a given cutting speed, a study which show a dependency of chip shape on cutting speed for a titanium alloy (Ti6Al4V), a set of examples which show the influence of the rake angle on chip shape, some examples are presented which show the influence of tool stiffness on cutting forces and chip shape and finally, and some examples study the influence of friction at the tool chip interface.

Chapter 4 present a sensibility analysis to geometric and cutting conditions like the tool velocity, the tool radius, the rake angle, and the undeformed chip thickness using PFEM by means of a Design of Experiments (DoE) methodology. Then, we compare the sensibility of process variables like cutting forces, feed forces, deformed chip thickness, and contact length, etc., to cutting conditions given by *PFEM* with the sensibility predicted through (Abaqus, AdvantEdge, Deform) and experiments. Also chapter 4 identifies the advantages and drawbacks of *PFEM* over *FEM* and meshless strategies.

The last chapter summarizes the main conclusions and achievements of the work and describes open lines of research.

Chapter 2

2 The Particle Finite Element Method in the numerical simulation of metal cutting processes

Numerical simulations of metal cutting process has proved to be particularly complex due to the diversity of the physical phenomena involved, including heat conduction, contact with friction, dynamics effects and thermo-mechanical coupling. This chapter presents the mathematical and numerical ingredients necessary to simulate metal cutting, including the balance of momentum and its finite element discretization, the balance of energy and its finite element discretization. In addition, the constitutive equations for the tool and the workpiece and its time discretization, the adaptative and remeshing scheme using the Particle Finite Element method (PFEM) applied to the workpiece, the contact problem between the tool and the workpiece, and the global finite differences time integration scheme are presented.

In the following section, we present the continuum formulation of the couple thermo-mechanical multi-body frictional contact problem.

2.1 Problem statement

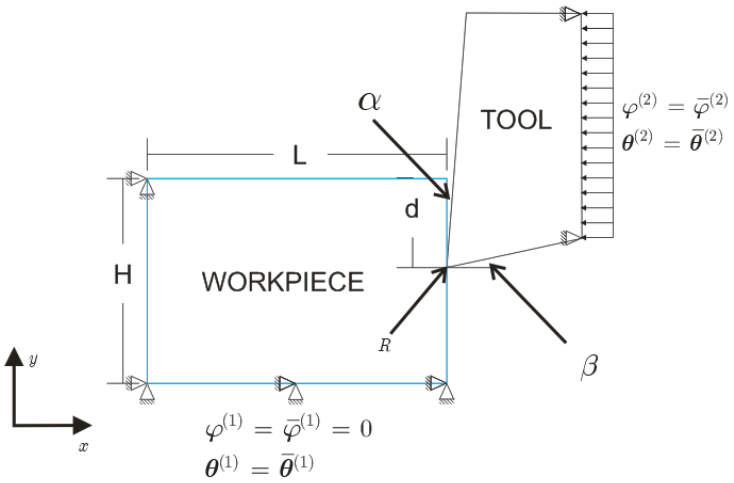

Figure 15. Model of unsteady chip formation

The model of unsteady chip formation to be studied is shown in Figure 15. The tool is considered rigid or deformable, having a given rake angle α, a flank angle β and tool radius R. The tool is moved at a constant speed in the negative x

direction. The workpiece is considered isotropic and initially unstressed, having a height H and a length L. Displacement constraints in the x and y direction are imposed on the left end and on the bottom of the workpiece. The cut depth is d . Body acceleration, heat generation through plastic work dissipation and friction, and heat transfer at the tool chip interface are included in the analysis.

2.2 Basic notation

Let $n_{\text{dim}} = 2$ be the space dimension and $I := [0,T]$ the time interval of interest. Let Ω^1 and Ω^2 with smooth boundaries $\partial\Omega^1$ and $\partial\Omega^2$, be the reference placement of two continuum bodies β^1 (the workpiece) and β^2 (the tool), with material particles labeled $\mathbf{X}^1 \in \Omega^1$ and $\mathbf{X}^2 \in \Omega^2$.

Denote by $\mathbf{x}^{(i)} = \boldsymbol{\varphi}^{(i)}(\mathbf{X}^{(i)},t)$ the deformation map of the body $\beta^{(i)}$, with displacement of a material particle $\mathbf{u}^{(i)}(\mathbf{X}^{(i)},t) = \boldsymbol{\varphi}^{(i)}(\mathbf{X}^{(i)},t) - \mathbf{X}^{(i)}$, with material velocity $\mathbf{V}^{(i)} := \partial_t \boldsymbol{\varphi}^{(i)}(\mathbf{X}^{(i)},t)$, with acceleration $\mathbf{A}^{(i)} := \partial_t \mathbf{V}^{(i)}(\mathbf{X}^{(i)},t)$, deformation gradient $\mathbf{F}^{(i)} = D\boldsymbol{\varphi}^{(i)}(\mathbf{X}^{(i)},t)$ and absolute temperature $\boldsymbol{\theta}^{(i)}$. Certain conditions must be imposed on the map $\boldsymbol{\varphi}^{(i)}(\mathbf{X}^{(i)},t)$ in order for it to represent the deformation of a material body. In particular, we assume (i) $\boldsymbol{\varphi}^{(i)}(\mathbf{X}^{(i)},t)$ is one to one (two or more materials points cannot simultaneously occupy the same spatial position), and (ii) $\det(\mathbf{F}^{(i)}) > 0$ (deformation should present the orientation of the body). For each time $t \in I$, $\boldsymbol{\varphi}^{(i)}(\mathbf{X}^{(i)},t)$ represent a one-parameter family configurations indexed by time $t \in I$, which maps the reference placement of the body $\beta^{(i)}$ onto its current placement $S_t^{(i)} = \boldsymbol{\varphi}^{(i)}(\beta^{(i)})$

In the current configuration, the velocity $\mathbf{v}^{(i)}(\mathbf{x}^{(i)},t)$ and acceleration $\mathbf{a}^{(i)}(\mathbf{x}^{(i)},t)$ of a particle which assumes a point $\mathbf{x}^{(i)}$ at time t is given by

$$\mathbf{v}^{(i)}(\mathbf{x}^{(i)},t) = \mathbf{v}^{(i)}(\boldsymbol{\varphi}^{(i)}(\mathbf{X}^{(i)},t),t) = \mathbf{V}^{(i)}(\mathbf{X}^{(i)},t) \tag{2.1}$$

$$\begin{aligned}\mathbf{a}^{(i)}(\mathbf{x}^{(i)},t) &= \mathbf{a}^{(i)}(\boldsymbol{\varphi}^{(i)}(\mathbf{X}^{(i)},t),t) = \mathbf{A}^{(i)}(\mathbf{X}^{(i)},t) \\ &= \frac{\partial \mathbf{v}^{(i)}(\mathbf{x}^{(i)},t)}{\partial t} + grad\ \ \mathbf{v}^{(i)}(\mathbf{x}^{(i)},t)\ \ \mathbf{v}^{(i)}(\mathbf{x}^{(i)},t)\end{aligned} \tag{2.2}$$

The first term is known as the local derivative and the second term is the convective part of the time derivative.

We will assume that no contact forces between the tool and the workpiece are present at the reference configuration. The movement of the tool cause the two bodies come in contact and produce interactive forces.

We will denote as the contact surface $\Gamma^{(i)} \subset \partial\Omega^{(i)}$ the part of the boundary of the body such that all material points where contact occurs at any time $t \in I$ are included. The current placement of the contact surface is given by $\gamma^{(i)} = \boldsymbol{\varphi}^{(i)}(\Gamma^{(i)}, t)$.

2.3 The coupled Thermo-mechanical IBVP with frictional Contact Constraints

We describe below the system of partial differential equations governing the evolution of the thermo-mechanical initial boundary value problem. To describe the workpiece behavior, we will adopt constitutive equations that incorporate finite strain elasto-plasticity and the multiplicative decomposition of the deformation gradient. To describe the tool behavior, we will use a Neo-Hookean material model. Frictional contact constraint will be introduced using a penalized technique and the Norton Hoff Constitutive Law.

2.3.1 Balance equations

The coupled thermo-mechanical initial boundary value problem is governed by the momentum and energy balance equations, restricted by the second law of thermodynamics. The material form of the local governing equations for the body $\beta^{(i)}$ can be written as

$$\begin{aligned} \dot{\boldsymbol{\varphi}}^{(i)} &= \mathbf{V}^{(i)} \\ \rho_0^{(i)} \dot{\mathbf{V}}^{(i)} &= \mathrm{DIV}(\mathbf{P}^{(i)}) + \mathbf{B}^{(i)} \\ \theta^{(i)} \dot{H}^{(i)} + \mathrm{DIV}(\mathbf{Q}^{(i)}) &= D_{\mathrm{int}}^{(i)} + R^{(i)} \end{aligned} \tag{2.3}$$

In the above equations $\rho_0^{(i)}$ is the reference density, $\mathbf{B}^{(i)}$ is the prescribed forces per unit of reference volume, is the reference divergence operator DIV , $\mathbf{P}^{(i)}$ and $\mathbf{S}^{(i)}$ are the first and the second Piola-Kirchhoff stress tensors, respectively. $\mathbf{V}^{(i)}$ is the velocity field, $H^{(i)}$ the entropy, $\mathbf{Q}^{(i)}$ the nominal heat flux, $R^{(i)}$ is the prescribed reference heat source and $D_{\mathrm{int}}^{(i)}$ is the internal dissipation per unite reference volume. In addition, the entropy $N^{(i)}$ and first Piola-Kirchhoff stress tensor $\mathbf{P}^{(i)}$ are formulated in terms of the free energy Ψ and subjected to the dissipation inequality often referred to as the Clausius Plank form of the second law of thermodynamics.

$$\begin{aligned} D_{\mathrm{int}}^{(i)} &= \mathbf{P}^{(i)} : \dot{\mathbf{F}}^{(i)} + \theta^{(i)} \dot{N}^{(i)} - \dot{E}^{(i)} \geq 0 \\ &= \mathbf{P}^{(i)} : \dot{\mathbf{F}}^{(i)} - \dot{\theta}^{(i)} N^{(i)} - \dot{\Psi}^{(i)} \geq 0 \end{aligned} \tag{2.4}$$

In (2.4), the free energy function is obtained from the internal energy via the Legendre transformation

$$\Psi^{(i)} = E^{(i)} - N\theta^{(i)} \tag{2.5}$$

The nominal heat flux $\mathbf{Q}^{(i)}$ is defined by Fourier's Law, subjected to the restriction on the dissipation by conduction $D_{con}^{(i)}$

$$D_{con}^{(i)} = -\frac{1}{\boldsymbol{\theta}}\mathrm{GRAD}(\boldsymbol{\theta}) \cdot \mathbf{Q}^{(i)} \geq 0 \tag{2.6}$$

The spatial form of the local governing equations for the body $\beta^{(i)}$ can be written as

$$\begin{aligned} \dot{\boldsymbol{\varphi}}^{(i)} &= \mathbf{v}^{(i)}(\mathbf{x}^{(i)}, t) \\ \rho^{(i)}\dot{\mathbf{v}}^{(i)} &= \mathrm{div}(\boldsymbol{\sigma}^{(i)}) + \mathbf{b}^{(i)} \\ \theta^{(i)}\dot{h}^{(i)} + \mathrm{div}(\mathbf{q}^{(i)}) &= D_{\mathrm{int}}^{*,(i)} + r^{(i)} \end{aligned} \tag{2.7}$$

In these equations, the motion $\boldsymbol{\varphi}^{(i)}$ and the absolute temperature $\boldsymbol{\theta}^{(i)}$ are regarded as the primary variables in the problem while $\mathbf{b}^{(i)}$ the body force per unit of spatial volume and $r^{(i)}$ the spatial description of the heat source per unit of spatial volume are prescribed data. In addition, the heat flux $\mathbf{q}^{(i)}$, the entropy $\eta^{(i)}$ as well as the Cauchy stress tensor $\boldsymbol{\sigma}^{(i)}$ are defined via constitutive equations. These constitutive equations are subjected to the following restrictions on the internal dissipation and the dissipation arising from heat conduction

$$\begin{aligned} D_{\mathrm{int}}^{*,(i)} &= \boldsymbol{\theta}^{(i)}\dot{\eta} + J^{(i)}\boldsymbol{\sigma}^{(i)} : \mathbf{d}^{(i)} - \dot{e}^{(i)} \geq 0 \\ D_{con}^{(i)} &= -\frac{\mathrm{grad}(\boldsymbol{\theta}^{(i)}) \cdot \mathbf{q}^{(i)}}{\boldsymbol{\theta}^{(i)}} \geq 0 \end{aligned} \tag{2.8}$$

where we have used the Legendre transformation

$$\hat{\psi} = e - \eta\theta \tag{2.9}$$

2.3.2 Boundary conditions

The basic governing equations (2.3) or (2.7) and the constitutive restrictions (2.4) -(2.6) or (2.8) are supplemented by the standard boundary conditions for the mechanical field

$$\begin{aligned} \boldsymbol{\varphi}^{(i)} &= \bar{\boldsymbol{\varphi}}^{(i)} && \text{on } \Gamma_{\boldsymbol{\varphi}}^{(i)} \\ \mathbf{t}^{(i)} &= \mathbf{P}^{(i)} \cdot \mathbf{N}^{(i)} = \bar{\mathbf{t}}^{(i)} && \text{on } \Gamma_{\boldsymbol{\sigma}}^{(i)} \end{aligned} \tag{2.10}$$

where $\bar{\boldsymbol{\varphi}}^{(i)}$, $\bar{\mathbf{t}}^{(i)}$ are prescribed deformation and nominal tractions.
Together with the analogous essential and natural boundary conditions for the thermal field, namely,

$$\begin{aligned} \boldsymbol{\theta}^{(i)} &= \bar{\boldsymbol{\theta}}^{(i)} && \text{on } \Gamma_{\boldsymbol{\theta}}^{(i)} \\ \mathbf{Q}^{(i)} \cdot \mathbf{N}^{(i)} &= Q^{(i)} && \text{on } \Gamma_{Q}^{(i)} \end{aligned} \tag{2.11}$$

where $\bar{\boldsymbol{\theta}}^{(i)}$ and $Q^{(i)}$ are prescribed temperature and normal heat flux maps.

As usual, it is assumed that the following conditions hold

$$\begin{aligned}
&\Gamma_{\boldsymbol{\varphi}}^{(i)} \cup \Gamma_{\boldsymbol{\sigma}}^{(i)} \cup \Gamma^{(i)} = \partial\Omega^{(i)} \\
&\Gamma_{\boldsymbol{\varphi}}^{(i)} \cap \Gamma_{\boldsymbol{\sigma}}^{(i)} = \Gamma_{\boldsymbol{\varphi}}^{(i)} \cap \Gamma^{(i)} = \Gamma_{\boldsymbol{\sigma}}^{(i)} \cap \Gamma^{(i)} = \varnothing \\
&\Gamma_{\boldsymbol{\theta}}^{(i)} \cup \Gamma_{Q}^{(i)} \cup \Gamma^{(i)} = \partial\Omega^{(i)} \\
&\Gamma_{\boldsymbol{\theta}}^{(i)} \cap \Gamma_{Q}^{(i)} = \Gamma_{\boldsymbol{\theta}}^{(i)} \cap \Gamma^{(i)} = \Gamma_{Q}^{(i)} \cap \Gamma^{(i)} = \varnothing
\end{aligned} \tag{2.12}$$

2.3.3 Initial conditions

Additionally, we assume that the following initial data is specified for the mechanical and thermal fields

$$\left.\begin{aligned}
&\boldsymbol{\varphi}^{(i)}(\mathbf{X}^{(i)},t)\Big|_{t=0} = \bar{\boldsymbol{\varphi}}_{0}^{(i)}(\mathbf{X}^{(i)}) \\
&\mathbf{V}^{(i)}(\mathbf{X}^{(i)},t)\Big|_{t=0} = \bar{\mathbf{V}}_{0}^{(i)}(\mathbf{X}^{(i)}) \\
&\theta(\mathbf{X}^{(i)},t)\Big|_{t=0} = \bar{\theta}_{0}^{(i)}(\mathbf{X}^{(i)})
\end{aligned}\right\} \quad in \quad \Omega^{(i)} \tag{2.13}$$

2.3.4 Boundary conditions at the tool-chip interface

For each material point $\mathbf{X}^{(1)} \in \Gamma^{(1)}$ at any time $t \in I$, we require that the contact force and normal heat conduction flux induced on the body β^2 (the tool) at the material point $\bar{\mathbf{X}}^{(2)}$ be equal and opposite to that produced on body β^1 (the workpiece) at $\mathbf{X}^{(1)}$. Mathematically, these equilibrium conditions take the form

$$\begin{aligned}
&\mathbf{t}^{(1)}(\mathbf{X}^{(1)},t)d\Gamma^{(1)} + \mathbf{t}^{(2)}(\bar{\mathbf{X}}^{(2)},t)d\Gamma^{(2)} = 0 \\
&Q_{hc}^{(1)}(\mathbf{X}^{(1)},t)d\Gamma^{(1)} + Q_{hc}^{(2)}(\bar{\mathbf{X}}^{(2)},t)d\Gamma^{(2)} = 0
\end{aligned} \tag{2.14}$$

$$Q_{hc}^{(i)} = Q^{(i)} + R_{fric}^{(i)} \tag{2.15}$$

Where $Q_{hc}^{(i)}$ is the normal heat conduction flux at the contact interface and $R_{fric}^{(i)}$ is the heat source due to friction at the tool workpiece interface.
The heat sources due to frictional dissipation at the tool workpiece interface are related through the relationships (2.16)

$$R_{fric}^{(1)}(\mathbf{X}^{(1)},t)d\Gamma^{(1)} + R_{fric}^{(2)}(\bar{\mathbf{X}}^{(2)},t)d\Gamma^{(2)} = D_{fric}(\mathbf{X}^{(1)},t)d\Gamma^{(1)} \tag{2.16}$$

2.4 Global operator split for finite deformation plasticity

The IBVP (2.7) can be written in a simple way. Suppose that

$$\dot{\mathbf{Z}}^{(i)} = \begin{bmatrix} \dot{\boldsymbol{\varphi}}^{(i)} \\ \rho^{(i)}\dot{\mathbf{v}}^{(i)} \\ \dot{\theta}^{(i)} \end{bmatrix} \quad and \quad \mathbf{Z}^{(i)} = \begin{bmatrix} \boldsymbol{\varphi}^{(i)} \\ \mathbf{v}^{(i)} \\ \theta^{(i)} \end{bmatrix} \tag{2.17}$$

Then equations can be written in a generalized form as

$$\dot{\mathbf{Z}}^{(i)} = \mathbf{A}(\mathbf{Z}^{(i)}) + \mathbf{f}^{(i)} \tag{2.18}$$

Where A is a nonlinear elliptic operator and $f^{(i)}$ a prescribed function.

The Cauchy stress tensor $\boldsymbol{\sigma}^{(i)}$, the heat flux vector $\mathbf{q}^{(i)}$, the total $\eta^{(i)}$ and the plastic $\eta^{(i),p}$ entropies, and the mechanical dissipation $D_{\text{int}}^{(i)}$ will be regarded as dependent variables in the problem, defined in terms of the primary variables $\mathbf{Z}^{(i)}$ and a set of internal strain-like variables Γ. The set of internal variables are defined in terms of a constrained problem of evolution driven by the primary variables, with the functional form

$$\dot{\boldsymbol{\Gamma}}^{(i)} = \lambda^{(i)} \Pi^{(i)}(\boldsymbol{\Gamma}^{(i)}, \mathbf{Z}^{(i)}) \tag{2.19}$$

where $\lambda^{(i)}$ is an additional variable determined by means of the Kuhn-Tucker conditions, as follows

$$\lambda^{(i)} \geq 0 \quad \phi^{(i)}(\boldsymbol{\Gamma}^{(i)}, \mathbf{Z}^{(i)}) \leq 0 \quad \text{and} \quad \lambda^{(i)} \phi^{(i)}(\boldsymbol{\Gamma}^{(i)}, \mathbf{Z}^{(i)}) = 0 \tag{2.20}$$

and $\phi^{(i)}(\boldsymbol{\Gamma}^{(i)}, \mathbf{Z}^{(i)})$ is the Mises yield function

Generally, the nonlinear operator $\mathbf{A}$ can be decomposed in two simpler operators $\mathbf{A}_1$ and $\mathbf{A}_2$, where $\mathbf{A} = \mathbf{A}_1 + \mathbf{A}_2$ [102]. The use of the additive operator split applied to the coupled system of nonlinear ordinary differential equations leads to the following two simple problems

2.4.1 Isothermal elastoplastic step

$$\dot{\mathbf{Z}}^{(i)} = \begin{bmatrix} \dot{\boldsymbol{\varphi}}^{(i)} \\ \rho^{(i)} \dot{\mathbf{v}}^{(i)} \\ \dot{e}^{(i)} \end{bmatrix} = \begin{bmatrix} \mathbf{v}^{(i)}(\mathbf{x}^{(i)}, t) \\ \operatorname{div}(\boldsymbol{\sigma}^{(i)}(\boldsymbol{\varphi}^{(i)}, \theta^{(i)}, \lambda(\boldsymbol{\varphi}^{(i)}, \theta^{(i)}))) \\ 0 \end{bmatrix} + \begin{bmatrix} 0 \\ \mathbf{b}^{(i)} \\ 0 \end{bmatrix} \tag{2.21}$$

along with a set of first order differential equations that describe the evolution of the internal variables

$$\dot{\boldsymbol{\Gamma}}^{(i)} = \lambda^{(i)} \Pi^{(i)}(\boldsymbol{\Gamma}^{(i)}, \mathbf{Z}^{(i)}) \tag{2.22}$$

where the consistency parameter $\lambda^{(i)}$ is the Lagrange multiplier satisfying the Kuhn-Tucker conditions

$$\lambda^{(i)} \geq 0 \quad \phi^{(i)}(\boldsymbol{\Gamma}^{(i)}, \mathbf{Z}^{(i)}) \leq 0 \quad \text{and} \quad \lambda^{(i)} \phi^{(i)}(\boldsymbol{\Gamma}^{(i)}, \mathbf{Z}^{(i)}) = 0 \tag{2.23}$$

2.4.2 Thermoplastic step at fixed configuration

$$\dot{\mathbf{Z}}^{(i)} = \begin{bmatrix} \dot{\boldsymbol{\varphi}}^{(i)} \\ \dot{\mathbf{v}}^{(i)} \\ \rho^{(i)} \dot{e}^{(i)} \end{bmatrix} = \begin{bmatrix} 0 \\ 0 \\ \text{-div}(\mathbf{q}^{(i)}(\boldsymbol{\varphi}^{(i)}, \theta^{(i)}, \lambda(\boldsymbol{\varphi}^{(i)}, \theta^{(i)}))) + D_{\text{int}}^{(i)} \end{bmatrix} + \begin{bmatrix} 0 \\ 0 \\ \rho^{(i)} r^{(i)} \end{bmatrix} \tag{2.24}$$

along with a set of first order differential equations that describe the evolution of the internal variables

$$\dot{\boldsymbol{\Gamma}}^{(i)} = \lambda^{(i)} \Pi^{(i)}(\boldsymbol{\Gamma}^{(i)}, \mathbf{Z}^{(i)}) \tag{2.25}$$

where the consistency parameter $\lambda^{(i)}$ is the Lagrange multiplier satisfying the Kuhn-Tucker conditions

$$\lambda^{(i)} \geq 0 \quad \phi^{(i)}(\boldsymbol{\Gamma}^{(i)}, \mathbf{Z}^{(i)}) \leq 0 \quad \text{and} \quad \lambda^{(i)}\phi^{(i)}(\boldsymbol{\Gamma}^{(i)}, \mathbf{Z}^{(i)}) = 0 \tag{2.26}$$

it should be stated that the Kuhn-Tucker conditions apply only for rate independent plasticity models.

The set of first order differential equations that describe the evolution of the internal variables are presented in the next section.

The additive operator split together with a product formula algorithm will be used to solve the coupled system of nonlinear ordinary differentials equations.

2.5 Constitutive models

2.5.1 Tool constitutive model

Tools must be strong enough and rigid enough to resist fracture and to give a minimum deflection under load. In terms of materials properties, the elastic modulus and the yield stress must be higher in the tool than in the workpiece (the tool does not deform plastically). Moreover, due to the high temperatures present in metal cutting, the volumetric change in response to the change in temperature is present in the tool, and should be considered in the model. At the same time, we considered the tool material as isotropic, common assumption made in metal elasticity. A Neo-Hookean material [103, 104] with the following free energy function is used to represent the phenomenology mentioned above.

$$\hat{\psi}(\mathbf{C}) = \frac{1}{2}\kappa \ln^2(J) \; + \frac{1}{2}\mu\left[tr(\bar{\mathbf{C}}) - 3\right] - 3\beta\kappa\frac{\ln(J)}{J}(\theta - \theta_0) \tag{2.27}$$

where $\mu > 0, \kappa > 0$ and β can be interpreted as the shear modulus, the bulk modulus, and the thermal expansion coefficient, respectively. $\mathbf{C}, \bar{\mathbf{C}}, J$ are the right Cauchy-Green tensor, the volume preserving right Cauchy-Green tensor, the Jacobian of the deformation gradient and the temperature, respectively.

The free energy function $\hat{\psi}(\mathbf{C})$ satisfy the two following important properties:

$\hat{\psi}(\mathbf{C})$ is invariant when the current configuration undergoes a rigid body rotation, because $\hat{\psi}(\mathbf{C})$ only depends on the stretching part $\mathbf{U} = \sqrt{\mathbf{C}}$ and is independent of the rotation part $\mathbf{R}$ of $\mathbf{F}$ (Objectivity).

$\hat{\psi}(\mathbf{C})$ on any translated and/or rotated reference configuration is the same at any time t (Isotropy).

From equation (2.27) and applying, the standard Coleman-Noll procedure leads to a constitutive equation expressed in terms of materials variables (2.28).

$$
\begin{aligned}
\mathbf{S} &= 2\frac{\partial \hat{\psi}}{\partial \mathbf{C}} \\
&= 2\kappa \ln(J)\frac{1}{J}\frac{\partial J}{\partial \mathbf{C}} - 6\beta\kappa\frac{1-\ln(J)}{J^2}(\theta-\theta_0)\frac{\partial J}{\partial \mathbf{C}} + \mu\frac{\partial tr(\bar{\mathbf{C}})}{\partial \mathbf{C}} \\
&= \kappa\left(\ln(J) - 3\beta\frac{1-\ln(J)}{J}(\theta-\theta_0)\right)\mathbf{C}^{-1} + 2\mu J^{-\frac{2}{3}}\left(\mathbf{I} - \frac{1}{3}tr(\mathbf{C})\mathbf{C}^{-1}\right)
\end{aligned}
\tag{2.28}
$$

or in terms of spatial variables(2.29)

$$
\begin{aligned}
\boldsymbol{\sigma} &= \frac{1}{J}\mathbf{F}\mathbf{S}\mathbf{F}^T \\
&= \frac{\kappa}{J}\left(\ln(J) - 3\beta\frac{1-\ln(J)}{J}(\theta-\theta_0)\right)\mathbf{i} + 2\mu J^{-\frac{5}{3}}\mathrm{dev}(\mathbf{b})
\end{aligned}
\tag{2.29}
$$

The main reason to use hyperelasticity instead of small strain elasticity is due to the large displacement of the tool during the cutting process.

2.5.2 Workpiece Constitutive Model.

During metal cutting, the workpiece undergoes large deformations, therefore is necessary to include material and geometrical non-linearities in the constitutive model. Experimental results have shown that the workpiece stress-strain relationship is affected by the strain rate and temperature during plastic deformation. For the same value of strain, (i) the stress is higher for higher strain rate and (ii) the stress is lower for higher temperatures.
In this section, we consider the formulation of thermo-plasticity at finite strains with isotropic hardening, following the approach proposed by Simo et al. [102, 104, 105]. The strain and strain rate hardening and the thermal softening are taking into account with the following hardening laws: (i) Voce[106] and Simo et al. [107] (ii) Johnson and Cook [108] and (iii) Baker [109].

2.5.2.1 J_2 thermo-plasticity at finite strains

The formulation of the constitutive equations is based on two basic assumptions:

- The stress response is isotropic. Therefore, the free energy is independent of the orientation of the reference configuration.
- Furthermore, we assume that the plastic flow is isochoric (standard assumption in metal plasticity). It means

$$
\begin{aligned}
\det(\mathbf{F}^p) &= \det(\mathbf{C}^p) = 1 \\
\det(\mathbf{F}) &= \det(\mathbf{F}^e) = J^e = J
\end{aligned}
\tag{2.30}
$$

With these two assumptions, we proceed to outline the governing equations of the model.

2.5.2.2 Multiplicative decomposition of the deformation gradient

The main hypothesis to finite strain elastoplasticity is the multiplicative decomposition of the deformation gradient, into elastic and plastic parts

$$\mathbf{F}(\mathbf{X},t) = \mathbf{F}^e(\mathbf{X},t)\mathbf{F}^p(\mathbf{X},t) \tag{2.31}$$

This assumption admits the existence of a local unstressed intermediate configuration.

Following the standard conventions in continuum mechanics relative to the reference placement of the body, the right Cauchy-Green tensors are defined

$$\mathbf{C} \coloneqq \mathbf{F}^T\mathbf{F} \tag{2.32}$$

Emanating from decomposition(2.31), the plastic part of the Cauchy-Green tensor is defined as

$$\mathbf{C}^p \coloneqq \mathbf{F}^{p^T}\mathbf{F}^p \tag{2.33}$$

In the same way, the total and the plastic Green Lagrange strain tensor are defined as

$$\mathbf{E} = \frac{1}{2}(\mathbf{C} - \mathbf{1}) \tag{2.34}$$

and

$$\mathbf{E}^p = \frac{1}{2}(\mathbf{C}^p - \mathbf{1}) \tag{2.35}$$

where $\mathbf{1}$ denote the symmetric unit tensor in the reference configuration.

Similarly, associated with the current configuration are the Eulerian tensors

$$\mathbf{b} = \mathbf{F}\mathbf{F}^T \tag{2.36}$$

and

$$\mathbf{b}^e = \mathbf{F}^e\mathbf{F}^{eT} \tag{2.37}$$

called the total and elastic left Cauchy-Green tensors, respectively. The inverse of the left Cauchy Green is called Finger deformation tensor

$$\mathbf{c} \coloneqq \mathbf{b}^{-1} = (\mathbf{F}\mathbf{F}^T)^{-1} = \mathbf{F}^{-T}\mathbf{F}^{-1} \tag{2.38}$$

and

$$\mathbf{c}^e \coloneqq \mathbf{b}^{e^{-1}} = (\mathbf{F}^e\mathbf{F}^{eT})^{-1} = \mathbf{F}^{e^{-T}}\mathbf{F}^{e^{-1}} \tag{2.39}$$

The eulerian strains tensor takes the form

$$\mathbf{e} = \frac{1}{2}(\mathbf{1} - \mathbf{c}) \tag{2.40}$$

and

$$\mathbf{e}^e = \frac{1}{2}(\mathbf{1} - \mathbf{c}^e) \tag{2.41}$$

where $\mathbf{1}$ is the symmetric unit tensor in the current configuration

As a consequence the following relationships emerges

$$\mathbf{b}^e = \mathbf{F}^e\mathbf{F}^{eT} = \mathbf{F}\mathbf{F}^{p^{-1}}\mathbf{F}^{p^{-T}}\mathbf{F}^T = \mathbf{F}(\mathbf{F}^{p^T}\mathbf{F}^p)^{-1}\mathbf{F}^T = \mathbf{F}\mathbf{C}^{p-1}\mathbf{F}^T \tag{2.42}$$

To simplify our notation, we use the same symbol for the unit tensor in both the reference and the current configurations.

2.5.2.3 The Lie derivative for the tensor $\mathbf{b}^e$

The Lie derivative for the tensor $\mathbf{b}^e$ is defined as

$$L_v\mathbf{b}^e = \mathbf{F}\left\{\frac{\partial}{\partial t}\left[\mathbf{F}^{-1}\mathbf{b}^e\mathbf{F}^{-T}\right]\right\}\mathbf{F}^T = \mathbf{F}\dot{\mathbf{C}}^{p-1}\mathbf{F}^T \tag{2.43}$$

The Lie derivative of $\mathbf{b}^e$ tensor is exactly the push forward of the time derivative of the pullback of the spatial tensor $\mathbf{b}^e$. More information about push-forward and pull-back operations is given in references [103, 110].

2.5.2.4 Deviatoric-Volumetric decomposition of the deformation gradient

The split in nonlinear theory based on the deformation gradient takes the following multiplicative form. Let $\bar{\mathbf{F}}$ denote the volume preserving part of the deformation gradient. Therefore $\det(\bar{\mathbf{F}}) = 1$. Also, recall that $J := \det(\mathbf{F})$ gives the volume change. Then set

$$\bar{\mathbf{F}} = J^{-\frac{1}{3}}\mathbf{F} \Rightarrow \det(\bar{\mathbf{F}}) = 1 \tag{2.44}$$

and

$$\mathbf{F} = J^{\frac{1}{3}}\bar{\mathbf{F}} \tag{2.45}$$

Associated with $\mathbf{F}$ and $\bar{\mathbf{F}}$ we define the volumetric preserving part of the right Cauchy-Green tensor as

$$\bar{\mathbf{C}} = J^{-\frac{2}{3}}\mathbf{C} = J^{-\frac{2}{3}}\mathbf{F}^t\mathbf{F} \tag{2.46}$$

and the volumetric preserving part of the Lagrangian stress tensor is given by the standard expression

$$\bar{\mathbf{E}} = \frac{1}{2}(\bar{\mathbf{C}} - \mathbf{1}) \tag{2.47}$$

Similarly, the volumetric preserving part of the elastic left Cauchy-Green tensor is

$$\bar{\mathbf{b}}^e = J^{-\frac{2}{3}}\mathbf{C} = J^{-\frac{2}{3}}\mathbf{b}^e \tag{2.48}$$

2.5.2.5 Stress response. Hyperelastic response

Consistent with the assumption of isotropy, we characterize the stress response by a stored energy of the form

$$\hat{\psi} = \hat{T}(\theta) + \hat{M}(\theta, J^e) + \hat{U}(J^e) + \hat{W}(\bar{\mathbf{b}}^e) + \hat{K}(\bar{e}^p, \theta) \tag{2.49}$$

The elastic part of the free energy is uncoupled into volumetric/deviatoric response described by the functions $\hat{U}(J^e)$ and $\hat{W}(\bar{\mathbf{b}}^e)$, respectively. The function $\hat{M}(\theta, J^e)$ describes the thermo-mechanical coupling due to thermal expansion and provides the potential for the associated elastic structural entropy,

while the function $\hat{T}(\theta)$ is the potential for the purely thermal entropy. The function $\hat{K}(\bar{e}^p,\theta)$ is a nonlinear function of the equivalent plastic strain $\bar{e}^p$ and temperature θ which describes the isotropic strain hardening via the relation $\beta = -\partial_{\bar{e}^p} K(\bar{e}^p,\theta)$. To make matters as concrete as possible, we consider the following explicit forms[102, 111]

$$\begin{aligned}
\hat{U}(J) &= \frac{1}{2}\kappa \ln^2(J) \\
\hat{\mathrm{W}}(\bar{\mathbf{b}}^{\mathbf{e}}) &= \frac{1}{2}\mu\left[tr(\bar{\mathbf{b}}^{\mathbf{e}}) - 3\right] = \frac{1}{2}\mu\left[tr(\bar{\mathbf{C}}^{\mathbf{e}}) - 3\right] \\
\hat{T}(\theta) &= c\left[(\theta - \theta_0) - \theta \ln(\frac{\theta}{\theta_0})\right] \\
\hat{\mathrm{M}}(\mathrm{J},\theta) &= -3\beta\kappa \frac{\ln(J)}{J}(\theta - \theta_0)
\end{aligned} \qquad (2.50),$$

where $\mu > 0, \kappa > 0, c > 0$ and β can be interpreted as the shear modulus, the bulk modulus, the heat capacity and the thermal expansion coefficient, respectively.

Some remarks can be made about the structure of the free energy function:

(i) the thermoelastic free energy is decoupled from the plastic contribution $\beta = K'(\bar{e}^p,\theta)$ associated with the hardening variable $\bar{e}^p$ (this assumption is motivated by the experimental observation that the lattice structure remains unaffected by the plastic deformation)[102];

(ii) The functions $\hat{U}(J^e)$ and $\hat{W}(\bar{\mathbf{b}}^e)$ generalize the linear isotropic elastic model.

(iii) The function $\hat{K}(\bar{e}^p,\theta)$ represents the visible (macroscopic) plastic deformations that are the result of microscopic dislocation (crystallographic defects in the crystal structure) motion and multiplication. Generally, the material exhibits high strength if there are either high levels of dislocations or no dislocations. In addition, the function $\hat{K}(\bar{e}^p,\theta)$ represents the yield stress decreasing as the grain size is increased [112] . Also, $\hat{K}(\bar{e}^p,\theta)$ represents the decrease in dislocation density due to the heating of the material above its critical temperature (thermal softening).

There are four main strengthening mechanisms for metals, each is a method to prevent dislocation motion and propagation, or make it energetically unfavorable for the dislocation to move (work hardening, solid solution strengthening, precipitation hardening and grain boundary strengthening).

In addition, there are other factors that affect the shape and the magnitude of the hardening potential among them [113]: (i) material composition, (ii) previous

heat treatment, (iii) the type of crystal structure and (iv) prior history of plastic deformation. Different hardening potentials that represent the work hardening phenomenon have been proposed in the literature, which reflect some of the strain hardening patterns observed in the experiments. Among them the following:

Voce and Simo hardening potential

Voce *[106]* presented and Simo *[102]* applied the following potential describing isotropic hardening:

$$\hat{K}(\bar{e}^p,\theta) = \frac{1}{2}h(\theta)\bar{e}^{p2} - \left[\sigma_0(\theta) - \sigma_\infty(\theta)\right]H(\bar{e}^p)$$
$$H(\bar{e}^p) = \begin{cases} \bar{e}^p - \dfrac{1-e^{-\delta\bar{e}^p}}{\delta} & for\ \delta \neq 0 \\ 0 & for\quad \delta \neq 0 \end{cases} \tag{2.51}$$

where δ is the saturation exponent and the functions $h(\theta),\sigma_0(\theta),\sigma_\infty(\theta)$ describe linear thermal softening

$$\begin{aligned} \sigma_0(\theta) &= \sigma_0(\theta_0)(1-\omega_0(\theta-\theta_0)) \\ \sigma_\infty(\theta) &= \sigma_\infty(\theta_0)(1-\omega_h(\theta-\theta_0)) \\ h(\theta) &= h(\theta_0)(1-\omega_h(\theta-\theta_0)) \end{aligned} \tag{2.52}$$

where $\sigma_0(\theta_0)$ is the initial yield stress, $\sigma_\infty(\theta_0)$ is the final saturation hardening stress, $h(\theta_0)$ is the linear hardening modulus, all obtained at the reference temperature θ_0, while ω_0 and ω_h are the flow stress softening and hardening softening parameter, respectively.
The above potential allows us to study materials exhibiting a combination of linear and saturation- type hardening.

Johnson and Cook

Johnson and Cook *[108]* present a potential to describe isotropic hardening in metals subjected to large strains, high strains rates and high temperatures

$$K(\bar{e}^p,\theta) = B\frac{(\bar{e}^p)^{n+1}}{n+1}\left[1-\left(\frac{\theta-\theta_0}{\theta_{melt}-\theta_0}\right)^m\right] \tag{2.53}$$

where $\bar{e}^p$ is the equivalent plastic strain, n is the constant work hardening exponent, B is the constant strength coefficient, θ_0 is the reference temperature and θ_{melt} is the reference melt temperature and m is a power coefficient of the thermal softening term. The dependence of hardening

potential on temperature represents the softening of the material when its temperature is increased and it is included in a multiplicative manner in the hardening potential. For most metals, $0.1 < n < 0.5$. It is important to remark, that if $n = 1$, $m = 1$ and $\frac{1}{\theta_{melt} - \theta_0} = \omega_h$, the Johnson and Cook hardening potential degenerates in the linear component of the Voce hardening potential. $n = 1$ is a reasonable approximation for heavily prestrained metals.

Bäker

Bäker [109] presents a potential to describe isotropic hardening in a titanium alloy

$$K(\overline{e}^p, \theta) = B(\theta)\frac{(\overline{e}^p)^{n+1}}{n+1} \tag{2.54}$$

where $\overline{e}^p$ is the equivalent plastic strain, n is a temperature dependent work hardening exponent, B is a temperature dependent strength coefficient and

$$B = B_0 \exp\left(-\left(\frac{\theta}{\theta_{melt}}\right)^m\right) \quad and \quad n = n_0 \exp\left(-\left(\frac{\theta}{\theta_{melt}}\right)^m\right) \tag{2.55}$$

where B_0 is the initial strength coefficient, n_0 is the initial work hardening exponent, θ_{melt} is the reference melt temperature and m is a power coefficient of the thermal softening term.
The hardening potential presented in [109] includes the thermal softening through the degradation with the temperature of the strength coefficient and the work hardening exponent.

2.5.2.6 Yield condition

Extreme conditions of strain, strain rate and temperature are encountered during cutting. Strain values in the range 0-10, strain rates rise to values as high as 1×10^6 and temperatures in the range of 200-1000ºC. In numerical analysis of metal cutting processes, accurate flow stress models are considered extremely necessary to represent work material constitutive behavior under high strain rate deformation conditions.
We consider the classical Mises-Hubber yield conditions, expressed in terms of Kirchhoff stress tensor, for the case of rate independent plasticity

$$\begin{aligned}\Phi(\tau, \overline{e}^p, \theta) &= \left\|dev(\tau)\right\| - \sqrt{\frac{2}{3}}(\sigma_y - K'(\overline{e}^p, \theta)) \\ &= \left\|dev(\tau)\right\| - \sqrt{\frac{2}{3}}(\sigma_y + \beta) \le 0\end{aligned} \tag{2.56}$$

and for rate dependent plasticity

$$
\begin{aligned}
f(\tau,\overline{e}^{p},\theta) &= \left\|dev(\tau)\right\| - \sqrt{\frac{2}{3}}(\sigma_{y} + \beta)(1 + g(\dot{\overline{e}}^{p})) \\
&= 0 \\
&= \Phi(\tau,\overline{e}^{p},\theta) - \sqrt{\frac{2}{3}}(\sigma_{y} + \beta)g(\dot{\overline{e}}^{p}) \\
&\quad if \quad \Phi(\tau,\overline{e}^{p},\theta) > 0
\end{aligned}
\tag{2.57}
$$

where $.\sigma_{y}$ .denotes the flow stress, σ_{y_0} denotes the flow stress at $\theta = \theta_0$, $\beta = -K'(\overline{e}^{p},\theta)$ the isotropic nonlinear hardening modulus, β_0 the isotropic hardening at $\theta = \theta_0$, $g(\dot{\overline{e}}^{p})$ the strain rate hardening modulus and $\overline{e}^{p}$ the hardening parameter. The expressions $(\sigma_{y} + \beta)$ and $g(\dot{\overline{e}}^{p})$ depends on the hardening law used.

Numerous empirical and semi-empirical flow stress models have been proposed. The following temperature, strain and strain-rate dependent models provide a sampling of the models in current use: (i) Simo[102], (ii) Johnson and Cook [108] and (iii) Bäker [109]

Simo flow model

$$
\begin{aligned}
(\sigma_{y} + \beta) &= \hat{\sigma}_{y} + \hat{H}\overline{e}^{p} + (\hat{K}_{\inf} - \hat{\sigma}_{y})(1 - \exp(-\delta\overline{e}^{p})) \\
\hat{\sigma}_{y} &= \sigma_{y}(1 - w_0(\theta - \theta_0)) \\
\hat{H} &= H(1 - w_h(\theta - \theta_0)) \\
\hat{K}_{\inf} &= K_{\inf}(1 - w_h(\theta - \theta_0)
\end{aligned}
\tag{2.58}
$$

This model describes the strain hardening and thermal softening for most steels in temperature range 300K and 400K [102]. Common values of materials constant of the Simo yield function are shown in Table 1.

σ_{y}	w_0	θ_0	H	w_h	$K_{\inf}$	δ
450 MPa	0.002	293K	129.24 MPa	0.002	715 MPa	19.93

Table 1. Simo yield function. Material properties.

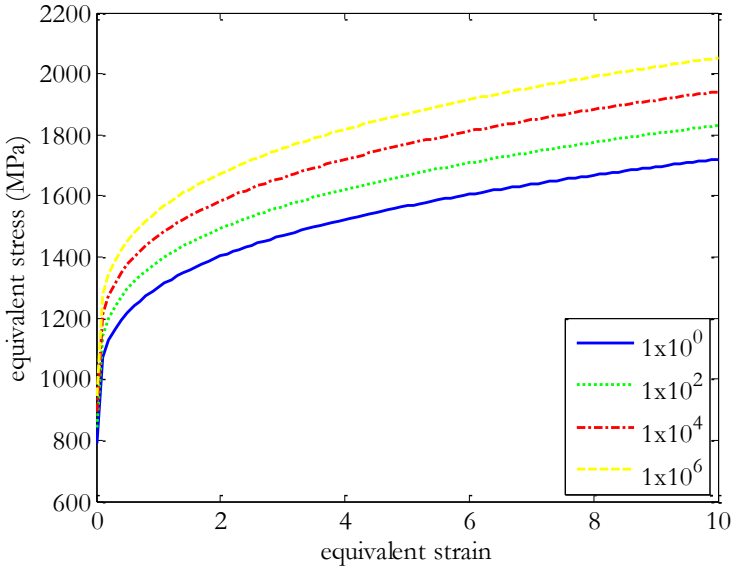

Figure 16. Variation of Simo yield function in terms of strains and temperatures.

Figure 16 shows the flow stress-strain curve for the Simo model at different temperatures for the material properties presented in Table 1.The effect of the thermal softening is shown in Figure 16

Johnson and Cook flow model

Johnson-Cook's constitutive equation is commonly used to model the thermo-visco-plastic behavior of workpiece material in numerical simulations of the chip formation process.

The three key material responses are strain hardening, strain-rate effects, and thermal softening. These three effects are combined, in a multiplicative manner, as is shown in the following lines

$$(\sigma_y + \beta)(1 + g(\dot{\bar{e}}^p)) = \; A + B(\bar{e}^p)^n \;\; (1 - \theta^{*m})\left(1 + C\ln(\left\langle \frac{\dot{\bar{e}}^p}{\dot{e}_0} \right\rangle)\right) \tag{2.59}$$

$$\theta^* = \begin{cases} 0 & \text{for } \theta < \theta_0 \\ \dfrac{\theta - \theta_0}{\theta_{melt} - \theta_0} & \text{for } \theta_0 < \theta < \theta_{melt} \\ 1 & \text{for } \theta > \theta_{melt} \end{cases} \tag{2.60}$$

$$\left\langle \frac{\dot{\bar{e}}^p}{\dot{e}_0} \right\rangle = \begin{cases} 1 & \text{if } \dot{\bar{e}}^p < \dot{e}_0 \\ \dfrac{\dot{\bar{e}}^p_{n+1}}{\dot{e}_0} & \text{if } \dot{\bar{e}}^p \geq \dot{e}_0 \end{cases} \tag{2.61}$$

where the first bracketed term represents the strain hardening of the yield stress, the next term represents the softening of the yield stress due to local thermal effects, and the final bracketed term models the increase in the yield stress at elevated strain rates.

$\bar{e}^p$ is the equivalent plastic strain, $\dot{\bar{e}}^p / \dot{e}_0$ is the dimensionless strain rate, θ^* is the homogenous temperature, θ_0 is the reference temperature and θ_{melt} is the reference melt temperature . A is the initial yield stress and B and n represent the effect of strain hardening. C is dimensionless strain rate hardening coefficient and m is a power coefficient of the thermal softening term.

Viscous effects are taken into account as soon as the equivalent viscoplastic strain-rate, $\dot{\bar{e}}^p$, becomes higher than the threshold $\dot{e}_0$. Strain-rate sensitivity is then governed by the viscoplastic parameter, C. In the same way, thermal softening is modeled as soon as the temperature, θ, becomes higher than a reference temperature θ_0.

Common values of materials constant of the Johnson-Cook yield function are shown in Table 2.

A	B	C	m	n	$\dot{e}_0$
792 MPa	510 MPa	0.014	1.03	0.26	1 1/s

Table 2. Parameters of the Johnson-Cook constitutive-law[108]

Figure 17 shows the flow stress-strain curves for the Johnson-Cook model at different temperatures (a) and at different strains rates (b), for the material properties presented in Table 2. The effect of the thermal softening is shown in Figure 16(a) and the effect of strain hardening is shown in Figure 17(b).

Bäker flow model

A material model that captures the main effects in chip formation at high cutting speeds. That is to say, this model allows us to study the transition from continuous to serrated chip as the tool speed is increased. Bäker yield stress is presented in the following equations:

$$(\sigma_y + \beta)(1 + g(\dot{\bar{e}}^p)) = B(\bar{e}^p)^n \left(1 + C\ln(\left\langle \frac{\dot{\bar{e}}^p}{\dot{e}_0} \right\rangle)\right)$$
$$\left\langle \frac{\dot{\bar{e}}^p}{\dot{e}_0} \right\rangle = \begin{cases} 1 & \text{if } \dot{\bar{e}}^p < \dot{e}_0 \\ \dfrac{\dot{\bar{e}}^p_{n+1}}{\dot{e}_0} & \text{if } \dot{\bar{e}}^p \geq \dot{e}_0 \end{cases} \qquad (2.62)$$

where $\bar{e}^p$ and $\dot{\bar{e}}^p$ are strain and strain rate, θ the temperature, B and n the temperature-dependent material parameters, and C is dimensionless strain rate

hardening coefficient. Viscous effects are taken into account as soon as the equivalent viscoplastic strain-rate, $\dot{\bar{e}}^p$, becomes higher than the threshold $\dot{e}_0$.

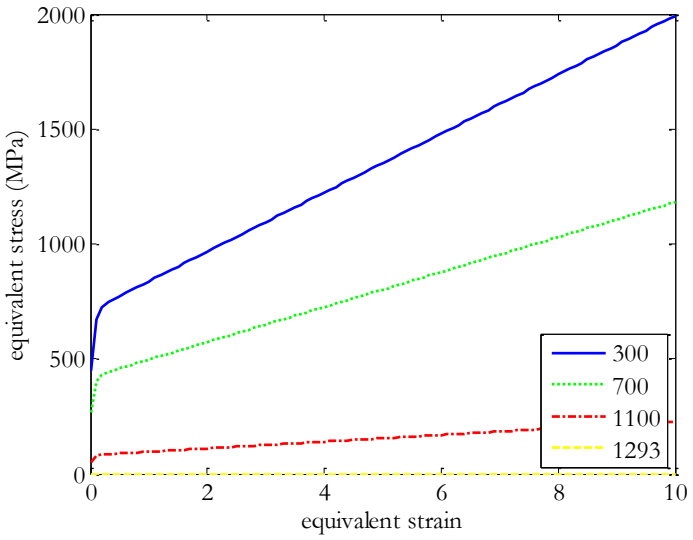

(a)

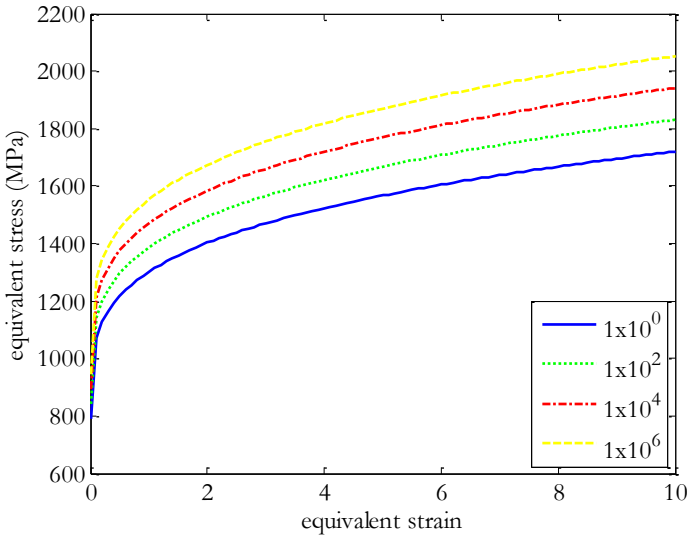

(b)

Figure 17. Flow stress strain curves for Johnson–Cook law at a strain rate of 1s^{-1} for (a) different temperatures and (b) different strain rates

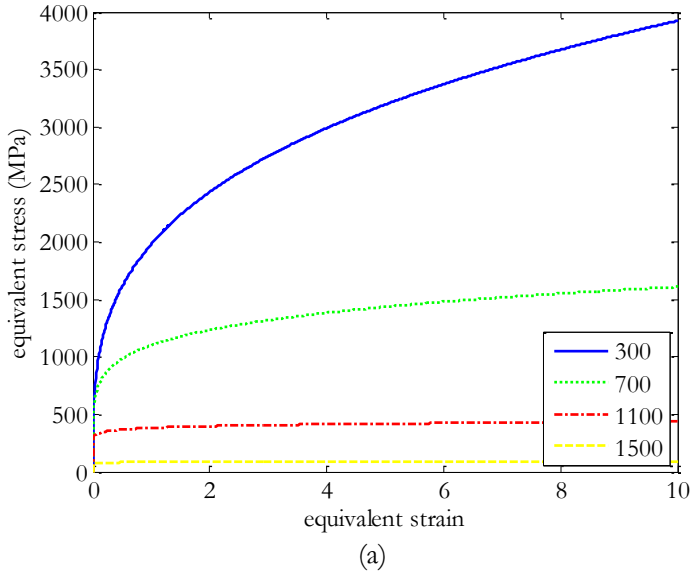

(a)

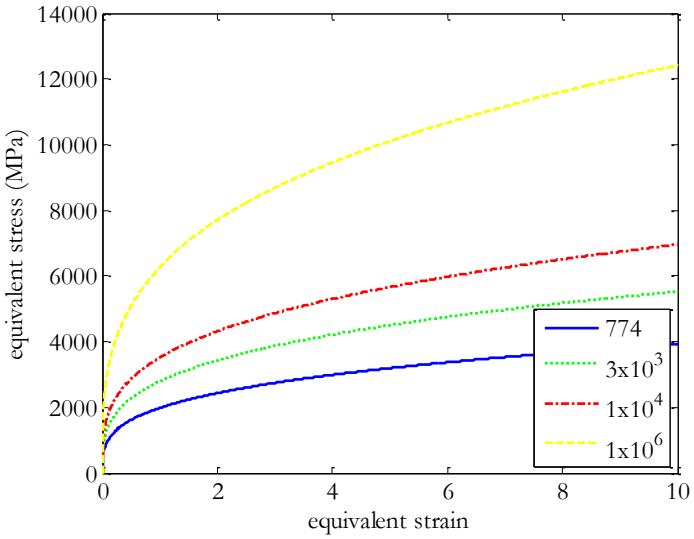

(b)

Figure 18. Flow stress strain curves for Bäker law at a strain rate of 1s-1 for (a) different temperature and (b) different strain rates.

The temperature dependent coefficient has the form

$$B = B_0 \exp(-\left(\frac{\theta}{\theta_{melt}}\right)^m) \qquad n = n_0 \exp(-\left(\frac{\theta}{\theta_{melt}}\right)^m) \tag{2.63}$$

where B_0 is the initial strength coefficient, n_0 is the initial work hardening exponent, θ_{melt} is the reference melt temperature and m is a power coefficient of the thermal softening term.
Common values of materials constant of the Bäker yield function are shown in Table 3.

B_0	n_0	C	$\dot{e}_0$	θ_{melt}
2260 MPa	0.339	0.302	774 1/s	825K

Table 3. Parameters of the Bäker constitutive-law[109]

Figure 18 shows the flow stress-strain curves for the Bäker model at different temperatures (a) and at different strains rates (b), for the material properties presented in Table 3. The effect of the thermal softening is shown in Figure 18(a) and the effect of strain hardening is shown in Figure 18 (b).

2.5.2.7 The associate flow rule

The functional form of the corresponding associate flow rule is uniquely determined by the principle of maximum plastic dissipation, given the stored energy function (2.49) and the yield function (2.57).
For the Mises-Hubber yield function (2.57) and the free energy function (2.49), Simo [104, 105] shows that the flow rule takes the form based on the principle of maximum plastic dissipation. A detail procedure about how to get the flow rule is shown in the following lines:
Due to the restriction to isotropy implied by the termoelastic domain, the functional form of the internal energy function can be written as

$$e = \hat{e}(\overline{\mathbf{b}}^e, \overline{e}^p, \eta^e) \quad with \quad \eta^e = \eta - \eta^p \tag{2.64}$$

The free energy expressed in terms of the internal energy via Legendre transformation

$$\hat{\psi}(\overline{\mathbf{b}}^e, \overline{e}^p, \theta) = \hat{e}(\overline{\mathbf{b}}^e, \overline{e}^p, \theta) - \eta^e \theta \tag{2.65}$$

Exploiting the Second Law of Thermodynamics, constitutive equations consistent with the assumed free energy are derived, as follows

$$\begin{aligned} D &= \tau \cdot \mathbf{d} + \theta\dot{\eta} - \dot{e} \\ &= \tau \cdot \mathbf{d} + \theta\dot{\eta} - \dot{\hat{\psi}} - \dot{\eta}^e\theta - \eta^e\dot{\theta} \end{aligned} \tag{2.66}$$

We differentiate the free energy function (2.49) with respect to time

$$\dot{\hat{\psi}} = \frac{\partial\hat{\psi}}{\partial\mathbf{b}^e}\dot{\mathbf{b}}^e + \frac{\partial\hat{\psi}}{\partial\overline{e}^p}\dot{\overline{e}}^p + \frac{\partial\hat{\psi}}{\partial\theta}\dot{\theta} \tag{2.67}$$

Taking the derivate of $\mathbf{b}^e$ with respect to time

$$\dot{\mathbf{b}}^e = \dot{\mathbf{F}}\mathbf{F}^{-1}\mathbf{F}\mathbf{C}^{p-1}\mathbf{F}^t + \mathbf{F}\mathbf{C}^{p-1}\mathbf{F}^t\mathbf{F}^{-t}\dot{\mathbf{F}}^t + \mathbf{F}\dot{\mathbf{C}}^{p-1}\mathbf{F}^t \tag{2.68}$$

Using the definition of the spatial velocity gradient $\mathbf{l} = \dot{\mathbf{F}}\mathbf{F}^{-1}$ and the Lie derivative of the elastic left Cauchy Green tensor $L_v\mathbf{b}^e$. The time derivate of $\mathbf{b}^e$ is written as

$$\dot{\mathbf{b}}^e = \mathbf{l}\mathbf{b}^e + \mathbf{b}^e\mathbf{l}^t + L_v\mathbf{b}^e \tag{2.69}$$

Inserting equation (2.69) into equation (2.67), the derivative of the free energy function (2.67) becomes

$$\dot{\hat{\psi}} = \frac{\partial\hat{\psi}}{\partial\mathbf{b}^e}(2\mathbf{l}\mathbf{b}^e + L_v\mathbf{b}^e) + \frac{\partial\hat{\psi}}{\partial\bar{e}^p}\dot{\bar{e}}^p + \frac{\partial\hat{\psi}}{\partial\theta}\dot{\theta} \tag{2.70}$$

By inserting the relation $\mathbf{d} = sym\left[\mathbf{l}\right]$ into (2.70) and using the Lengendre Transformation (2.65), the dissipation inequality becomes

$$D = \dot{\eta}^p\theta + \left(-\frac{\partial\hat{\psi}}{\partial\theta} - \eta + \eta^p\right)\dot{\theta} + \left(\tau - 2\frac{\partial\hat{\psi}}{\partial\mathbf{b}^e}\mathbf{b}^e\right)\mathbf{d} - \frac{\partial\hat{\psi}}{\partial\mathbf{b}^e}L_v\mathbf{b}^e - \frac{\partial\hat{\psi}}{\partial\bar{e}^p}\dot{\bar{e}}^p \geq 0 \tag{2.71}$$

By demanding that (2.71) hold for all admissible processes, the Kirchhoff stress tensor is obtained by the general expression:

$$\begin{aligned}\boldsymbol{\tau} &= 2\frac{\partial\hat{\psi}}{\partial\mathbf{b}^e}\mathbf{b}^e \\ &= 2\mathbf{F}^e\frac{\partial W}{\partial\mathbf{C}^e}\mathbf{F}^{eT} \\ &= J^e\left[-3\beta\kappa\frac{(1-\ln(J))}{J^2}(\theta-\theta_0) + \kappa\frac{\ln(J^e)}{J^e}\right]\mathbf{1} + \mu dev\ \bar{\mathbf{b}}^e\end{aligned} \tag{2.72}$$

The hydrostatic and deviatoric parts of the Kirchhoff stress tensor are

$$\begin{aligned}p &:= \left[-3\beta\kappa\frac{(1-\ln(J))}{J}(\theta-\theta_0) + \ln(J^e)\right]\mathbf{1} \\ \mathbf{s} &:= \mu dev(\bar{\mathbf{b}}^e)\end{aligned} \tag{2.73}$$

and the entropy constitutive equation

$$\begin{aligned}\eta &= \eta^p - \frac{\partial\hat{\psi}}{\partial\theta} \\ &= \eta^p - \partial_\theta\hat{T}(\theta) - \partial_\theta\hat{M}(\theta, J^e) - \partial_\theta\hat{K}(\alpha,\theta)\end{aligned} \tag{2.74}$$

The dissipation inequality becomes

$$D = \dot{\eta}^p\theta - \frac{\partial\hat{\psi}}{\partial\mathbf{b}^e}L_v\mathbf{b}^e - \frac{\partial\hat{\psi}}{\partial\bar{e}^p}\dot{\bar{e}}^p \geq 0 \tag{2.75}$$

2.5.2.8 Evolution equations and maximum plastic dissipation.

Now, we need to define the evolution equations for the internal variables in the model in order to complete the constitutive theory of plasticity at finite strains.

Based on the thermomechanical principle of maximum dissipation, the problem is to find (τ,β,θ) such that the dissipation function (2.75) attains a maximum subject to the constraint $\Phi(\tau,\overline{e}^{\,p},\theta)\leq 0$ (rate-independent plasticity), prescribed intermediate configuration ($\mathbf{b}^e$ is fixed) and prescribed rates $(\mathbf{L}_v\mathbf{b}^e,\dot{\overline{e}}^{\,p},\dot{\theta})$. The problem can be reformulated as a constrained minimization of the negative of the dissipation

$$\begin{aligned}(\tau,\beta,\theta) &= \arg\left[\min_{\Phi(\tau,\overline{e}^{\,p},\theta)\leq 0}(-D)\right]\\ &= \arg\left[\min_{\Phi(\tau,\overline{e}^{\,p},\theta)\leq 0}\left(-\dot{\eta}^p\theta+\frac{\partial\hat{\psi}}{\partial\mathbf{b}^e}L_v\mathbf{b}^e+\frac{\partial\hat{\psi}}{\partial\overline{e}^{\,p}}\dot{\overline{e}}^{\,p}\right)\right]\end{aligned} \tag{2.76}$$

But the problem can be expressed as an unconstrained minimization problem by introducing a Lagrangian functional

$$\begin{aligned}L^p(\tau,\beta,\theta;\lambda) &= -D(\tau,\beta,\theta)+\lambda\Phi(\tau,\overline{e}^{\,p},\theta)\\ &= -\dot{\eta}^p\theta+\frac{1}{2}\tau\bullet L_v\mathbf{b}^e\mathbf{b}^{e-1}-\beta\dot{\overline{e}}^{\,p}+\lambda\Phi(\tau,\overline{e}^{\,p},\theta)\end{aligned} \tag{2.77}$$

The solution to the problem is given by

$$\begin{aligned}\partial_{\tau}L^p(\tau,\beta,\theta;\lambda) &= \frac{1}{2}L_v\mathbf{b}^e\mathbf{b}^{e-1}+\lambda\partial_{\tau}\Phi(\tau,\overline{e}^{\,p},\theta)=0\\ \partial_{\beta}L^p(\tau,\beta,\theta;\lambda) &= -\dot{\overline{e}}^{\,p}+\lambda\partial_{\beta}\Phi(\tau,\overline{e}^{\,p},\theta)=0\\ \partial_{\theta}L^p(\tau,\beta,\theta;\lambda) &= -\dot{\eta}^p+\lambda\partial_{\theta}\Phi(\tau,\overline{e}^{\,p},\theta)=0\end{aligned} \tag{2.78}$$

where the consistency parameter $\lambda\geq 0$ is the Lagrange multiplier satisfying the Kuhn Tucker conditions

$$\lambda\geq 0\qquad \Phi(\tau,\overline{e}^{\,p},\theta)\leq 0\qquad \lambda\Phi(\tau,\overline{e}^{\,p},\theta)=0 \tag{2.79}$$

It is important to remark that the Kuhn Tucker conditions are equivalent to the loading-unloading conditions.

In summary, the evolution equations of the internal variables are

$$\begin{aligned}L_v\mathbf{b}^e &= -2\lambda\partial_{\tau}\Phi(\tau,\overline{e}^{\,p},\theta)\mathbf{b}^e\\ \dot{\overline{e}}^{\,p} &= \lambda\partial_{\beta}\Phi(\tau,\overline{e}^{\,p},\theta)\\ \dot{\eta}^p &= \lambda\partial_{\theta}\Phi(\tau,\overline{e}^{\,p},\theta)\end{aligned} \tag{2.80}$$

From expressions (2.43) and (2.42), the Lie derivative of the elastic left Cauchy-Green tensor can be expressed in material description as

$$\begin{aligned}\dot{\mathbf{C}}^{p-1} &= -2\lambda\partial_{\tau}f(dev(\tau),\overline{e}^{\,p},\theta)\mathbf{C}^{p-1}=-2\lambda\frac{dev\ \tau}{\|dev\ \tau\|}\mathbf{C}^{p-1}=-2\lambda\frac{\mathbf{s}}{\|\mathbf{s}\|}\mathbf{C}^{p-1}\\ \dot{\overline{e}}^{\,p} &= \lambda\sqrt{\frac{2}{3}}\\ \dot{\eta}^p &= \lambda\sqrt{\frac{2}{3}}(\partial_{\theta}\sigma_y+\partial_{\theta}\beta)\end{aligned} \tag{2.81}$$

Using the specific constitutive equations and decomposing $\mathbf{b}^e$ into its spherical and deviatoric parts, the exact flow rule (2.80) becomes

$$L_v\mathbf{b}^e = -2\lambda J^{-\frac{2}{3}}\mathbf{n}^2\frac{\|\mathbf{s}\|}{\mu} - 2\lambda J^{-\frac{2}{3}}\frac{1}{3}tr(\bar{\mathbf{b}}^e)\mathbf{n} \tag{2.82}$$

The first term in (2.82) can be neglected in most metals, because this term is of the order of the flow stress over the shear modulus, which for metal plasticity, is of the order of 10^{-3} [102]. We arrive at the modified flow rule

$$\begin{aligned} L_v\mathbf{b}^e &= -2\lambda J^{-\frac{2}{3}}\frac{1}{3}tr(\bar{\mathbf{b}}^e)\mathbf{n} \\ \bar{\mathbf{F}}\dot{\mathbf{C}}^{p-1}\bar{\mathbf{F}}^t &= -2\lambda\frac{1}{3}tr(\bar{\mathbf{b}}^e)\mathbf{n} \end{aligned} \tag{2.83}$$

In equation (2.83) we have used that $\bar{\mathbf{F}} = J^{-\frac{1}{3}}\mathbf{F}$

i. Free energy function

$$\hat{\psi} = \hat{T}(\theta) + \hat{M}(\theta, J^e) + \hat{U}(J^e) + \hat{W}(\bar{\mathbf{b}}^e) + \hat{K}(\bar{e}^p, \theta)$$

ii. Kirchhoff stress

$$\boldsymbol{\tau} = J^e p + \mu dev(\bar{\mathbf{b}}^e) \qquad \eta = \eta^p + \eta^e + \eta^t$$

$$p := \left[-3\beta\kappa\frac{(1-\ln(J))}{J}(\theta-\theta_0) + \ln(J^e)\right]\mathbf{1} \qquad \eta^e := -\partial_\theta\hat{T}(\theta)$$

$$\eta^t := -\partial_\theta\hat{M}(\theta, J^e) - \partial_\theta\hat{K}(\alpha, \theta)$$

$$\mathbf{s} := \mu dev(\bar{\mathbf{b}}^e)$$

iii. Von Mises yield criterion

$$\Phi(\tau, \bar{e}^p, \theta) = \|dev(\tau)\| - \sqrt{\frac{2}{3}}(\sigma_y + \beta) \le 0$$

iv. Evolution equations $\lambda \ge 0 \qquad \Phi \le 0 \qquad \lambda\Phi = 0$

$$\begin{aligned} L_v\mathbf{b}^e &= -2\lambda J^{-\frac{2}{3}}\frac{1}{3}tr(\bar{\mathbf{b}}^e)\mathbf{n} \\ \dot{\bar{e}}^p &= \lambda\sqrt{\frac{2}{3}} \\ \dot{\eta}^p &= \lambda\sqrt{\frac{2}{3}}(\partial_\theta\sigma_y + \partial_\theta\beta) \end{aligned}$$

Box 1. Coupled thermomechanical J_2 flow theory. Rate independent plasticity

The evolution equations (2.80) for the rate independent theory can be easily extended to incorporate rate-temperature-dependent response. Consider a regularized dissipation function D_C depending on a regularization parameter $C \in (0, \infty)$, defined as

$$D_C = D(\tau,\beta,\theta) + h(z) \tag{2.84}$$

where

$$z = (\Phi(\tau,\beta,\theta), C) \tag{2.85}$$

In equation (2.84), $h(z)$ is a differentiable function satisfying the conditions (a) $h(z) \geq 0$, for all $z \in \mathrm{R}$, and (b) $h(z) = 0$ if and only if $z \leq 0$. The regularization function $h(z)$ depends on the isotropic hardening law used (Johnson Cook, Bäker).

The principle of maximum dissipation leads to a flow rule identical to (2.80) with the Kuhn-Tucker conditions replaced by the constitutive equation

$$\lambda = \begin{cases} \dfrac{\partial h(z)}{\partial \Phi} = \dot{e}_0 \, \mathrm{e}^{\left(\sqrt{\frac{3}{2}}\frac{\Phi(\tau,\bar{e}^p,\theta)}{C(\sigma_y+\beta)}\right)}, & \Phi>0 \\ 0, & \text{otherwise} \end{cases} \tag{2.86}$$

In, conclusion, the viscoplastic constitutive model is a penalty regularization of the rate-independent model, and the solution of the viscoplastic problem converges to the solution of the rate independent problem as the penalty (fluidity) parameter $C \to 0$

i. Free energy function

$$\hat{\psi} = \hat{T}(\theta) + \hat{M}(\theta, J^e) + \hat{U}(J^e) + \hat{W}(\bar{\mathbf{b}}^e) + \hat{K}(\bar{e}^p, \theta)$$

ii. Kirchhoff stress

$$\boldsymbol{\tau} = J^e p + \mu dev(\bar{\mathbf{b}}^e) \qquad \eta = \eta^p + \eta^e + \eta^t$$

$$p := \left[-3\beta\kappa \frac{(1-\ln(J))}{J}(\theta-\theta_0) + \ln(J^e)\right]\mathbf{1} \qquad \eta^e := -\partial_\theta \hat{T}(\theta)$$

$$\eta^t := -\partial_\theta \hat{M}(\theta, J^e) - \partial_\theta \hat{K}(\alpha,\theta)$$

$$\mathbf{s} := \mu dev(\bar{\mathbf{b}}^e)$$

iii. Plastic multiplier $\Phi > 0$

$$\lambda = \dot{e}_0 \, \mathrm{e}^{\left(\sqrt{\frac{3}{2}}\frac{\Phi(\tau,\bar{e}^p,\theta)}{C(\sigma_y+\beta)}\right)}$$

iv. Evolution equations

$$L_v \mathbf{b}^e = -2\lambda J^{-\frac{2}{3}} \frac{1}{3} tr(\bar{\mathbf{b}}^e)\mathbf{n}$$

$$\dot{\bar{e}}^p = \lambda\sqrt{\frac{2}{3}}$$

$$\dot{\eta}^p = \lambda\sqrt{\frac{2}{3}}(\partial_\theta \sigma_y + \partial_\theta \beta)$$

Box 2. Coupled thermomechanical J_2 flow theory. Rate dependent plasticity

2.6 Frictional contact constrains

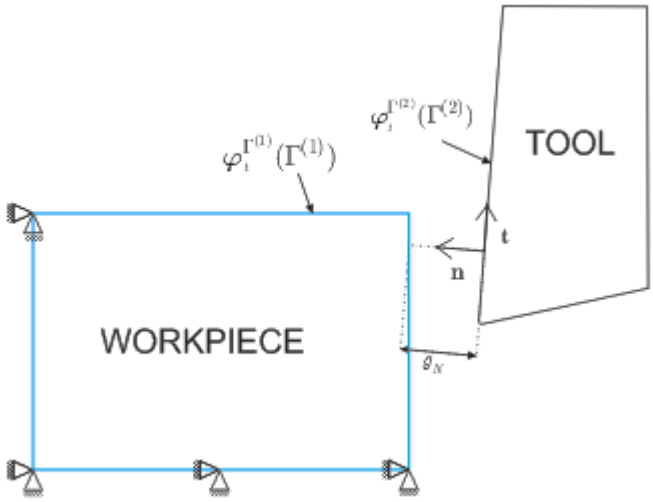

Figure 19. Evolution of frictional contact between the tool and the workpiece

With reference to Figure 19, at the stage of deformation process corresponding to the deformation mappings $\varphi^{(1)}$ and $\varphi^{(2)}$ of the workpiece and tool bodies, respectively, the gap, separating a material point $\mathbf{X}^{(1)}$ on $\Gamma^{(1)}$ from the tool boundary, is defined in the spatial description by

$$g_N = \left[\varphi^{(1)}(\mathbf{X}^{(1)}) - \varphi^{(2)}(\widehat{\mathbf{X}}^{(2)})\right]\bullet\mathbf{n} \tag{2.87}$$

Where $\widehat{\mathbf{X}}^{(2)}$ is the material point on $\Gamma^{(2)}$ defined by the closed point projection, which is given by

$$\varphi^{(2)}(\widehat{\mathbf{X}}^{(2)}) = \arg\min_{\mathbf{X}^{(2)}\in\Gamma^{(2)}} \left\|\varphi^{(1)}(\mathbf{X}^{(1)}) - \varphi^{(2)}(\mathbf{X}^{(2)})\right\| \tag{2.88}$$

The unit normal vector $\mathbf{n}$ is defined in a standard way as the outward unit normal to $\varphi^{(2)}(\mathbf{X}^{(2)})$ at $\mathbf{x}^{(2)} = \varphi^{(2)}(\widehat{\mathbf{X}}^{(2)})$.

Assume that contact has been established between the tool and the workpiece, that is $g_N = 0$, there is no contact among them $g_N > 0$ and finally, there is penetration when $g_N < 0$

2.6.1 Normal behavior

In the definition of the normal contact behavior, it is assumed that penetration between the two bodies is admissible. In addition, a linear relationship between the normal contact force and the penetration is postulated resulting in the following constitutive equation

$$P_N = \begin{cases} \kappa g_N & \text{if } g_N < 0 \\ 0 & \text{otherwise} \end{cases} \tag{2.89}$$

2.6.2 Tangential behavior

Friction occurs at the tool chip interface under extreme conditions of temperature, pressure and strain. Its mechanism is not well understood yet, most of the numerical studies of machining process, it has been usual to idealize it by a Coulomb type friction.

$$\|P_T\| - \mu P_N \leq 0 \tag{2.90}$$

Sometimes, is usual to use the following constitutive law for the tangential force at the tool chip interface

$$P_T = \kappa_T g_T \tag{2.91}$$

where κ_T is the tangential penalty factor and g_T is the tangential relative displacement .

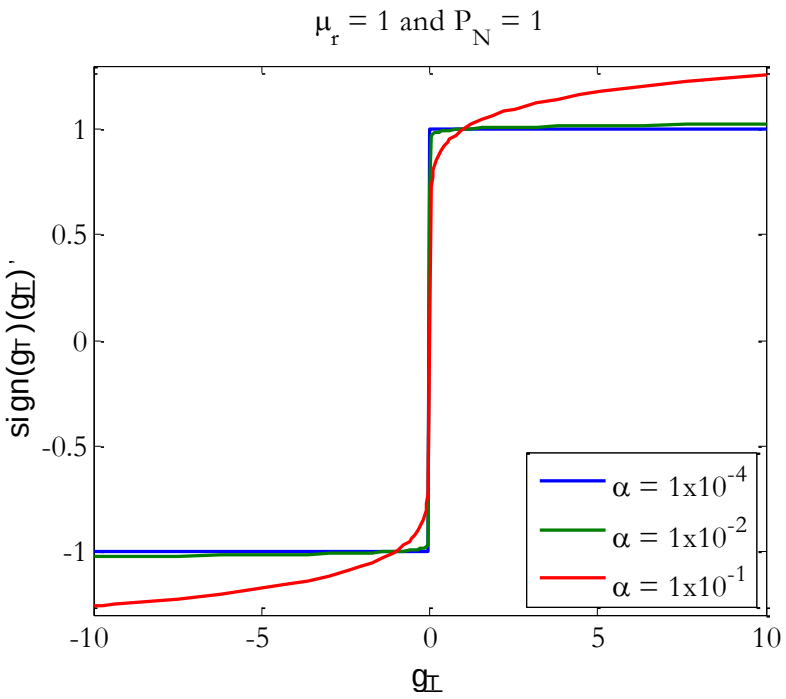

Figure 20. Regularization of the Coulomb friction law

Then, the Coulomb friction law can be re written as

$$P_T = \begin{cases} \kappa_T g_T & \text{if } \|P_T\| - \mu P_N < 0 \quad \text{stick} \\ \mu P_N sign(\dot{g}_T) & \text{otherwise} \quad \text{slip} \end{cases} \tag{2.92}$$

So often, a Coulomb's law regularization is used, which is most robust and simple when it is implemented using the finite element method. This regularization is presented in the following lines

$$P_T = \mu_r sign(\dot{g}_T)(|\dot{g}_T|)^{\alpha} P_N \tag{2.93}$$

where equation (2.93) represents in comparison with equation (2.92) a smooth transition from stick to slip. In equation (2.93) as α tends to zero the regularization approaches the Coulomb law. This regularization receives the name of Norton-Hoff friction law. In Figure 20, the function $sign(\dot{g}_T)(|\dot{g}_T|)^{\alpha}$ is plotted against $\dot{g}_T$ for different values of the parameter α. It can be seen that as α tends to zero, the function $sign(\dot{g}_T)(|\dot{g}_T|)^{\alpha}$ tends to the function $sign(\dot{g}_T)$, showing that in the limit the regularization is exactly, the Coulomb friction law.

2.6.3 Heat transfer at the tool chip interface

In what follows we formulate the constitutive relationships for the heat flux Q and the dissipation D_{fric} at the tool chip interface.

The heat flux in the contact zone also needs a constitutive equation for its determination. We assume the following structure for the constitutive equation for the heat flux:

$$Q_{hc} := Q_{hc}^{(1)} = h(\theta^{(1)}, \overline{\theta}^{(2)}, P_N)(\theta^{(1)} - \overline{\theta}^{(2)}) = h(\theta^{(1)}, \overline{\theta}^{(2)}, P_N) g_Q \tag{2.94}$$

where $\theta^{(i)}$ are the temperatures of both contact surfaces and $h(\theta^{(1)}, \overline{\theta}^{(2)}, P_N)$ the thermal conductance coefficient. $\overline{\theta}^{(2)}$ is the temperature at $\mathbf{x}^{(2)} = \boldsymbol{\varphi}^{(2)}(\widehat{\mathbf{X}}^{(2)})$, where $\widehat{\mathbf{X}}^{(2)}$ is the material point on $\Gamma^{(2)}$ defined by the closed point projection (2.88). The heat transfer coefficient $h(\theta^{(1)}, \overline{\theta}^{(2)}, P_N)$ depends upon the surface temperatures and the contact pressure.

Due to the technical impossibility of obtaining perfectly plane surfaces, the real contact area is always limited and corresponds to a series of spots. Determination of the true contact area is fundamental for the modeling of thermal phenomena. Therefore, heat exchange at the tool chip interface is possible by heat conduction through the spots, heat conduction through the gas contained in the cavities and radiation between micro-cavity surfaces. The assumption that the mentioned mechanisms act in parallel is well accepted, leads to the following relationship for the thermal conductance coefficient

$$h(\theta^{(1)}, \overline{\theta}^{(2)}, P_N) = h_s(\theta^{(1)}, \overline{\theta}^{(2)}, P_N) + h_g(\theta^{(1)}, \overline{\theta}^{(2)}, P_N) + h_r(\theta^{(1)}, \overline{\theta}^{(2)}, P_N) \tag{2.95}$$

where h_s is the thermal conductance coefficient due to conduction through the spots, h_g is the thermal conductance coefficient due to conduction through the

gas contained in the cavities and h_r is the thermal conductance coefficient due to heat transfer by radiation between micro-cavity surfaces.
The contact pressure is the factor of most influence on contact thermal conductance coefficient. As contact pressure grows, contact conductance grows. This is attributed to the fact that the contact surface between the bodies increases as the contact pressure increases. When the contact pressure is increased to such an extent that the real contact area of contact is a large portion of the apparent contact area, it is no longer possible for the real contact area to increase proportionately to the load. Contact between the tool and the work surface is so nearly complete over a large part of the total area, such that the thermal conductance coefficient is independent of the contact pressure. For simplicity, in this work, we will assume that the thermal conductance coefficient is independent of the temperatures of the bodies in contact. Such that equation (2.94) is simplified as

$$Q_{hc} \coloneqq Q_{hc}^{(1)} = h(\theta^{(1)} - \overline{\theta}^{(2)}) = hg_Q \tag{2.96}$$

When two bodies, say a cutting tool and a workpiece, are in contact, the rate at which heat is generated, is shared between the two bodies. This heat must be apportioned between the tool and the chip. The heat entering the tool and the workpiece is given by [24]

$$\begin{aligned} R_{fric}^{(1)} &= \frac{\sqrt{\rho^{(1)}c^{(1)}k^{(1)}}}{\sqrt{\rho^{(1)}c^{(1)}k^{(1)}} + \sqrt{\rho^{(2)}c^{(2)}k^{(2)}}} D_{fric} = \phi_1 D_{fric} \\ R_{fric}^{(2)} &= \frac{\sqrt{\rho^{(2)}c^{(2)}k^{(2)}}}{\sqrt{\rho^{(1)}c^{(1)}k^{(1)}} + \sqrt{\rho^{(2)}c^{(2)}k^{(2)}}} D_{fric} = \phi_2 D_{fric} \end{aligned} \tag{2.97}$$

where the heat generation due to friction at the tool chip interface is given by

$$D_{fric} = P_T \dot{g}_T = \mu_r sign(\dot{g}_T)(\left|\dot{g}_T\right|)^{\alpha} P_N \dot{g}_T \tag{2.98}$$

And where $\rho^{(i)}$, $c^{(i)}$ and $k^{(i)}$ represent thermal properties namely mass density, conductivity and specific heat respectively.

2.7 Variational Formulation. Weak Form of the IBVP Including Frictional Contact Constraints

We define the set of admissible displacements and admissible temperatures of $\beta^{(i)}$ as the set of all sufficiently regular displacement and temperature functions that satisfy the essential boundary condition, denoted here respectively as

$$\begin{aligned} U^{(i)} &\coloneqq \boldsymbol{\varphi}^{(i)}(\beta^{(i)}) \to \mathrm{R}^2 : \det(\mathbf{F}) > 0 \ \text{ and } \ \boldsymbol{\varphi}^{(i)}\Big|_{\gamma_{\varphi}^{(i)}} = \overline{\boldsymbol{\varphi}}^{(i)} \\ \Theta^{(i)} &\coloneqq \theta^{(i)}(\beta^{(i)}) \to \mathrm{R}^1 : \theta^{(i)} > 0 \ \text{ and } \theta^{(i)}\Big|_{\gamma_{\theta}^{(i)}} = \overline{\theta}^{(i)} \end{aligned} \tag{2.99}$$

The spatial version of the virtual work principle states that the body $\beta^{(i)}$ is in equilibrium if, and only if, its Cauchy stress satisfies the equation. The weak form of the momentum balance equation (2.7) (b) can be justified by taking the L_2 inner product of (2.7) (b) with any $\boldsymbol{\eta}^{(i)} \in \mathrm{V}^{(i)}$, and, making use of the divergence theorem, leading to the following expression:

$$\begin{aligned} &\int_{S_t^{(i)}} \boldsymbol{\sigma}^{(i)} : \nabla^s \boldsymbol{\eta}^{(i)} dS_t^{(i)} - \boldsymbol{\eta}^{(i)}(\mathbf{b}^{(i)} - \rho^{(i)}\dot{\mathbf{v}}^{(i)}) dS_t^{(i)} - \int_{\gamma_{\boldsymbol{\sigma}}^{(i)}} \mathbf{t}^{(i)} \cdot \boldsymbol{\eta}^{(i)} d\gamma^{(i)} \\ &- \int_{\gamma^{(i)}} \mathbf{t}^{(i)} \cdot \boldsymbol{\eta}^{(i)} d\gamma^{(i)} = 0 \quad \forall\ \boldsymbol{\eta}^{(i)} \in \mathrm{V}^{(i)} \end{aligned} \tag{2.100}$$

where $V^{(i)}$ is the space of virtual displacements of $\beta^{(i)}$

$$V^{(i)} = \left\{ \boldsymbol{\eta}^{(i)} \middle| \varphi(\beta^{(i)}) \to \mathrm{R}^2 : \boldsymbol{\eta}^{(i)}\big|_{\gamma_{\varphi}^{(i)}} = 0 \right\} \tag{2.101}$$

The dynamic weak form of the energy balance equations on the body $\beta^{(i)}$ can be obtained by taking the L_2 inner product of (2.7) (c) with any $\zeta^{(i)} \in T^{(i)}$, and, making use of the divergence theorem, leading to the following expression:

$$\begin{aligned} \int_{S_t^{(i)}} \zeta^{(i)} \theta^{(i)} \dot{h}^{(i)} dS_t^{(i)} = &\int_{S_t^{(i)}} \nabla \zeta^{(i)} \cdot \mathbf{q}^{(i)} dS_t^{(i)} \\ &+ \int_{S_t^{(i)}} \zeta^{(i)} (D *_{\mathrm{int}}^{(i)} + r^{(i)}) dS_t^{(i)} - \int_{\gamma_{\mathbf{q}}^{(i)}} \zeta^{(i)} (\mathbf{q}^{(i)} \cdot \boldsymbol{n}) d\gamma_{\mathbf{q}}^{(i)} \\ &- \int_{\gamma^{(i)}} \zeta^{(i)} (\mathbf{q}^{(i)} \cdot \boldsymbol{n}) d\gamma^{(i)} \quad \forall\ \zeta^{(i)} \in T^{(i)} \end{aligned} \tag{2.102}$$

where $T^{(i)}$ is the space of virtual temperatures of $\beta^{(i)}$ such that $\boldsymbol{\eta}^{(i)}\big|_{\gamma_{\theta}^{(i)}} = 0$.

For simplicity the L_2 inner product will be represented as $\langle \cdot, \cdot \rangle$ and with a slight abuse in notation $\langle \cdot, \cdot \rangle_{\gamma_{\boldsymbol{\sigma}}^{(i)}}$, $\langle \cdot, \cdot \rangle_{\gamma^{(i)}}$ and $\langle \cdot, \cdot \rangle_{\gamma_{\mathbf{q}}^{(i)}}$ will denote the L_2 inner product on the boundaries $\gamma_{\sigma}^{(i)}$, $\gamma^{(i)}$ and $\gamma_q^{(i)}$, respectively.

As a consequence, equations (2.100) and (2.102) can be written as

$$\begin{aligned} \left\langle \boldsymbol{\sigma}^{(i)}, \nabla^s \boldsymbol{\eta}^{(i)} \right\rangle - \left\langle \boldsymbol{\eta}^{(i)}, \mathbf{b}^{(i)} - \rho^{(i)} \dot{\mathbf{v}}^{(i)} \right\rangle \\ - \left\langle \mathbf{t}^{(i)}, \boldsymbol{\eta}^{(i)} \right\rangle_{\gamma_{\boldsymbol{\sigma}}^{(i)}} - \left\langle \mathbf{t}^{(i)}, \boldsymbol{\eta}^{(i)} \right\rangle_{\gamma^{(i)}} = 0 \\ \left\langle \zeta^{(i)}, \rho^{(i)} \dot{e}^{(i)} \right\rangle - \left\langle \nabla \zeta^{(i)}, \mathbf{q}^{(i)} \right\rangle - \left\langle \zeta^{(i)}, D_{\mathrm{int}}^{(i)} \right\rangle \\ + \left\langle \zeta^{(i)}, \mathbf{q}^{(i)} \cdot \boldsymbol{n}^{(i)} \right\rangle_{\gamma_q^{(i)}} + \left\langle \zeta^{(i)}, \mathbf{q}^{(i)} \cdot \boldsymbol{n}^{(i)} \right\rangle_{\gamma^{(i)}} = 0 \end{aligned} \tag{2.103}$$

Denoting by $G_{dym,mech}^{(i)}$ and $G_{stat,mech}^{(i)}$ the dynamic and quasi-static weak forms of the momentum balance equations, respectively, excluding frictional contact

contribution, and by $G^{(i)}_{c,mech}$ the frictional contact contribution to the weak form of the momentum balance equations, respectively defined as

$$\begin{aligned} G^{(i)}_{dyn,mech} &= G^{(i)}_{stat,mech} + \left\langle \boldsymbol{\eta}, \rho^{(i)} \dot{\mathbf{v}}^{(i)} \right\rangle \\ G^{(i)}_{stat,mech} &= \left\langle \boldsymbol{\sigma}^{(i)}, \nabla^s \boldsymbol{\eta}^{(i)} \right\rangle - \left\langle \boldsymbol{\eta}^{(i)}, \mathbf{b}^{(i)} \right\rangle - \left\langle \mathbf{t}^{(i)}, \boldsymbol{\eta}^{(i)} \right\rangle_{\gamma^{(i)}_{\sigma}} \\ G^{(i)}_{c,mech} &= -\left\langle \mathbf{t}^{(i)}, \boldsymbol{\eta}^{(i)} \right\rangle_{\gamma^{(i)}} \end{aligned} \tag{2.104}$$

And denoting by $G^{(i)}_{dyn,therm}$ and $G^{(i)}_{stat,therm}$ the dynamic and quasi-static weak forms of the energy balance equations, respectively, excluding thermal frictional contact contribution, , and by $G^{(i)}_{c,therm}$ the thermal frictional contact contribution to the weak form of the energy balance equations, respectively defined as

$$\begin{aligned} G^{(i)}_{dyn,therm} &= \left\langle \zeta^{(i)}, \theta^{(i)} \dot{h}^{(i)} \right\rangle + G^{(i)}_{stat,therm} \\ G^{(i)}_{stat,therm} &= -\left\langle \nabla \zeta^{(i)}, \mathbf{q}^{(i)} \right\rangle - \left\langle \zeta^{(i)}, D^{(i)}_{\text{int}} + r^{(i)} \right\rangle + \left\langle \zeta^{(i)}, \mathbf{q}^{(i)} \cdot \boldsymbol{n} \right\rangle_{\gamma^{(i)}_{q}} \\ G^{(i)}_{c,therm} &= \left\langle \zeta^{(i)}, \mathbf{q}^{(i)} \cdot \boldsymbol{n} \right\rangle_{\gamma^{(i)}} \end{aligned} \tag{2.105}$$

The weak form of the momentum balance and energy equations for body $\beta^{(i)}$ can be expressed in short notation as

$$\left.\begin{aligned} G^{(i)}_{dyn,mech} + G^{(i)}_{c,mech} &= 0 \\ G^{(i)}_{dyn,therm} + G^{(i)}_{c,therm} &= 0 \end{aligned}\right\} \forall \boldsymbol{\eta}^{(i)} \in \mathrm{V}^{(i)},\ \forall \zeta^{(i)} \in \mathrm{T}^{(i)} \tag{2.106}$$

For the contact problem between the workpiece and the tool, the momentum balance and energy equations take the form

$$\left.\begin{aligned} \sum_{i=1}^{2} G^{(i)}_{dyn,mech} + \sum_{i=1}^{2} G^{(i)}_{c,mech} &= 0 \\ \sum_{i=1}^{2} G^{(i)}_{dyn,therm} + \sum_{i=1}^{2} G^{(i)}_{c,therm} &= 0 \end{aligned}\right\} \forall \boldsymbol{\eta}^{(i)} \in \mathrm{V}^{(i)},\ \forall \zeta^{(i)} \in \mathrm{T}^{(i)} \tag{2.107}$$

The locking problems. A mixed displacement-pressure formulation.

It is well known that pure displacement formulations are not suitable for problems in which the constitutive behavior exhibit incompressibility since they tend to locking. Locking means, in this connection, that the constraint conditions due to incompressibility which are related to the pure volumetric mode (in the elastic case the condition is $\det(\mathbf{F}^e) = 1$ and for plastic flow the condition $\det(\mathbf{F}^p) = \det(\mathbf{C}^p) = 1$ holds) cannot be satisfied. Thus, this behavior is also called volume locking. As locking is present in the machining problem, we adopt a mixed formulation in the momentum balance equation of the workpiece. Introducing a pressure/deviatoric decomposition of the Cauchy stress tensor, the standard expression of the equilibrium equation becomes

$$
\begin{aligned}
G^{(1)}_{dyn,mech} &= G^{(1)}_{stat,mech} + \left\langle \boldsymbol{\eta}^{(1)}, \rho^{(1)}\dot{\mathbf{v}}^{(1)} \right\rangle \\
G^{(1)}_{stat,mech} &= \left\langle dev(\boldsymbol{\sigma}^{(1)}) + p^{(1)}\mathbf{1}, \nabla^s \boldsymbol{\eta}^{(1)} \right\rangle - \left\langle \boldsymbol{\eta}^{(1)}, \mathbf{b}^{(1)} \right\rangle - \left\langle \mathbf{t}^{(1)}, \boldsymbol{\eta}^{(1)} \right\rangle_{\gamma^{(i)}_{\sigma}} \\
G^{(1)}_{c,mech} &= -\left\langle \mathbf{t}^{(1)}, \boldsymbol{\eta}^{(1)} \right\rangle_{\gamma^{(1)}}
\end{aligned}
\tag{2.108}
$$

The pressure field $p^{(1)}$ in the variational equation (2.108) is an additional variable determined by the following. The variational equation then represents the weak form of the pressure constitutive equation.

$$
\begin{aligned}
G^{(1)}_{comp,mech} &= \left\langle p^{(1)}, q^{(1)} \right\rangle - G^{(1)}_{volu,mech} \\
G^{(1)}_{volu,mech} &= \left\langle \kappa \ln(J^{(1)}) - 3\beta\kappa \frac{(1 - \ln(J^{(1)}))}{J^{(1)}}(\theta - \theta_0), q^{(1)} \right\rangle
\end{aligned}
\tag{2.109}
$$

Taking into account the mixed formulation used at the workpiece, the momentum and energy balance equations for the contact problem between the tool and the workpiece (2.107) take the form

$$
\begin{aligned}
&\sum_{i=1}^{2} G^{(i)}_{dyn,mech} + \sum_{i=1}^{2} G^{(i)}_{c,mech} = 0 \\
&\sum_{i=1}^{2} G^{(i)}_{dyn,therm} + \sum_{i=1}^{2} G^{(i)}_{c,therm} = 0 \\
&G^{(1)}_{comp,mech} = \left\langle p^{(1)}, q^{(1)} \right\rangle - G^{(1)}_{volu,mech} = 0
\end{aligned}
\tag{2.110}
$$

where

$$
G^{(1)}_{volu,mech} = \left\langle \kappa \ln(J^{(1)}) - 3\beta\kappa \frac{(1 - \ln(J^{(1)}))}{J^{(1)}}(\theta - \theta_0), q^{(1)} \right\rangle \forall q^{(1)} \in Q^1 \tag{2.111}
$$

Stabilization via the Polynomial Pressure Projection(PPP)

Mixed formulations have to fulfill additional mathematical conditions, which guarantee its stability. This condition is known as BB-condition, named after its inventors Babuska and Brezzi. Linear triangle finite elements do not satisfy BB-condition; consequently, a stabilization of the pressure field is needed. In our approach we use a stabilized formulation based in the so-called Polynomial Pressure Proyection(PPP) presented and applied to Stokes equation in [13, 14]. The method is obtained by modification of the mixed variational equation by using local L_2 polynomial pressure projections. Application of pressure projections in conjunction with minimization of the pressure-displacement mismatch eliminates inconsistency of equal-order approximations and leads to a stable variational formulation. Unlike other stabilization methods, the Polynomial pressure projection (PPP) does not require specification of a stabilization parameter or calculation of higher-order derivatives. In addition, PPP can be implemented at the element level and reduces to a simple modification of the weak continuity equation (incompressibility constrain). In this work, we extend the PPP to solid mechanics problems involving large strains.

Given a function $p^{(1)} \in L_2$, the L_2 projection operator $\breve{p}^{(1)} : L_2 \rightarrow P^0$ is defined by

$$G^{(1)}_{proj,mech} = \int_{S_t^{(i)}} \breve{q}^{(1)}(p^{(1)} - \breve{p}^{(1)})dS_t^{(i)} = 0 \quad \forall \breve{q}^{(1)} \in P^0 \tag{2.112}$$

where $\breve{p}^{(1)}$ is the best approximation of $p^{(1)}$ in the space of polynomials of order 0 (P^0).

To stabilize the mixed form (2.108)-(2.109), we add the projection operator to equation (2.109)

$$G^{(1)}_{stab,mech} = \int_{S_t^{(i)}} (q^{(1)} - \breve{q}^{(1)}) \frac{\alpha}{\mu^{(1)}} (p^{(1)} - \breve{p}^{(1)})dS_t^{(i)} \tag{2.113}$$

where α is the stabilization parameter and $\mu^{(1)}$ is the workpiece shear modulus.

Application of the projection operator to the pressure test and trial functions serves to remove the approximation inconsistency present for equal-order displacement and pressure spaces.

The role of the form $G^{(1)}_{stab,mech}$ is to further penalize pressure variation away from the range of the divergence operator. Taking into account the mixed formulation and the polynomial pressure stabilization terms to deal with the incompressibility phenomena in the workpiece, the momentum and energy balance equations for the contact problem between the tool and the workpiece (2.107) take the form

$$\begin{aligned}
&\sum_{i=1}^{2} G^{(i)}_{dyn,mech} + \sum_{i=1}^{2} G^{(i)}_{c,mech} = 0 \\
&\sum_{i=1}^{2} G^{(i)}_{dyn,therm} + \sum_{i=1}^{2} G^{(i)}_{c,therm} = 0 \\
&G^{(1)}_{comp,mech} = \left\langle p^{(1)}, q^{(1)} \right\rangle - G^{(1)}_{volu,mech} + G^{(1)}_{stab,mech} = 0
\end{aligned} \tag{2.114}$$

where

$$\begin{aligned}
&G^{(1)}_{volu,mech} = \left\langle \kappa \ln(J^{(1)}) - 3\beta\kappa \frac{(1 - \ln(J^{(1)}))}{J^{(1)}} (\theta - \theta_0), q^{(1)} \right\rangle \\
&G^{(1)}_{stab,mech} = \int_{S_t^{(i)}} (q^{(1)} - \breve{q}^{(1)}) \frac{\alpha}{\mu^{(1)}} (p^{(1)} - \breve{p}^{(1)})dS_t^{(i)} \\
&G^{(1)}_{proj,mech} = \int_{S_t^{(i)}} \breve{q}^{(1)}(p^{(1)} - \breve{p}^{(1)})dS_t^{(i)} = 0 \\
&\forall q^{(1)} \in Q^1, \forall \breve{p}^{(1)}, \breve{q}^{(1)} \in P^0
\end{aligned} \tag{2.115}$$

The set of governing equations for the displacement, pressure and temperature variables is completed by adding the following constraint equation to the set of governing equations.

In particular, for two interacting bodies $\beta^{(1)}$ and $\beta^{(2)}$, the frictional contact mechanical and thermal contributions to the weak form of the momentum and energy balance equations, at the spatial contact points $\mathbf{x}^{(1)} = \boldsymbol{\varphi}^{(1)}(\mathbf{X}^{(1)}) \in \gamma^{(1)}$ and $\mathbf{x}^{(2)} = \boldsymbol{\varphi}^{(2)}(\widehat{\mathbf{X}}^{(2)}) \in \gamma^{(2)}$, at any time $t \in I$

$$\begin{aligned} G^{(1,2)}_{c,mech} &:= G^{(1)}_{c,mech} + G^{(2)}_{c,mech} \\ G^{(1,2)}_{c,therm} &:= G^{(1)}_{c,therm} + G^{(2)}_{c,therm} \end{aligned} \tag{2.116}$$

The weak form of the equilibrium conditions at the tool chip interface given by (2.14), can be expressed as

$$\begin{aligned} \left\langle \mathbf{t}^{(2)}, \boldsymbol{\eta}^{(2)} \right\rangle_{\gamma^{(2)}} &= -\left\langle \mathbf{t}^{(1)}, \boldsymbol{\eta}^{(2)} \right\rangle_{\gamma^{(1)}} \\ \left\langle Q^{(2)}_{hc}, \zeta^{(2)} \right\rangle_{\gamma^{(2)}} &= -\left\langle Q^{(1)}_{hc}, \zeta^{(2)} \right\rangle_{\gamma^{(1)}} \end{aligned} \tag{2.117}$$

Using (2.117) the mechanical and thermal contact contribution to the weak form of the momentum and energy balance equations take the simple form

$$\begin{aligned} G^{(1,2)}_{c,mech} &:= -\left\langle \mathbf{t}^{(1)}, \boldsymbol{\eta}^{(1)} \right\rangle_{\gamma^{(1)}} + \left\langle \mathbf{t}^{(1)}, \boldsymbol{\eta}^{(2)} \right\rangle_{\gamma^{(1)}} = -\left\langle \mathbf{t}^{(1)}, \boldsymbol{\eta}^{(1)} - \overline{\boldsymbol{\eta}}^{(2)} \right\rangle_{\gamma^{(1)}} \\ G^{(1,2)}_{c,therm} &:= -\left\langle Q^{(1)}_{hc}, \zeta^{(1)} \right\rangle_{\gamma^{(1)}} + \left\langle Q^{(1)}_{hc}, \zeta^{(2)} \right\rangle_{\gamma^{(1)}} = -\left\langle Q^{(1)}_{hc}, \zeta^{(1)} - \overline{\zeta}^{(2)} \right\rangle_{\gamma^{(1)}} \end{aligned} \tag{2.118}$$

2.8 Numerical Integration Algorithm

2.8.1 The incremental boundary value problem. Finite element discretization

Consider a spatial discretization $\Omega^{(i)} = \cup_{e=1}^{nelem} \Omega^{(i)}_e$ into a disjoint collection of non-overlapping elements $\Omega^{(i)}_e$ with characteristic size $h^{(e)}$.

The finite element method for numerical solution of problem (2.110) consists of replacing the functional sets $U^{(i)}, V^{(i)}$, $\Theta^{(i)}, T^{(i)}$ and $P^{(1)}, Q^{(1)}$ with discrete subsets $U^{(i),h}, V^{(i),h}$, $\Theta^{(i),h}, T^{(i),h}$ and $P^{(1),h}$, ${}^{h}Q^{(1),h}$ generated by a finite element discretization h of the domain $\Omega^{(i)}$. Let $a^{(i)}(\mathbf{X}^{(i)})$ be a generic field defined over the domain $\Omega^{(i)}_e$ of the element. The finite element interpolation of the field a within element e of body i is obtained as

$$a^{(i),h}(\mathbf{X}^{(i)}) = \sum_{j=1}^{nnode} a^{(i)}_j N^{(i),e}_j(\mathbf{X}^{(i)}) \tag{2.119}$$

where a^j is the value of a at node j, and $N^{(i),e}_j$ is the shape function such that is value is 1 at the node j and zero at any other node of the element.

The interpolated function, now defined over the approximated domain is given by

$$a^{(i),h}(\mathbf{X}^{(i)}) = \sum_{j=1}^{npo\,\mathrm{int}} a_j^{(i)} N_j^{(i)}(\mathbf{X}^{(i)}) \tag{2.120}$$

where $N_j^{(i)}$ is a piecewise polynomial function – the global shape function – associated with the global node j and $npo\,\mathrm{int}$ is the total number of nodal points in the finite element mesh.

With the introduction of the above interpolation procedure, we generate the finite dimensional sets

$$\begin{aligned}
U^{(i),h} &:= \left\{ \boldsymbol{\varphi}^{(i),h}(\mathbf{X}^{(i)}) = \sum_{j=1}^{npo\,\mathrm{int}} \boldsymbol{\varphi}_j^{(i)} N_j^{(i)}(\mathbf{X}^{(i)}) : \boldsymbol{\varphi}^{(i),h}\Big|_{\gamma_\varphi^{(i),h}} = \bar{\boldsymbol{\varphi}}^{(i)} \right\} \\
\Theta^{(i),h} &:= \left\{ \theta^{(i),h}(\mathbf{X}^{(i)}) = \sum_{j=1}^{npo\,\mathrm{int}} \theta_j^{(i)} N_j^{(i)}(\mathbf{X}^{(i)}) : \theta^{(i),h}\Big|_{\gamma_\theta^{(i),h}} = \bar{\theta}^{(i)} \right\} \\
P^{(1),h} &:= \left\{ p^{(1),h}(\mathbf{X}^{(1)}) = \sum_{j=1}^{npo\,\mathrm{int}} p_j^{(1)} N_j^{(1)}(\mathbf{X}^{(1)}) \right\}
\end{aligned} \tag{2.121}$$

and

$$\begin{aligned}
V^{(i),h} &= \left\{ \boldsymbol{\eta}^{(i),h} = \sum_{j=1}^{npo\,\mathrm{int}} \boldsymbol{\varphi}_j^{(i)} N_j^{(i)}(\mathbf{X}^{(i)}) : \boldsymbol{\eta}^{(i),h}\Big|_{\gamma_\varphi^{(i),h}} = 0 \right\} \\
T^{(i),h} &= \left\{ \zeta^{(i),h} = \sum_{j=1}^{npo\,\mathrm{int}} \zeta_j^{(i)} N_j^{(i)}(\mathbf{X}^{(i)}) : \zeta^{(i),h}\Big|_{\gamma_\theta^{(i),h}} = 0 \right\} \\
Q^{(1),h} &= \left\{ q^{(1),h} = \sum_{j=1}^{npo\,\mathrm{int}} q_j^{(1)} N_j^{(1)}(\mathbf{X}^{(i)}) : q^{(1),h}\Big|_{\gamma_\theta^{(1),h}} = 0 \right\}
\end{aligned} \tag{2.122}$$

The finite element approximation to the continuum variational problem (2.110) is then obtained by replacing the functional sets $U^{(i)}, V^{(i)}$, $\Theta^{(i)}, T^{(i)}$ and $P^{(1)}, Q^{(1)}$ with discrete subsets $U^{(i),h}, V^{(i),h}$, $\Theta^{(i),h}, T^{(i),h}$ and $P^{(1),h}, Q^{(1),h}$.

To derive the discretized form of (2.110) it is convenient to introduce the standard matrix notations that follow

$$\begin{aligned}
\boldsymbol{\varphi}^{(i),h} &= \mathbf{N}^{(i)} \boldsymbol{\varphi}^{(i)} \\
\theta^{(i),h} &= \mathbf{N}^{(i)} \boldsymbol{\theta}^{(i)} \\
p^{(1),h} &= \mathbf{N}^{(1)} \boldsymbol{p}^{(1)}
\end{aligned} \tag{2.123}$$

and

$$\begin{aligned}
\boldsymbol{\eta}^{(i),h} &= \mathbf{N}^{(i),g} \boldsymbol{\eta}^{(i)} \\
\zeta^{(i),h} &= \mathbf{N}^{(i),g} \boldsymbol{\zeta}^{(i)} \\
q^{(1),h} &= \mathbf{N}^{(1),g} \boldsymbol{q}^{(1)}
\end{aligned} \tag{2.124}$$

where $\boldsymbol{\varphi}^{(i)}, \boldsymbol{\theta}^{(i)}.\boldsymbol{p}^{(1)}, \boldsymbol{\eta}^{(i)}, \boldsymbol{\zeta}^{(i)}, \boldsymbol{q}^{(1)}$ are the vector of nodal displacements, nodal temperatures, nodal pressures, virtual displacements, virtual temperatures and virtual pressure, respectively.
It is also convenient to introduce the global strain-displacement matrix, which in two dimensions has the format

$$\mathbf{B}^{u} = \begin{bmatrix} N^{g}_{1,1} & 0 & N^{g}_{2,1} & 0 & \cdots & N^{g}_{npoin,1} & 0 \\ 0 & N^{g}_{1,2} & 0 & N^{g}_{2,2} & \cdots & 0 & N^{g}_{npo\,\mathrm{int},2} \\ N^{g}_{1,2} & N^{g}_{1,1} & N^{g}_{2,2} & N^{g}_{2,1} & \cdots & N^{g}_{npo\,\mathrm{int},2} & N^{g}_{npoin,1} \end{bmatrix} \tag{2.125}$$

and the global gradient-temperature matrix

$$\mathbf{B}^{\theta} = \begin{bmatrix} N_{1,1} & N_{2,1} & \cdots & N_{npoin,1} \\ N_{1,2} & N_{2,2} & \cdots & N_{npo\,\mathrm{int},2} \end{bmatrix} \tag{2.126}$$

For the vector field $\boldsymbol{\varphi}^{(i),h} = \mathbf{N}^{(i)}\boldsymbol{\varphi}^{(i)}$, the multiplication of $\mathbf{B}^{u}$ by a global vector of nodal displacement gives an array of strains and for the field $\theta^{(i),h} = \mathbf{N}^{(i)}\boldsymbol{\theta}^{(i)}$ the multiplication of $\mathbf{B}^{\theta}$ by a global vector of nodal temperatures gives the arrays of the temperature gradients.
Finally, the array of Cauchy stress component is defined as

$$\sigma = \left[\sigma_{11}, \sigma_{22}, \sigma_{12}\right]^{T} \tag{2.127}$$

With the above notation at hand, the replacement of $U^{(i)}, V^{(i)}$, $\Theta^{(i)}, T^{(i)}$ and $P^{(1)}, Q^{(1)}$ with $U^{(i),h}, V^{(i),h}$, $\Theta^{(i),h}, T^{(i),h}$ and $P^{(1),h}, Q^{(1),h}$. in (2.110) and since (2.110) equations are satisfied for all vectors $\boldsymbol{\eta}^{(i)}, \boldsymbol{\zeta}^{(i)}, \boldsymbol{q}^{(1)}$, the discrete counterpart of (2.110) is given by the equations

$$\begin{aligned} &\int_{S_t^{(i)}} ({}^{u}\boldsymbol{B}^{(i),g})^{T}\boldsymbol{\sigma}^{(i)} dS_t^{(i)} - (\boldsymbol{N}^{(i),g})^{T}(\mathbf{b}^{(i)} - \rho^{(i)}\dot{\mathbf{v}}^{(i)}) dS_t^{(i)} \\ &- \int_{\gamma_{\sigma}^{(i)}} (\boldsymbol{N}^{(i),g})^{T}\mathbf{t}^{(i)} d\gamma^{(i)} - \int_{\gamma^{(i)}} (\boldsymbol{N}^{(i),g})^{T}\mathbf{t}^{(i)} d\gamma^{(i)} = 0 \end{aligned} \tag{2.128}$$

$$\begin{aligned} &\int_{S_t^{(i)}} \rho^{(i)} c^{(i)} \boldsymbol{N}^{(i),g} (\boldsymbol{N}^{(i),g})^{T} \dot{\boldsymbol{\theta}}^{(i)} dS_t^{(i)} - \int_{S_t^{(i)}} ({}^{\theta}\boldsymbol{B}^{(i),g})^{T}\mathbf{q}^{(i)} dS_t^{(i)} \\ &- \int_{S_t^{(i)}} (\boldsymbol{N}^{(i),g})^{T} D_{\mathrm{int}}^{(i)} dS_t^{(i)} + \int_{\gamma_{\mathbf{q}}^{(i)}} (\boldsymbol{N}^{(i),g})^{T}(\mathbf{q}^{(i)} \cdot \boldsymbol{n}) d\gamma_{\mathbf{q}}^{(i)} \\ &+ \int_{\gamma^{(i)}} (\boldsymbol{N}^{(i),g})^{T}(\mathbf{q}^{(i)} \cdot \boldsymbol{n}) d\gamma^{(i)} = 0 \end{aligned} \tag{2.129}$$

$$\int_{S_t^{(1)}} \boldsymbol{N}^{(i),g} (\boldsymbol{N}^{(i),g})^T \, p^1 dS_t^{(i)}$$
$$- \int_{S_t^{(1)}} (\boldsymbol{N}^{(i),g})^T \left(\ln(J^{(1)}) - 3\beta\kappa \frac{(1 - \ln(J^{(1)}))}{J^{(1)}} (\theta - \theta_0) \right) dS_t^{(i)} = 0 \tag{2.130}$$

The finite element discrete boundary value problem is then formulated as follows. Find the vector of global displacements, global pressures and global temperatures, such that

$$\begin{aligned}
&\mathbf{F}^{(i),\mathrm{int},mech}(\mathbf{u}^{(i)}, \mathbf{p}^{(i)}) - \mathbf{F}^{(i),ext,mech} - \mathbf{F}^{(i),c,mech} = \mathbf{F}^{(i),dyn,mech}(\ddot{\mathbf{u}}^{(i)}) \\
&\mathbf{F}^{(i),\mathrm{int},therm}(\boldsymbol{\theta}^{(i)}) - \mathbf{F}^{(i),ext,therm} - \mathbf{F}^{(i),c,therm} = \mathbf{F}^{(i),dyn,therm}(\dot{\boldsymbol{\theta}}^{(i)}) \\
&\mathbf{F}^{(1),press,mech} - \mathbf{F}^{(1),volu,mech} = 0
\end{aligned} \tag{2.131}$$

where

$$\begin{aligned}
\mathbf{F}^{(i),\mathrm{int},mech}(\mathbf{u}^{(i)}, \mathbf{p}^{(i)}) &= \int_{S_t^{(i)}} ({}^u\boldsymbol{B}^{(i),g})^T \boldsymbol{\sigma}^{(i)} dS_t^{(i)} \\
\mathbf{F}^{(i),ext,mech} &= \int_{\gamma_{\boldsymbol{\sigma}}^{(i)}} (\boldsymbol{N}^{(i),g})^T \mathbf{t}^{(i)} d\gamma^{(i)} \\
\mathbf{F}^{(i),c,mech} &= \int_{\gamma_{\boldsymbol{\sigma}}^{(i)}} (\boldsymbol{N}^{(i),g})^T \mathbf{t}^{(i)} d\gamma^{(i)} \\
\mathbf{F}^{(i),dyn,mech}(\mathbf{u}^{(i)}) &= \int_{S_t^{(i)}} \rho^{(i)} \dot{\mathbf{v}}^{(i)} dS_t^{(i)}
\end{aligned} \tag{2.132}$$

$$\begin{aligned}
\mathbf{F}^{(i),\mathrm{int},therm}(\boldsymbol{\theta}^{(i)}) &= \int_{S_t^{(i)}} ({}^\theta\boldsymbol{B}^{(i),g})^T \mathbf{q}^{(i)} dS_t^{(i)} \\
&\quad + \int_{S_t^{(i)}} (\boldsymbol{N}^{(i),g})^T D_{\mathrm{int}}^{(i)} dS_t^{(i)} \\
\mathbf{F}^{(i),ext,therm} &= \int_{\gamma_{\mathbf{q}}^{(i)}} (\boldsymbol{N}^{(i),g})^T (\mathbf{q}^{(i)} \cdot \boldsymbol{n}) d\gamma_{\mathbf{q}}^{(i)} \\
\mathbf{F}^{(i),c,therm} &= \int_{\gamma^{(i)}} (\boldsymbol{N}^{(i),g})^T (\mathbf{q}^{(i)} \cdot \boldsymbol{n}) d\gamma^{(i)} \\
\mathbf{F}^{(i),dyn,therm}(\dot{\boldsymbol{\theta}}^{(i)}) &= \int_{S_t^{(i)}} \rho^{(i)} c^{(i)} \boldsymbol{N}^{(i),g} (\boldsymbol{N}^{(i),g})^T \dot{\boldsymbol{\theta}}^{(i)} dS_t^{(i)}
\end{aligned} \tag{2.133}$$

$$\begin{aligned}
\mathbf{F}^{(1),press,mech} &= \frac{1}{\kappa} \int_{S_t^{(1)}} \boldsymbol{N}^{(1),g} (\boldsymbol{N}^{(1),g})^T dS_t^{(1)} p^1 \\
\mathbf{F}^{(1),volu,mech} &= \int_{S_t^{(1)}} (\boldsymbol{N}^{(1),g})^T \left(\ln(J^{(1)}) - 3\beta \frac{(1 - \ln(J^{(1)}))}{J^{(1)}} (\theta - \theta_0) \right) dS_t^{(1)}
\end{aligned} \tag{2.134}$$

In actual finite element computations, the above force vectors are obtained as the assemblies of element vectors. The finite element assembly operator, $\overset{nelem}{\underset{e=1}{\mathbf{A}}}$,

implies that each component of the global force associated with a particular global node is obtained as the sum of the corresponding contributions from the element force vectors of all elements that share that global node.
In this work, the element force vectors are evaluated using Gaussian quadratures. The standard element shape function of the three-noded linear triangle are defined as

$$\begin{aligned} N_1^{(i),(e)}(\xi,\eta) &= 1-\xi-\eta \\ N_2^{(i),(e)}(\xi,\eta) &= \xi \\ N_3^{(i),(e)}(\xi,\eta) &= \eta \end{aligned} \tag{2.135}$$

This elements shape functions are used to discretize the displacement, pressure and temperature fields.
Finite elements, which are derived from mixed methods, have to fulfill additional mathematical conditions, which guarantee the stability of the element formulation. This condition is known as BB-condition, named after its inventors Babuska and Brezzi.
The FEM solution of the variables in the (incompressible) solid (workpiece) domain implies solving the momentum and incompressibility equations. This is not such as simple problem as the incompressibility condition limits the choice of the FE approximations for the displacement and pressure to overcome the well-known div-stability condition. In our work, we use a stabilized mixed FEM based on the Polynomial Pressure Projection (PPP) approach, which allows for a linear approximation for the displacement, temperature and pressure variables.
The discrete counterpart of projection operator for linear triangle finite elements is given by (2.136), where we have used that the pressure projection is constant and discontinuous among finite elements

$$\mathbf{F}^{(1),stab,mech,(e)} = \frac{\alpha}{\mu^{(1)}}\Big(\int_{S_t^{(1),(e)}} \boldsymbol{N}^{(1),(e)T}\boldsymbol{N}^{(1),(e)} - \tilde{\boldsymbol{N}}^{(1),(e)T}\tilde{\boldsymbol{N}}^{(1),(e)} dS_t^{(1),(e)}\Big)p^{(1),(e)} \tag{2.136}$$

To stabilize the mixed form, we add the discrete projection operator (2.136) to equation(2.134).

Finally, the resulting set of discretized equations that we need to solve to model metal cutting has the following form:

$$\begin{gathered} \text{Momentum} \\ \mathbf{F}^{(i),\text{int},mech} - \mathbf{F}^{(i),ext,mech} - \mathbf{F}^{(i),c,mech} = \mathbf{F}^{(i),dyn,mech} = \mathbf{M}^m\mathbf{a}^{(i)} \\ \text{Energy} \\ \mathbf{F}^{(i),\text{int},therm} - \mathbf{F}^{(i),ext,therm} - \mathbf{F}^{(i),c,therm} = \mathbf{F}^{(i),dyn,therm} = \mathbf{M}^t\dot{\theta}^{(i)} \\ \text{Imcompressibility} \\ \mathbf{F}^{(1),press,mech} - \mathbf{F}^{(1),volu,mech} + \mathbf{F}^{(1),stab,mech} = 0 \end{gathered} \tag{2.137}$$

2.8.2 The incremental boundary value problem. Time discretization

2.8.2.1 Implicit coupled algorithm (Monolithic scheme)

For simplicity, a partition of the time domain $I := \left[0, T\right]$ into N time steps, of the same length Δt is considered. Let us focus on the time step $t_n \rightarrow t_{n+1}$, where $\Delta t = t_{n+1} - t_n$. The application of an implicit backward-Euler time integration scheme to the problem (displacement, velocities and temperatures) (2.137) yields the following algorithm defined by the initial conditions

Coupled system of equations

Momentum

$$\mathbf{F}^{(i),dyn,mech}(\dot{\mathbf{v}}^{(i)}_{n+1}) = \mathbf{F}^{(i),\mathrm{int},mech}(\boldsymbol{\sigma}^{(i)}_{n+1}(\mathbf{u}^{(i)}_{n+1}, \mathbf{p}^{(i)}_{n+1}, \boldsymbol{\theta}^{(i)}_{n+1}; \lambda_{n+1}(\mathbf{u}^{(i)}_{n+1}, \boldsymbol{\theta}^{(i)}_{n+1}))) - \mathbf{F}^{(i),ext,mech}(\mathbf{u}^{(i)}_{n+1}) - \mathbf{F}^{(i),c,mech}(\mathbf{u}^{(i)}_{n+1})$$

Incompressibility

$$\left(\frac{1}{\kappa}\mathbf{M}^{p} + \frac{1}{G}\mathbf{M}^{stab}\right)\mathbf{p}^{(1)}_{n+1} = \mathbf{F}^{(1),volu,mech}(J^{(1)}_{n+1}(\mathbf{u}^{(1)}_{n+1}, \boldsymbol{\theta}^{(1)}_{n+1}))$$

Energy

$$\mathbf{F}^{(i),dyn,therm}(\dot{\boldsymbol{\theta}}^{(i)}_{n+1}) = \mathbf{F}^{(i),\mathrm{int},therm}(q(\dot{\boldsymbol{\theta}}^{(i)}_{n+1}); D^{(i)}_{\mathrm{int}}(\mathbf{u}^{(i)}_{n+1}, \boldsymbol{\theta}^{(i)}_{n+1}; \lambda_{n+1}(\mathbf{u}^{(i)}_{n+1}, \boldsymbol{\theta}^{(i)}_{n+1})) - \mathbf{F}^{(i),ext,therm} - \mathbf{F}^{(i),c,therm}$$

Update nodal variables

$$\mathbf{v}^{(i)}_{n+1} = \mathbf{v}^{(i)}_{n} + \dot{\mathbf{v}}^{(i)}_{n+1}\Delta t$$
$$\mathbf{u}^{(i)}_{n+1} = \mathbf{u}^{(i)}_{n} + \mathbf{v}^{(i)}_{n+1}\Delta t$$
$$\mathbf{p}^{(1)}_{n+1} = \mathbf{p}^{(1)}_{n} + \Delta\mathbf{p}^{(1)}_{n+1}$$
$$\boldsymbol{\theta}^{(i)}_{n+1} = \boldsymbol{\theta}^{(i)}_{n} + \dot{\boldsymbol{\theta}}^{(i)}_{n+1}\Delta t$$

Box 3. Implicit coupled solution scheme.

The set of equations presented in Box 3, show a simultaneous solution scheme of the coupled systems of equations where the temperature varies during the mechanical step and the configuration varies during the thermal step. At first glance, the simultaneous solution is the obvious one, but a depth analysis show that is a computationally intensive procedure [102]. The monolithic scheme is unconditionally stable due to its fully implicit character. The different time scales associated with the thermal and mechanical fields suggested that an effective numerical integration of the coupled problem should take advantage of these different time scales. One of the effective integration schemes is the so-called staggered algorithms, whereby the problem is partitioned into several smaller sub-problems that are solved sequentially (splitting each time step in several pseudo-time steps). Most of the time, this technique is especially attractive from a computational viewpoint since the large and no symmetric system that result from a simultaneous solution scheme is replaced by a much smaller, subsystem. Based on the global operator split for finite deformation plasticity presented in

equations(2.17), (2.21) and (2.24), a formal split of the problem into a mechanical phase with the temperature held constant, followed by a thermal phase at a fixed configuration is presented in the following lines:

2.8.2.2 Isothermal split

The following lines present a summary of the isothermal split, developed in [102]. Let t_n and t_{n+1} be the initial and final time step. Let $\Delta t = t_{n+1} - t_n$ be the time increment

Momentum equation for fixed initial temperature

$$\mathbf{F}^{(i),dyn,mech}(\dot{\mathbf{v}}_{n+1}^{(i),*}) =$$

$$\mathbf{F}^{(i),\mathrm{int},mech}(\boldsymbol{\sigma}_{n+1}^{(i)}(\mathbf{u}_{n+1}^{(i),*}, \mathbf{p}_{n+1}^{(i),*}, \boldsymbol{\theta}_{n}^{(i),*}; \lambda_{n+1}^{(i)}(\mathbf{u}_{n+1}^{(i),*}, \boldsymbol{\theta}_{n}^{(i),*}))) - \mathbf{F}^{(i),ext,mech}(\mathbf{u}_{n+1}^{(i),*})$$

$$-\mathbf{F}^{(i),c,mech}(\mathbf{u}_{n+1}^{(i),*})$$

Incompressibility

$$\left(\frac{1}{\kappa}\mathbf{M}^{p} + \frac{1}{G}\mathbf{M}^{stab}\right)\mathbf{p}_{n+1}^{(1),*} = \mathbf{F}^{(1),volu,mech}(J_{n+1}^{(1),*}(\mathbf{u}_{n+1}^{(1),*}, \boldsymbol{\theta}_{n}^{(1),*}))$$

Update nodal variables

$$\mathbf{v}_{n+1}^{(i)} = \mathbf{v}_{n}^{(i)} + \dot{\mathbf{v}}_{n+1}^{(i)}\Delta t$$

$$\mathbf{u}_{n+1}^{(i),*} = \mathbf{u}_{n}^{(i),*} + \mathbf{v}_{n+1}^{(i),*}\Delta t$$

$$\mathbf{p}_{n+1}^{(1),*} = \mathbf{p}_{n}^{(1),*} + \Delta\mathbf{p}_{n+1}^{(1),*}$$

Energy equation at updated fixed configuration

$$\mathbf{F}^{(i),dyn,therm}(\dot{\boldsymbol{\theta}}_{n+1}^{(i),*}) =$$

$$\mathbf{F}^{(i),\mathrm{int},therm}(q(\boldsymbol{\theta}_{n+1}^{(i),*}); D_{\mathrm{int}}^{(i),*}(\mathbf{u}_{n+1}^{(i),*}, \boldsymbol{\theta}_{n+1}^{(i),*}; \lambda_{n+1}^{(i)}(\mathbf{u}_{n+1}^{(i),*}, \boldsymbol{\theta}_{n+1}^{(i),*})) - \mathbf{F}^{(i),ext,therm} - \mathbf{F}^{(i),c,therm}$$

Update nodal variables

$$\boldsymbol{\theta}_{n+1}^{(i),*} = \boldsymbol{\theta}_{n}^{(i)} + \dot{\boldsymbol{\theta}}_{n+1}^{(i),*}\Delta t$$

Box 4. Implicit isothermal split.

The above algorithm is based on the application of an implicit backward-Euler difference formula to the momentum equation for fixed initial temperature (temperature at previous time step) and the application of an implicit backward-Euler difference scheme to the energy equation at fixed configuration (configuration obtained as a solution of the mechanical problem).

The solution of the balance of momentum equation for fixed initial temperature, gives an update of the primary variables $\mathbf{u}_{n+1}^{(i),*}, \mathbf{p}_{n+1}^{(i),*}$ and a first update of the internal variables of the form

$$\mathbf{b}_{n}^{e}, \overline{e}_{n}^{p}, \eta_{n}^{p} \quad \rightarrow \quad \tilde{\mathbf{b}}_{\mathrm{n+1}}^{\mathrm{e}}, \tilde{\overline{e}}_{n+1}, \tilde{\eta}_{n+1}^{p} \tag{2.138}$$

Along with an incremental value of the consistency parameter satisfying the Kuhn-Tucker conditions and denoted by $\Delta\tilde{\lambda}_{n+1}$.

The solution of the balance of energy with initial conditions $\mathbf{u}_{n+1}^{(i),*}, \mathbf{p}_{n+1}^{(i),*}, \boldsymbol{\theta}_{n}^{(i),*}$ and initial internal variables $\mathbf{b}_n^e, \overline{e}_n^p, \eta_n^p$ gives an update of the primary variable $\boldsymbol{\theta}_{n+1}^{(i),*}$ and a second update of the internal plastic variables (at fixed configuration) of the form

$$\mathbf{b}_n^e, \overline{e}_n^p, \eta_n^p \quad \rightarrow \quad \tilde{\tilde{\mathbf{b}}}_{\mathrm{n+1}}^{\mathrm{e}}, \tilde{\tilde{\overline{e}}}_{n+1}^{p}, \tilde{\tilde{\eta}}_{n+1}^{p} \tag{2.139}$$

Along with an incremental value of the consistency parameter satisfying the Kuhn-Tucker conditions and denoted by $\Delta\tilde{\tilde{\lambda}}_{n+1}$. In general, $\Delta\tilde{\lambda}_{n+1} \neq \Delta\tilde{\tilde{\lambda}}_{n+1}$ as a consequence $\mathbf{b}_n^e, \overline{e}_n^p, \eta_n^p \neq \tilde{\tilde{\mathbf{b}}}_{\mathrm{n+1}}^{\mathrm{e}}, \tilde{\tilde{\overline{e}}}_{n+1}^{p}, \tilde{\tilde{\eta}}_{n+1}^{p}$.

In summary, the isothermal split solves the mechanical problem with a predicted value of temperature equal to the temperature of the last converged time step and, then, solves the thermal problem using the configuration obtained as a solution of the mechanical problem. A full Newton-Raphson scheme is used for the solution of the non-linear system; the necessary linearization will be presented later in this chapter.

The well-known restriction to conditional stability is the crucial limitation of the isothermal approach, which often becomes critical for strongly coupled problems. However, this restriction is not significant for metal plasticity[102]. Armero and Simo [114] provide the sufficient conditions for stability of the isothermal split:

$$\frac{\Delta t}{h} \leq K \frac{2\sqrt{\rho^{(i)} c^{(i)}}}{m^{(i)}} \Leftrightarrow \frac{\Delta t}{h} \leq K \frac{2\sqrt{2\mu^{(i)} c^{(i)}}}{m^{(i)}} \sqrt{\frac{\rho^{(i)}}{\lambda^{(i)} + 2\mu^{(i)}}} \tag{2.140}$$

where $\lambda^{(i)}, \mu^{(i)} > 0$ are the Lamé constant, $m^{(i)}$ the thermal expansion coefficient, $\rho^{(i)}, c^{(i)}$ the density and the specific heat and $h, \Delta t, K$ are the minimum element size of the mesh, the maximum allowed time step, and a constant. In case where the mechanical inertia can be considered negligible, Armero and Simo [114] provide the sufficient conditions for stability of the isothermal split:

$$\frac{\Delta t}{h^2} \geq \frac{m^{(i)2} - 2E^{(i)} c^{(i)}}{2E^{(i)} k^{(i)}} \leftrightarrow \frac{\Delta t}{h^2} \geq \frac{c^{(i)}}{2k^{(i)}} \left(\frac{m^{(i)2}}{E^{(i)} c^{(i)}} - 2 \right) \tag{2.141}$$

where $m^{(i)}$ the thermal expansion coefficient, $E^{(i)}$ the elastic modulus, $\rho^{(i)}, c^{(i)}$ the density and the specific heat and $h, \Delta t$ are the minimum element size of the mesh and the allowed time step.

Previous restrictions demonstrates that algorithms based on the isothermal split are not suitable for strongly coupled problems, since the stability restriction phrased in terms of the Courant number becomes increasingly restrictive the higher the coupling (increase in the thermal expansion coefficient). The numerical simulation of metal cutting can be considered a weakly coupled

problem (the thermal expansion coefficient of metals is usually small), as a result, the isothermal split will perform well in most of the numerical simulations of metal cutting presented in this work. The stability restriction of the isothermal split is circumvented using an isentropic split, in which one must solve first a mechanical problem at constant entropy (estimates the temperature change in the mechanical problem), followed by a thermal heat conduction problem at constant (fixed) configuration [114].

2.8.2.3 Isothermal IMPL-EX split

Momentum equation for fixed initial temperature

(elastic problem with shear modulus changing from element to element)

$$\mathbf{F}^{(i),dyn,mech}(\dot{\mathbf{v}}_{n+1}^{(i),**}) = \mathbf{F}^{(i),\mathrm{int},mech}(\boldsymbol{\sigma}_{n+1}^{(i)}(\mathbf{u}_{n+1}^{(i),**},\mathbf{p}_{n+1}^{(i),**},\boldsymbol{\theta}_{n}^{(i),**};\lambda_{n}^{(i)})) - \mathbf{F}^{(i),ext,mech}(\mathbf{u}_{n+1}^{(i),**}) - \mathbf{F}^{(i),c,mech}(\mathbf{u}_{n+1}^{(i),**})$$

Incompressibility

$$\left(\frac{1}{\kappa}\mathbf{M}^{p} + \frac{1}{G}\mathbf{M}^{stab}\right)\mathbf{p}_{n+1}^{(1),**} = \mathbf{F}^{(1),volu,mech}(J_{n+1}^{(1),**}(\mathbf{u}_{n+1}^{(1),*},\boldsymbol{\theta}_{n}^{(1),*}))$$

Update nodal variables

$$\mathbf{v}_{n+1}^{(i),**} = \mathbf{v}_{n}^{(i),**} + \dot{\mathbf{v}}_{n+1}^{(i)}\Delta t$$
$$\mathbf{u}_{n+1}^{(i),**} = \mathbf{u}_{n}^{(i),**} + \mathbf{v}_{n+1}^{(i),**}\Delta t$$
$$\mathbf{p}_{n+1}^{(1),**} = \mathbf{p}_{n}^{(1),**} + \Delta\mathbf{p}_{n+1}^{(1),**}$$

Energy equation at updated fixed configuration

(thermal problem with temperature dependent external heat source)

$$\mathbf{F}^{(i),dyn,therm}(\dot{\boldsymbol{\theta}}_{n+1}^{(i),**}) = \mathbf{F}^{(i),\mathrm{int},therm}(q(\boldsymbol{\theta}_{n+1}^{(i),**});D_{\mathrm{int}}^{(i),**}(\mathbf{u}_{n+1}^{(i),**},\boldsymbol{\theta}_{n+1}^{(i),**};\lambda_{n}^{(i)})) - \mathbf{F}^{(i),ext,therm} - \mathbf{F}^{(i),c,therm}$$

Update nodal variables

$$\boldsymbol{\theta}_{n+1}^{(i),**} = \boldsymbol{\theta}_{n}^{(i)} + \dot{\boldsymbol{\theta}}_{n+1}^{(i),**}\Delta t$$

Constitutive equation and update internal variables (Plastic algorithm)

$$(\tilde{\tilde{\mathbf{b}}}_{\mathrm{n+1}}^{\mathrm{e}},\tilde{\tilde{\bar{e}}}_{n+1}^{p},\tilde{\tilde{\eta}}_{n+1}^{p}) = f((\mathbf{u}_{n+1}^{(i),**},\boldsymbol{\theta}_{n+1}^{(i),**}),(\mathbf{b}_{n}^{e},\bar{e}_{n}^{p},\eta_{n}^{p}))$$

Box 5. Isothermal IMPL-EX split

The isothermal scheme presented in [102] decouples the thermo mechanical problem in two more simple problems, but, yet, the mechanical problem is coupled with the evolution equations of internal variables and the thermal problem is coupled with the evolution equations of the internal variables, both of them are coupled through the plastic multiplier. The above reason, suggests decoupling the problem in the following three simple problems: (i) an elastic problem with shear modulus changing from element to element, (ii) a thermal

problem with a temperature dependent plastic heat source and (iii) a relaxation process affecting the stress and the internal variables at the integration points.
In this work, we present a new staggered algorithm, which is based on the isothermal split presented in [102] and the *IMPL-EX* integration scheme of the constitutive equations presented in [115]. Using the ingredients presented above, the solution of the coupled system of ODE (2.137) could be decoupled in the three simple problems mentioned in the previous paragraph. In addition, the elastic and the thermal problems update the internal variables according to a predicted plastic multiplier (explicit), while the constitutive equations leave the displacements, velocities and temperatures unchanged (implicit).
For simplicity, a partition of the time domain $I := \left[0, T\right]$ into N time steps, of the same length Δt is considered. Let us focus on the time step $t_n \to t_{n+1}$, where $\Delta t = t_{n+1} - t_n$. An implicit backward-Euler difference formula is applied to the momentum equation and to the energy equation. In first step the extrapolation of the plastic multiplier $\Delta\lambda_{n+1} = \Delta\lambda_n$ is done. Then, the stresses $\boldsymbol{\sigma}_{n+1}^{(i)}$ are computed via an implicit backward-Euler integration of (2.81) and the balance of momentum (2.3) is solved implicitly providing the nodal displacement and pressure for fixed initial temperature. The solution of the balance of momentum provided a fixed initial temperature and an extrapolated value of the internal variable constitute a non-linear system of equation due to geometrical nonlinearities, which has to be iteratively, solved repeating until convergence is achieved. The solution of the balance of momentum equation for fixed initial temperature, gives an update of the primary variables $\mathbf{u}_{n+1}^{(i),**}, \mathbf{p}_{n+1}^{(i),**}$ and a first update of the internal variables of the form

$$\mathbf{b}_n^e, \overline{e}_n^p, \eta_n^p \quad \to \quad \tilde{\mathbf{b}}_{n+1}^e, \tilde{\overline{e}}_{n+1}^n, \tilde{\eta}_{n+1}^p \tag{2.142}$$

Then, in the second step, the solution of the balance of energy with initial conditions $\mathbf{u}_{n+1}^{(i),**}, \mathbf{p}_{n+1}^{(i),**}, \boldsymbol{\theta}_n^{(i)}$, initial internal variables $\mathbf{b}_n^e, \overline{e}_n^p, \eta_n^p$ and the extrapolation of the plastic multiplier $\Delta\lambda_{n+1} = \Delta\lambda_n$ gives an update of the primary variable $\boldsymbol{\theta}_{n+1}^{(i),**}$ and a second update of the internal plastic variables (at fixed configuration) of the form

$$\mathbf{b}_n^e, \overline{e}_n^p, \eta_n^p \quad \to \quad \tilde{\tilde{\mathbf{b}}}_{n+1}^e, \tilde{\tilde{\overline{e}}}_{n+1}^p, \tilde{\tilde{\eta}}_{n+1}^p \tag{2.143}$$

Finally, in the third step, the values of $\mathbf{u}_{n+1}^{(i),**}, \mathbf{p}_{n+1}^{(i),**}, \boldsymbol{\theta}_{n+1}^{(i),**}$ remain fixed, and an implicit backward-Euler integration of the constitutive model (2.81) is done using as initial internal variables $\mathbf{b}_n^e, \overline{e}_n, \eta_n^p$. Given, as a consequence a finally update of the internal variables of the form

$$\mathbf{b}_n^e, \overline{e}_n^p, \eta_n^p \quad \rightarrow \quad \tilde{\tilde{\mathbf{b}}}_{n+1}^{e}, \tilde{\tilde{\overline{e}}}_{n+1}^{p}, \tilde{\tilde{\eta}}_{n+1}^{p} \tag{2.144}$$

The set of internal variables obtained at the end of this time step, will be the set of internal variables used as the starting point in the next step of the fractional step method proposed in this work.

As summary about the isothermal IMPL-EX split is shown in Box 5.

It is interesting to note that the boundary values of the momentum equation are included in the elastic equations with shear modulus changing from element to element and the boundary values of the balance of energy are imposed on the thermal problem with temperature dependent plastic heat source. In addition, the plastic algorithm consists of a collection of systems of ordinary differential equations, each one of which pertains to a different integration point. A full Newton-Raphson scheme is used for the solution of the non-linear system; the necessary linearization will be presented later in this chapter.

2.8.2.4 Semi-explicit integration scheme

The application of a forward-Euler time integration scheme to the mechanical and the thermal problem yields the following algorithm

Momentum

$$\mathbf{F}^{(i),dyn,mech} = \mathbf{M}^m \dot{\mathbf{v}}_n^{(i)} =$$

$$\mathbf{F}^{(i),\text{int},mech}(\boldsymbol{\sigma}_n(\mathbf{u}_n^{(i)}, \mathbf{p}_n^{(i)}, \boldsymbol{\theta}_n^{(i)})) - \mathbf{F}^{(i),ext,mech}(\mathbf{u}_n^{(i)}) - \mathbf{F}^{(i),c,mech}(\mathbf{u}_n^{(i)})$$

Update nodal velocities and displacements

$$\mathbf{v}_{n+1}^{(i)} = \mathbf{v}_n^{(i)} + \dot{\mathbf{v}}_n^{(i)} \Delta t = \mathbf{v}_n^{(i)} + \mathbf{M}^{m-1} \mathbf{F}^{(i),dyn,mech} \Delta t$$

$$\mathbf{u}_{n+1}^{(i)} = \mathbf{u}_n^{(i)} + \mathbf{v}_n^{(i)} \Delta t$$

Energy

$$\mathbf{F}^{(i),dyn,therm} = \mathbf{M}^t \dot{\boldsymbol{\theta}}_n^{(i)} =$$

$$\mathbf{F}^{(i),\text{int},therm}(q(\boldsymbol{\theta}_n^{(i)}); D_{\text{int}}^{(i)}(\mathbf{u}_n^{(i)}, \boldsymbol{\theta}_n^{(i)}; \lambda_n(\mathbf{u}_n^{(i)}, \boldsymbol{\theta}_n^{(i)}))) - \mathbf{F}^{(i),ext,therm} - \mathbf{F}^{(i),c,therm}$$

Update nodal temperatures

$$\boldsymbol{\theta}_{n+1}^{(i)} = \boldsymbol{\theta}_n^{(i)} + \dot{\boldsymbol{\theta}}_n^{(i)} \Delta t = \boldsymbol{\theta}_n^{(i)} + \mathbf{M}^{t-1} \mathbf{F}^{(i),dyn,therm} \Delta t$$

Incompressibility

$$\mathbf{F}^{(1),press,mech}(\mathbf{p}_{n+1}^{(1)}) - \mathbf{F}^{(1),volu,mech} J_{n+1}^{(1)}((\mathbf{u}_{n+1}^{(1)}, \boldsymbol{\theta}_{n+1}^{(i)})) + \mathbf{F}^{(1),stab,mech}(\mathbf{p}_{n+1}^{(1)}) = 0$$

Box 6. Semi-explicit integration scheme

The main steps in the solution of coupled thermo-mechanical problem are presented in the following lines. First, a mechanical step is taken based on the current distribution of temperatures, and the velocities and displacement are updated using an explicit forward-Euler. Second, the heat generated is transferred to the thermal problem and the temperatures are updated using a forward-Euler algorithm. Then, the resulting temperatures are transferred to the mechanical problem and incorporated into the thermal softening constitutive

model. Finally, the nodal pressure is updated implicitly in order to deal with the incompressibility constraint imposed by J_2 plasticity.

Explicit scheme are conditionally stable, it means that the time step used in the simulations should be less or equal than a given critical time step, the critical time step correspond to the time that takes to a wave to travel through the small finite element of the mesh. In case of an elastic material, the critical time step depends on the mesh size, the elastic modulus, the Poisson ratio, and the density of the material.

$$\Delta t_c = \frac{h}{\sqrt{\frac{3\kappa\ (1-\nu)}{\rho\ (1+\nu)}}} \tag{2.145}$$

where $h, \Delta t_v$ are the minimum element size of the mesh and the maximum allowed time step, and, κ, ν, ρ are the bulk modulus, the Poisson ratio and the material density, respectively.

The restriction imposed on the time step by the explicit schemes, allows thinking that for numerical simulation that involves long period of computing time or low speeds implicit schemes are more favorable in comparison with explicit schemes. On the contrary, when velocities are high and the contact conditions are complex, is necessary to decrease the time step used in implicit formulations, so in this case explicit formulations appear as an effective and an efficient tool, with an interesting computing time.

In the next chapter, some cutting examples will show a comparison between implicit isothermal split, implicit isothermal IMPL-EX split and the semi-explicit scheme.

2.8.3 Workpiece constitutive law: time discretization

The problem of integrating numerically the initial-value ODE equations represented by (2.81) in conjunction with the condition (2.79) is the focus of this section.

2.8.3.1 Implicit Backward-Euler

Let $\mathbf{C}_n^{p-1}, \bar{e}_n^p, \theta_n$ denote the initial state at time t_n, and assume that the deformation gradient and temperature field $\mathbf{F}_{n+1}, \theta_{n+1}$ at time t_{n+1} are prescribed. Let us focus on the time step $t_n \rightarrow t_{n+1}$, where $\Delta t = t_{n+1} - t_n$. Using an implicit unconditionally stable scheme on (2.83) and the scalar equations of (2.80) gives

$$\begin{aligned}\bar{\mathbf{F}}_{n+1}(\mathbf{C}_{n+1}^{p-1}-\mathbf{C}_{n}^{p-1})\bar{\mathbf{F}}_{n+1}^{t} &= -2\lambda_{n+1}\Delta t\frac{1}{3}tr(\bar{\mathbf{b}}_{n+1}^{e})\mathbf{n}_{n+1}\\ \bar{e}_{n+1}^{p}-\bar{e}_{n}^{p} &= \lambda_{n+1}\Delta t\sqrt{\frac{2}{3}}\\ \eta_{n+1}^{p}-\eta_{n}^{p} &= \lambda_{n+1}\Delta t\sqrt{\frac{2}{3}}(\partial_{\theta}\sigma_{y}+\partial_{\theta}\beta)\end{aligned} \tag{2.146}$$

The right hand side of equation (2.146) in terms of spatial variables becomes

$$\bar{\mathbf{b}}_{n+1}^{e}-\bar{\mathbf{F}}_{n,n+1}\mathbf{b}_{n}^{e}\bar{\mathbf{F}}_{n,n+1}^{t} = -2\lambda_{n+1}\Delta t\frac{1}{3}tr(\bar{\mathbf{b}}_{n+1}^{e})\mathbf{n}_{n+1} \tag{2.147}$$

along with the following counterpart of the loading-unloading conditions:

$$\begin{aligned}&\lambda_{n+1}\Delta t\geq 0 \quad f_{n+1}(\tau_{n+1},\bar{e}_{n+1}^{p},\theta_{n+1})\leq 0\\ &\lambda_{n+1}\Delta t f_{n+1}(\tau_{n+1},\bar{e}_{n+1}^{p},\theta_{n+1})=0\end{aligned} \tag{2.148}$$

where the yield condition is defined by the Mises criteria

$$f_{n+1}(\tau_{n+1},\bar{e}_{n+1}^{p},\theta_{n+1}) = \left\|dev(\tau_{n+1})\right\|-\sqrt{\frac{2}{3}}(\sigma_{y,n+1}+\beta_{n+1}) \tag{2.149}$$

A closed form solution of these equations is obtained by defining the thermoelastic state by the relations

$$\begin{aligned}\bar{\mathbf{b}}_{n+1}^{e,trial} &= \bar{\mathbf{F}}_{n+1}\mathbf{C}_{n}^{p-1}\bar{\mathbf{F}}_{n+1}^{t} = \bar{\mathbf{F}}_{n,n+1}\mathbf{b}_{n}^{e}\bar{\mathbf{F}}_{n,n+1}^{t}\\ \mathbf{s}_{n+1}^{trial} &= \mu dev(\bar{\mathbf{b}}_{n+1}^{e,trial})\\ f_{n+1}^{trial} &= \left\|\mathbf{s}_{n+1}^{trial}\right\|-\sqrt{\frac{2}{3}}(\sigma_{y,n}+\beta_{n+1}(\bar{e}_{n}^{p}))\end{aligned} \tag{2.150}$$

We observe that the trial state is determined solely in terms of the initial conditions $\mathbf{b}_{n}^{e},\bar{e}_{n}^{p},\theta_{n}$ and the given incremental deformation gradient $\bar{\mathbf{F}}_{n,n+1}$. We remark that this state may not, correspond to any actual state, unless the incremental process is elastic.

An analysis of equation (2.150) reveals two alternative situations:

First, we consider the case for which

$$f_{n+1}^{trial}<0 \tag{2.151}$$

It follows that the trial state is admissible in the sense that

$$\begin{aligned}\bar{\mathbf{b}}_{n+1}^{e} &= \bar{\mathbf{b}}_{n+1}^{e,trial} = \bar{\mathbf{F}}_{n+1}\mathbf{C}_{n}^{p-1}\bar{\mathbf{F}}_{n+1}^{t} = \bar{\mathbf{F}}_{n,n+1}\mathbf{b}_{n}^{e}\bar{\mathbf{F}}_{n,n+1}^{t}\\ \mathbf{s}_{n+1} &= \mathbf{s}_{n+1}^{trial}\\ \mathbf{s}_{n+1}^{trial} &= \mu dev(\bar{\mathbf{b}}_{n+1}^{e,trial})\\ \bar{e}_{n+1}^{p} &= \bar{e}_{n}^{p}\end{aligned} \tag{2.152}$$

and satisfy

1. The stress – strain relationship
2. The flow rule and the hardening law with $\Delta\lambda_{n+1}=\lambda_{n+1}\Delta t=0$
3. The Kuhn-Tucker conditions, since

$$f_{n+1}(\tau_{n+1},\bar{e}^{p}_{n+1},\theta_{n+1}) = f^{trial}_{n+1} \le 0$$
$$\Delta\lambda_{n+1} = 0 \tag{2.153}$$

satisfy (2.148).

Next, we consider the case for which $f^{trial}_{n+1} > 0$. Cleary, the trial state cannot be a solution to the incremental problem since $\bar{\mathbf{b}}^{e,trial}_{n+1},\bar{e}^{p}_{n},\theta_{n}$ violates the constraint condition $f_{n+1}(\tau_{n+1},\bar{e}^{p}_{n+1},\theta_{n+1}) \le 0$. As a result, we require that $\Delta\lambda_{n+1} > 0$ so that $\bar{e}^{p}_{n+1} \neq \bar{e}^{p}_{n}$ to obtain . $\mathbf{s}_{n+1} \neq \mathbf{s}^{trial}_{n+1}$.

To summarize our results, the conclusion that an incremental process for given incremental deformation gradient is elastic or plastic is drawn solely on the basis of the trial state according to the criterion

$$f^{trial}_{n+1}\begin{cases} \le 0 \Rightarrow & \text{elastic step} \quad \Delta\lambda_{n+1} = 0 \\ > 0 \Rightarrow & \text{plastic step} \quad \Delta\lambda_{n+1} > 0 \end{cases} \tag{2.154}$$

Here we examine the algorithmic problem for an incremental plastic process characterized by the conditions

$$f^{trial}_{n+1} > 0 \Leftrightarrow f_{n+1}(\tau_{n+1},\bar{e}^{p}_{n+1},\theta_{n+1}) = 0 \tag{2.155}$$

and

$$\Delta\lambda_{n+1} > 0 \tag{2.156}$$

The objective is to determine the solution $(\bar{\mathbf{b}}^{e}_{n+1},\bar{e}^{p}_{n+1},\theta_{n+1},\mathbf{s}_{n+1},\Delta\lambda_{n+1})$ to the problem(2.147),(2.148) and (2.149). To accomplish this we express the Kirchhoff stress tensor $\mathbf{s}_{n+1}$ in terms of $\mathbf{s}^{trial}_{n+1}$ and $\Delta\lambda_{n+1}$ as follows

$$\begin{aligned} \mathbf{s}_{n+1} &= \mu dev(\bar{\mathbf{b}}^{e}_{n+1}) \\ &= \mu dev(\bar{\mathbf{F}}_{n,n+1}\mathbf{b}^{e}_{n}\bar{\mathbf{F}}^{t}_{n,n+1}) - 2\Delta\lambda_{n+1}\mu\frac{1}{3}tr(\bar{\mathbf{b}}^{e}_{n+1})\mathbf{n}_{n+1} \\ &= \mathbf{s}^{trial}_{n+1} - 2\Delta\lambda_{n+1}\mu\frac{1}{3}tr(\bar{\mathbf{b}}^{e}_{n+1})\mathbf{n}_{n+1} \end{aligned} \tag{2.157}$$

The update of Kirchhoff stress tensor and the tensor $\mathbf{b}^{e}_{n+1}$ need the determination of the trace of $\mathbf{b}^{e}_{n+1}$. By taking the trace of equation (2.147) and using (2.150) we conclude that

$$tr(\bar{\mathbf{b}}^{e}_{n+1}) = tr(\bar{\mathbf{b}}^{e,trial}_{n+1}) \tag{2.158}$$

Then substituting (2.158) in (2.147) we get

$$\bar{\mathbf{b}}^{e}_{n+1} = \bar{\mathbf{b}}^{e,trial}_{n+1} - 2\lambda_{n+1}\Delta t\frac{1}{3}tr(\bar{\mathbf{b}}^{e,trial}_{n+1})\mathbf{n}_{n+1} \tag{2.159}$$

and using the hyperelastic relationships yields

1 Thermoelastic trial state: Given initial data $\bar{\mathbf{b}}^e_n, \bar{e}^p_n, \eta^p_n$

and the current values $\mathbf{F}_{n,n+1}, \theta_{n+1}$, let $\bar{\mathbf{F}}_{n,n+1} = J^{-\frac{1}{3}}\mathbf{F}_{n,n+1}$ and set

$$f^{trial}_{n+1} = \left\|\mathbf{s}^{trial}_{n+1}\right\| - \sqrt{\frac{2}{3}}(\sigma_{y,n} + \beta_{n+1}(\bar{e}^p_n))$$

IF $f^{trial}_{n+1} \leq 0$ set $\bar{\mathbf{b}}^e_{n+1}, \bar{e}^p_{n+1}, \eta^p_n = \bar{\mathbf{b}}^{e,trial}_{n+1}, \bar{e}^p_n, \eta^p_n$ and EXIT

ELSE

2 Consistency parameter: Set $\bar{\mu} = \frac{\mu}{3} tr(\bar{\mathbf{b}}^{e,trial}_{n+1})$ and

compute $\Delta\lambda_{n+1}$ by solving

$$\begin{aligned} g(\Delta\lambda_{n+1}) = f^{trial}_{n+1} &- 2\mu\Delta\lambda_{n+1}\frac{1}{3}tr(\bar{\mathbf{b}}^{e,trial}_{n+1}) \\ &+\sqrt{\frac{2}{3}}(\sigma_{y,n} + \beta_n(\bar{e}^p_n)) \\ &-\sqrt{\frac{2}{3}}(\sigma_{y,n+1} + \beta_{n+1}(\bar{e}^p_{n+1})) \\ &= 0 \end{aligned}$$

Return map: Set $\mathbf{n}_{n+1} = \frac{\mathbf{s}^{trial}_{n+1}}{\left\|\mathbf{s}^{trial}_{n+1}\right\|}$ and perform the update

$$\begin{aligned} \mathbf{s}_{n+1} &= \mathbf{s}^{trial}_{n+1} - 2\Delta\lambda_{n+1}\mu\frac{1}{3}tr(\bar{\mathbf{b}}^{e,trial}_{n+1})\mathbf{n}_{n+1} \\ \bar{e}^p_{n+1} &= \bar{e}^p_n + \lambda_{n+1}\Delta t\sqrt{\frac{2}{3}} \\ \eta^p_{n+1} &= \eta^p_n - \sqrt{\frac{2}{3}}\Delta\lambda_{n+1}\partial_\theta(\sigma_{y,n+1} + \beta_{n+1}(\bar{e}^p_{n+1})) \end{aligned}$$

3 Update the intermediate configuration by the closed form formula

$$\bar{\mathbf{b}}^e_{n+1} = \bar{\mathbf{b}}^{e,trial}_{n+1} - 2\lambda_{n+1}\Delta t\frac{1}{3}tr(\bar{\mathbf{b}}^{e,trial}_{n+1})\mathbf{n}_{n+1}$$

END

$$\mathbf{s}_{n+1} = \mathbf{s}^{trial}_{n+1} - 2\Delta\lambda_{n+1}\mu\frac{1}{3}tr(\bar{\mathbf{b}}^{e,trial}_{n+1})\mathbf{n}_{n+1} \tag{2.160}$$

From (2.157) and the definition $\mathbf{s}_{n+1} = \left\|\mathbf{s}_{n+1}\right\|\mathbf{n}_{n+1}$, the normal $\mathbf{n}_{n+1}$ is determined in terms of the trial stress $\mathbf{s}^{trial}_{n+1}$

$$
\begin{aligned}
&\left\|\mathbf{s}_{n+1}\right\|\mathbf{n}_{n+1} = \left\|\mathbf{s}_{n+1}^{trial}\right\|\mathbf{n}_{n+1}^{trial} - 2\mu\Delta\lambda_{n+1}\frac{1}{3}tr(\bar{\mathbf{b}}_{n+1}^{e,trial})\mathbf{n}_{n+1} \\
&\left[\left\|\mathbf{s}_{n+1}\right\| + 2\mu\Delta\lambda_{n+1}\frac{1}{3}tr(\bar{\mathbf{b}}_{n+1}^{e,trial})\right]\mathbf{n}_{n+1} = \left\|\mathbf{s}_{n+1}^{trial}\right\|\mathbf{n}_{n+1}^{trial} \\
&\left\|\mathbf{s}_{n+1}^{trial}\right\|\mathbf{n}_{n+1} = \left\|\mathbf{s}_{n+1}^{trial}\right\|\mathbf{n}_{n+1}^{trial} \\
&\mathbf{n}_{n+1} = \mathbf{n}_{n+1}^{trial}
\end{aligned}
\tag{2.161}
$$

By taking the dot product of (2.157) with $\mathbf{n}_{n+1}$ and using (2.149), we obtain the following scalar nonlinear equations that determines the consistency parameter $\Delta\lambda_{n+1}$:

$$
\begin{aligned}
g(\Delta\lambda_{n+1}) &= \left\|\mathbf{s}_{n+1}^{trial}\right\| - 2\mu\Delta\lambda_{n+1}\frac{1}{3}tr(\bar{\mathbf{b}}_{n+1}^{e,trial}) - \sqrt{\frac{2}{3}}(\sigma_{y,n+1} + \beta_{n+1}(\bar{e}_{n+1}^{p})) \\
&= f_{n+1}^{trial} - 2\mu\Delta\lambda_{n+1}\frac{1}{3}tr(\bar{\mathbf{b}}_{n+1}^{e,trial}) + \sqrt{\frac{2}{3}}(\sigma_{y,n} + \beta_{n}(\bar{e}_{n}^{p})) - \\
&\quad \sqrt{\frac{2}{3}}(\sigma_{y,n+1} + \beta_{n+1}(\bar{e}_{n+1}^{p})) \\
&= 0
\end{aligned}
\tag{2.162}
$$

Equation (2.162) is effectively solved by a local Newton iterative procedure since $g(\Delta\lambda_{n+1})$ is a convex function for the isotropic hardening functions used in this work, and then convergence of the Newton-Raphson is guaranteed.

Once $\Delta\lambda_{n+1}$ is determined from (2.162) the intermediate configuration, the hardening variable and plastic entropy are updated from (2.146).

2.8.3.2 IMPLEX integration scheme

The IMPLEX (Implicit-EXplicit) adopted herein is the one pioneered by *Oliver et. al. [115],* originally conceived for addressing the problem of robustness and stability arising in the numerical simulation of material failure. The essence of the method is to solve explicitly for some variables, in the sense that the values at the beginning of the increment are presumed known, and implicit for other variables, with the primary motivation to enhance the spectral properties of the algorithmic tangent moduli.

However, our primary motivation of using IMPLEX is to reduce the equation solving effort associated to the solution of the fully implicit scheme. The explicit integration of some variables in the coupled thermomechanical J_2 flow theory and therefore, the use of extrapolated values in the balance of momentum and energy, allow us to solve a coupled thermo-mechanical problem as a sequence of three uncoupled problems. First, an elastic problem with shear modulus changing from element to element; second, a thermal problem with a temperature dependent plastic heat source and finally, a relaxation process affecting the stress and the internal variables at the integration points. It is important, to remark, that the mechanical and thermal problem are solved using

an IMPLEX integration scheme of the J_2 plasticity model, while relaxation steps calculates stresses and internal variables using the implicit Back-Euler time integration presented in the previous section.

The arguments in support of IMPLEX integration scheme in the numerical simulation of metal cutting were already put forward above. Here we simply choose the variable to be treated explicitly and derive the stress update algorithm

Given initial data $\bar{\mathbf{b}}_n^e, \bar{e}_n^p, \eta_n^p$ and the current values $\mathbf{F}_{n,n+1}, \theta_{n+1}$,

1 Explicit extrapolation

$$\Delta\tilde{\lambda}_{n+1} = \sqrt{\frac{3}{2}}\Delta\lambda_n \frac{\Delta t_{n+1}}{\Delta t_n}$$
$$\tilde{\bar{e}}_{n+1}^p = \bar{e}_n^p + \sqrt{\frac{2}{3}}\Delta\tilde{\lambda}_{n+1}$$

2 Let $\bar{\mathbf{F}}_{n,n+1} = J^{-\frac{1}{3}}\mathbf{F}_{n,n+1}$ and set

$$\bar{\mathbf{b}}_{n+1}^{e,trial} = \bar{\mathbf{f}}_{n+1}\bar{\mathbf{b}}_n^e\bar{\mathbf{f}}_{n+1}^T$$
$$\mathbf{s}_{n+1}^{trial} = \mu dev\left[\bar{\mathbf{b}}_{n+1}^{e,trial}\right]$$

3 Compute the stresses and the plastic entropy : Set $\bar{\mu} = \frac{\mu}{3} tr(\bar{\mathbf{b}}_{n+1}^{e,trial})$

and $\mathbf{n}_{n+1} = \frac{\mathbf{s}_{n+1}^{trial}}{\left\|\mathbf{s}_{n+1}^{trial}\right\|}$. Perform the update

$$\tilde{\mathbf{s}}_{n+1} = \mathbf{s}_{n+1}^{trial} - 2\bar{\mu}\Delta\tilde{\lambda}_{n+1}\mathbf{n}_{n+1}$$
$$\tilde{\eta}_{n+1}^p = \eta_n^p - \sqrt{\frac{2}{3}}\Delta\tilde{\lambda}_{n+1}\partial_\theta(\tilde{\sigma}_{y,n+1} + \beta_{n+1}(\tilde{\bar{e}}_{n+1}^p))$$

4 Compute the Plastic Power

$$\tilde{D}_{mec}^{n+1} = \chi\sqrt{\frac{2}{3}}(\tilde{\sigma}_y + \tilde{\beta})_{n+1}\frac{\Delta\tilde{\lambda}_{n+1}}{\Delta t}$$

Box 8. IMPLEX explicit stage for thermo-elasto-plastic models.

arising from this choice.
By definition, the equivalent plastic strain is a monotonically increasing function of time, $\dot{\bar{e}}^p \geq 0$. For this reason, it is a logical candidate to be treated explicitly, since its evolution can be predicted more accurately than other variables exhibiting non-monotonic behavior. The following analysis pursues, to develop an expression for explicitly updating the equivalent plastic strain at t_{n+1} using

values obtained in previous time steps by an implicit Backward-Euler integration procedure.

Let us consider, the Taylor expansion of the equivalent plastic strain at t_{n-1} around t_n :

$$\bar{e}^p_{n-1} = \bar{e}^p_n - \left.\frac{\partial \bar{e}^p}{\partial t}\right|_{t_n} (t_n - t_{n-1}) + O(\Delta^2 t_n) \tag{2.163}$$

Next, the Taylor expansion is carried out at t_{n+1} around t_n, yielding

$$\bar{e}^p_{n+1} = \bar{e}^p_n + \left.\frac{\partial \bar{e}^p}{\partial t}\right|_{t_n} (t_{n+1} - t_n) + O(\Delta^2 t_{n+1}) \tag{2.164}$$

The standard explicit difference scheme is obtained truncating the remainder terms $O(\Delta^2 t_{n+1})$.

The above explicit difference equation presents an inconvenience that ensure that the yield condition is not enforced at t_{n+1} and as a result, it is possible for the solution, over many time steps, to drift away from the yield surface. In order to avoid that this drift from the yield surface grows unboundedly, Oliver et al. propose to approximate the derivate in (2.164) using the derivative appearing in (2.163).

Hence, truncating the terms $O\ \Delta^2 t_n$ in equation (2.163), one gets

$$\bar{e}^p_n = \bar{e}^p_{n-1} + \left.\frac{\partial \bar{e}^p}{\partial t}\right|_{t_n} (\Delta t_n) \tag{2.165}$$

The above equation is a Backward-Euler integration of the equivalent plastic strain, in the sense that the equivalent plastic strain at t_n, $\bar{e}^p_n$, is obtained by an expression that uses a derivative evaluated at t_n. As a result, $\bar{e}^p_n$ and $\bar{e}^p_{n-1}$ are obtained at times t_n and t_{n-1} using the implicit scheme presented in the previous section. From (2.165), we can deduce that

$$\left.\frac{\partial \bar{e}^p}{\partial t}\right|_{t_n} = \frac{\bar{e}^p_n - \bar{e}^p_{n-1}}{\Delta t_n} \tag{2.166}$$

Finally, inserting the above expression into (2.164), and truncating the remainder terms, yields

$$\tilde{\bar{e}}^p_{n+1} = \bar{e}^p_n + (\bar{e}^p_n - \bar{e}^p_{n-1}) \frac{\Delta t_{n+1}}{\Delta t_n} \tag{2.167}$$

This expression constitutes an explicit extrapolation of the equivalent plastic strain at t_{n+1} in terms of the implicit values computed at t_n and t_{n-1}. Note

that the IMPLEX algorithm is a multistep method, since two points are used to advance the solution in time to point t_{n+1}.

The algorithmic plastic multiplier resulting from this extrapolation reads:

$$\begin{aligned}\Delta\tilde{\lambda}_{n+1} &= \sqrt{\frac{3}{2}}()\tilde{\bar{e}}^{p}_{n+1} - \bar{e}^{p}_{n} \\ &= \sqrt{\frac{3}{2}}(\bar{e}^{p}_{n} - \bar{e}^{p}_{n-1})\frac{\Delta t_{n+1}}{\Delta t_{n}} \\ &= \sqrt{\frac{3}{2}}\Delta\lambda_{n}\frac{\Delta t_{n+1}}{\Delta t_{n}}\end{aligned} \tag{2.168}$$

Expression (2.168) reveals that the elastic or plastic nature of the response predicted by the IMPLEX integration scheme at t_{n+1} is dictated by the response computed implicitly at t_n. This may give rise to overshoots and oscillations in the transitions from elastic to inelastic and vice versa.

Now, steps 3 and 4 in Box 7 can be pursued in terms of extrapolated plastic multiplier yielding the IMPLEX integrated values of the remaining variables $\tilde{\mathbf{s}}_{n+1}, \tilde{\bar{e}}^{p}_{n+1}$ and $\tilde{\eta}^{p}_{n+1}$.

Those IMPLEX results are then substituted in Box 5 to fulfill the momentum and energy equations. The IMPLEX explicit stage for both cases is summarized in Box 8.

2.8.3.3 Algorithmic constitutive tensor

The ultimate goal in the numerical simulation of metal cutting processes is to solve an initial boundary value problem (IBVP) for the displacement and temperature fields. The numerical solution of this problem relies on the spatial discretization, via a Galerkin finite element, of the momentum and energy equations and a time discretization of the displacement, velocity and temperature fields. In case of an implicit discretization the response in obtained by solving a sequence of linearized problems.

The theories underlying the spatial and temporal discretization were presented in sections 2.8.1 and 2.8.2. The linearization of the weak form of the momentum and energy equation are not address in this work. We refer the reader to [103, 110] for further details.

In the following lines, we provide an expression for the algorithmic tangent moduli, which is a key aspect in the linearization of the weak form of the momentum equation. In addition, we provide a linearization of the plastic power relevant in the linearization of the weak form of the energy equation.

Algorithmic constitutive tensor: *implicit integration scheme*

The expression for the tangent moduli for the implicit stress updated algorithm will be presented in the following lines

$$\frac{\partial \mathbf{S}_{n+1}}{\partial \mathbf{C}_{n+1}} = \delta_1 \mathbf{A}_{dev}^{trial} + \delta_2 \mathbf{N}_{n+1} \otimes \mathrm{DEV}(\mathbf{N}_{n+1}^2) + \delta_3 \mathbf{N}_{n+1} \otimes \mathbf{N}_{n+1} \tag{2.169}$$

where the coefficients δ_1, δ_2 and δ_3 are defined by the expressions

$$\begin{aligned}
\delta_1 &= \left(1 - \frac{2\overline{\mu}\Delta\lambda_{n+1}}{\left\| \mathbf{S}_{n+1}^{trial} \right\|} \right) \\
\delta_2 &= 2\left(\overline{\mu}\Delta\lambda_{n+1} - \frac{\overline{\mu}\left\| \mathbf{S}_{n+1}^{trial} \right\|}{\left(2\overline{\mu} + \frac{2}{3}\frac{d\left[\sigma_y + \beta \right]}{d\Delta\lambda_{n+1}} \right)} \right) \\
\delta_3 &= \left(\frac{2\overline{\mu}^2\Delta\lambda_{n+1}}{\left\| \mathbf{S}_{n+1}^{trial} \right\|} + \frac{2\overline{\mu}\frac{2}{3}\Delta\lambda_{n+1}\left\| \mathbf{S}_{n+1}^{trial} \right\| - 2\overline{\mu}^2}{\left(2\overline{\mu} + \frac{2}{3}\frac{d\left[\sigma_y + \beta \right]}{d\Delta\lambda_{n+1}} \right)} - \frac{2}{3}\Delta\lambda_{n+1}\left\| \mathbf{S}_{n+1}^{trial} \right\| \right)
\end{aligned} \tag{2.170}$$

And, where $\mathbf{A}_{dev}^{trial}$ is given by

$$\begin{aligned}
\mathbf{A}_{dev}^{trial} &= \frac{\partial \mathbf{S}_{n+1}^{trial}}{\partial \mathbf{C}_{n+1}} = \overline{\mu}_{n+1}\left(\frac{1}{3}\mathbf{C}_{n+1}^{-1} \otimes \mathbf{C}_{n+1}^{-1} + \mathbf{I}_{n+1} \right) \\
&\quad -\frac{1}{3}\mu J^{-\frac{2}{3}}\ \mathbf{C}_n^{p-1} \otimes \mathbf{C}_{n+1}^{-1} + \mathbf{C}_{n+1}^{-1} \otimes \mathbf{C}_n^{p-1}
\end{aligned} \tag{2.171}$$

where $\mathbf{I}_{n+1}$ the operator has the following component form

$$\mathrm{I}_{n+1,ijkl} = -\frac{1}{2}\ C_{n+1,ik}^{-1} C_{n+1,jl}^{-1} + C_{n+1,il}^{-1} C_{n+1,jk}^{-1} \tag{2.172}$$

It is important to remark that, the consistent deviatoric tangent modulus is nonsymmetrical.

The last point to complete the derivation of the consistent tangent modulus is to calculate the derivatives of the isotropic hardening function used in this work with respect to the plastic multiplier. The following equations present the derivatives of the Voce and Simo, Johnson Cook and Bäker isotropic hardening functions. In case of the Johnson Cook and Bäker models the derivative depends on the equivalent plastic strain rate as showed in equations (2.59) and (2.62).

First, in case of the *Voce and Simo* model the derivative takes the following value

$$\frac{\partial(\sigma_y + \beta)_{n+1}}{\partial \overline{e}_{n+1}^p} = \begin{pmatrix} H(1 - w_h(\theta - \theta_0)) \\ +(K_{\inf}(1 - w_h(\theta - \theta_0) - K_0(1 - w_0(\theta - \theta_0))\delta \exp(-\delta \overline{e}_{n+1}^p) \end{pmatrix} \tag{2.173}$$

Second, in case of the *Johnson Cook* the derivative takes the following value if the plastic strain rate is less than the threshold strain rate $\dot{e}_0$

If $\dot{\bar{e}}^p_{n+1} < \dot{e}_0$

$$\begin{aligned}\frac{\partial(\sigma_y + \beta)_{n+1}}{\partial \bar{e}^p_{n+1}} &= \left(1 - \left(\frac{\theta - \theta_0}{\theta_{melt} - \theta_0}\right)^m\right)\frac{\partial}{\partial \bar{e}^p_{n+1}}(A + B(\bar{e}^p_{n+1})^n) \\ &= \left(1 - \left(\frac{\theta - \theta_0}{\theta_{melt} - \theta_0}\right)^m\right) nB(\bar{e}^p_{n+1})^{n-1}\end{aligned} \tag{2.174}$$

In addition, in case the plastic strain rate is greater than the threshold strain rate $\dot{e}_0$ the derivative takes the following value

If $\dot{\bar{e}}^p_{n+1} \geq \dot{e}_0$

$$\begin{aligned}\frac{\partial(\sigma_y + \beta)_{n+1}}{\partial \bar{e}^p_{n+1}} &= \left(1 + C\ln(\frac{\dot{\bar{e}}^p_{n+1}}{\dot{e}_0})\right)\left(1 - \left(\frac{\theta - \theta_0}{\theta_{melt} - \theta_0}\right)^m\right) nB(\bar{e}^p_{n+1})^{n-1} \\ &+(A + B(\bar{e}^p_{n+1})^n)\left(1 - \left(\frac{\theta - \theta_0}{\theta_{melt} - \theta_0}\right)^m\right)\left(C\frac{1}{\dot{\bar{e}}^p_{n+1}\Delta t}\right)\end{aligned} \tag{2.175}$$

Finally, the derivative takes the following form in case of the *Bäker* model

If $\dot{\bar{e}}^p_{n+1} < \dot{e}_0$

$$\begin{aligned}\frac{\partial(\sigma_y + \beta)_{n+1}}{\partial \bar{e}^p_{n+1}} &= \frac{\partial}{\partial \bar{e}^p_{n+1}}\left(K_0 \exp(-\frac{\theta}{\theta_{melt}})(\bar{e}^p_{n+1})^{n_0 \exp(-\frac{\theta}{\theta_{melt}})}\right) \\ &= \left(K_0 \exp(-\frac{\theta}{\theta_{melt}}) n_0 \exp(-\frac{\theta}{\theta_{melt}})(\bar{e}^p_{n+1})^{n_0 \exp(-\frac{\theta}{\theta_{melt}})-1}\right)\end{aligned} \tag{2.176}$$

If $\dot{\bar{e}}^p_{n+1} \geq \dot{e}_0$

$$\begin{aligned}\frac{\partial(\sigma_y + \beta)_{n+1}}{\partial \bar{e}^p_{n+1}} &= \left(1 + C\ln(\frac{\dot{\bar{e}}^p_{n+1}}{\dot{e}_0})\right)\left(K_0 \exp(-\frac{\theta}{\theta_{melt}}) n_0 (\bar{e}^p_{n+1})^{n_0 \exp(-\frac{\theta}{\theta_{melt}})-1}\right) \\ &+\left(K_0 \exp(-\frac{\theta}{\theta_{melt}})(\bar{e}^p_{n+1})^{n_0 \exp(-\frac{\theta}{\theta_{melt}})}\right)\left(C\frac{1}{\dot{\bar{e}}^p_{n+1}\Delta t}\right)\end{aligned} \tag{2.177}$$

In equations (2.176) and (2.177) we have used

$$\frac{\partial\ a^{g(x)}}{\partial x} = a^{g(x)}\frac{\partial g(x)}{\partial x}\ln(a) \tag{2.178}$$

Since, the stress update formula is cast in terms of spatial quantities; it is convenient to transform the material algorithmic tangent moduli (2.169) into the spatial configuration via a pull-forward operation as follows

$$\mathbf{a}_{dev} = \frac{\partial \mathbf{s}_{n+1}}{\partial \mathbf{1}_{n+1}} = \mathbf{F}_{n+1}\mathbf{F}_{n+1}\mathbf{F}_{n+1}\mathbf{F}_{n+1}\mathbf{A}_{dev} \tag{2.179}$$

$$\frac{\partial \mathbf{s}_{n+1}}{\partial \mathbf{1}_{n+1}} = \delta_1 \frac{\partial \mathbf{s}^{trial}_{n+1}}{\partial \mathbf{1}_{n+1}} + \delta_2 \mathbf{n}_{n+1} \otimes \mathbf{n}_{n+1} + \delta_3 \mathbf{n}_{n+1} \otimes \mathrm{dev}(\mathbf{n}^2_{n+1}) \tag{2.180}$$

Algorithmic constitutive tensor: *IMPLEX integration scheme*

The derivation of the algorithmic tangent moduli for the IMPLEX stress update algorithm follows a similar procedure to that used for the implicit scheme.

The nonsymmetrical expression for the consistent deviatoric elastoplastic module for the IMPLEX stress update scheme is given by

$$\bar{\mathbf{A}}_{dev} = \frac{\partial \mathbf{S}_{n+1}}{\partial \mathbf{C}_{n+1}} = \bar{\delta}_1 \mathbf{A}^{trial}_{dev} + \bar{\delta}_2 \mathbf{N}_{n+1} \otimes \mathrm{DEV}(\mathbf{N}^2_{n+1}) + \bar{\delta}_3 \mathbf{N}_{n+1} \otimes \mathbf{N}_{n+1} \tag{2.181}$$

where the coefficients $\bar{\delta}_1, \bar{\delta}_2$ and $\bar{\delta}_3$ are defined by the expressions

$$\begin{aligned}
\bar{\delta}_1 &= \left(1 - \frac{2\bar{\mu}\Delta\bar{\lambda}_{n+1}}{\left\|\mathbf{S}^{trial}_{n+1}\right\|}\right) \\
\bar{\delta}_2 &= 2\bar{\mu}\Delta\bar{\lambda}_{n+1} \\
\bar{\delta}_3 &= \left(\frac{2\bar{\mu}^2}{\left\|\mathbf{S}^{trial}_{n+1}\right\|} - \frac{2}{3}\left\|\mathbf{S}^{trial}_{n+1}\right\|\right)\Delta\bar{\lambda}_{n+1} \\
\Delta\bar{\lambda}_{n+1} &= \Delta\lambda_n \frac{\Delta t_{n+1}}{\Delta t_n}
\end{aligned} \tag{2.182}$$

and $\mathbf{A}^{trial}_{dev}$ is given by equation (2.171).

As was said above, a comparison of the coefficients of equation (2.182) and equation (2.170) shows that the algorithmic tangent modulus is simpler in IMPLEX scheme that in implicit scheme. Also, equation (2.182) shows that the tangent moduli of the IMPLEX scheme is independent of the isotropic hardening function used, by the above reason the task of implementing a new hardening function inside the IMPLEX scheme is simpler than in the implicit scheme.

Since, the stress update formula is cast in terms of spatial quantities; it is convenient to transform the material algorithmic tangent moduli (2.181) into the spatial configuration via a pull-forward operation as follows

$$\bar{\mathbf{a}}_{dev} = \frac{\partial \bar{\mathbf{s}}_{n+1}}{\partial \mathbf{1}_{n+1}} = \mathbf{F}_{n+1}\mathbf{F}_{n+1}\mathbf{F}_{n+1}\mathbf{F}_{n+1}\bar{\mathbf{A}}_{dev} \tag{2.183}$$

$$\frac{\partial \bar{\mathbf{s}}_{n+1}}{\partial \mathbf{1}_{n+1}} = \bar{\delta}_1 \frac{\partial \mathbf{s}^{trial}_{n+1}}{\partial \mathbf{1}_{n+1}} + \bar{\delta}_2 \mathbf{n}_{n+1} \otimes \mathbf{n}_{n+1} + \bar{\delta}_3 \mathbf{n}_{n+1} \otimes \mathrm{dev}(\mathbf{n}^2_{n+1}) \tag{2.184}$$

2.8.3.4 Linearization of the algorithmic dissipation

In the same way, the solution of the mechanical problem using an implicit integration scheme requires the algorithmic elastoplastic tangent moduli, the solution of the thermal problem requires the linearization of the algorithmic dissipation.

The mechanical dissipation (2.75) that comes from the free energy (2.49) depends only on the initial flow stress σ_y.This feature, however, is not consistent with the experimental observation on metals which suggest that part of the work hardening possess a dissipative character. In order to accommodate the experimental observations introduced above into the phenomenological thermoplastic constitutive model, an additional dissipation hypothesis concerning the amount of mechanical dissipation must be introduced. In practice, this is accomplished by assuming that the mechanical dissipation is a fraction of the total plastic power.

$$D_{mech} = \chi\sqrt{\frac{2}{3}}(\sigma_y + \beta)\dot{\lambda} \tag{2.185}$$

where $\chi \in \left[0,1\right]$ is a constant dissipation factor chosen in the range of $\left[0.85, 0.95\right]$

Linearization of the algorithmic dissipation: implicit integration scheme

An implicit Backward-Euler time discretization of the plastic dissipation is shown in the next equation

$$D_{mech}^{n+1} = \chi\sqrt{\frac{2}{3}}(\sigma_y + \beta)_{n+1}\frac{\Delta\lambda_{n+1}}{\Delta t} \tag{2.186}$$

The derivative of the dissipation with respect to the temperature is given by the following expression

$$\frac{\partial D_{mec}^{n+1}}{\partial\theta} = a\left[\Delta\lambda_{n+1} - \frac{\sqrt{\frac{2}{3}}(\sigma_y + \beta)_{n+1}}{\left(2\bar{\mu} + \frac{2}{3}b\right)}\right] \tag{2.187}$$

where the coefficients a and b are given by the expressions

$$\begin{aligned} a &= \frac{\chi}{\Delta t}\sqrt{\frac{2}{3}}\frac{\partial(\sigma_y + \beta)_{n+1}}{\partial\theta} \\ b &= \frac{\partial(\sigma_y + \beta)_{n+1}}{\partial\Delta\lambda_{n+1}} \end{aligned} \tag{2.188}$$

The terms a and b depends on the yield functions $\sigma_y + \beta_{n+1}$. The term b has been calculated in the previous section. Therefore, it is only necessary to calculate the derivative of the yield functions with respect to the temperature field, as is show in the following lines

First, the derivate with respect to temperature of the *Simo and Voce* yield function is

$$\frac{\partial(\sigma_y + \beta)_{n+1}}{\partial\theta} = \begin{pmatrix} -\sigma_y + K_0(1-\exp(-\delta\bar{e}^p_{n+1})) & w_0 \\ -H + K_{\inf}(1-\exp(-\delta\bar{e}^p_{n+1})) & w_h \end{pmatrix} \tag{2.189}$$

Second, the derivate with respect to temperature of the Johnson-Cook yield function is

If $\dot{\bar{e}}^p_{n+1} < \dot{e}_0$

$$\frac{\partial(\sigma_y + \beta)_{n+1}}{\partial\theta} = -m(A + B(\bar{e}^p_{n+1})^n)\left(\left(\frac{\theta-\theta_0}{\theta_{melt}-\theta_0}\right)^{m-1}\right)\frac{1}{\theta_{melt}-\theta_0} \tag{2.190}$$

If $\dot{\bar{e}}^p_{n+1} \geq \dot{e}_0$

$$\frac{\partial(\sigma_y + \beta)_{n+1}}{\partial\theta} = \left(1 + C\ln(\frac{\dot{\bar{e}}^p_{n+1}}{\dot{e}_0})\right)\frac{\partial(\sigma_y + \beta)_{n+1}}{\partial\theta}\bigg|_{\dot{\bar{e}}^p_{n+1}<\dot{e}_0} \tag{2.191}$$

Finally, the derivative with respect to temperature of *Bäker* yield functions is given by

If $\dot{\bar{e}}^p_{n+1} < \dot{e}_0$

$$\frac{\partial(\sigma_y + \beta)_{n+1}}{\partial\theta} = K_0\begin{pmatrix} \exp(-\frac{\theta}{\theta_{melt}})\left(-\frac{1}{\theta_{melt}}(\bar{e}^p_{n+1})^{n_0\exp(-\frac{\theta}{\theta_{melt}})}\ln(\bar{e}^p_{n+1})\right) \\ -\frac{1}{\theta_{melt}}(\bar{e}^p_{n+1})^{n_0\exp(-\frac{\theta}{\theta_{melt}})}\left(\exp(-\frac{\theta}{\theta_{melt}})\right) \end{pmatrix} \tag{2.192}$$

If $\dot{\bar{e}}^p_{n+1} \geq \dot{e}_0$

$$\frac{\partial(\sigma_y + \beta)_{n+1}}{\partial\theta} = K_0\left(1 + C\ln(\frac{\dot{\bar{e}}^p_{n+1}}{\dot{e}_0})\right)\frac{\partial(\sigma_y + \beta)_{n+1}}{\partial\theta}\bigg|_{\dot{\bar{e}}^p_{n+1}<\dot{e}_0} \tag{2.193}$$

From equations(2.190), (2.191), (2.192) and (2.193), it is important to note that the linearization of the plastic dissipation is piecewise defined.

Linearization of the algorithmic dissipation: IMPLEX integration scheme

Starting from the extrapolated value of the plastic multiplier, the plastic dissipation at t_{n+1} could be written as

$$\bar{D}^{n+1}_{mech} = \chi\sqrt{\frac{2}{3}}(\sigma_y + \beta)_{n+1}\frac{\Delta\bar{\lambda}_{n+1}}{\Delta t} \tag{2.194}$$

As the extrapolated value of the plastic multiplier is held constant during the time increment, the linearization of the IMPLEX dissipation is given by

$$\frac{\partial\bar{D}^{n+1}_{mec}}{\partial\theta} = \chi\sqrt{\frac{2}{3}}\frac{\partial(\sigma_y + \beta)_{n+1}}{\partial\theta}\frac{\Delta\bar{\lambda}_{n+1}}{\Delta t} \tag{2.195}$$

A comparison of equations (2.195) and (2.187) shows how simple it is to linearize the plastic dissipation in case of using IMPLEX.
The derivative of the yield function with respect to the temperature field for each of the models used in this work have been presented in equations (2.189), (2.190),(2.191),(2.192) and (2.193).
Using the coefficients introduced in equation(2.188), the linearization in case of IMPLEX is simplified as

$$\frac{\partial \bar{D}_{mec}^{n+1}}{\partial \theta} = a\Delta\bar{\lambda}_{n+1} \tag{2.196}$$

2.8.4 Discretization of the frictional contact model

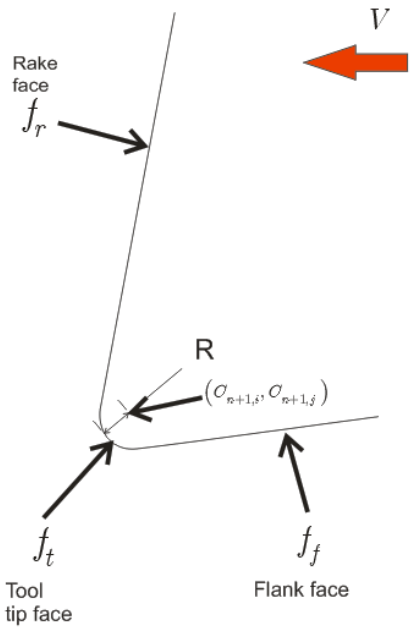

Figure 21. Rigid tool discretization

2.8.4.1 Contact between the workpiece and a rigid tool

The purpose of this section is to describe an approach for modeling the tool as a rigid body. The tool is modeled as three surfaces moving at constant speed (tool speed), each of these surfaces representing the rake face, the tool tip and the flank face, respectively (*Figure 21*).

Mathematically, a workpiece particle has penetrated the tool if it satisfies the inequalities presented in the following equation

$$TOOL = \begin{cases} f_r = y_{n+1,j} - \text{ctg}(\beta)(y_{n+1,i} + R\cos\beta - C_{n+1,i}) - C_{n+1,j} - Rsen(\beta) \leq 0 \\ f_t = \begin{cases} (y_{n+1,i} - C_{n+1,i})^2 + (y_{n+1,j} - C_{n+1,j})^2 - R^2 \leq 0 \\ \pi - \beta \leq \tan^{-1}\left(\dfrac{y_{n+1,j} - C_{n+1,j}}{y_{n+1,i} - C_{n+1,i}}\right) \leq \dfrac{3\pi}{2} + \alpha \end{cases} \\ f_f = y_{n+1,j} - \tan(\beta)(y_{n+1,i} - C_{n+1,i} - Rsen(\beta)) - C_{n+1,j} + R\cos(\beta) \geq 0 \end{cases} \quad (2.197)$$

where R is the tool radius, α the rake angle, β the flank angle, C_{n+1} the center of the tool tip and $(y_{n+1,i}, y_{n+1,j})$ are all points that lie within or on the surface of the tool. A workpiece particle is in contact with the tool if it satisfies any of the equalities presented in the above equation. Otherwise, the particle is not in contact with the tool.

Next, we describe the procedure to calculate the contact forces between the tool and the workpiece using a strategy of gap penalization (penetration) presented in section 2.3.4
Given the set of particles that have penetrated the tool, calculate the particle projection on each of the surfaces using the equations presented in Table 4.

	Closest point projection	
Rake face	$\alpha = 0$	$\bar{x}^k_{n+1,i} = (C_{n+1,i} - R)$ $\bar{x}^k_{n+1,j} = x^k_{n+1,j}$
	$\alpha > 0$	$\bar{x}^k_{n+1,i} = \dfrac{x^k_{n+1,i} + mx^k_{n+1,j} - m^2(R\cos(\alpha) - C_{n+1,i}) - mC_{n+1,j} - mRsen(\alpha)}{1+m^2}$ $\bar{x}^k_{n+1,j} = \dfrac{m^2x^k_{n+1,j} + mx^k_{n+1,i} + m(R\cos(\alpha) - C_{n+1,i}) + C_{n+1,j} + Rsen(\alpha)}{1+m^2}$
Tool tip	$\bar{x}^k_{n+1} = R\dfrac{\mathbf{x}^k_{n+1} - C_{n+1}}{\left\|\mathbf{x}^k_{n+1} - C_{n+1}\right\|} + C_{n+1}$	
Flank face	$\beta = 0$	$\bar{x}^k_{n+1,i} = x^k_{n+1,i}$ $\bar{x}^k_{n+1,j} = (C_{n+1,j} - R)$
	$\beta > 0$	$\bar{x}^k_{n+1,i} = \dfrac{x^k_{n+1,i} + nx^k_{n+1,j} + n(n(C_{n+1,i} + Rsen(\beta)) - C_{n+1,j} + R\cos(\beta))}{1+n^2}$ $\bar{x}^k_{n+1,j} = \dfrac{n^2x^k_{n+1,j} + nx^k_{n+1,i} - (n(C_{n+1,i} + Rsen(\beta)) - C_{n+1,j} + R\cos(\beta))}{1+n^2}$

Table 4. Closest point projection of a workpiece particle.

	Normal	Gap
Rake face	$\mathbf{n} = \ -\cos\ \alpha\ , sen\ \alpha$	$g_{n+1}^k = -\ \mathbf{x}_{n+1}^k - \bar{\mathbf{x}}_{n+1}^k\ \bullet \mathbf{n}_{n+1}^k$
Tool tip	$\mathbf{n}_{n+1}^k = \dfrac{\bar{\mathbf{x}}_{n+1}^k - C_{n+1}}{R}$	
Flank face	$\mathbf{n} = \ sen\ \beta\ , -\cos\ \beta$	

Table 5. Normal vector to the surface of the tool and gap definition

	Contact force	Contact stiffness matrix
Rake face	$\mathbf{F}_{c,n+1}^k = \kappa g_{n+1}^k \mathbf{n}_{n+1}^k$	$-\kappa \mathbf{n} \otimes \mathbf{n}$
Tool tip		$\kappa\left[-\dfrac{R}{\left\|\mathbf{x}_{n+1}^k - C_{n+1}\right\|}\mathbf{n}_{n+1}^k \otimes \mathbf{n}_{n+1}^k + \dfrac{g_{n+1}^k}{\left\|\mathbf{x}_{n+1}^k - C_{n+1}\right\|}\delta\right]$
Flank face		$-\kappa \mathbf{n} \otimes \mathbf{n}$

Table 6. Contact force and contact stiffness against a rigid tool using a penalty approach.

Then calculate the surface normal at the closed point projection using equations presented in Table 5 and calculate the distance between a particle and its closed point projection (gap) for each of the surfaces.

For each particle, select the surface having the minimum gap. That is to say, each particle has been associated with the distance that has penetrated into the tool and the normal to the surface to which it has penetrated.

In the last step, a contact force proportional to the gap in the direction to the surface normal is applied to the particle (Table 6). In the global implicit scheme developed in this work, the linearization of the contact force is necessary to ensure quadratic convergence; therefore, it is also presented in Table 6.

The mathematical procedure to derive the equations presented in Table 4, Table 5 and Table 6 is based on the solution of the minimal distance problem between the tool surface discretized in three surfaces and the workpiece particle. The minimal distance problem is presented in the following equation

$$\bar{\mathbf{x}}_{n+1}^k \ = \arg\left[\min_{f(\mathbf{y}_{n+1})=0} \left\|\mathbf{x}_{n+1}^k - \mathbf{y}_{n+1}\right\|\right] \tag{2.198}$$

where $\mathbf{y}_{n+1}$ is the update position of the workpiece particle and $\bar{\mathbf{x}}_{n+1}^k$ is its closest point projection. A detailed solution of the problem (2.198) for each of the three surfaces that describe the tool is not presented because it is a long but a simple calculation.

The position of the surface tool depends on the center of the tool tip, as is show in equation(2.197). Likewise, the center of the tool tip depends on tool velocity and time through the next equation

$$\mathbf{C}_{n+1} = \mathbf{C}_n - \left[0; V\right]\Delta t \tag{2.199}$$

In case of the explicit integration scheme, equations presented in Table 4 performs the correction of the position of the particle using a minimum distance criterion.

2.8.4.2 Contact between the workpiece and an elastic tool

The node-to-segment (NTS) contact element is one of the most commonly used discretization in large deformation finite element simulation of contact problems. Consider that a workpiece particle s with coordinate $\mathbf{x}_s^{(1)}$ and $\theta_s^{(1)}$ temperature comes into contact with the master (tool) segment defined by the nodal coordinates $\mathbf{x}_1^{(2)}, \mathbf{x}_2^{(2)}$ and nodal temperatures $\theta_1^{(2)}, \theta_2^{(2)}$. By introducing the surface coordinate ξ along the master surface, we have

$$\mathbf{x}^{(2)}(\xi) = \mathbf{x}_1^{(2)} + (\mathbf{x}_2^{(2)} - \mathbf{x}_1^{(2)})\xi \tag{2.200}$$

and

$$\theta^{(2)}\ \xi\ = \theta_1^{(2)} + (\theta_2^{(2)} - \theta_1^{(2)})\xi \tag{2.201}$$

where $\mathbf{x}^{(2)}(\xi)$ and $\theta^{(2)}(\xi)$ are linear interpolations of the master surface and the master surface temperature respectively.

The normalized tangent vector of the master segment can be easily computed as

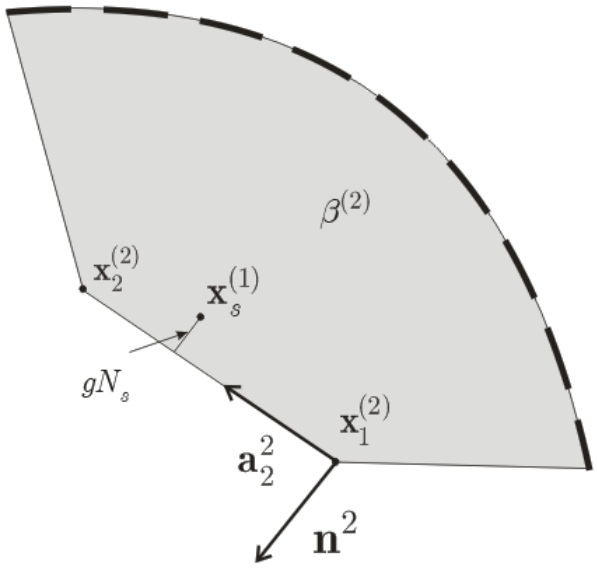

Figure 22. Node-to-segment contact element.

$$\mathbf{a}_1^{(2)} = \frac{\partial_\xi \hat{\mathbf{x}}^{(2)}(\xi)}{l} = \frac{(\mathbf{x}_2^{(2)} - \mathbf{x}_1^{(2)})}{l} \tag{2.202}$$

where $l = \left\| \mathbf{x}_2^{(2)} - \mathbf{x}_1^{(2)} \right\|$ is the length of the master segment. The unit normal to the master segment can be computed as

$$\mathbf{n}^{(2)} = \mathbf{e}_3 \times \mathbf{a}_1^{(2)} \tag{2.203}$$

The finite element discretization of equation (2.87) can be written as

$$g_N = \left[\mathbf{x}_s^{(1)} - (1 - \overline{\xi})\mathbf{x}_1^{(2)} - \overline{\xi}\,\mathbf{x}_2^{(2)} \right] \bullet \mathbf{n}^{(2)} \tag{2.204}$$

where $\overline{\xi}$ is the projection of the workpiece particle $\mathbf{x}_s^{(1)}$ onto the master segment. Mathematically, the projection is written as

$$\overline{\xi} = \frac{1}{l}(\mathbf{x}_s^{(1)} - \mathbf{x}_1^{(2)}) \bullet \mathbf{a}_1^{(2)} \tag{2.205}$$

The term g_N in equation (2.204) is also known as the relative displacement in the direction normal to the tool.

The constitutive relationships for the normal force P_N are given in equation (2.89) and its discrete version is given by

$$P_N = \kappa g_N \tag{2.206}$$

Now, we introduce the discrete relative tangential velocity by

$$\dot{g}_T = \frac{(\overline{\xi} - \overline{\xi}_0)l}{\Delta t} \tag{2.207}$$

And the discrete relative displacement

$$g_T = (\overline{\xi} - \overline{\xi}_0)l \tag{2.208}$$

where $\overline{\xi}_0$ is the projection at the beginning and $\overline{\xi}$ is the projection at the end of the time step.

Introducing equation (2.207) in equation (2.93), the discrete counterpart of the Norton-Hoff friction law is written as

$$P_T = \kappa \mu g_N (\dot{g}_T)^\alpha sign(\dot{g}_T) \tag{2.209}$$

The finite element discretization of the thermal gap represented in equation (2.94) is given by

$$g_Q = \left[\theta_s^{(1)} - (1 - \overline{\xi})\theta_1^{(2)} - \theta_2^{(2)}\overline{\xi} \right] \tag{2.210}$$

From (2.96) and using (2.210) the discrete contact heat flux is written as

$$Q = h\left[\theta_s^{(1)} - (1 - \overline{\xi})\theta_1^{(2)} - \theta_2^{(2)}\overline{\xi} \right] \tag{2.211}$$

and the discrete frictional dissipation

$$D_{fric} = \mu_r sign(\overline{\xi} - \overline{\xi}_0)\left(\left| \frac{\overline{\xi} - \overline{\xi}_0 \;\; l}{\triangle t} \right| \right)^\alpha P_N \dot{g}_T \tag{2.212}$$

The contributions of the thermo-mechanical contact in the mechanical and thermal weak forms (2.114) take the form

$$\begin{aligned} G_{c,mech}^{(1,2)} &= P_N \delta g_N - P_T \delta g_T \\ G_{c,therm}^{(1,2)} &= Q \delta g_Q - D_{fric} \delta g_D \end{aligned} \tag{2.213}$$

For the discrete slave particle the mechanical variations are given by

$$\begin{aligned} \delta g_N &= \left[\eta_s^{(1)} - (1-\overline{\xi}) \eta_1^{(2)} - \overline{\xi} \eta_2^{(2)} \right] \bullet \mathbf{n}^{(2)} \\ \delta g_T &= l \delta \overline{\xi} \\ &= \left[\eta_s^{(1)} - (1-\overline{\xi}) \eta_1^{(2)} - \overline{\xi} \eta_2^{(2)} \right] \bullet \mathbf{a}_1^{(2)} + \frac{g_N}{l} (\eta_2^{(2)} - \eta_1^{(2)}) \bullet \mathbf{n}^{(2)} \end{aligned} \tag{2.214}$$

where we have set $\eta_s^{(1)} = \delta \mathbf{x}_s^{(1)}$ and $\eta_i^{(1)} = \delta \mathbf{x}_i^{(1)}$

And the thermal variations

$$\begin{aligned} \delta g_Q &= \left[v_s^{(1)} - (1-\overline{\xi}) v_1^{(2)} - \overline{\xi} v_2^{(2)} \right] \\ \delta g_D &= \left[\phi_1 v_s^{(1)} + \phi_2 ((1-\overline{\xi}) v_1^{(2)} + \overline{\xi} v_2^{(2)}) \right] \end{aligned} \tag{2.215}$$

where ϕ_1 and ϕ_2 are the portions of the flux D_{fric} entering bodies (1) and (2) respectively. Mathematical expressions for ϕ_1 and ϕ_2 are given by equation (2.97). In equation (2.215) we have set $v_s^{(1)} = \delta \theta_s^{(1)}$ and $v_i^{(1)} = \delta \theta_i^{(1)}$.

For a global algorithmic treatment using Newton's method (implicit and IMPLEX integration schemes), we have to linearize equations (2.213). Explicit expressions for the tangent stiffness matrix associated to a normal force given by equation (2.206) were first derived by Wriggers and Simo in [65]. For completeness, the linearization of the contact contribution will be discussed here for the case of penalty methods (equation (2.206)). Within the penalty approach, the starting equation for the NTS-element is the contribution of the normal contact force to the virtual work principle given by the next equation

$$P_N \delta g_N = \kappa g_N \delta g_N \tag{2.216}$$

The linearization of this expressions yields

$$\Delta (P_N \delta g_N) = \kappa \Delta g_N \delta g_N + \kappa g_N \Delta \delta g_N \tag{2.217}$$

where Δg_N is given by the expression

$$\Delta g_N = \left[\Delta \mathbf{u}_s^{(1)} - (1-\overline{\xi}) \Delta \mathbf{u}_1^{(2)} - \overline{\xi} \Delta \mathbf{u}_2^{(2)} \right] \bullet \mathbf{n}^{(2)} \tag{2.218}$$

and $\Delta \delta g_N$ takes the form

$$\Delta\delta g_N = -\frac{1}{l}\Big[\Delta\mathbf{u}_s^{(1)} - (1-\overline{\xi})\Delta\mathbf{u}_1^{(2)} - \overline{\xi}\Delta\mathbf{u}_2^{(2)}\Big]\bullet\mathbf{a}_1^{(2)}(\eta_2^{(2)} - \eta_1^{(2)})\bullet\mathbf{n}^{(2)}$$
$$-\frac{gN_s}{l^2}(\Delta\mathbf{u}_2^{(2)} - \Delta\mathbf{u}_1^{(2)})\bullet\mathbf{n}^{(2)}(\eta_2^{(2)} - \eta_1^{(2)})\bullet\mathbf{n}^{(2)} \tag{2.219}$$
$$-\Big(\Big[\eta_s^{(1)} - (1-\overline{\xi})\eta_1^{(2)} - \overline{\xi}\eta_2^{(2)}\Big]\bullet\mathbf{a}_1^{(2)}\Big)\frac{\mathbf{n}^{(2)}\bullet(\Delta\mathbf{u}_2^{(2)} - \Delta\mathbf{u}_1^{(2)})}{l}$$

where we have used the linearization of the normalized tangent vector of the master segment,

$$\Delta\mathbf{a}_1^{(2)} = (\mathbf{n}^{(2)} \otimes \mathbf{n}^{(2)})\frac{(\Delta\mathbf{u}_2^{(2)} - \Delta\mathbf{u}_1^{(2)})}{l} \tag{2.220}$$

the linearization of the unit normal to the master segment,

$$\Delta\mathbf{n}^{(2)} = -(\mathbf{a}_1^{(2)} \otimes \mathbf{n}^{(2)})\frac{(\Delta\mathbf{u}_2^{(2)} - \Delta\mathbf{u}_1^{(2)})}{l} \tag{2.221}$$

the linearization of the master segment length

$$\Delta l = (\Delta\mathbf{u}_2^{(2)} - \Delta\mathbf{u}_1^{(2)})\bullet\mathbf{a}_1^{(2)} \tag{2.222}$$

and the linearization of the projection of the slave node onto the master segment

$$\Delta\overline{\xi} = \frac{1}{l}\Big[\Delta\mathbf{u}_s^{(1)} - (1-\overline{\xi})\Delta\mathbf{u}_1^{(2)} - \overline{\xi}\Delta\mathbf{u}_2^{(2)}\Big]\bullet\mathbf{a}_1^{(2)} + \frac{gN_s}{l^2}(\Delta\mathbf{u}_2^{(2)} - \Delta\mathbf{u}_1^{(2)})\bullet\mathbf{n}^{(2)} \tag{2.223}$$

Introducing

$$\Delta\mathbf{u}_s = \begin{Bmatrix}\Delta\mathbf{u}_s^{(1)}\\ \Delta\mathbf{u}_1^{(2)}\\ \Delta\mathbf{u}_2^{(2)}\end{Bmatrix}, \quad \eta_s = \begin{Bmatrix}\eta_s^{(1)}\\ \eta_1^{(2)}\\ \eta_2^{(2)}\end{Bmatrix}, \tag{2.224}$$

$$\mathbf{T}_s = \begin{Bmatrix}\mathbf{a}_1^{(2)}\\ -(1-\overline{\xi})\mathbf{a}_1^{(2)}\\ -\overline{\xi}\,\mathbf{a}_1^{(2)}\end{Bmatrix}_s, \qquad \mathbf{T}_{0s} = \begin{Bmatrix}0\\ -\mathbf{a}_1^{(2)}\\ \mathbf{a}_1^{(2)}\end{Bmatrix}_s, \tag{2.225}$$

and

$$\mathbf{N}_s = \begin{Bmatrix}\mathbf{n}_1^{(2)}\\ -(1-\overline{\xi})\mathbf{n}_1^{(2)}\\ -\overline{\xi}\,\mathbf{n}_1^{(2)}\end{Bmatrix}_s, \qquad \mathbf{N}_{0s} = \begin{Bmatrix}0\\ -\mathbf{n}^{(2)}\\ \mathbf{n}^{(2)}\end{Bmatrix}_s \tag{2.226}$$

we can stay the matrix form of $\Delta\delta g_N$

$$\Delta\delta g_N = \eta_s^T\mathbf{K}_{\Delta\delta}\Delta\mathbf{u}_s \tag{2.227}$$

with

$$\mathbf{K}_{\Delta\delta} = -\frac{1}{l}\Big[\mathbf{N}_{0s}\mathbf{T}_s^T + \mathbf{T}_s\mathbf{N}_{os}^T + \frac{g_N}{l}\mathbf{N}_{0s}\mathbf{N}_{os}^T\Big] \tag{2.228}$$

In case of the penalty method

$$\Delta\ P_N \delta g_N\ = \kappa \eta_s^T \left[\mathbf{N}_{0s}\mathbf{N}_{os}^T + gN_s \mathbf{K}_{\Delta\delta} \right] \Delta \mathbf{u}_s \tag{2.229}$$

This yields the stiffness matrix $\mathbf{K}_{Ns}^p$

$$\begin{aligned} \mathbf{K}_{Ns}^p &= \kappa \mathbf{N}_s \mathbf{N}_s^T + \kappa g_N \mathbf{K}_{\Delta\delta} \\ &= \kappa \mathbf{N}_s \mathbf{N}_s^T - \kappa \frac{g_N}{l} \left[\mathbf{N}_{0s}\mathbf{T}_s^T + \mathbf{T}_s \mathbf{N}_{os}^T + \frac{g_N}{l} \mathbf{N}_{0s}\mathbf{N}_{os}^T \right] \end{aligned} \tag{2.230}$$

The point of departure in the case of frictional contact using Norton-Hoff friction law is the contribution of the friction law to the virtual work principle given by the next equation

$$P_T \delta g_T = \kappa \mu \left| g_N \right| \left(\frac{\left| (\bar{\xi} - \bar{\xi}_0) \right| l}{\Delta t} \right)^{\alpha} sign(\dot{g}_T) \delta g_T \tag{2.231}$$

Linearization of the above expression yields

$$\begin{aligned} \Delta(P_T \delta g_T) = &-\kappa\mu \left(\frac{\left| g_T \right|}{\Delta t} \right)^{\alpha} \Delta g_N \delta g_T sign(\dot{g}_T) \\ &+\kappa\mu \left| g_N \right| \alpha \left(\frac{\left| g_T \right|}{\Delta t} \right)^{\alpha-1} \frac{l}{\Delta t} \Delta\bar{\xi} \delta g_T \\ &+\kappa\mu \left| g_N \right| \alpha \left(\frac{\left| g_T \right|}{\Delta t} \right)^{\alpha-1} \frac{(\bar{\xi} - \bar{\xi}_0)}{\Delta t} \Delta l \delta g_T sign(\dot{g}_T) \\ &+\kappa\mu \left| g_N \right| \left(\frac{\left| g_T \right|}{\Delta t} \right)^{\alpha} \Delta \delta g_T sign(\dot{g}_T) \end{aligned} \tag{2.232}$$

The linearization of the normal gap Δg_N, the linearization of the projection of the slave node onto the master segment $\Delta\bar{\xi}$, the linearization of the current master segment length Δl has been presented in equations (2.218),(2.223) and (2.222).

The linearization of the variation δg_T is

$$\Delta \delta g_T = l \Delta \delta \bar{\xi} + \delta \bar{\xi} \Delta l \tag{2.233}$$

The linearization of the variation $\delta\bar{\xi}$ is obtained after some algebra

$$
\begin{aligned}
\Delta\delta\bar{\xi} = & \frac{1}{l^2}\Big[\Delta\mathbf{u}_s^{(1)} - (1-\bar{\xi})\Delta\mathbf{u}_1^{(2)} - \bar{\xi}\Delta\mathbf{u}_2^{(2)}\Big]\bullet\mathbf{a}_1^{(2)}(\eta_1^{(2)} - \eta_2^{(2)})\bullet\mathbf{a}_1^{(2)} \\
& - \frac{(\Delta\mathbf{u}_2^{(2)} - \Delta\mathbf{u}_1^{(2)})\bullet\mathbf{a}_1^{(2)}\Big[\eta_s^{(1)} - (1-\bar{\xi})\eta_1^{(2)} - \bar{\xi}\eta_2^{(2)}\Big]\bullet\mathbf{a}_1^{(2)}}{l^2} \\
& + \frac{1}{l}\Big[\eta_s^{(1)} - (1-\bar{\xi})\eta_1^{(2)} - \bar{\xi}\eta_2^{(2)}\Big]\bullet\mathbf{n}^{(2)}\frac{(\Delta\mathbf{u}_2^{(2)} - \Delta\mathbf{u}_1^{(2)})\bullet\mathbf{n}^{(2)}}{l} \\
& + \frac{\Big[\Delta\mathbf{u}_s^{(1)} - (1-\bar{\xi})\Delta\mathbf{u}_1^{(2)} - \bar{\xi}\Delta\mathbf{u}_2^{(2)}\Big]\bullet\mathbf{n}^{(2)}}{l^2}(\eta_2^{(2)} - \eta_1^{(2)})\bullet\mathbf{n}^{(2)} \\
& - \frac{2g_N}{l^3}(\Delta\mathbf{u}_2^{(2)} - \Delta\mathbf{u}_1^{(2)})\bullet\mathbf{n}^{(2)}(\eta_2^{(2)} - \eta_1^{(2)})\bullet\mathbf{a}_1^{(2)} \\
& - 2g_N\frac{(\Delta\mathbf{u}_2^{(2)} - \Delta\mathbf{u}_1^{(2)})\bullet\mathbf{a}_1^{(2)}}{l^3}(\eta_2^{(2)} - \eta_1^{(2)})\bullet\mathbf{n}^{(2)}
\end{aligned}
\tag{2.234}
$$

The product between the linearization of the variation $\delta\bar{\xi}$ and Δl is equal to

$$
\begin{aligned}
\delta\bar{\xi}\Delta l = & \frac{1}{l}\Big[\eta_s^{(1)} - (1-\bar{\xi})\eta_1^{(2)} - \bar{\xi}\eta_2^{(2)}\Big]\bullet\mathbf{a}_1^{(2)}(\Delta\mathbf{u}_2^{(2)} - \Delta\mathbf{u}_1^{(2)})\bullet\mathbf{a}_1^{(2)} \\
& + \frac{g_N}{l^2}(\eta_2^{(2)} - \eta_1^{(2)})\bullet\mathbf{n}^{(2)}(\Delta\mathbf{u}_2^{(2)} - \Delta\mathbf{u}_1^{(2)})\bullet\mathbf{a}_1^{(2)}
\end{aligned}
\tag{2.235}
$$

Inserting equations (2.234) and (2.235) in equation(2.233), the linearization of the variation δg_T could be written as

$$
\begin{aligned}
\Delta\delta g_T = & \Big[\eta_s^{(1)} - (1-\bar{\xi})\eta_1^{(2)} - \bar{\xi}\eta_2^{(2)}\Big]\bullet\mathbf{n}^{(2)}\frac{(\Delta\mathbf{u}_2^{(2)} - \Delta\mathbf{u}_1^{(2)})\bullet\mathbf{n}^{(2)}}{l} \\
& + \frac{\Big[\Delta\mathbf{u}_s^{(1)} - (1-\bar{\xi})\Delta\mathbf{u}_1^{(2)} - \bar{\xi}\Delta\mathbf{u}_2^{(2)}\Big]\bullet\mathbf{n}^{(2)}}{l}(\eta_2^{(2)} - \eta_1^{(2)})\bullet\mathbf{n}^{(2)} \\
& - \frac{1}{l}\Big[\Delta\mathbf{u}_s^{(1)} - (1-\bar{\xi})\Delta\mathbf{u}_1^{(2)} - \bar{\xi}\Delta\mathbf{u}_2^{(2)}\Big]\bullet\mathbf{a}_1^{(2)}(\eta_2^{(2)} - \eta_1^{(2)})\bullet\mathbf{a}_1^{(2)} \\
& - g_N\frac{\mathbf{a}_1^{(2)}\bullet(\Delta\mathbf{u}_2^{(2)} - \Delta\mathbf{u}_1^{(2)})}{l^2}(\eta_2^{(2)} - \eta_1^{(2)})\bullet\mathbf{n}^{(2)} \\
& - 2\frac{g_N}{l^2}(\Delta\mathbf{u}_2^{(2)} - \Delta\mathbf{u}_1^{(2)})\bullet\mathbf{n}^{(2)}(\eta_2^{(2)} - \eta_1^{(2)})\bullet\mathbf{a}_1^{(2)}
\end{aligned}
\tag{2.236}
$$

In matrix form, the linearization of the variation of $\Delta\delta g_T$ is written as follows

$$
\Delta\delta g_T = \eta_s^T\mathbf{K}_{\Delta\delta}^{sl}\Delta\mathbf{u}_s \tag{2.237}
$$

with

$$
\mathbf{K}_{\Delta\delta}^{sl} = \begin{bmatrix} \dfrac{1}{l}\ \mathbf{N}_s\mathbf{N}_{0s}^T + \mathbf{N}_{0s}\mathbf{N}_s^T - \mathbf{T}_{0s}\mathbf{T}_s^T \\ -\dfrac{g_N}{l^2}\ \mathbf{N}_{0s}\mathbf{T}_{0s}^T + 2\mathbf{T}_{0s}\mathbf{N}_{os}^T \end{bmatrix} \tag{2.238}
$$

Furthermore, expressing the products $\Delta g_N \delta g_T, \Delta\bar{\xi}\delta g_T$ and $\Delta l \delta g_T$ in matrix form

$$\begin{aligned}
\Delta g_N \delta g_T &= \eta_s^T \left[\mathbf{T}_s \mathbf{N}_s^T + \frac{g_N}{l} \mathbf{N}_{0s} \mathbf{N}_s^T \right] \Delta \mathbf{u}_s \\
\Delta \bar{\xi} \delta g_T &= \eta_s^T \left[\begin{array}{l} \frac{1}{l}\left(\mathbf{T}_s \mathbf{T}_s^T + \frac{g_N}{l} \mathbf{N}_{0s} \mathbf{T}_s^T \right) \\ + \frac{g_N}{l^2} \mathbf{T}_s \mathbf{N}_{0s}^T + \frac{(g_N)^2}{l^3} \mathbf{N}_{0s} \mathbf{N}_{0s}^T \end{array} \right] \Delta \mathbf{u}_s \\
\Delta l \delta g_T &= \eta_s^T \left[\mathbf{T}_s \mathbf{T}_{0s}^T + \frac{g_N}{l} \mathbf{N}_{0s} \mathbf{T}_{0s}^T \right] \Delta \mathbf{u}_s
\end{aligned} \tag{2.239}$$

Using expression in (2.239), equation number (2.232) can be expressed as follows

$$\Delta(P_T \delta g_T) = \eta_s^T \mathbf{K}^{NH} \Delta \mathbf{u}_s \tag{2.240}$$

with

$$\begin{aligned}
\mathbf{K}^{NH} = & -\kappa\mu \left(\frac{|g_T|}{\Delta t} \right)^{\alpha} sign(\dot{g}_T) \left[\mathbf{T}_s \mathbf{N}_s^T + \frac{g_N}{l} \mathbf{N}_{0s} \mathbf{N}_s^T \right] \\
& + \kappa\mu |g_N| \alpha \left(\frac{|g_T|}{\Delta t} \right)^{\alpha-1} \frac{l}{\Delta t} \left[\begin{array}{l} \frac{1}{l}\left(\mathbf{T}_s \mathbf{T}_s^T + \frac{g_N}{l} \mathbf{N}_{0s} \mathbf{T}_s^T \right) \\ + \frac{g_N}{l^2} \mathbf{T}_s \mathbf{N}_{0s}^T + \frac{(g_N)^2}{l^3} \mathbf{N}_{0s} \mathbf{N}_{0s}^T \end{array} \right] \\
& + \kappa\mu |g_N| \alpha \left(\frac{|g_T|}{\Delta t} \right)^{\alpha} \frac{1}{l} sign(\dot{g}_T) \left[\mathbf{T}_s \mathbf{T}_{0s}^T + \frac{g_N}{l} \mathbf{N}_{0s} \mathbf{T}_{0s}^T \right] \\
& + \kappa\mu |g_N| \left(\frac{|g_T|}{\Delta t} \right)^{\alpha} sign(\dot{g}_T) \mathbf{K}_{\Delta\delta}^{sl}
\end{aligned} \tag{2.241}$$

The above equation represents the tangent stiffness matrix associated to the Norton-Hoff friction law. Note that this matrix is unsymmetrical which corresponds to the non-associativity of the Norton-Hoff friction law.

Sometimes, the penetration or gap g_N is much lower than the master side length l, that is, $g_N << l$. In the above situation, most of the terms of the stiffness matrix (2.241) are negligible. In this case, the stiffness matrix can be simplified as

$$\mathbf{K}^{NH} = -\kappa\mu \left(\frac{|g_T|}{\Delta t} \right)^{\alpha} sign(\dot{g}_T) \mathbf{T}_s \mathbf{N}_s^T + \kappa\mu |g_N| \frac{\alpha}{\Delta t} \left(\frac{|g_T|}{\Delta t} \right)^{\alpha'1} \mathbf{T}_s \mathbf{T}_s^T \tag{2.242}$$

Most of the times, in the numerical simulation of metal cutting, the tool advance per time step are much smaller than the characteristic mesh size of the tool. Therefore, most of the numerical simulation of metal cutting carried out in this

work has been carried out using the stiffness matrix (2.242). The stiffness matrix presented in equations (2.241) will be used only in case that the tool advance per time step is comparable with the size of the tool element or when convergence problems exist.
In the same way that the mechanical problem involves the linearization of the contribution of normal and friction forces to the virtual work principle with respect to displacement, the thermal problem involves the linearization of the contribution of the contact heat flux and frictional dissipation to the virtual thermal work with respect to temperature. Then, the following lines present the linearization of the virtual thermal work with respect to temperature for the NTS contact element

$$\Delta_\theta G_{c,therm}^{(1,2)} = \Delta_\theta Q \delta g_Q \tag{2.243}$$

In (2.243) the discrete contact heat flux Q follows from (2.211) , whereas the discrete frictional dissipation D_{fric} is given by equation (2.212). The linearization of the discrete contact heat flux takes the form

$$\Delta_\theta Q = h\left[1, -(1-\overline{\xi}), -\overline{\xi}\right] \tag{2.244}$$

In matrix form, the thermal stiffness matrix associated to the heat transfer at the tool chip interface is given by the following expression

$$\mathbf{K}^\theta = h\begin{bmatrix} 1 & -(1-\overline{\xi}) & -\overline{\xi} \\ -(1-\overline{\xi}) & (1-\overline{\xi})^2 & \overline{\xi}(1-\overline{\xi}) \\ -\overline{\xi} & \overline{\xi}(1-\overline{\xi}) & \overline{\xi}^2 \end{bmatrix} \tag{2.245}$$

2.9 Meshing in the Particle Finite Element Method (*PFEM*)

The initial developments of the Particle Finite Element Method (*PFEM*) took place in the field of fluid mechanics [97], because PFEM facilitates tracking and modeling of free surfaces. Later on, the Particle Finite Element (*PFEM*) was applied in a variety of simulation problems: fluid structure interaction with rigid bodies, erosion processes, mixing processes, coupled thermo-viscous processes and thermal diffusion problems [98, 99]. First applications of *PFEM* to solid mechanics were done in problems involving large strains and rotations, multi body contacts and creation of new surfaces (riveting, powder filling and machining) [100]. In this work, we extended the Particle Finite Element Method to the numerical simulation of metal cutting processes.

The Particle Finite Element Method is based on three main ingredients: 1) the Delaunay triangulation, 2) the α-shape method and 3) the finite element method. The finite element method was explained earlier in this chapter. The following lines will make a brief introduction to the Delaunay triangulation and α-shape method, as well as we will justify their use.

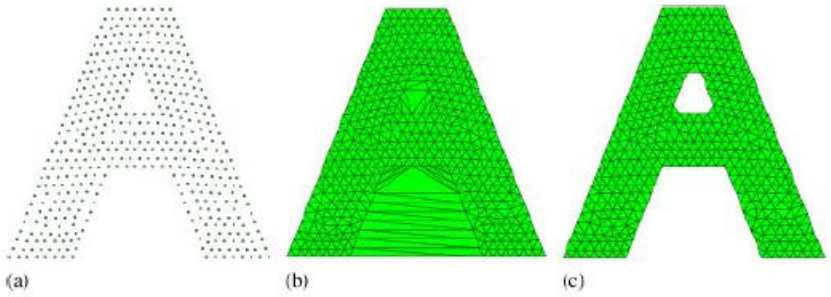

Figure 23. Remeshing steps using the standard PFEM. (a) Distribution of points; (b) Delaunay triangulation; (c) Delaunay triangulation; with α shape.[11]

A Delaunay triangulation for a set P of points in a plane is a triangulation $DT(P)$ such that no point in P is inside the circumcircle of any triangle in $DT(P)$. Delaunay triangulations maximize the minimum angle of all the angles of the triangles in the triangulation; they tend to avoid skinny triangles. To avoid global remeshing and interpolation from mesh to mesh, in the Particle Finite Element Method (PFEM) mesh quality is improved by performing a re-triangulation of the domain which consists of re-computing element connectivity using a Delaunay triangulation where the current position of the particles (i.e. of the mesh nodes) is kept fixed.

Mesh distortion is alleviated in the spirit of the Particle Method (PFEM), because whenever the mesh quality is no longer satisfactory, according to some criteria associated to element distortion, the connectivity of existing nodes is recomputed using a Delaunay triangulation.

This choice has some important implication, the Delaunay triangulation generates the convex figure of minimum area which encloses all the points and which may be not conformal with the external boundaries. A possibility to overcome this problem is to couple the Delaunay triangulation with the so-called α-shape method.

The main idea of the α-shape method consists in removing the unnecessary (too large and too distorted) triangles from the mesh using a criterion based on the mesh distortion. For every triangle e of the mesh the radius R_e of the circumcircle of the element is computed. Moreover, a typical dimension of the mesh h_e is calculated as

$$h_e = \frac{1}{\text{ndim}} \sum_{j=1}^{\text{ndim}} \sum_{i=1}^{n_b} \frac{\left| \mathbf{x}_i - \mathbf{x}_j \right|}{n_{b,i}} \tag{2.246}$$

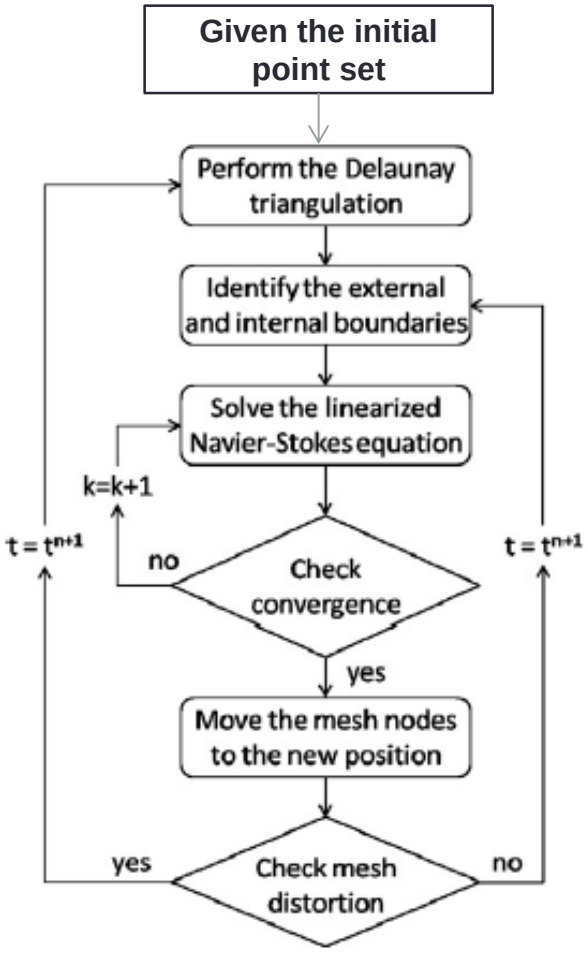

Figure 24. Particle finite element (PFEM) flowchart in computational fluid mechanics problems.

where n_b is the number of neighbor particles, which are defined as the particles contained in the same simplices as particle j and ndim is the dimension of the problem. The index of an element distortion α_e is computed as:

$$\alpha_e = \frac{R_e}{h_e} \tag{2.247}$$

All the triangles that do not satisfy the condition:

$$\alpha_e \leq \bar{\alpha} \tag{2.248}$$

are removed from the mesh, where $\bar{\alpha} \geq 1$ is a parameter to be assigned on the basis of the geometric accuracy required for the considered problem.
The α-shape method can generate particles that do not belong to any element.

There are several options for the treatment of isolated particles. The first one is let them move freely, because they can be rejoined to the body in future time steps. The second one is remove the particle from the analysis. This is recommended when particles do not contribute anymore to the mechanical properties of the domain. An example of the remeshing scheme using PFEM is shown in Figure 27.

In the Lagrangian approach, the particles move because of the medium flow and it may happen that particles concentrate in same regions of the domain and, on the contrary, in other regions the number of particles becomes too low to obtain an accurate solution. To overcome these difficulties PFEM adds and removes particles. If the distance d_{nodes} between two nodes is $d_{nodes} << h$, one of the nodes is removed. If the radius r of an element circumsphere is $r >> h$, a new node is added at the center of the circumsphere. The flow variables in the new node are linearly interpolated from that of the element nodes, and the assigned material properties are the ones of the elements.

The PFEM consists of the following steps. The initial analysis domain is filled with a set of points referred to as "particles" which are endowed with initial velocity, pressure and position. The accuracy of the numerical solution is clearly dependent on the considered number of particles. An initial finite element mesh is generated using the particles as nodes through a Delaunay triangulation and external boundaries are identified by means of the α-shape technique. As long as mesh distortion is acceptable, solve the non-linear Lagrangian form of the governing equations finding velocity and pressure at every node of the mesh. A flowchart solution scheme using PFEM applied to fluid mechanics problems is presented in Figure 24.

In the PFEM, the size of each time step is assumed small enough to avoid remeshing during the iterations for the solution of the non-linear equations in the time step itself. Mesh distortion is checked only at convergence.

2.9.1 Meshing in the Particle Finite Element Method: numerical simulation of metal cutting process

The standard PFEM presents some weaknesses when applied in orthogonal cutting simulation. For example, the external surface generated using α-shape may affect the mass conservation (Figure 25 and Figure 26), the chip shape and sometimes generates an unphysical welding of the workpiece and the chip (Figure 26).

To deal with this problem, in this work we propose the use of a constrained Delaunay algorithm. Furthermore, addition and remotion of particles are the principal tools, which we employ for sidestepping the difficulties, associated with deformation-induced element distortion, and for resolving the different scales of the solution. The insertion of nodes is based on the equidistribution of plastic power, such that, elements exceeding the prescribed tolerance *TOL*

$$\int_{S_t^{(i),(e)}} \bar{D}_{mech}^{n+1} dS_t^{(e)} > TOL \tag{2.249}$$

are targeted for refinement. Here, $\bar{D}_{mech}^{n+1}$ is given by equation (2.186) and $dS_t^{(e)}$ denotes the domain of the element. A particle is inserted in the gauss point of the finite element.

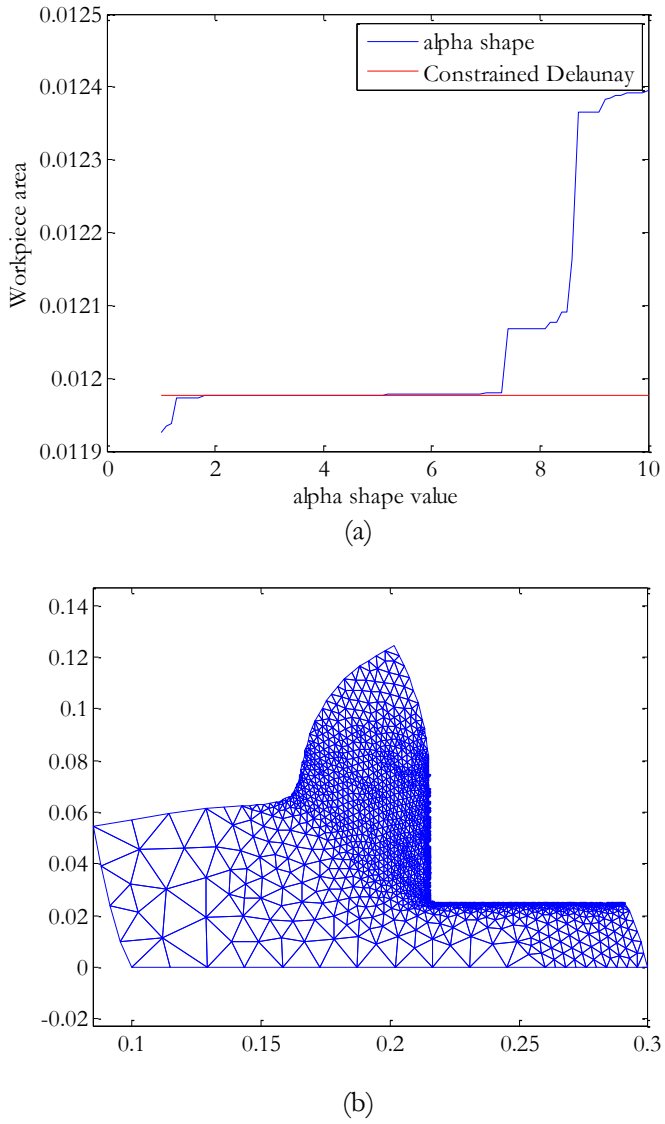

Figure 25. Weaknesses of the alpha shape method in numerical simulation of machining (a) workpiece volume dependency on the alpha shape value (b) workpiece shape using an alpha shape=2.

The remotion on nodes is based on a Zienkiewicz and Zhu [79, 116] error estimator defined by the following expression

$$\mathbf{e} = \left| \bar{e}^* - \bar{e} \right| \Big/ \bar{e}_{\max} \tag{2.250}$$

where $\bar{e}^*$ is the recovered equivalent plastic strain and $\bar{e}_{\max}$ is the maximum equivalent plastic strain. A particle is removed if and only if, the error in all the elements belonging to the particle is less than a given tolerance and the size of the elements is less than a maximum value $h_{\max}$.

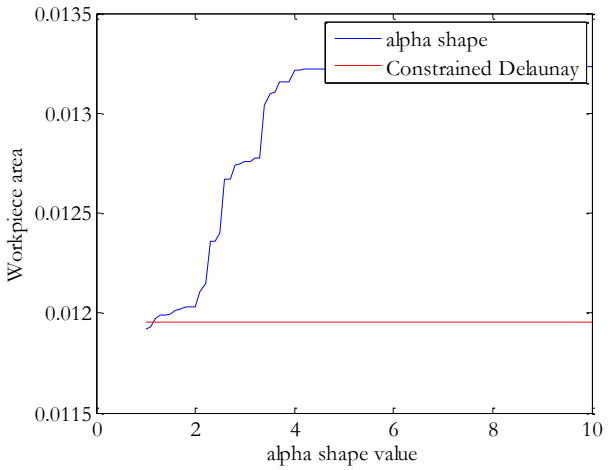

(a)

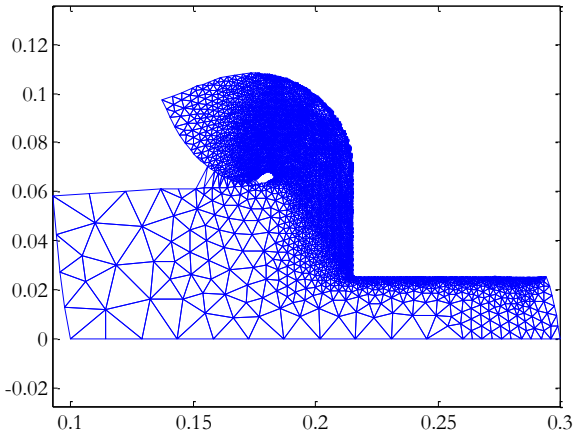

(b)

Figure 26.Weaknesses of the alpha shape method in numerical simulation of machining (a) workpiece volume dependency on the alpha shape value (b) unphysical welding of the workpiece and the chip due to the alpha shape.

In the numerical simulation of metal cutting process, despite the continuous Delaunay triangulation, elements arise with unacceptable aspect ratios; for this reason, the mesh is also subjected to laplacian smoothing. Laplacian smoothing is an algorithm to smooth a mesh. For each node in a mesh, a new position is chosen based on the position of neighbors and the node is moved there. In the case that a mesh is topologically a rectangular grid then this operation produces the Laplacian of the mesh.
More formally, the smoothing operation may be described per-node as:

$$\bar{\mathbf{x}}_i = \sum_{j=1}^{N} \frac{\mathbf{x}_j}{N} \tag{2.251}$$

Where N is the number of adjacent vertices to node i and $\bar{\mathbf{x}}_i$ is the new position for node i.
All the information necessary in subsequent time steps has now to be transferred to the new mesh, it includes nodal information like displacements, temperatures, pressure and Gauss point information like internal variables.
The main feature of the PFEM is that finite elements are only a mean for the computation, but they are not necessarily kept. This means that the mesh that defines the domain for a

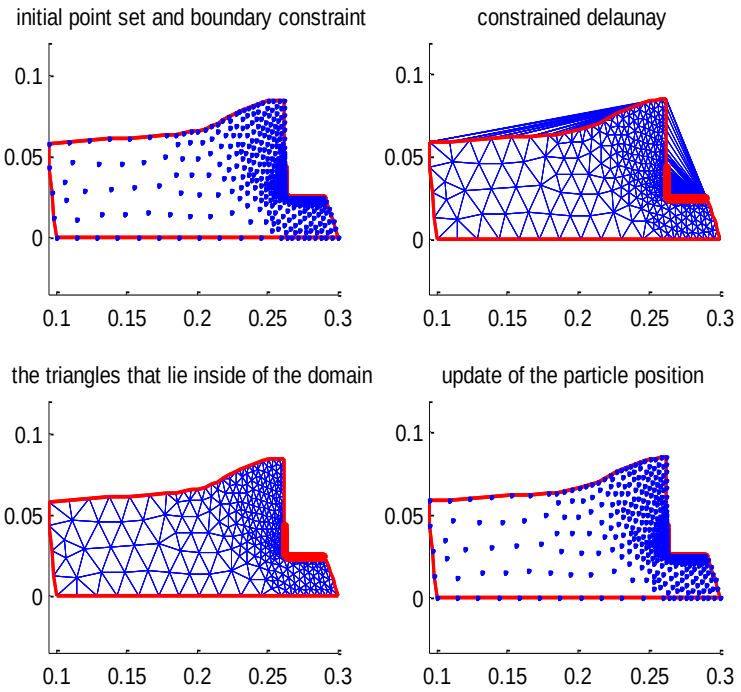

Figure 27. Remeshing steps in the numerical simulation of metal cutting.

given time step can change for the next time step. This is the reason for assigning all the problem variables to the particles. Consequently, the history of the continua remains in the particles. They become the spatial reference and all information of the analysis is kept on them.
The standard PFEM[100] transfer internal variables using the transfer operators presented in [83] or its incremental version presented in [117]. Although the scheme presented in [117] decrease the numerical diffusion of the state fields in comparison with the scheme presented in [83], in both schemes, the transferred variables violate the constitutive equation, generating as a result an unphysical spring back of the machined surface.

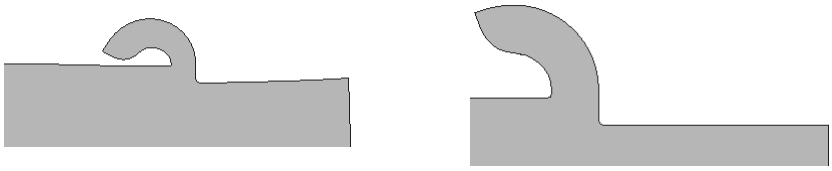

Figure 28. Predicted chip shape using different transfer operators (a) smoothing, (b) projection

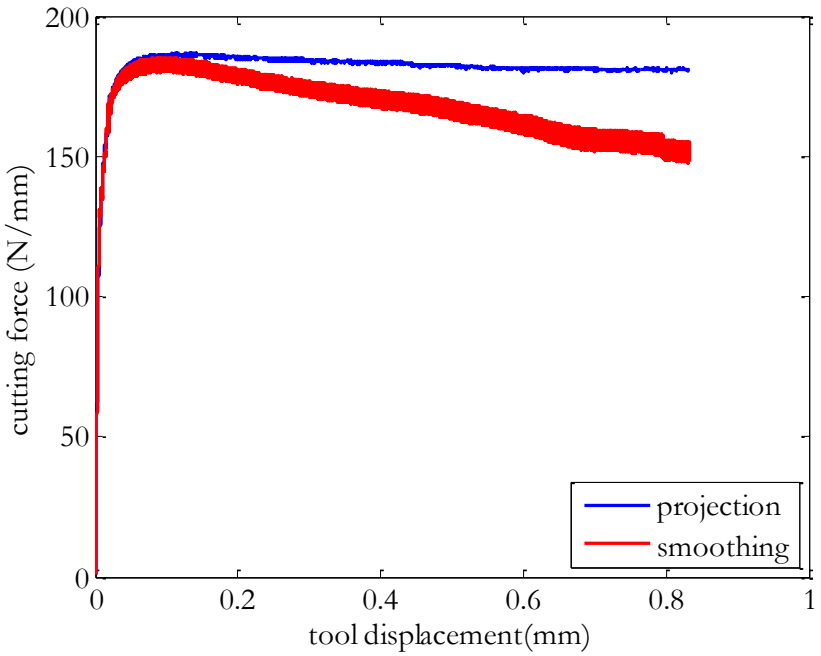

Figure 29. Predicted cutting forces using different transfer operators.

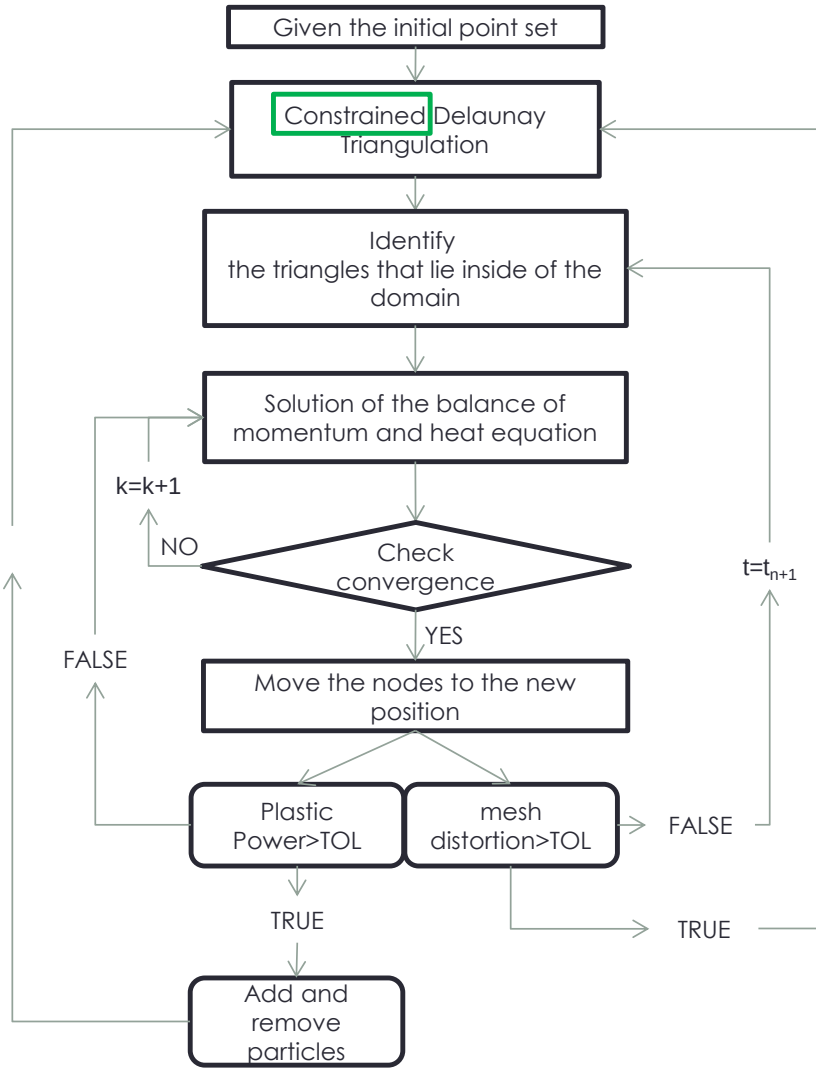

Figure 30. Flowchart of the solution scheme in the numerical simulation of metal cutting processes.

Figure 28 shows the predicted chip shape at the same time step using the smoothing and the projection transfer operators. A comparison shows that the smoothing transfer operator predict an unphysical spring back due to excessive numerical diffusion, due to the unphysical spring back the smoothing transfer operator is unable to predict the residual stresses over the machined surface. Furthermore, Figure 28 shows that the bending of the chip is more pronounced in the numerical simulation using the smoothing than in the projection transfer operator. Figure 29 shows that the predicted cutting force using the projection operator reaches a steady state, while, the smoothing operator predicts a cutting

force that decreases as the tool moves. Due to the previous reasons, the projection operator from one mesh to another using former and new integration points will be used in all the numerical simulation of metal cutting presented in this work. Although, the projection breaks the philosophy of particle based methods like PFEM and increase the computational cost in comparison with the smoothing operator, the unphysical results predicted with the smoothing operator justifies using the projector operator.

The procedure we follow in this work in order to adapt the mesh is the following:

1. Update the particle positions
2. Add particles in their Gauss point if their plastic power is greater than a given value.
3. Based on curvature information and plastic power refine the boundary that describes the workpiece.
4. Remove particles if error estimators in plastic strains are less or equal than a given value. We remove a particle if in all the old finite elements joined to a particle the error is less or equal to a given tolerance.
5. Develop Delaunay Triangulation constrained by the refined old mesh boundary and delete the triangles outside the boundary.
6. Estimates mesh quality. If mesh quality is less or equal than a given tolerance, develop a Laplacian smoothing of the updated particle positions.
    - Find smoothed particles in the new mesh.
    - Transfer particle information (displacement, pressure, temperature) using shape functions
7. Calculate the global coordinates of the gauss points of the new triangulation.
8. Find which triangle of the old triangulations contains each of the Gauss points of the new triangulation.
9. Using the information of 4, update the internal variables of the new triangulation. This step uses that the Gauss information of finite element of the new mesh is the Gauss information of the closest finite element of the old mesh.

It is important to remark that step 4 and 6 are optional. The main advantage of the proposed strategy is: it is not necessary to create a complete new mesh; we only adapt the mesh with the addition and remotion of particles and improve mesh quality using Delaunay triangulation. shows a summary about the remeshing scheme used in the numerical simulation of metal cutting.

Finally, Figure 30 shows the solution scheme of a metal cutting problem using the particle finite element method (PFEM).

Chapter 3

3 Numerical modeling of metal cutting processes using PFEM

This chapter presents numerical simulations using the formulation proposed in this work. First of all, numerical simulations of two benchmark (Cook Membrane and Taylor impact test) tests are present and validated qualitatively and quantitatively with solutions reported in the literature. Furthermore, a traction test validates the locking free element type proposed in this work in thermo-mechanical problems. Finally, the proposed formulation is used in the numerical simulation of continuous and serrated chip formation.

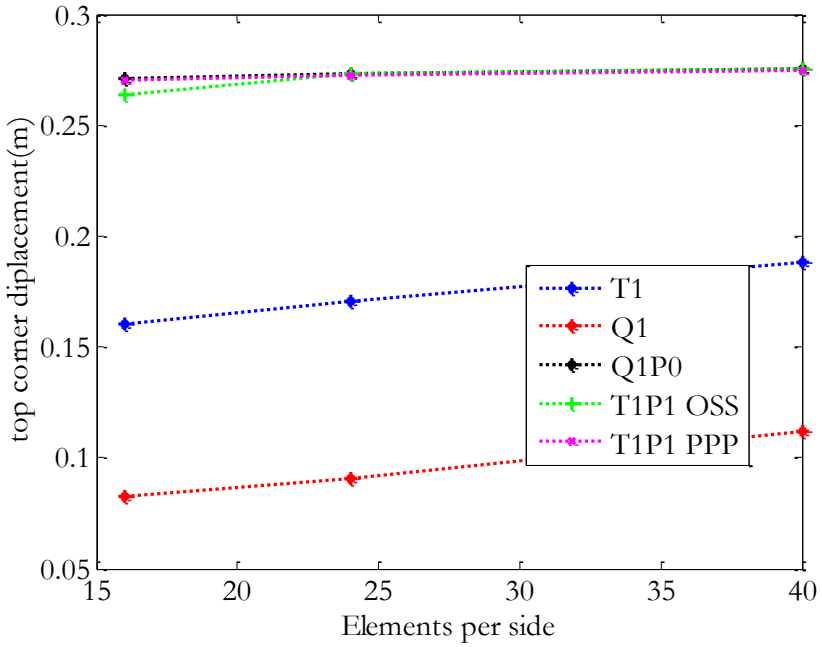

Figure 31. Plane strain Cook`s Problem: convergence of different formulations for incompressible elasticity. T1 standard displacement for triangular elements, Q1 standard displacement for quadrilaterals elements, Q1P0 mixed mean dilatation/pressure approach for quadrilateral elements, T1P1 OSS mixed formulation for linear triangles using orthogonal sub grid scale as a stabilization strategy, T1P1 PPP mixed formulation for linear triangles using Polynomial pressure projection.

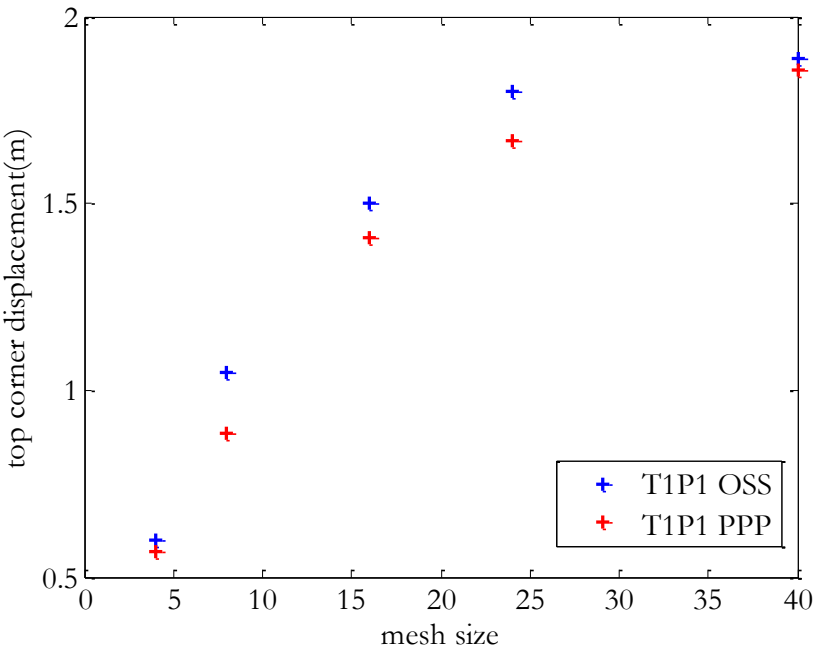

Figure 32. Plane strain Cook`s Problem: convergence of different formulations for J2-Plasticity. T1P1 OSS mixed formulation for linear triangles using orthogonal sub grid scale as a stabilization strategy, T1P1 PPP mixed formulation for linear triangles using Polynomial pressure projection.

3.1 Plane strain Cook's Membrane problem

The Cook Membrane problem is a bending dominated example that has been used by many authors as a reference test to check their element formulation. Here it will be used to validate the proposed formulation in incompressible elasticity and plasticity. The results of our formulation will be compared against Q1P0 finite element and a mixed finite element using Orthogonal Subgrid Scale as a stabilization strategy. The problem consists in a tapered panel, clamped on one side and subjected to a shearing load at the free end. In order to test the convergence behavior of different formulations, the problem has been discretized into $16 \times 16, 24 \times 24$ and 40×40. The following materials properties are assumed: Young`s Modulus = 70, Poisson`s ratio =0.4999 and applied force = 1.

Figure 31 shows the behavior of both quadrilateral and triangular finite elements in case of nearly incompressible elasticity. The figure shows the poor performance of the Q1 and T1 standard elements within the context of nearly incompressible elasticity, due to an extreme locking. Furthermore, the figure

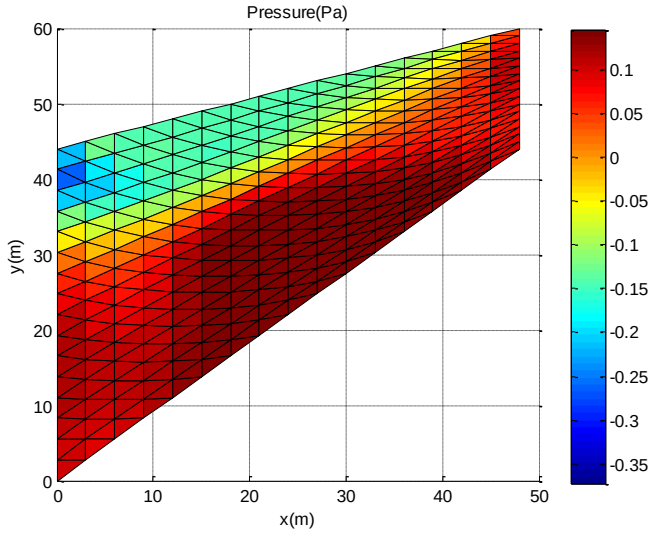

(a) Orthogonal Sub grid Scale c=1

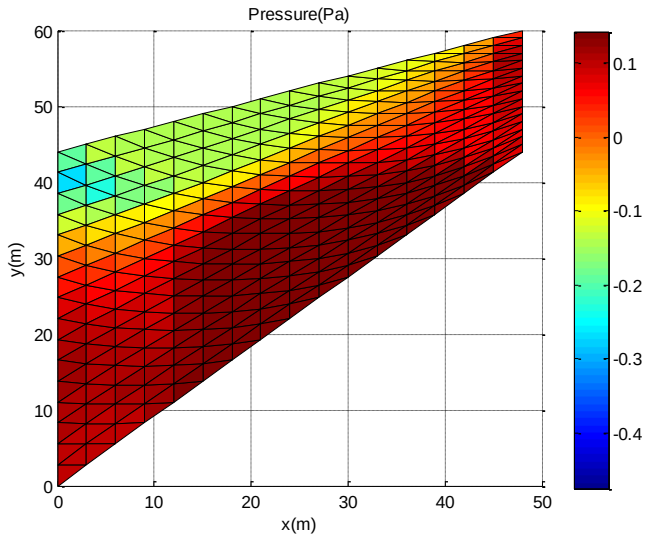

(b) Polynomial Pressure Projection c=1

Figure 33. Pressure field for mixed formulation using Orthogonal Sub Grid Scale and Polynomial Pressure Projection as stabilization strategies and J2-Plasticity.

shows that the proposed formulation converges similarly to OSS but a low computational cost. It is important to remark that in Polynomial pressure projection strategy the stabilization parameter is mesh size independent and that the stabilization terms added to the mixed formulation are elementary depend. It

shows that our proposal allows getting similar results to the OSS strategy but a low computational cost. The stabilization parameter used in PPP and OSS was 1.
Next examples involves Cook`s Membrane but J2-plasticity and the following assumed materials properties: Young`s Modulus = 70, Poisson`s ratio = 0.4999, yield stress = 0.243 hardening modulus = 0.135 and kinematic hardening modulus 0.015 and an applied force of 1.8 in 50 increments.
Figure 32 shows a comparison of the top corner displacement for the mixed finite element using OSS and PPP as stabilization strategies. Figure 32 shows that the convergence behavior of two formulations is really similar. As we say in case of elastic behavior, PPP is simple to implement and do not need and extra calculation like the projected pressure gradient in OSS.
Figure 33 presents pressure contour at the same time (final) of the deformation process. A smooth contour field can be identified in both mixed formulations. At the same time, the predicted results are very similar quantitatively.

3.2 Taylor impact test

The problem consists of the impact of a cylindrical bar with initial velocity of 227m/s into a rigid wall. The bar has an initial length of 32.4 mm and an initial radius of 3.2 mm. Material properties of the bar are typical of copper: density $\rho = 8930kg/m^3$, Young`s modulus $E = 1.17 \times 10^5 MPa$, Poisson`s ratio $v = 0.35$, initial yield stress $\sigma_Y = 400MPa$ and hardening modulus $H = 100MPa$. A period of $80\mu s$ has been analyzed. Our results present a 2D axisymmetric simulation
We will compare qualitatively and quantitatively the results predicted with the proposed formulation with the results predicted with Caracteristic Base Split (CBS)[59] and Average Nodal Pressure (ANP)[48]. The final geometry of the bar is in good agreement with the results obtained in the literature. We obtained similar results to Zienkiewicz with CBS, Bonet with Average Nodal Pressure formulation and De Micheli with his recently developed formulation for explicit dynamics. The final radius using the proposed formulation gives a final radius of

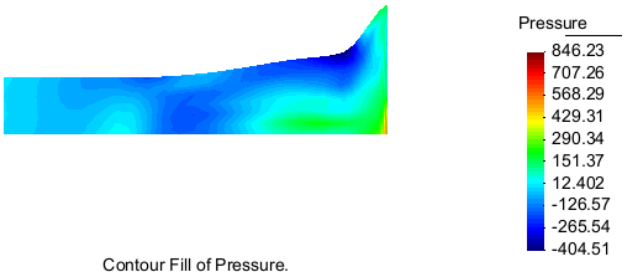

Figure 34. Pressure field $80\mu s$ after the impact for the proposed formulation.

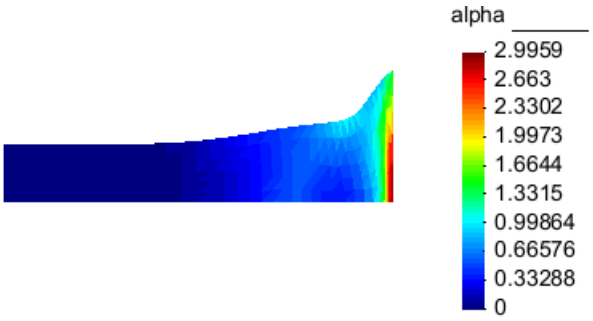

Figure 35. Equivalent plastic strain distribution $80\mu s$ ***after the impact for the proposed formulation.***

7.26. Table 1 shows the comparison of the final radius obtained with our formulations with the results presented in the literature.

Formulation	De Micheli[118]	CBS[59]	ANP[48]	This work
Final radius	7,07	7,07	6,99	7,26

Table 7. Final radius of the rod after the impact obtained with De Micheli formulation, CBS formulation, ANP formulation and the proposed formulation of this work.

Figure 34 and Figure 35 show the numerical results of the pressure and effective plastic strain distribution using the formulation proposed in this work. The values for the equivalent plastic strain and pressure field obtained with the present formulation coincide well with those given by FIC and CBS formulation.

3.3 Thermo-mechanical traction test

We consider a rectangular specimen in plane strain submitted to uniform traction forces. The specimen considered in the simulation has a width of 12.866 mm and a length of 53.334 mm. Figure 36 despites the mesh of the initial configuration. The bar is assumed insulated along its lateral face, while the temperature is held constant and equal to 273K on the upper and lower faces. The total value of imposed displacement is increased to 5mm applied in 100 equal time steps, with a rate of increase of 1mm/s. The chosen values of thermo mechanical properties of the specimen are given in Table 2, they correspond to steel. We consider the source term in the energy equation defined as a fraction of the plastic work, in this example we use a factor of 0.9. Due to the symmetry of the solution, only one quarter of the specimen is discretized, imposing the corresponding symmetry boundary conditions. As a solution strategy we use a mixed linear displacement-linear pressure finite element and the Polynomial Pressure Projection as a stabilization strategy.

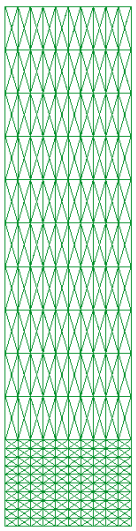

Figure 36. Plain strain nearly adiabatic shear banding. Initial configuration.

Elastic Modulus	206900 MPa
Poisson	0,3
Density	7800 Kg/m^3
Yield Stress	450 MPa
Saturation Stress	715 MPa
Strain Hardening Modulus	129,24 MPa
Hardening Exponent	16,93
Heat Conductivity	45 N/sK
Heat Capacity	0,49e9mm^2/s^{2}K
Thermal expansion	1e-5 (1/K)
Thermal softening modulus	0,002 (1/K)

Table 8. Plane strain nearly adiabatic shear banding-Materials properties.

The simulations are performed under quasistatic conditions with the *isothermal implicit split* proposed by Simo [102], presented in the previous chapter and the *isothermal IMPLEX split* proposed in this work .

Figure 37 shows the temperature and von Mises field at the final configuration. Figure 38 shows the load/displacement obtained with the proposed formulation. Results presented in Figure 37 and Figure 38 have been obtained using the implicit isothermal split presented in previous chapter. Furthermore, Figure 38 shows a comparison with the results presented by Ibrahimbehovic [119] using a four node element with incompatible modes and Beni and Movahhedy [120] using an Arbitrary Lagrangian Eulerian formulation. The predicted forces are

similar during the strain hardening part of the force displacement curve, but in the softening branch of the force displacement curve the predicted forces are different for the three formulations. Our formulation predicts the smaller force among the formulations available in the literature, showing that our proposed formulation does not lock in softening.

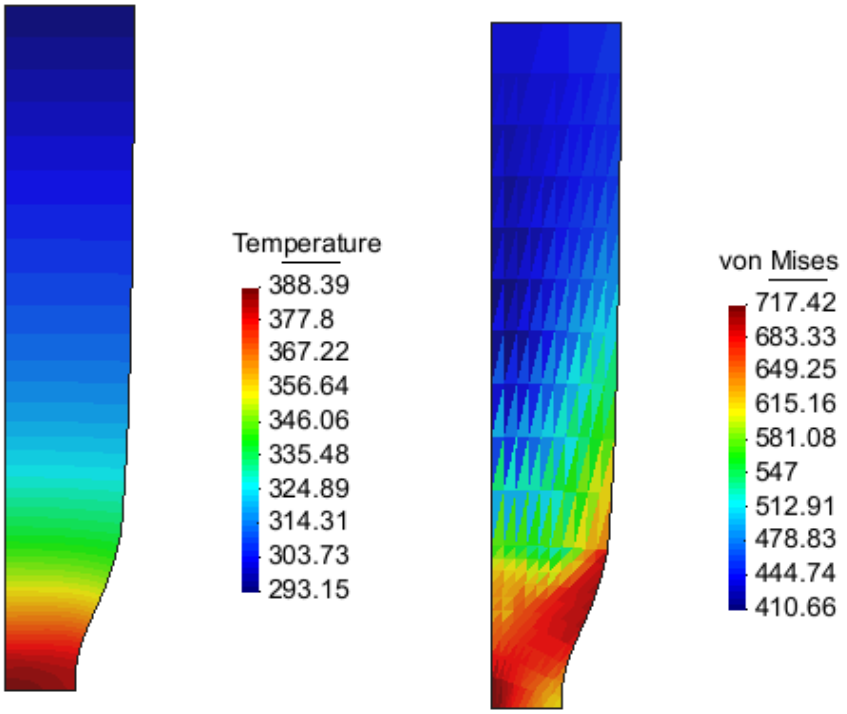

Temperature(K) von Mises(MPa)

Figure 37. Plane strain nearly adiabatic shear banding. Temperature and von Mises stress field at 5 mm.

The load displacement curve obtained using the *isothermal IMPLEX split* proposed in this work is presented in Figure 39. The total value of imposed displacement is increased to 5mm and applied in 100-500-1000-2000 equal time steps to analyze the overshoots and oscillations in the transitions from elastic to inelastic state. The results presented in Figure 39 show that the overshoot decreases by increasing the number of time steps used. Using 2000 time steps, the unphysical overshot predict by the isothermal *IMPLEX* split is negligible, although, the results predicted with 500 time steps can be considerable satisfactory, taking into account that we identify the overshoot as an unphysical prediction that comes from the integration scheme.

The computing time need to solve the thermo-mechanical traction test using the *isothermal IMPLEX split* is greater that the computing time needed by the *isothermal implicit split*, considering that in both cases we are getting the same accuracy. Nevertheless, the *isothermal IMPLEX split* will be considered as an

alternative in the numerical modeling of metal machining, because in metal cutting the size of the time steps is restricted by the contact conditions between the tool and the workpiece, in such a way that for the time steps of interest, both schemes give results with similar accuracy. In the previous situation, the *IMPLEX* is a better choice because its needs less computing time per time step in comparison with the implicit split. A set of examples will be presented in section 3.6 that show the advantages of the *IMPLEX* scheme in the numerical simulation of metal cutting processes.

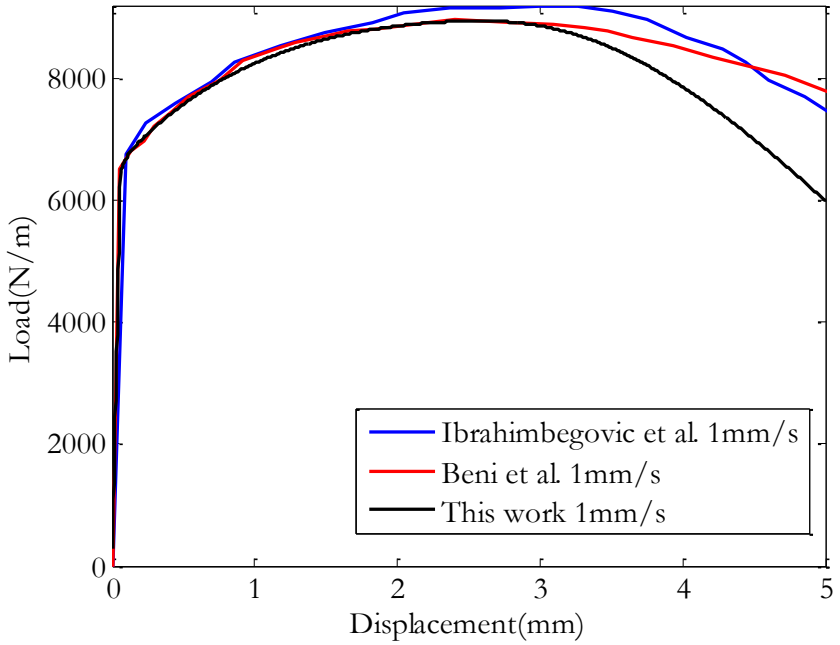

Figure 38. Plane strain nearly adiabatic shear banding. Load/displacement curve

3.4 Machining steel using a rate independent yield function

Our first application concerns the cutting of a rectangular block of a common steel of length 7mm and width 3.6mm at a velocity of 3.33 m/s, a cutting depth of 0.15 mm, a rake angle of 0º, and a tool radius of 0.025 mm. Material behavior is given by a Simo law that takes into account thermal softening (Table 8). Conductivity and specific heat does not depend on temperature, we consider them constant. The following assumptions are made: First, the tool is supposed to be rigid and friction is neglected. Furthermore, the thermal exchange between the part and the tool are also neglected. The inertia of the part is neglected. Implicit dynamics was used. Time steps were of 1.25×10^{-8} which necessitates

of 2.5×10^4 steps for a tool travel of 1.6 mm. The assumption that the tool is rigid is reasonable, since the deformation of the tool is secondary relatively to the excessive plastic deformation of the workpiece.

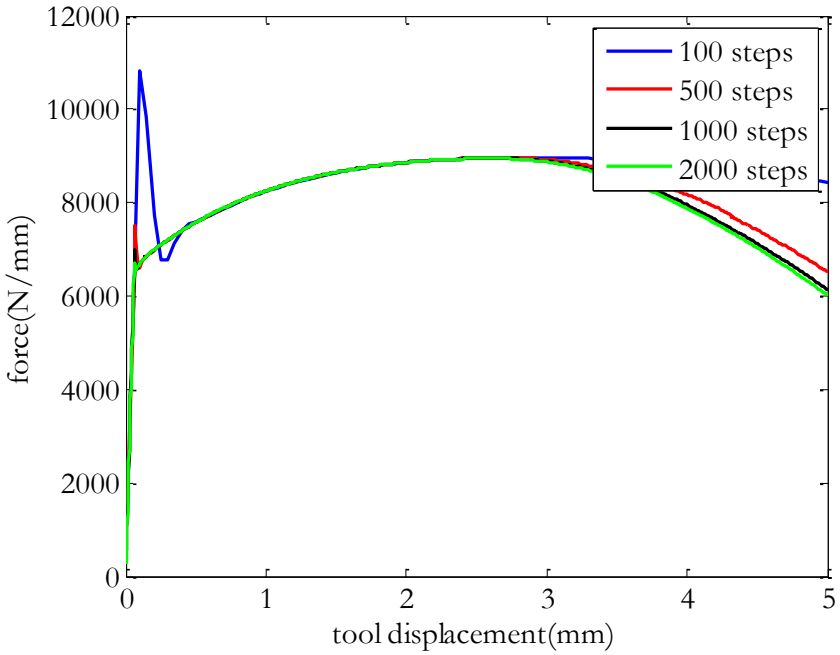

Figure 39. Plane strain nearly adiabatic shear banding. Load/displacement curve. Isothermal IMPLEX split.

Temperature, effective plastic strain rate and von Mises contours are presented in Figure 40. Von Mises stress shown in Figure 40, demonstrates that relatively high stresses arise in the primary shear zone and at the tool chip interface. The localization of this zone agrees with simplified models, but it differs in that the maximum stress is not confined to only a plane of excessive shear. It is also important to note the development of residual stresses at and below the surface of the produced new surface and in the upper part of the chip, especially near the tool-chip interface where unloading due to curling of the chip occurred. The effective strain rate in the primary and the secondary shear zone is of the order of 10^5 and has its highest value close to the tool tip. Finally, temperature distribution is shown in the workpiece. Temperature reaches its peak on the tool tip and on the machined surface. Figure 41 depicts cutting and thrust forces applied on the tool, obtained from the simulations. Nevertheless, the predicted chip is continuous; the cutting and thrust force does not reach a steady state due to the strong dependency of the yield hardening function on the linear hardening modulus.

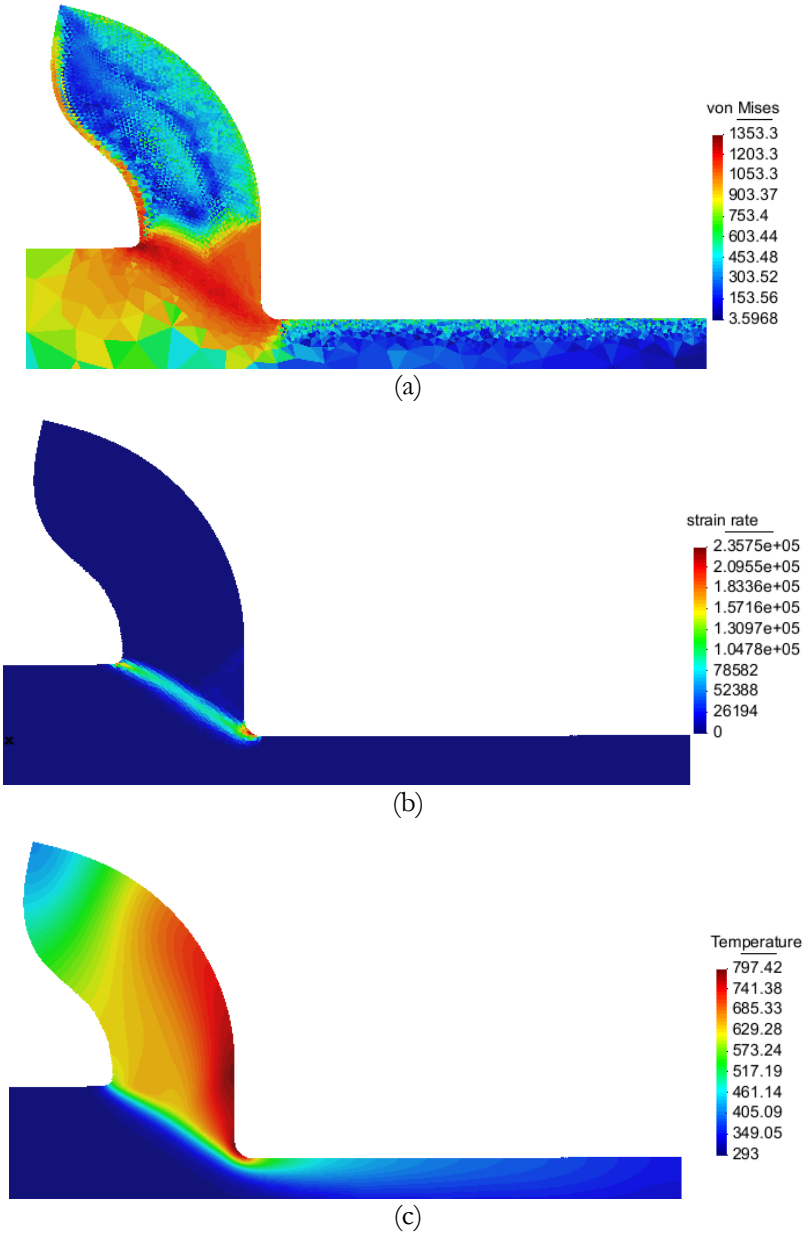

Figure 40. Continuous chip formation using a rate independent yield function: (a) von Mises (MPa) ; (B) strain rate(1/s); (c) temperature(K)

The contact length between the tool and the workpiece, the deformed chip thickness and the shear angle are 0.16 mm, 0.25 mm and 22º.

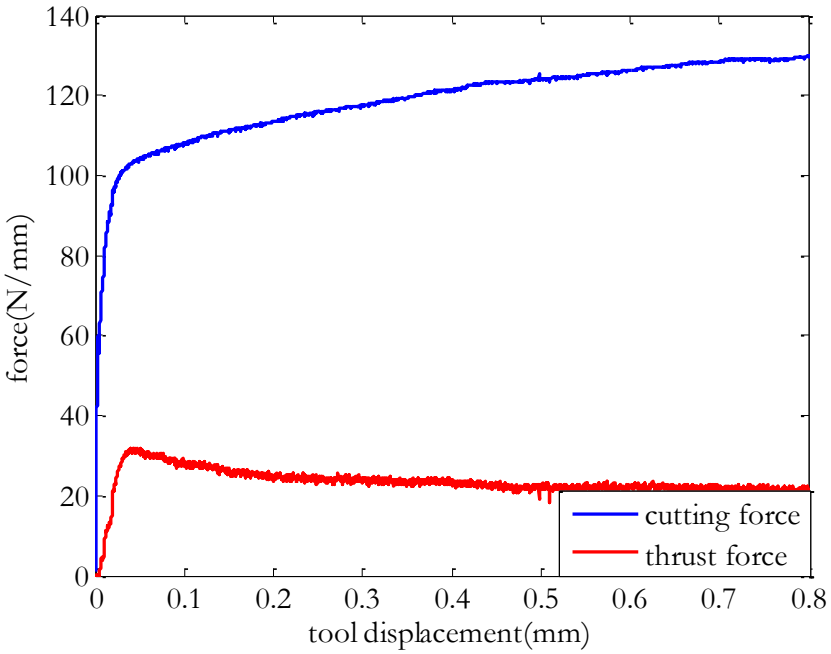

Figure 41. Cutting and thrust force vs. cutting tool displacement for a rate independent yield function

3.5 Machining an AISI 4340 using different rake angles

The second application concerns the cutting of a rectangular block of high strength AISI 4340 steel of length 7mm and width 3.6mm, at a velocity of 3.33 m/s, a cutting depth of 0.1 mm and a rake angle of 0º and 6º. Material behavior is given by a Johnson Cook law that takes into account thermal softening and strain rate hardening (Table 11). Conductivity and specific heat does not depend on temperature, we consider them constant. The following assumptions are made: First, the tool is supposed to be rigid and friction is neglected. Furthermore, the thermal exchange between the part and the tool are also neglected. The inertia of the part is neglected. Implicit dynamics was used. Time steps were of 1.25×10^{-8} which necessitates of 2.5×10^{4} steps for a tool travel of 1.1 mm. Only insertion of particles was used in this example.

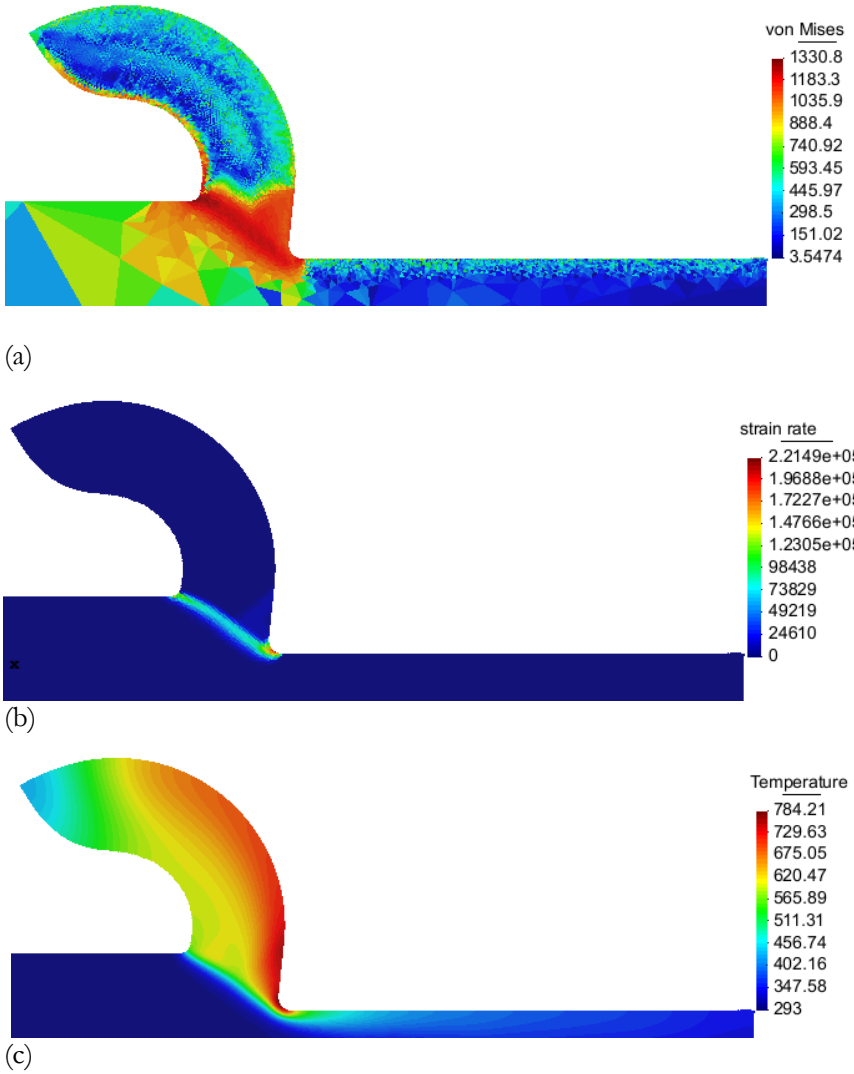

Figure 42. Continuous chip formation using the rate dependent Johnson Cook hardening law and a rake angle of 6° : (a) von Mises (MPa) ; (B) strain rate(1/s); (c) temperature(K)

For a tool rake angle of 6º, deformation is largely confined to the primary shear zone and to the boundary layer adjacent to the tool (Figure 42). No shear localization occurs and a continuous chip formation is predicted. A typical distribution of temperature field within the workmaterial is shown in Figure 42. Highest temperatures are observed on the outside surface of the chip currently in contact with the rake face. Temperature in the direction of the shear plane is found to vary from high of about 780 K near the cutting edge to about 500K near the unmachined free surface. Also temperature along the rake face changes

from 780K near the cutting edge to 750K at the point where the contact between the tool and the chip come to an end.

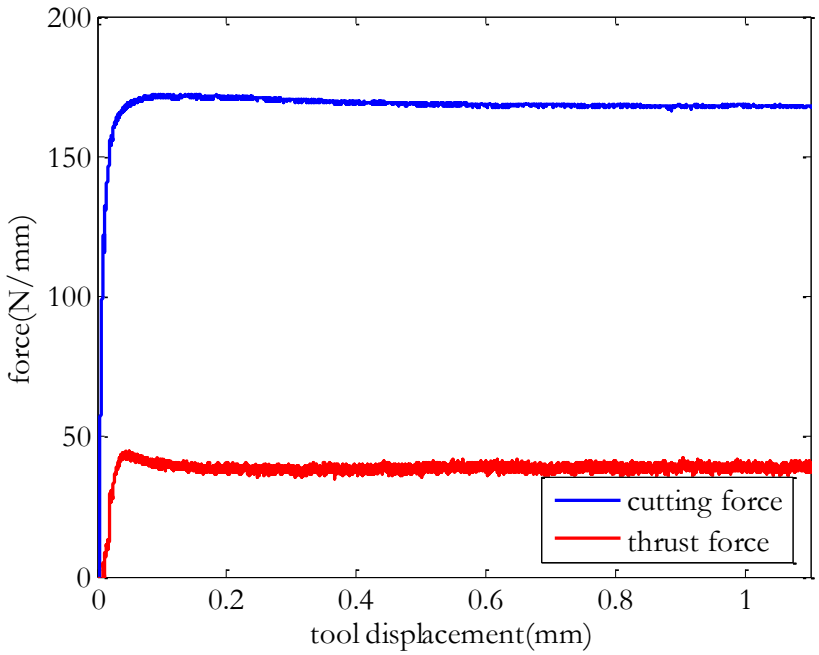

Figure 43. Cutting and thrust force vs. tool displacement for a rate dependent Johnson Cook hardening law and a rake angle of 6º

The largest accumulated plastic strains occur within the boundary layer adjacent to the tool. In this region, the flow of the material is facilitated by thermal softening and the plastic strains attain values up to 4. Strains in the chip interior remains within 1-1.5 range upon exit from the primary shear zone. Figure 43 shows the horizontal and vertical predicted cutting forces. It is found that horizontal cutting force rise quickly to a value of 170N per mm of width of cut within a short distance of 0.05mm. Then as the chip thickness and cutting temperatures in the deforming zone stabilize, the horizontal cutting force holds to a constant value of 170N/mm. The steady state vertical force component, also known as thrust force was found to average around 42 N per mm width of cut. The contact length between the tool and the workpiece, the deformed chip thickness and the shear angle are 0.15 mm, 0.16 mm and 30º.

For a tool rake angle of 0º, deformation is largely confined to the primary shear zone and to the boundary layer adjacent to the tool (Figure 44). No shear localization occurs and a continuous chip formation is predicted. The maximum number of particles is near 3325. A typical distribution of temperature field within the workmaterial is shown in Figure 44. Highest temperatures are observed on the outside surface of the chip currently in contact with the rake face. Temperature in the direction of the shear plane is found to vary from high

of about 790 K near the cutting edge to about 510K near the unmachined free surface. Also temperature along the rake face changes from 790K near the cutting edge to 760K at the point where the contact between the tool and the chip come to an end.

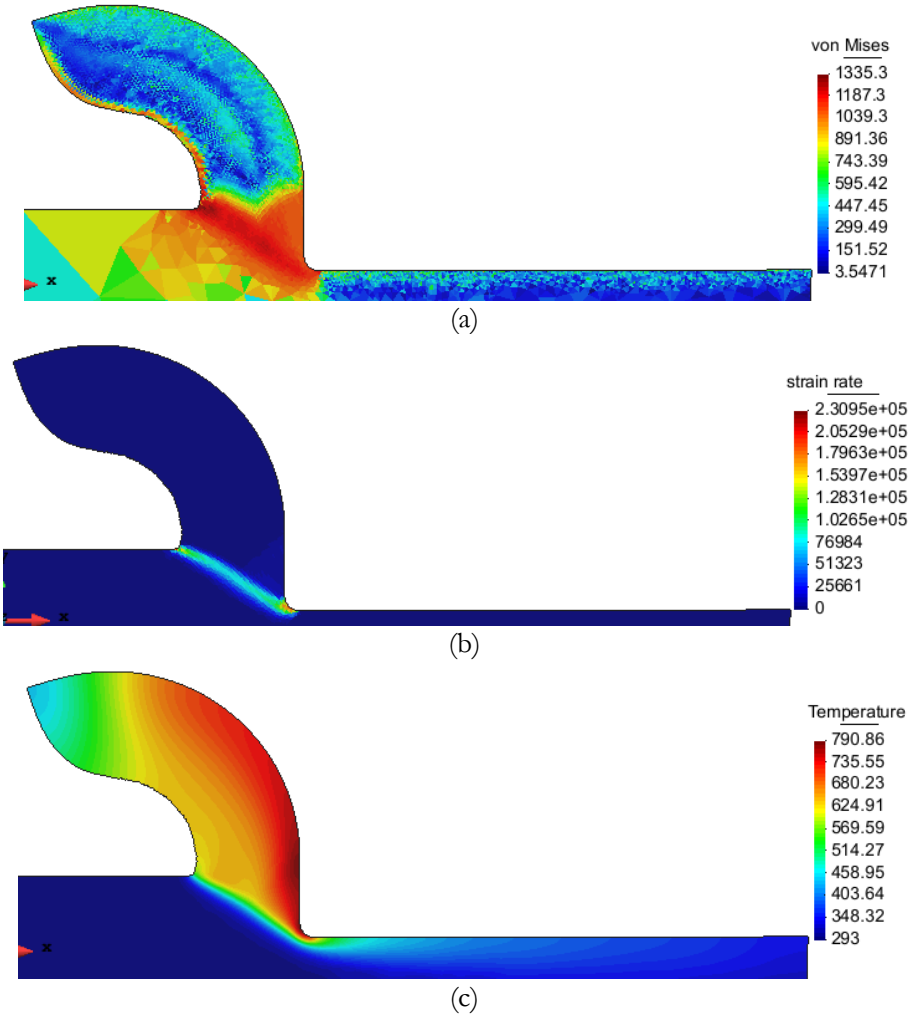

Figure 44. Continuous chip formation using the rate dependent Johnson Cook hardening law and a rake angle of 0º : (a) von Mises (MPa) ; (B) strain rate(1/s); (c) temperature(K)

The largest accumulated plastic strains occur within the boundary layer adjacent to the tool. In this region, the flow of the material is facilitated by thermal softening and the plastic strains attain values up to 3,5 . Strains in the chip interior remains within 1-2 range upon exit from the primary shear zone. Figure 45 shows the horizontal and vertical predicted cutting forces. It is found that horizontal cutting force rise quickly to a value of 180N per mm of width of cut

within a short distance of 0.05mm. Then as the chip thickness and cutting temperatures in the deforming zone stabilize, the horizontal cutting force held to a constant value of 180N/mm. The steady state vertical force component, also known as thrust force was found to average around 50 N per mm width of cut. The contact length between the tool and the workpiece, the deformed chip thickness and the shear angle are 0.16 mm, 0.167 mm and 28º.

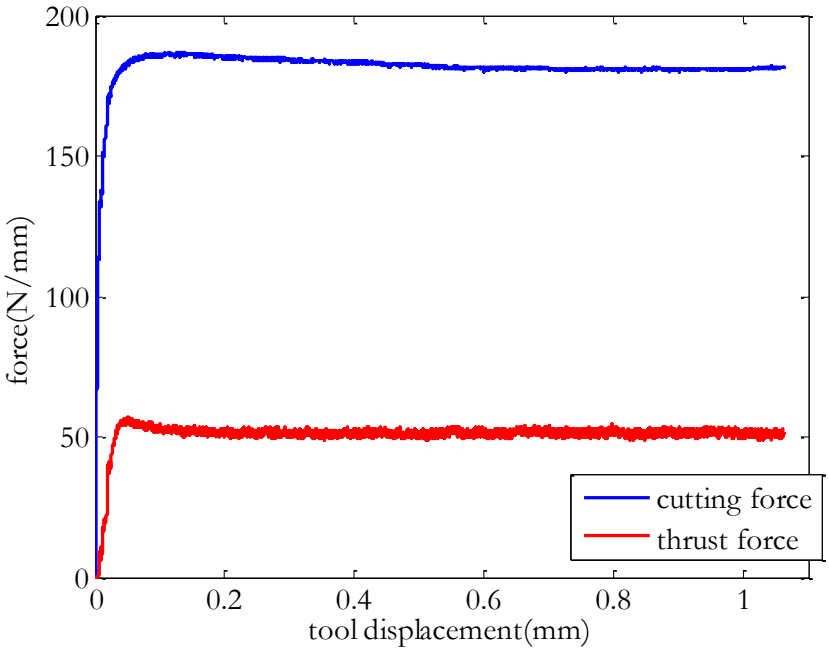

Figure 45. Cutting and thrust force vs. cutting tool displacement for a rate dependent Johnson Cook hardening law and a rake angle of 0º

A comparison of the predicted cutting and thrust forces for two different rake angles (0º and 6º) shows that an increase in rake angle implies a decrease in forces, due to thermal softening phenomena is more localized when the rake angle is increased. Furthermore, with a rake angle of the 6º the contact length is reduced and the shear angle is increased due to the faster curling of the chip. Finally, the deformed chip thickness is reduced due to an increase in the rake angle.

3.6 Implicit, IMPLEX or explicit time integration schemes in the numerical simulation of metal cutting processes?

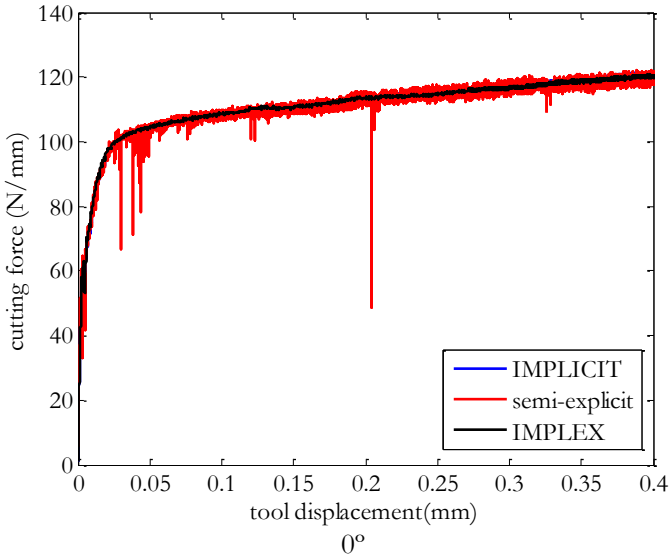

0°

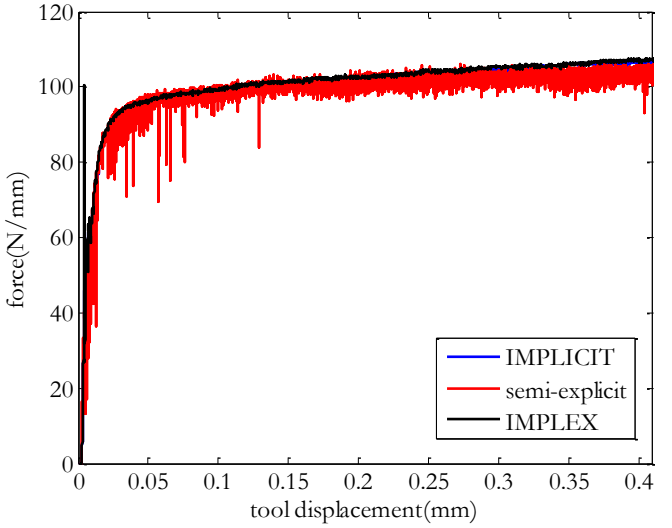

6°

Figure 46. Predicted cutting forces using implicit, semi-explicit and IMPLEX time integration schemes for different rake angles (Simo yield function)

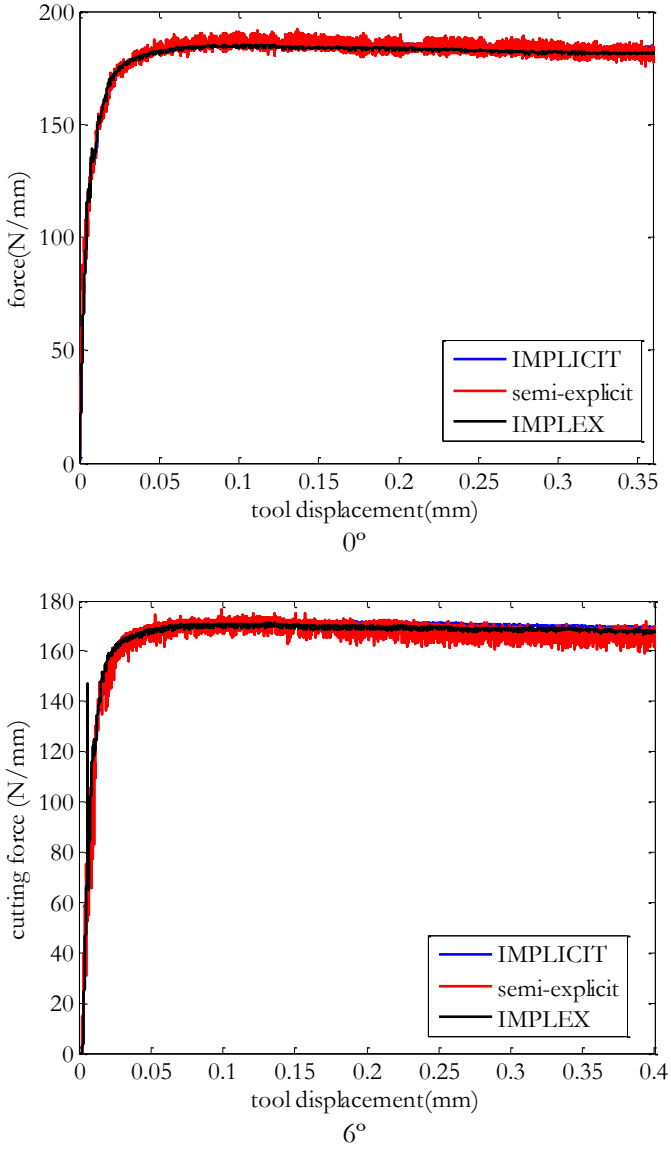

Figure 47. Predicted cutting forces using implicit, semi-explicit and IMPLEX time integration schemes for different rake angles (Johnson Cook yield function)

As one of the main objectives of this work is decrease the computing time that is necessary to carry out the numerical simulation of a typical orthogonal cutting tests. We present here a comparison of an implicit, *IMPLEX* and semi-explicit time integration schemes in terms of predicted cutting forces and computing time. The proposed test is the same presented in section 3.4-3.5 for AISI 4340

steel and for common steel with the yield function proposed by Simo. Cutting speed, undeformed chip thickness, rake and release angles and material properties are the same as used in section 3.4-3.5.

	Rake angle	Time integration scheme	Computing time (hours)	Time increments	Tool displacement (mm)	Max number of particles
AISI 4340	**6º**	Semi-explicit	45	1024000	0,41	3555
		Implicit	5,5	10000	0,41	3305
		IMPLEX	3,75	100000	0,41	3532
	0	Semi-explicit	39,5	960000	0,41	3545
		Implicit	5,17	10000	0,41	3325
		IMPLEX	3,5	100000	0,41	3488
Simo	**6º**	Semi-explicit	47	1090000	0,41	3679
		Implicit	6,15	10000	0,41	3325
		IMPLEX	3,8	100000	0,41	3476
	0	Semi-explicit	44	980000	0,41	3778
		Implicit	5,5	10000	0,41	3224
		IMPLEX	4	100000	0,41	3541

Table 9. Numerical simulations of orthogonal cutting processes using implicit, IMPLEX and explicit time integrations schemes: Computing time

The following assumptions are made: First, the tool is supposed to be rigid and friction is neglected. Furthermore, the thermal exchange between the part and the tool are also neglected. The inertia of the part is neglected in implicit dynamics and the *IMPLEX* approaches.

In case of *semi-explicit* dynamics, time steps were on the order of 3×10^{-10} which necessitates of 1×10^{6} steps and in case of *implicit and IMPLEX schemes*, time steps were of 1.25×10^{-8} which necessitates of 1×10^{4} steps for a tool travel of 0.4mm.

Figure 46 and Figure 47 allow us to remark the following topics about the time integrations schemes:

- Predicted cutting forces using *implicit* time integration schemes have less noise than *IMPLEX and semi-explicit* numerical schemes. This characteristic represents one of the advantages of implicit time integrations schemes over other schemes usually reported in the literature.
- Horizontal and vertical cutting forces predicted for both schemes are qualitatively similar, although in *implicit and IMPLEX* scheme we neglect inertial forces. We can conclude that in proposed cutting conditions inertial terms are negligible.

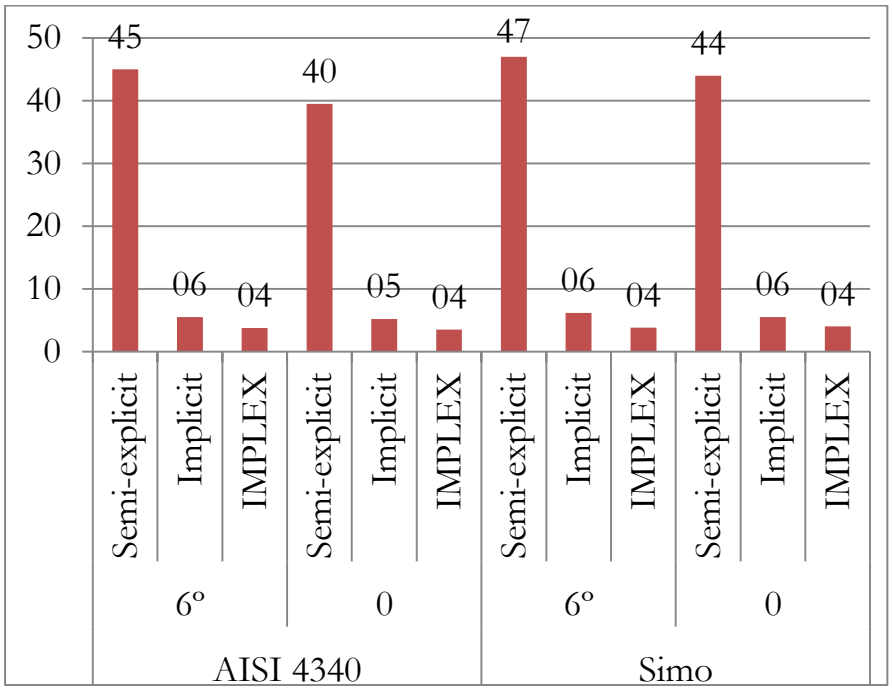

Figure 48. Numerical simulations of orthogonal cutting processes using implicit, IMPLEX and explicit time integrations schemes: Computing time

- The noise in *implicit* predicted forces is due to spatial discretization and reconnection and data transfer of historical variables.

In Table 9 and Figure 48, we can observe the computing time to predict the chip formation process in an orthogonal cutting test using each of the time integration schemes presented in this work. More or less as Table 9 shows, an implicit scheme needs more or less 7.8 times less calculation time than a semi-explicit scheme for a tool displacement of 0.41 mm and the *IMPLEX* scheme needs 11.5 times less computing than a semi-explicit scheme. An addition of particles and a reconnection of them is done each 50 increments in *implicit* and *IMPLEX* schemes and each 6.25×10^{-7} in semi-explicit scheme, as a consequence at the end of the simulation all schemes will had more or less the same number of particles. Due to this reason, the comparison of both schemes does not depend on the number of particles.

It is important to remark that the I*MPLEX* and the implicit scheme will be more efficient in terms of computing time than the explicit schemes at low cutting speeds as the results presented in this work shown, but, as the cutting speed is increased the efficiency decrease up to the point in which explicit schemes are more efficient than the other schemes presented in Chapter 2. In conclusion, the

most appropriate integration scheme should be selected according to the cutting conditions of interest.
IMPLEX integration scheme represents a major step towards the standardization of numerical methods as design tools in the metal machining industry, because the calculation time is a factor that makes unreachable its use.

3.7 Machining a titanium alloy (Ti6Al4V) at different cutting speeds. The effect on cutting forces and chip shapes

Physical parameters	
Density	4420 kg/m^3
Elastic parameters	
Poisson	0,3
Elastic modulus	105GPa
Thermal Parameters	
Heat Conductivity at 20ºC	6,785 N/sK
Heat Conductivity at 1185ºC	24,375 N/sK
Heat Capacity at 20ºC	0,49e9mm^2/s^{2}K
Heat Capacity at 1185ºC	0,756e9mm2/s2K
Inelastic parameters	
Material Constant C	0,302
Material Constant K_0	2260 MPa
Material Constant n_0	0,339
Material Constant T_{mt}	825K
Material Constant m	2

Table 10. Thermo-mechanical and material parameters for Ti6Al4V

The third application concerns the cutting of a rectangular block of Ti6Al4V alloy of length 200 μm and width 60 μm, a cutting depth of 35 μm, a rake angle of 0º and a tool radius of 2μm. The cutting speed has been varied between 0.1 a 20 m/s. Material behavior is given by a modified Johnson-Cook law (Bäker law) with the materials properties shown in Table 10. The conductivity and specific heat depend linearly in the temperature. The tool has been assumed to be mechanically rigid, the friction and the thermal exchange between the workpiece and the tool are neglected. The solution scheme used in the present example is based on the isothermal implicit scheme and the remeshing is based on the particle finite element method (PFEM) presented in chapter 2. Insertion and remotion of particles is used in this example to save computing time and in order to improve the localization phenomenon. Material separation in front of

the tool has been modeled by considering the chip formation process as a pure deformation where material flows visco-plastically around the tool tip. An additional tool is used in order to avoid chip penetration in the workpiece. A total of 4000 time steps were needed in order to calculate any of the chips shown in Figure 49, Figure 50 and Figure 51, the standard computing time was 2.5 to 9 hours on a computer running with the processor Intel ® Core ™ 2 Duo @ 2.53 Ghz. The example presented in this section has been taken from Bäker [109] and De Micheli [52].

An especially appealing feature of high-speed cutting processes is that the specific cutting force for most materials strongly decreases with increasing the cutting speed.

The frequently observed transition between continuous and segmented chip is reproduced by the model Figure 49, Figure 50, Figure 51 show the temperature field for seven different values of cutting speed. At small cutting speed, continuous chip are formed with increasing the shear angle. Chip segmentation is observed at cutting speeds higher than 5m/s and the segmentation increases with increasing the cutting speed.

Plots of the cutting force are shown in Figure 52 and Figure 53. The plots are distance-resolved, in such a way that results for different cutting speeds are comparable. For continuous chip, the cutting force tends to a constant value, whereas, for segmented chip, the cutting force oscillates around a mean value. The observed decrease in the cutting force at high cutting speed can be thus explained as follows: increasing the cutting speed causes an increase in the temperature. Although the strain rate increases, causes a larger isothermal flow stress, the temperature increase leads to thermal softening, so that the mean flow stress is reduced. In conclusion, the simulations show a strong decrease of the cutting force with increasing cutting speed is mainly a result of thermal softening which changes the effective stress-strain curve and increase the shear angle. Figure 49, Figure 50 and Figure 51 show another interesting phenomenon: the width of the shear zone in the continuous chip becomes smaller with increasing the cutting speed. As the increasing temperature cause a decrease in hardening, the width of the shear zone becomes smaller so that strain rates becomes larger.

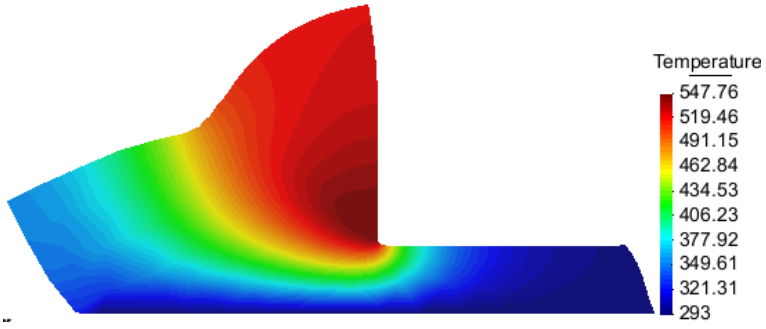

0.1 m/s

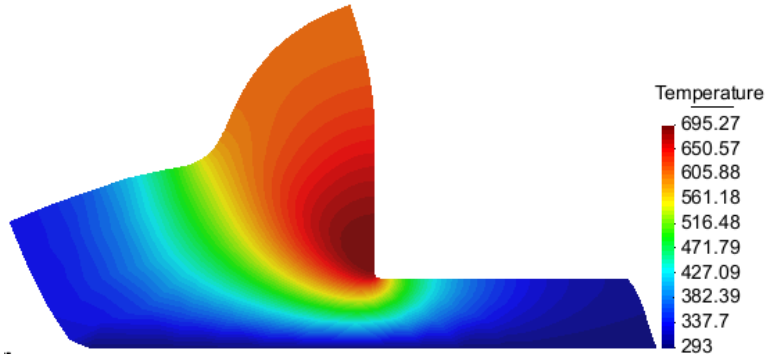

0.2m/s

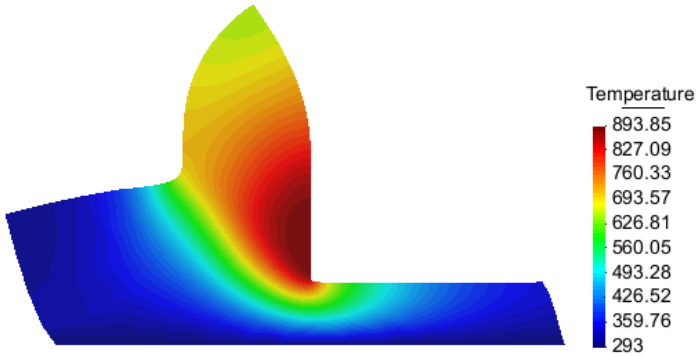

0.5 m/s

Figure 49.Comparison of chip morphologies of TiASl4V at different cutting speeds

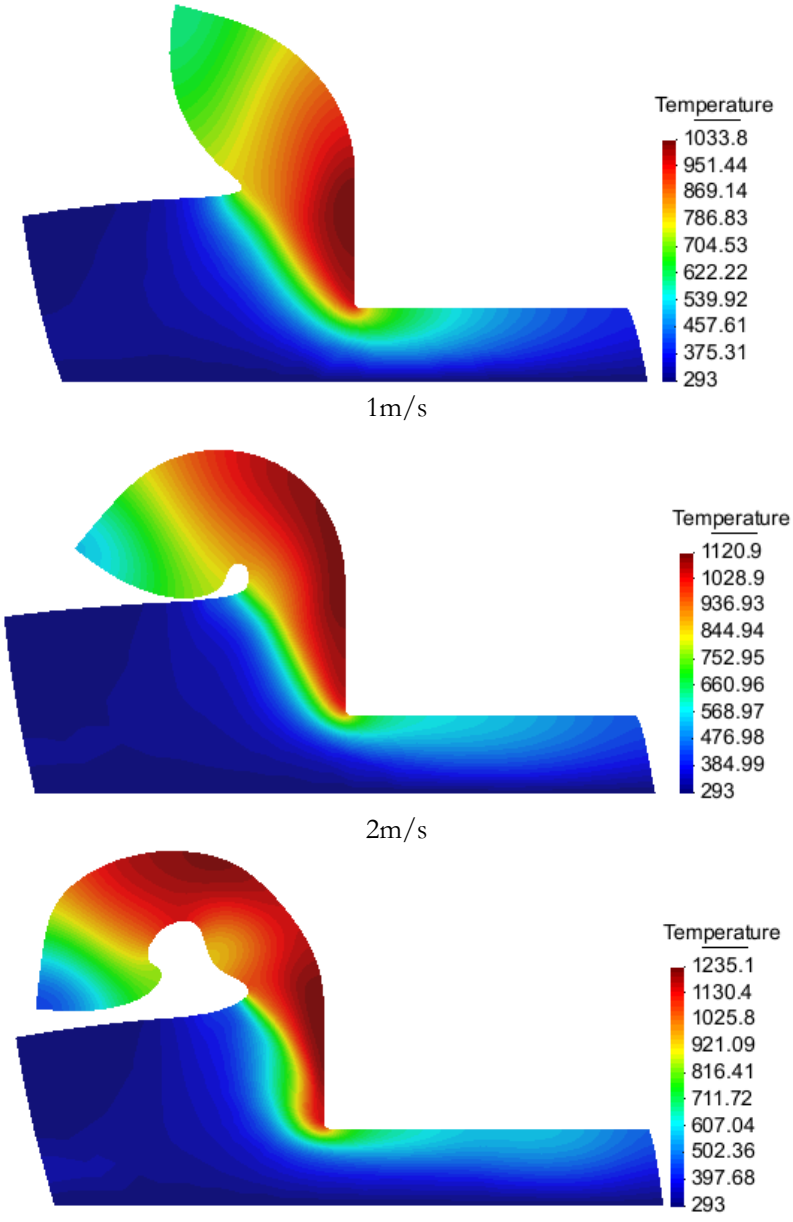

Figure 50.Comparison of chip morphologies of TiASl4V at different cutting speeds

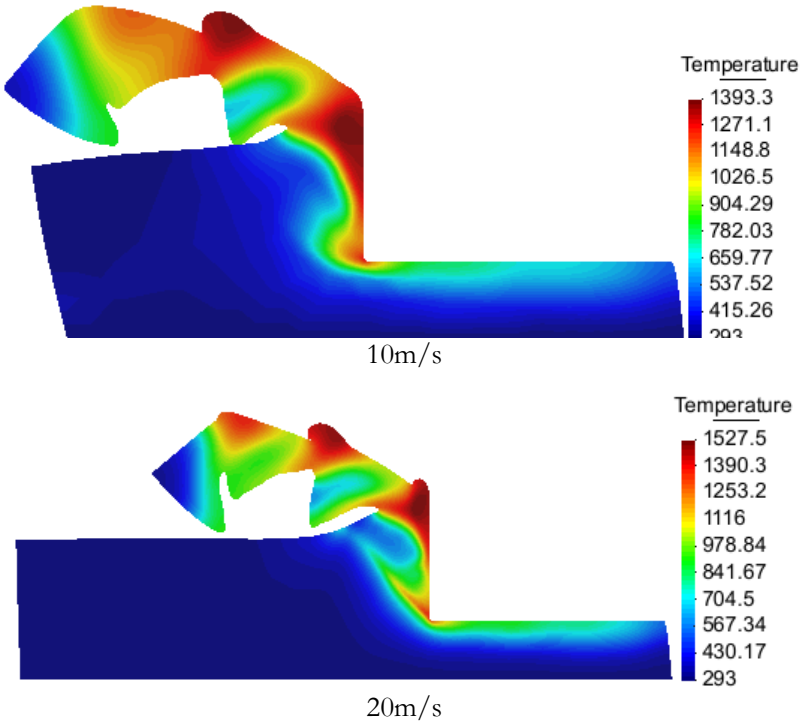

Figure 51. .Comparison of chip morphologies of TiASl4V at different cutting speeds

Adiabatic shear band formation process

In Figure 54**,** we can observe in details the chip formation of an adiabatic shear band in our simulation at 20m/s. Figure 54 shows the von Mises stress inside a forming segment. Subfigure (a) shows a state where one shear band is nearly fully developed and deformation occurs mainly along this strongly curved band. In subfigure (b) deformation occurs in this band, but there is also some deformation in the region behind this shear band, leading to a damming of the material. Deformation concentration begins at the tool tip, but subfigure (c) shows that a second deformation concentration starts at the free surface before the shear band is fully formed. The cutting force increase during the first stages and reaches a maximum during this phase because the newly forming shear band. Although the deformation concentrates during the stage of subfigures (c) and (d), this is not shear localization on the usual sense as the plots of the von Mises stress show. During this face, the von Mises stress inside the zone where deformation concentrates is larger than in the adjacent zones, mainly due to the higher strains rates in this region. In stage (e), true strain localization has begun near the tool tip as the von Mises stress is strongly reduced there. This is correlated with a strong increase in the temperature field. This figure also shows

that the zone of deformation concentration at the free surface is not a localized zone as the von Mises stress is larger here than in the adjacent zones.

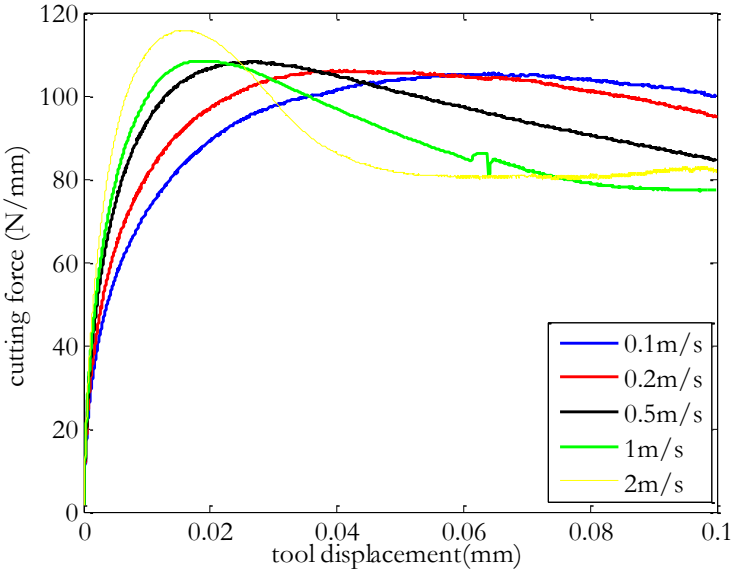

Figure 52. Cutting forces of TiASl4V at different cutting speeds

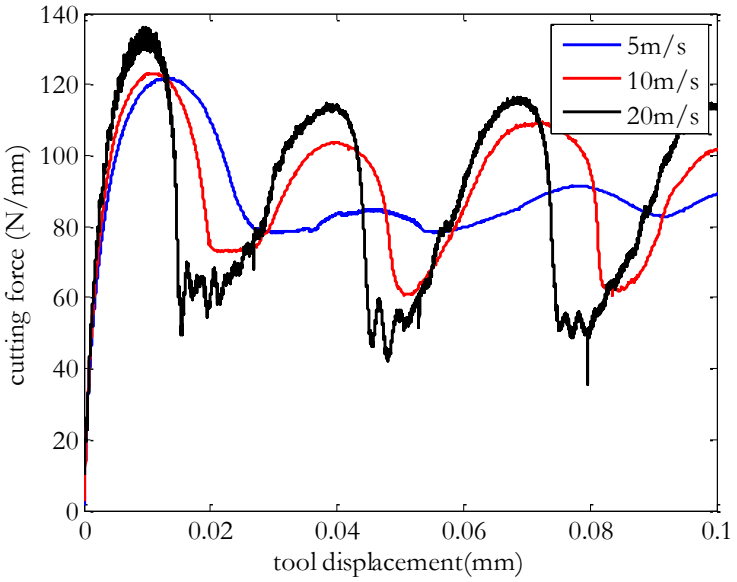

Figure 53. Cutting forces of TiASl4V at different cutting speeds

Therefore, although there are two zones of deformation concentration which afterwards joint, the zone of deformation localization grows continuously from the tool tip. Subsequently localization has started; no further deformation takes place in the dammed region behind the shear band. After deformation localization has set in, the two zones of deformation concentration joint and the deformation strongly localizes inside the shear band (Subfigure (f)).

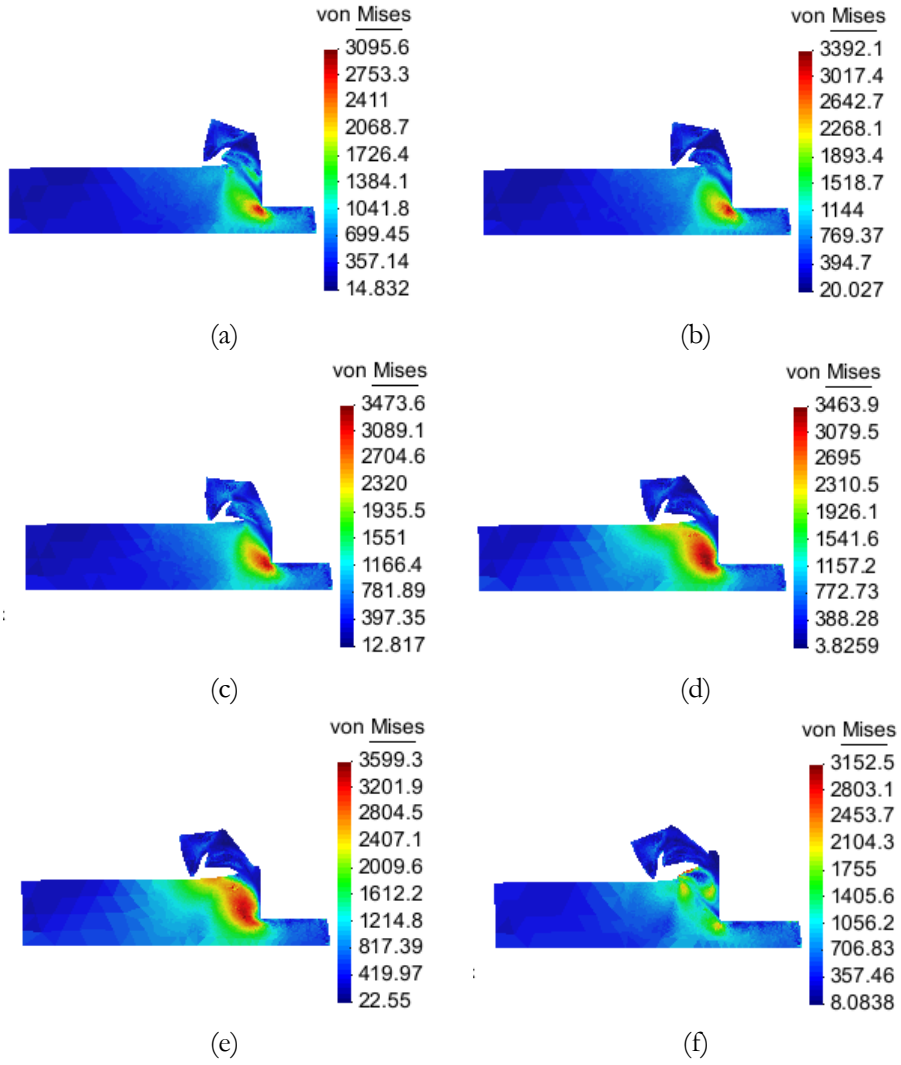

Figure 54. Development of the von Mises stress inside a chip for a cutting speed of 20 m/s

3.8 Orthogonal cutting of AISI 4340 steel using a deformable tool. A frictionless approach

The next example concerns the cutting of a rectangular block of high strength AISI 4340 steel modeled using the Johnson-Cook hardening law with the tool considered as a deformable body. The friction and the thermal exchange between the workpiece and the tool are neglected. The materials and processes parameters are collected in Table 11. Conductivity and specific heat of the workpiece and the tool does not depend on temperature, we consider them constant. Workpiece dimensions were taken as 3.5mm (length) × 1.25 mm (depth). Cutting speed was 3.33 m/s and the deep of cut was 0.1 mm. Cutting tool geometry was as follows

$$\begin{aligned} &\text{Rake angle } \alpha = 0^o \quad \text{Relief angle } \beta = 10^o \\ &\text{radius of the cutting edge= } 0.025\text{mm} \end{aligned} \tag{2.252}$$

Each time increment was designed to correspond to a tool travel of 5.5556e-05 mm. Simulation was continued until the chip comes into contact with the tool. Actually a tool travel of 1.11 mm was covered in 20000 implicit increments.

Tool	
Elastic Modulus	540000 MPa
Poisson	0,22
Workpiece	
Elastic Modulus	200500 MPa
Poisson	0,3
Material Constant A	792MPa
Material Constant B	510 MPa
Material Constant C	0,0014
Material Constant n	0,26
Material Constant m	1,03
Heat Conductivity	50 N/sK
Heat Capacity	0,49e9mm^2/s^{2}K
Thermal expansion	1e-5 (1/K)
Density	7844 Kg/m^3

Table 11. Mechanical and thermal properties of AISI 4340 steel

Figure 55 shows the contours of equivalent strain rate and the contours of equivalent stress. It is observed that the maximum values of equivalent strain rate and von Misses occur near the cutting edge and are of the order of 250000 and 1080 MPa.

In Figure 55 a comparison between the predicted forces using a deformable and a rigid tool is shown, it can be observed that the obtained cutting force is slightly

lower and the feed force slightly higher using a deformable tool, due to the change in the local cutting edge geometry.

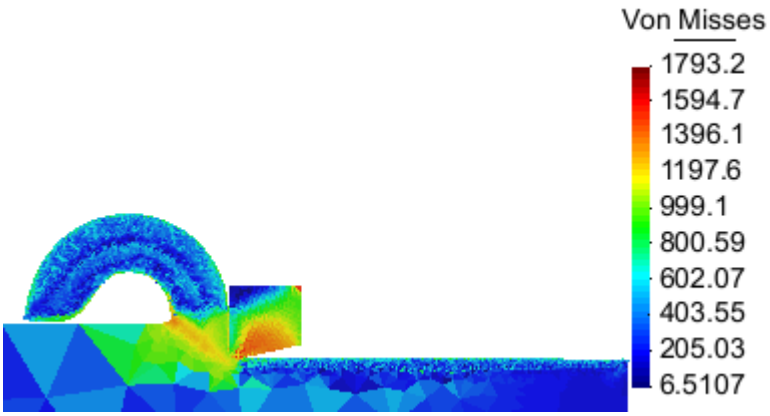

von Mises (MPa)

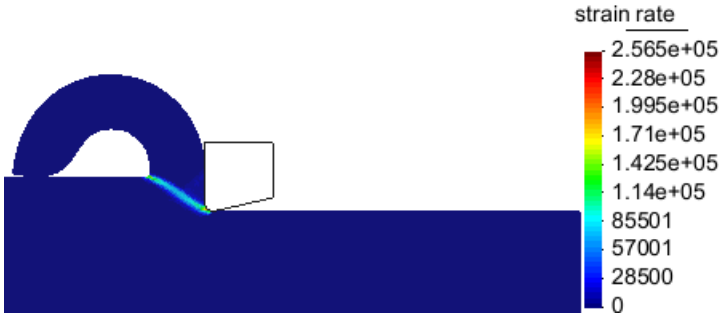

Equivalent strain rate (1/s)

Figure 55. Mises equivalent stress and equivalent strain field using a deformable tool. A frictionless approach

The contact length between the tool and the workpiece, the deformed chip thickness and the shear angle are 0.16 mm, 0.14 mm and 30º.

3.9 Orthogonal cutting of AISI 4340 steel using a deformable tool: Heat transfer and friction between the tool and the workpiece

Orthogonal dry machining of AISI 4340 steel by a high strength steel tool has been simulated, at cutting speed of 3.33 m/s, at a feed of 0.1 mm, a rake angle of 0° and a clearance angle of 10º. The friction at the tool-chip interface is modeled using the Norton-Hoff friction law presented in chapter 2 with frictional properties $\mu_r = 9 \times 10^{-5}$ and $\alpha = 1$ .The mechanical and thermal properties of the workpiece and the tool are the same used in section 3.8.

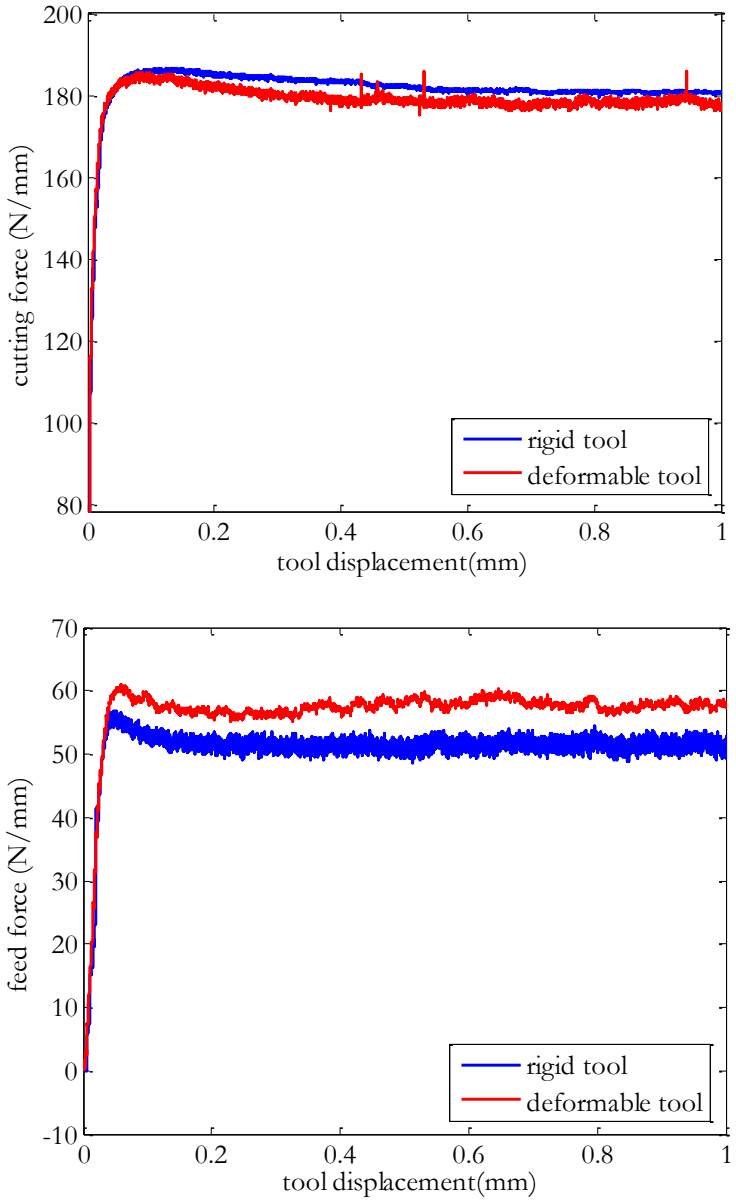

Figure 56. Cutting and feed forces. A rigid vs. a deformable tool.

The thermal properties of the tool are supposed to be matched to those of the workpiece, giving an equal portion of frictional heat allowed to the tool and the chip. The thermal conductance coefficient h used was 10^9 W/(m^{2}K), in order to ensure that the thermal gap at the tool-chip interface will be negligible.

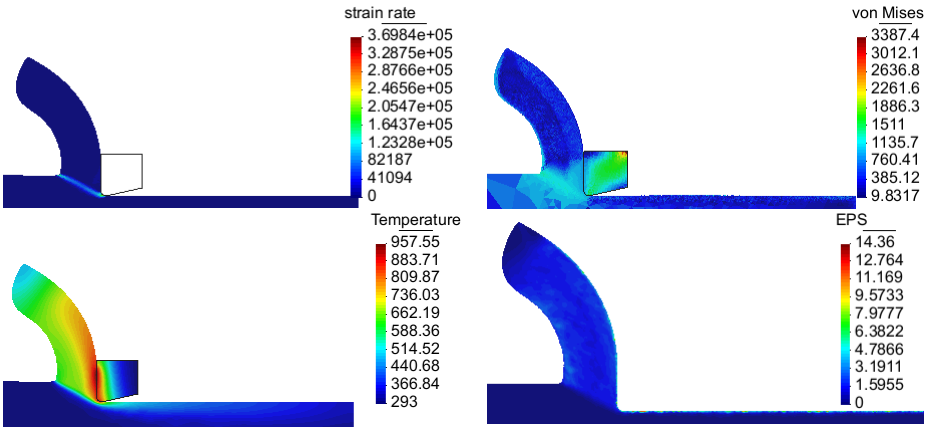

Figure 57. Continuous chip formation: Deformable tool, and friction and heat transfer at the tool chip interface

Figure 57 (a) shows the calculated distributions of strain rate. Deformation is concentrated, as expected, near the shear plane and along the rake face. The strain rate reaches 350000 (1/s) in front of the cutting edge.
Figure 57(b) shows the temperature fields in the tool and the workpiece. The maximum temperature is 958 K and takes places along the rake face. Figure 57(c) shows the plastic-strain distribution, extremely high values, close to 14, are found. Figure 57 (d) shows the von Mises stress distribution, the maximum stress appears in the tool, close to the cutting edge. In the workpiece, the magnitude of the stress rises in the deformation zone because of work hardening, but it is limited to 1250 MPa by thermal softening.
The contact length between the tool and the workpiece, the deformed chip thickness and the shear angle are 0.19 mm, 0.18 mm and 29º.
A comparison with the frictionless case of section 3.8 is presented in Figure 58. This comparison shows that the cutting force increases 65N/mm while the thrust force increases 35N/mm. Similarly, the contact length and the undeformed chip thickness increase with friction, because friction hinders the rotational movement of the chip.

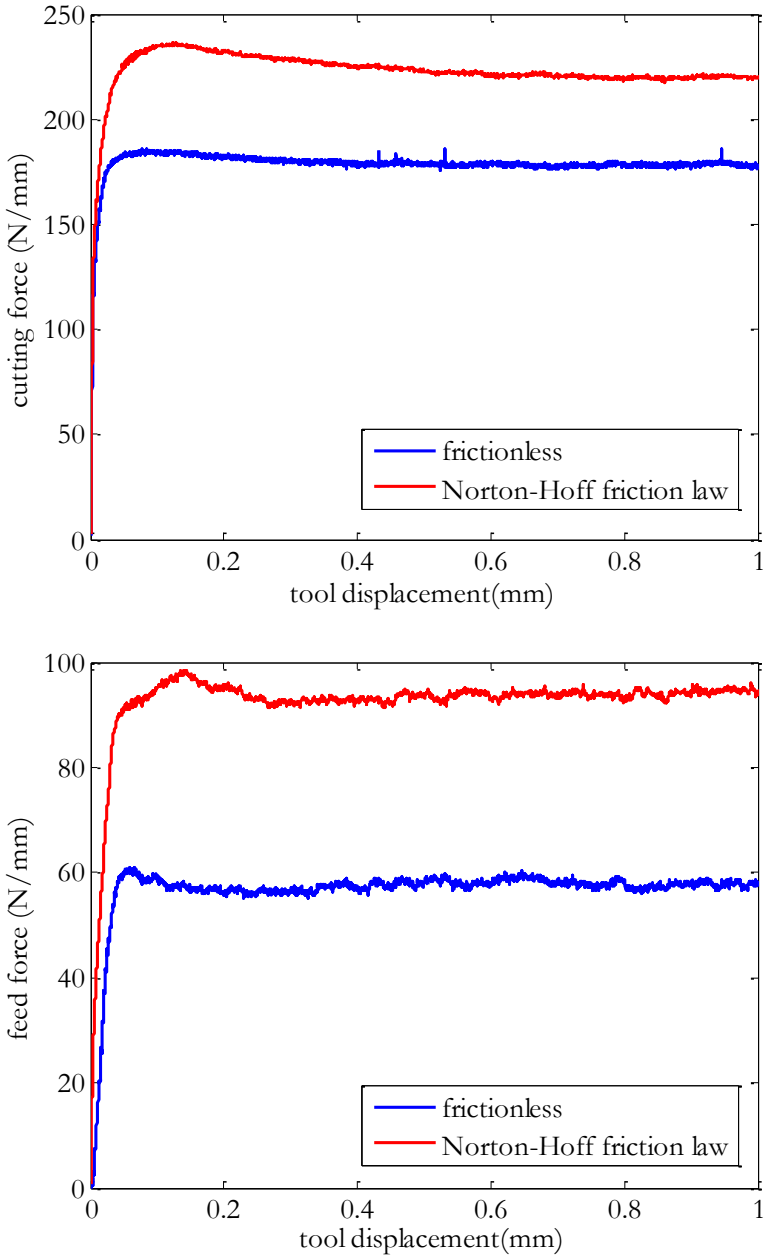

Figure 58. Cutting and thrust forces: Deformable tool, and friction and heat transfer at the tool chip interface

3.10 Orthogonal cutting of 42CD4 steel: An experimental comparison

Material Properties	Conductivity(N/sK)	Workpiece	42,6 at 373K
			42,3 at 473K
			37,7 at 673K
			33,1 at 873K
	Specific Heat(mm2/s2K)	Tool(P10)	25
		Workpiece	473(423K-473K)
		(42CD4)	519(623K-673K)
			561(823K-873K)
		Tool(P10)	200
	Thermal expansion coefficient (1/K)		0 at 293K
			14,5.10-6 at 673K
	Percentage of plastic power into heat		0,9
	Density(Kg/m3)	Workpiece (42CD4)	7800
		Tool(P10)	10600
	Elastic Modulus (Gpa) (42CD4)		210
	Poisson (42CD4)		0,3
	Plasticity	A(MPa)	598
	Johnson-Cook	B(MPa)	768
	Workpiece(42CD4)	C	0,0137
	Tamb = 293K	M	0,807
	Tfus = 1793K	N	0,2092

Contact	Thermal Properties	Thermal Conductance (W/(m2K))	1,00E+08
		Partition coefficient	0,5
	Mechanical Properties	Friction Coefficient	0,23
		Norton Hoff Coefficient	6,00E-05
		Percentage of friction Energy converted into heat	1

Table 12. Mechanical and thermal properties of the workpiece and the tool

In order to validate PFEM strategy, a cutting process of 42CD4 steel at 300m/min, with a tool radius of 0.04 mm, a rake angle of 6º and a cutting depth is proposed. Materials and contact properties used are the same presented in [121]. A summary of all the inputs parameters are found in Table 12 .

The time step used during the simulation was 1.1×10^{-8} seconds, as a result 20000 time steps were needed for a tool displacement of 1mm.

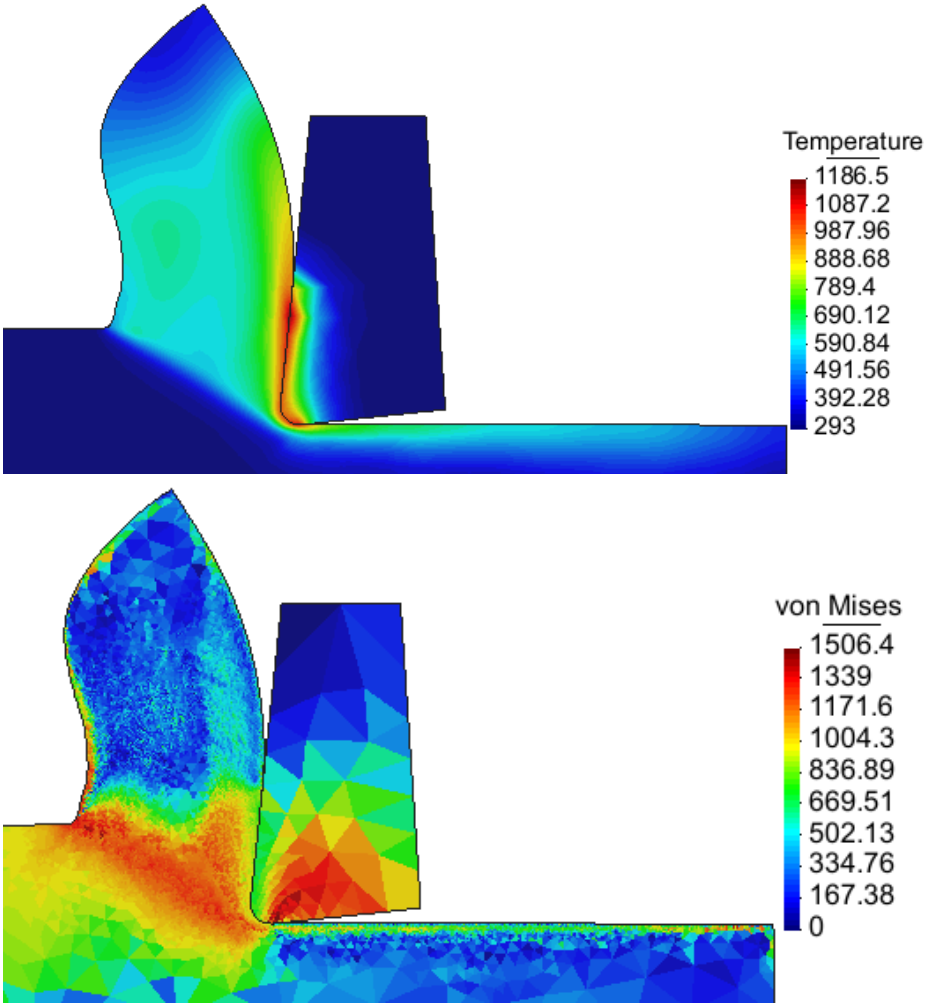

Figure 59. Orthogonal cutting of 42CD4 steel

Figure 59 shows the temperature filed after a cutting length of 1 mm. The maximum tool temperature reached is about 1186K. It is located far from the cutting edge, and approximately at a distance of 1.25 times the undeformed chip thickness. The maximum von Mises stress inside the chip-piece takes place in the

primary shear zone, while the maximum von Mises inside the tool is close to the point where the tool loses the contact with the machined surface.

	h (mm)	t_2 (mm)	F_c (N)	F_f (N)
PFEM	0,26	0,35	383	105
Experimental	0,49	0,32	395	170

Table 13. Experimental and numerical results

Data about experimental results have been obtained from fata reported in the literature[121]. Table 13 compares the numerical and the experimental cutting and feed forces results obtained for the example presented in this section. It is observed a good agreement between the experimental and the numerical cutting forces. Table 13 shows large differences between experimental and numerical feed forces. Regarding the chip thickness a relatively good agreement was found between experiments and numerical simulations. However, the tool-chip contact length measured in the experiments is about two times greater than the length predicted by the numerical simulations.

Chapter 4

4 A Sensibility Analysis to Geometric and Cutting Conditions using the Particle Finite Element Method (PFEM)

The objectives of this chapter are mainly three: The first one is to validate PFEM strategies as an efficient tool for numerical simulation of metal cutting processes by a detailed comparison (forces, stresses, strains, temperature, etc.) with results provided by commercial finite element software (Abaqus, AdvantEdge, Deform) and experimental results. The second is to carry out a sensibility analysis to geometric and cutting conditions using PFEM by means of a Design of Experiments (DoE) methodology. And the third one is to identify the advantages and drawbacks of PFEM over FEM and meshless strategies.

Also, this chapter presents some advantages of PFEM that directly apply to the numerical simulation of machining processes: (i) allows the separation of chip and workpiece without using a physical or geometrical criterion (ii) presents negligible numerical diffusion of state variables due to continuous triangulation, (iii) is an efficient numerical scheme in comparison with FEM.

The results presented in this chapter were carried out during the research stay at Mondragón University under the supervision of Professor Pedro Arrazola.

Before starting with the PFEM validation, in the next section, we will introduce the theory of design of experiments.

4.1 Design of Experiments (DoE)

Assume that a certain parameter (response variable) depends on several independent variables. In order to study the effect of the variables on the parameter, one has to generate data either from experiments or from numerical simulation. An efficient way of studying this effect is through a proper design of experiments (DoE). The main objective of the design of experiments is to obtain a large amount of information with a limited number of experiments.

The traditional method of experimentation is the 'one factor at a time' method. In this method, only one of several variables is changed at a time, keeping all other independent variables constant at some values. Although this approach is simple and one gets inference before all experiments are finished, it does not reveal the effect of interaction among variables. Most of the time, the effect of one variable on the dependent parameter may be strongly influenced by the value of other independent variables. This is called the interaction effect, which cannot be estimated properly in the 'one factor at a time' method. Therefore, the traditional method is considered an inefficient and costly approach.

In the full factorial method of experimentation, each independent variable (factor) is divided into different levels. In some cases the variables take only

discrete values and they need not be numbers *e.g.*, presence or absence of a lubricant in metal forming. One can decide to divide the range into three or more levels if more number of experiments can be conducted. Once all the factors have been divided into a number of levels, all possible combinations of levels are considered.

Total number of combinations of factors is dependent on the number of factors and the levels, as follows $\#\text{experiments} = \#\text{levels}^{\#\text{factors}}$. For example, if there are 7 factors at 2 levels, total combinations would be $2^7 = 128$. Hence, in full factorial method, one would need to do 128 experiments. If the variables are divided into 3 levels, total combinations will be $3^7 = 2187$, an enormously high number. Thus, many times, full factorial design is not reasonable and the fractional factorial method is to be used.

To give an example, first consider the full factorial design for three factors at two levels. The first level is represented by –1 and the second level by +1. The 2^3 factorial design is shown in Table 14 . In this table, column AxB indicates the interaction effect of factor AxB. The level +1 indicates that both A and B are at the same level and – 1 indicates that both are at different levels. Similarly, AxBxC is the column of interaction of three factors.

Experiment	A	B	C	AxB	BxC	CxA	AxBxC
1	-1	-1	-1	+1	+1	+1	-1
2	-1	-1	+1	+1	-1	-1	+1
3	-1	+1	-1	-1	-1	+1	+1
4	-1	+1	+1	-1	+1	+1	-1
5	+1	-1	-1	-1	+1	-1	+1
6	+1	-1	+1	-1	-1	+1	-1
7	+1	+1	-1	+1	-1	-1	-1
8	+1	+1	+1	+1	+1	+1	+1

Table 14. A full factorial design for three factors at two levels.

With a design of experiments, one can find the main and interaction effects of a factor. The main effect indicates the individual contribution of the factors to the total variability inherent in the experimental results. For a two level factor, the main effect is obtained as

$$\text{Effect of factor} = \frac{\sum_{i=1}^{\#\text{experiments}} X_i \times level_i}{\frac{\#\text{experiments}}{2}} \tag{4.1}$$

where X_i is the value of the dependent variable in each of the experiments and the variable $level_i$ takes the values $-1/+1$ depending if X_i is a response at level1/level 2 of the factor.

Apart from the main effects, one might need to know the effect of interaction. This effect is found in a similar manner. In the orthogonal array, we can make the columns corresponding to interaction of two variables and then treat that

column as corresponding to a separate factor. For example, in Table 14, AxB, BxC, CxA and AxBxC are treated like factors with levels +1 and –1 for finding out its effect.

Usually, the design of experiments is used to study how some variables like the cutting speed, the feed and the cutting depth influence the lifetime of the tool. For knowing the tool life in the machining, we propose a DoE with three factors (cutting speed, the cutting depth and the feed) at two levels. For each factor, one level corresponds to the low values and the other level corresponds to the high values. Table 15 presents the tool life of a TiN coated carbide tool cutting a medium carbon steel at different cutting parameters.

Experiment	Cutting speed(m/min)	Feed (mm/rev)	Cutting depth(mm)	Tool life(min)
1	135	0.04	0.3	160
2	135	0.04	1.2	120
3	135	0.32	0.3	110
4	135	0.32	1.2	20
5	270	0.04	1.2	60
6	270	0.04	+1	50
7	270	0.32	0.3	7
8	270	0.32	1.2	2

Table 15. A Design of experiments to study the dependence of tool life on cutting parameters[122]

Using equations (4.1) and the data presented in Table 15, the main effects of cutting speed, the feed and the cutting depth are given by

$$\text{Effect of cutting speed} = \frac{60+50+7+2 \;-\; 160+110+110+20}{\frac{8}{2}} = -97.75 \qquad (4.2)$$

$$\text{Effect of feed} = \frac{110+20+7+2 \;-\; 160+120+60+50}{\frac{8}{2}} = -62.75 \qquad (4.3)$$

$$\text{Effect of cutting depth} = \frac{120+20+50+2 \;-\; 160+110+60+7}{\frac{8}{2}} = -36.25 \qquad (4.4)$$

Thus, it is seen that in the given ranges of the process parameters, the cutting speed has the maximum effect on the tool life followed by the feed and depth of cut. The negative value of the parameters indicates that increasing these parameters decreases the tool life.

In the next section, we will present a orthogonal cutting simulation of 42CD4 steel using PFEM, this is the same test presented in section 3.10 of this work.

4.2 Orthogonal cutting simulation of 42CD4 steel using the Particle Finite Element (PFEM)

In order to validate PFEM strategy as an effective strategy to predict chip formation in orthogonal cutting process, in this work a cutting process of 42CD4 steel at 300m/min, with a tool radius of 0.04mm, rake angle of 6° and cutting depth 0.2 mm is proposed.

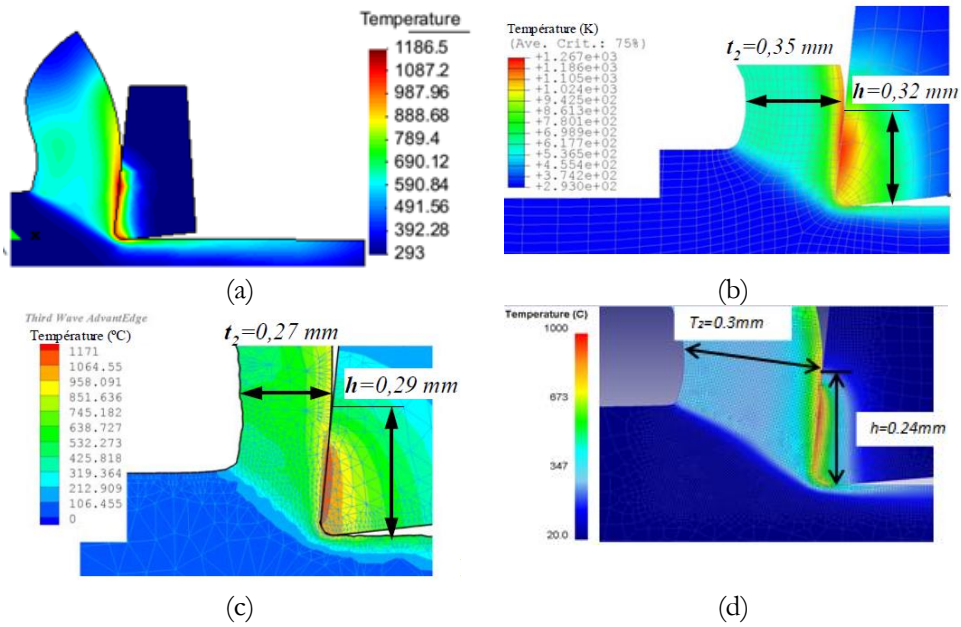

Figure 60. Comparisons of temperature fields given by (a) PFEM, (b) Abaqus, (c) AdvantEdge and (d) Deform.

The workpiece is considered as a deformable body in which the adaptive mesh strategy is based on PFEM. In the workpiece large elastic and plastic strains, heat conduction, and heat generation due to plasticity are considered. The tool is considered as a deformable body in which a standard finite element method is used. Small elastic strain and heat transfer due to conduction takes place inside the tool.

A triangle finite element with linear displacement, pressure and temperature able to deal with the incompressibility constraint imposed by the plastic phenomena was used in the work-piece. In the tool a triangle finite element with linear displacement and temperature was used.

The contact strategy between the tool and the workpiece is a penalty node-to-segment approach. The contact between the tool and the workpiece includes heat transfer due to conduction and friction. Heat transfer due to convection and radiation to the external environment is considered negligible.

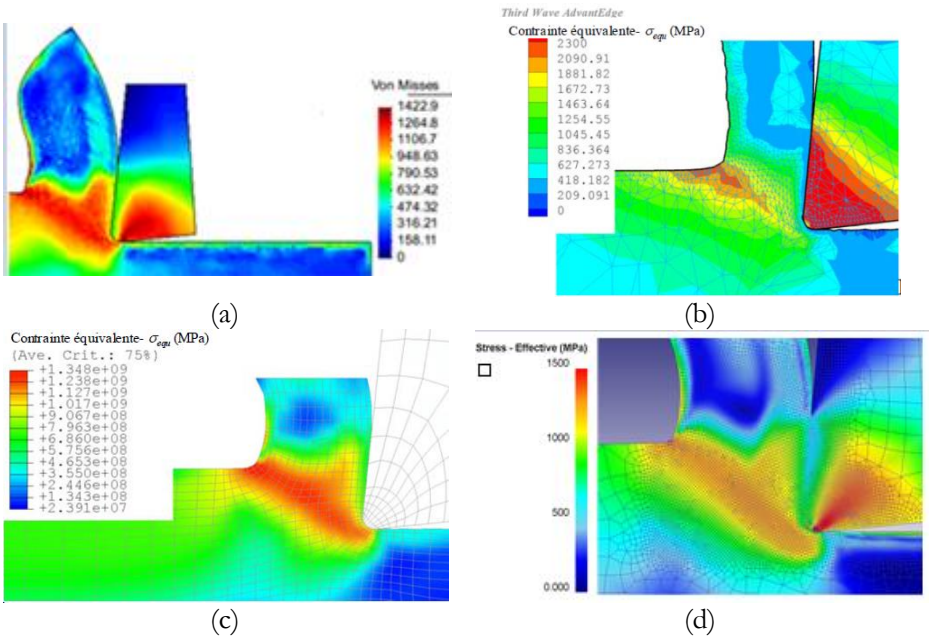

Figure 61. Comparisons of von Mises fields given by (a) PFEM, (b) Abaqus, (c) AdvantEdge and (d) Deform.

The distance between particles in the primary and the secondary shear zones was selected according to information given by finite element errors estimators and on the tool radius size.

Numerical simulation of chip formation requires a thermo-elasto-visco-plastic law for the workpiece material behavior. In this work, the Johnson-Cook yield function is used. This material law is used in materials in which its yield stress depends on its equivalent strain, rate of strain and temperature.

Materials and contact properties used in the numerical simulations are the same used in the example 3.10 presented in chapter 3 of this work.

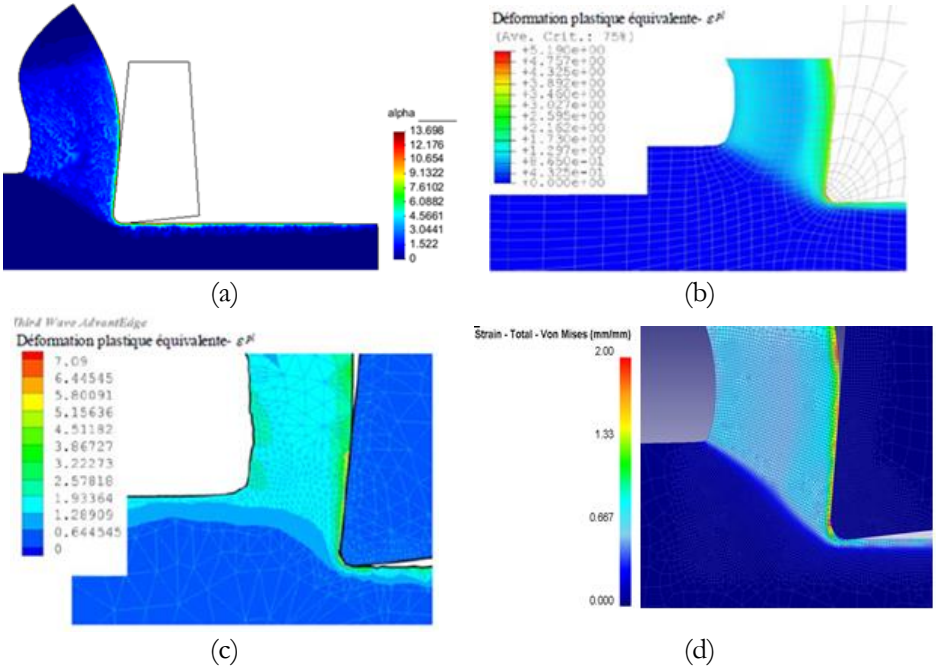

Figure 62. Comparisons of equivalent plastic strain given by (a) PFEM, (b) Abaqus, (c) AdvantEdge and (d) Deform.

As a consequence of the error estimators and the tool radius size, the particle distance in the primary and the secondary shear zone is more or less 3.5 micrometres. Far away from the primary shear zone the maximum particle distance is more or less 0.5 mm. The maximum number of particles used during the simulation was 11386. The number of nodes used in the tool was 116. The time step used during the simulation was constant and of the order of 1.1e-8 seconds, meaning that for a tool displacement of 1 mm at a cutting speed of 300m/min, it needs around 20000 steps. The calculation time was approximately 24 hours in the case of a computer running with 4Gb and the following processor: Intel® Core™ 2 Duo CPU P8700 @2.55GHz.

Figure 60 (a) shows the temperature field over the workpiece, chip and tool and after a cutting length of 1mm. This is 0.2 milliseconds of machining time at the cutting speed of 300 m/min. The maximum tool temperature reached is about 1186K. It is located far from the cutting edge, and approximately at the distance of the 1.25 times the undeformed chip thickness (t1).

Moreover Figure 62 (a) shows the plastic strain field over the workpiece and the chip. The most significant plastic strain occurs over the machined surface and along the surface that is contact with the tool. Along this new surface, the plastic strains reaches a value greater or equal than 10. Also, Figure 61(a) shows von Mises stress field. The maximum von Mises stress, inside the chip-piece takes places in the primary shear zone, while the maximum von Mises stress inside the tool is close to the point where the tool loses the contact with the machined

surface, exactly the point where tool failure takes place in real machining processes. Furthermore, Figure 63 (a) shows the strain rate field inside the workpiece. The maximum value of strain rate is 400000 and takes place inside the primary shear zone. As expected, the strain rate decreases rapidly to a value close to zero in the limits of the primary shear zone. Numerical results shows that in machining, temperatures greater than 1000K, strains greater than 10 and strain rates greater than 105 appear. In order to fit numerical simulations with experimental results of machining process, it is necessary to develop an experimental setup able to characterize workpiece material in extreme conditions that take place in machining processes.

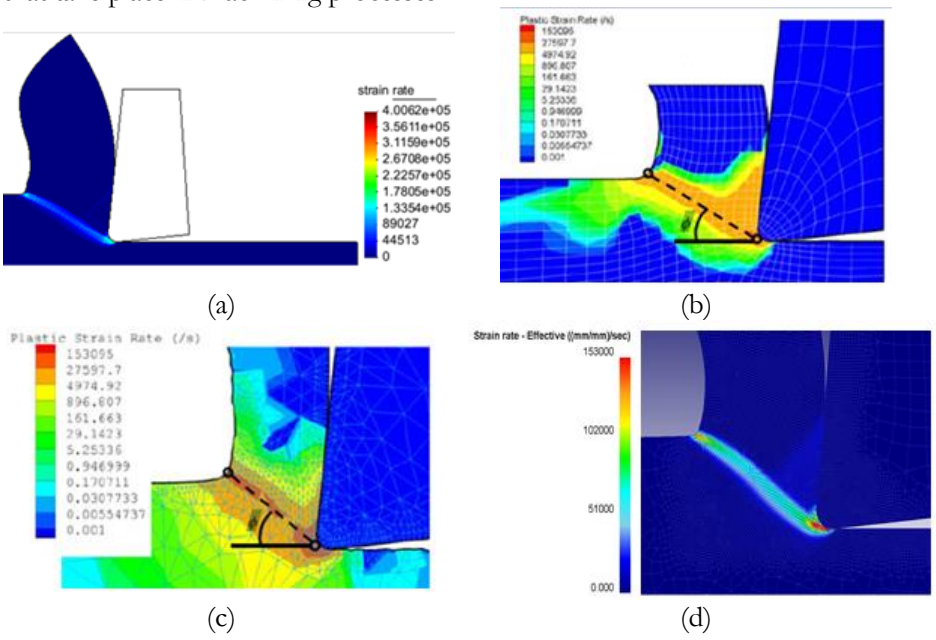

Figure 63. Comparisons of strain rate given by (a) PFEM, (b) Abaqus, (c) AdvantEdge and (d) Deform.

In the next section, we will present a orthogonal cutting simulation of 42CD4 steel using PFEM and a detailed comparison (forces, stresses, strains, temperature, etc.) with results provided by commercial finite element software (Abaqus, AdvantEdge, Deform) and experiments.

4.3 Numerical and Experimental validation of the PFEM strategy

Data about experimental results, specially cut-ting forces, feed forces, chip thickness and tool-chip contact length have been obtained from data reported in the literature [121].

Validation was carried out comparing numerical results with experimental ones and numerical results obtained from the commercial software Abaqus, Deform

and AdvantEdge. It is important to mention, some differences and similarities between the formulations, time integrations schemes, boundary conditions, materials models and contact laws used in each of the numerical simulations:

- PFEM, Deform and Abaqus model use Johnson Cook yield function. (Table 1)
- Abaqus, AdvantEdge and Deform use Coulomb friction law at the tool chip interface, with a friction coefficient of 0.23. (Table 2)
- PFEM and Deform use a Norton-Hoff friction law with a Norton Hoff constant value of 6e-5.
- In AdvantEdge, workpiece material behavior is governed by Marusich law.
- PFEM, Deform and AdvantEdge consider the tool as a deformable (P10) while Abaqus consider the tool as a rigid body.

Furthermore, PFEM, AdvantEdge and Deform use a Lagrangian description of motion while Abaqus uses an Arbitrary Lagragian Eulerian description of motion. Also, PFEM and Deform use implicit time integration while AdvantEdge and Abaqus use explicit time integration.
More information about the constitutive model, boundary conditions used in the numerical models developed in Abaqus and AdvantEdge are explained in detail in [121].

Program	Formulation	Constitutive Model	Friction Model	Processes variables (DoE)
PFEM	Lagrangian	Johnson Cook	Norton-Hoff	1. Temperature(Tool) 2. Contact length 3. Temperature(Chip) 4. Von Mises (Chip) 5. Plastic strain 6. Plastic strain rate 7. Chip thickness 8. Shear angle 9. Cutting force 10. Feed force
Abaqus	ALE	Johnson Cook	Coulomb	
AdvantEdge	Lagrangian	Marusich Law	Coulomb	
Deform	Lagrangian	Johnson Cook	Norton-Hoff	

Table 16. Formulations, constitutive models and friction models used in each of the numerical simulations.

Table 16 presents a summary about the formulations, constitutive models and frictions models used in each of the numerical simulations.

Table 17 compares the numerical and the experimental cutting and feed forces results obtained for the reference cutting test. It is observed a good agreement between the experimental and numerical cutting forces predicted by PFEM, Deform and Abaqus. Instead, comparing experimental cutting forces with AdvantEdge results, higher differences were found.
Table 17 shows the large differences between the experimental and numerical feed forces. AdvantEdge predicts a feed force that is 34% greater, Deform 24% smaller, Abaqus 20% smaller, PFEM 38% smaller than the experimental feed force.
Regarding to the chip thickness (t2) a relatively quite good agreement was found for all the results. However, the tool-chip contact length (h) measured in the experiments is about two times greater than the length predicted by the numerical simulations.

	T (k)	h (mm)	V.M. (MPa)	e ()	t_2 (mm)	F_c (N)	F_f (N)
PFEM	1173	0,26	1400	13	0,35	383	105
Abaqus	1240	0,32	1348	5.2	0,35	412	135
AdvantEdge	1442	0,29	2343	7	0,27	647	228
Deform	1107	0,24	1210	3,57	0,3	365	129
Experimental	-	0,49	-	-	0,32	395	170

Table 17. Experimental and numerical results (PFEM, Abaqus, AdvantEdge, Deform)

Comparing results for the maximum tool temperature it is observed that the larger difference occurs between Deform-AdvantEdge, while the smaller takes place between PFEM and Deform. The differences are due to material model and friction law used in each one of the soft-ware (stated before).
In the case of the von Mises stress the results predicted by PFEM, Deform, Abaqus are really similar, however the maximum von Mises stress predicted by Advantedge is 1000 MPa greater than the average stress predicted by the other software. The differences and similarities among the predicted results are because of those existing ones between PFEM, Abaqus, Deform and AdvantEdge (stated before).
Figure 60, Figure 61, Figure 62 and Figure 63 show a comparison of the temperature field, von Mises stress field, plastic strain field and strain rate field. The temperature fields predicted by PFEM, Abaqus, Deform and Advantedge are similar. The von Mises stresses are similar for PFEM, Deform and Abaqus, while AdvantEdge shows a different field possibly due to the constitutive model used. Plastic strain fields predicted by PFEM, AdvanEdge, Abaqus and Deform are similar; all the numerical simulations show that the most significant plastic strains take place over the machined surface and over the surface that is in contact with the tool.
Thus, the numerical model set up with PFEM is considered to be accurate enough to carry out a sensitivity analysis to process parameters like tool radius, rake angle, cutting velocity and cut-ting depth.

4.4 A Design of Experiments with PFEM and its comparison with a DoE with the commercial software (Abaqus, AdvantEdge and Deform)

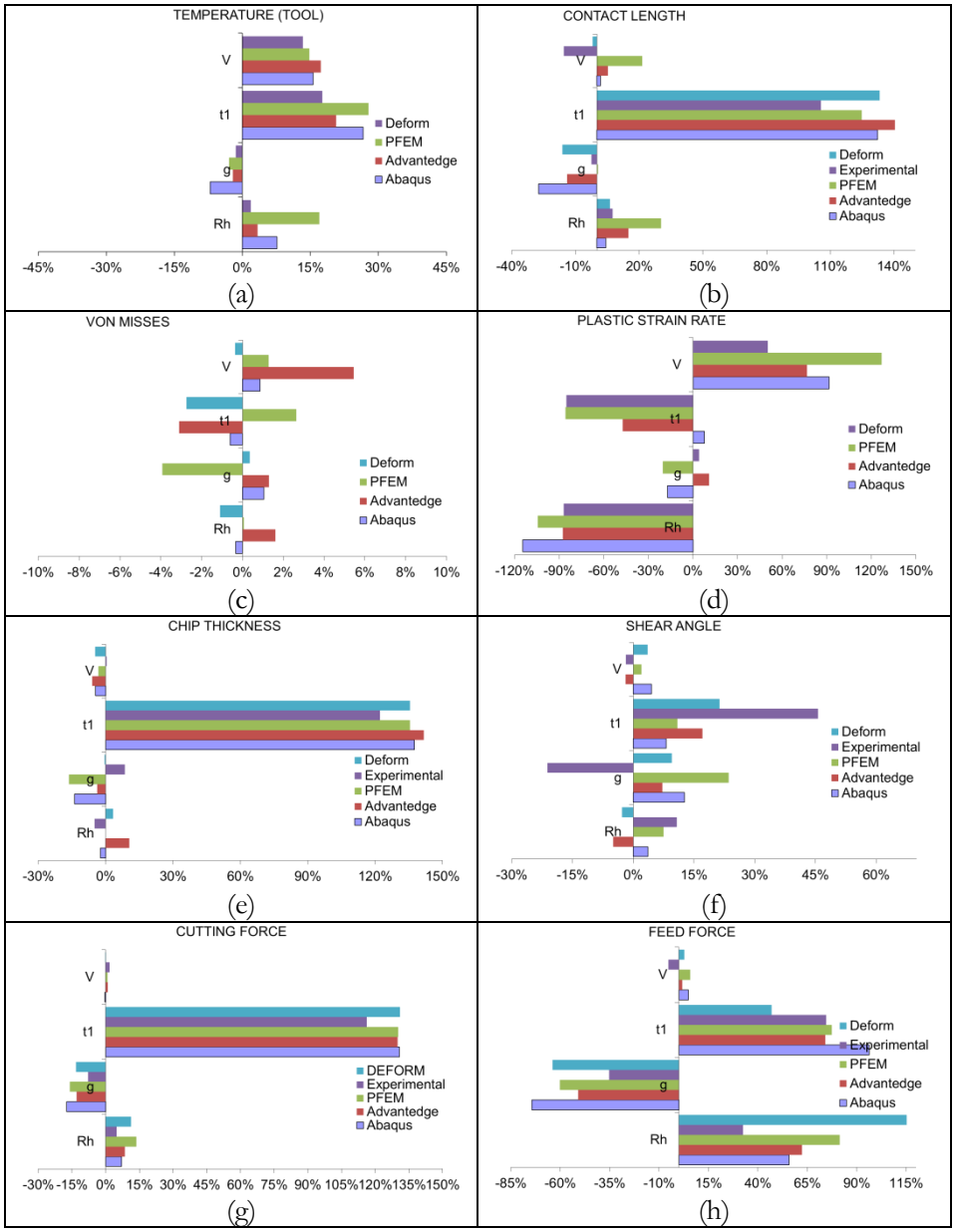

Figure 64. Numerical and Experimental effects obtained after sensibility analysis.

This section presents a DoE in order to study the influence of cutting conditions (like tool radius, rake angle, tool velocity and undeformed chip thickness) on output variables like the maximum tool temperature, the maximum chip temperature, the maximum workpiece von Mises stress, the maximum workpiece strain rate, the tool-chip contact-length, the deformed chip thickness, the cutting force and the feed force using PFEM. At the same time, we compare a DoE developed with PFEM with a DoE carried out using Abaqus, Deform AdvantEdge and experimental results (in those cases where results are available). Two different tool radius (0.05mm/0.005mm), two different tool velocities (150m/min.300m/min), two rake angles (6º and -6º) and two different undeformed chip thickness (0.05mm/0.3mm) were used. As a result, 16 numerical simulations were carried out using each of the numerical tools, and a total of 64 numerical simulations were done. It is important to remark that the chosen values represent cutting conditions typically used in industrial applications.

In Figure 64, V represents the tool velocity, t1 represents undeformed chip thickness, g represents the rake angle and Rh represents the tool radius.

Figure 64 (a) shows that PFEM predicts that chip thickness has the greatest (28%) and rake angle has the smallest (-5.5%) influence on maxi-mum tool temperature. Furthermore, the effect of tool velocity, chip thickness and tool radius on tool temperature is similar in all the numerical simulations. angle 12º.

Figure 64 (b) shows the effect of cutting conditions on contact length. PFEM predicts that increasing 6 times the chip thickness implies an increase of 125% in the contact length, the chip thickness being the most significant cutting conditions on contact length. The effect of the rake angle predicted by PFEM is opposite to other numerical simulations and experiments, possibly due to the friction law used in the model developed with PFEM. The effect of the tool velocity predicted by PFEM, Abaqus and AdvantEdge is different from the effect given by the experiments, suggesting that something is missing in the models of orthogonal cutting developed so far. The effect predicted by Deform is close to be negligible.

Most of the numerical simulations carried out in this work, display that the dependency of maxi-mum von Mises, inside the primary shear zone, on cutting conditions is less than 2%, that is close to be negligible (Figure 64(c)).

PFEM predicts that the most significant increase in strain rate in the primary shear zone is due to an increase in the tool velocity, while the less significant is the effect of an increase in the rake angle (Figure 64 (d)). The effect of the tool velocity is similar in all the numerical simulations, the effect of the chip thickness predicted by Abaqus is opposite in compassion to other numerical simulations and the effect of the tool radius is similar in all the numerical simulations. Numerical simulations does not show a clear pattern about the effect of the rake angle in strain rate in the primary shear zone, possible due to its strong dependency on mesh size and friction law used at tool-chip interface.

As expected, PFEM predicts that the most significant effect on deformed chip thickness is the undeformed chip thickness (Figure 64(e)), quite similar to the effect predicted by the other numerical simulations. All the numerical simulations predicts an opposite effect of the rake angle on deformed chip thickness, showing that is necessary to improve the friction law used at tool-chip interface as suggested by [16, 17]. PFEM and Deform show a negligible effect of the tool radius on deformed chip thickness, the reason to that behavior is the contact law used in the model developed with PFEM (Norton Hoff friction law say that friction force depends linearly on relative velocity, it means close to zero friction force when relative velocity is close to zero). Abaqus, AdvantEdge, Deform and PEM predict a decrease in the chip thickness increasing cutting speed, while experiments show that increasing tool velocity has a negligible effect on chip thickness.

Figure 64 (f) shows the effects of cutting conditions on shear angle. The results illustrates that the effect of chip thickness on the shear angle, predicted by numerical simulations is smaller than the results given by experiments. The effect of rake angle in shear angle given by the experiments is opposite to the effect predicted by the numerical simulations. AdvantEdge and Deform predict a contrary effect of tool radius on shear angle, due to the constitutive law used. Most of the numerical simulations and experiments predict that the effect of the tool velocity on shear angle is close to be negligible. The big differences between experiments and numerical simulations indicate that is necessary to improve the constitute law to describe the behavior of the workpiece material and to use a more sophisticate friction law at chip tool inter-face.

The effects on cutting forces of the tool radius, the rake angle, the chip thickness and the tool velocity predicted by the numerical simulations and experiments are in fact similar, showing that tool velocity has a negligible effect while increasing 6 times the chip thickness implies increasing 130% the cutting force (Figure 64(g)). Furthermore, according to PFEM, changing tool radius implies a larger increase and increasing rake angle implies a smaller decrease of cutting forces. The differences are due to the friction law used in PFEM and the smaller inter-particle distance used in PFEM in comparison with the mesh size used in other numerical simulations. This indicates again that is necessary to improve the workpiece constitutive law and the friction law used at the chip-tool interface in or-der to fit the phenomenology shown by experimental results.

PFEM, other numerical simulations and experiments predict an increase in feed forces due to an increase in tool radius and undeformed chip thickness; while increasing rake angle implies decreasing the feed force (Figure 64(h)). All the numerical simulations show that the tool radius and the rake angle effect is more than two times the effects given by the experimental results. For the cutting speeds used in this work, in-creasing tool velocity 2 times implies more or less the same feed forces.

4.5 Conclusions

The numerical simulations present PFEM as a promising strategy to simulate metal cutting processes, because PFEM overcomes some disadvantages of numerical schemes developed until now. For example, (i) allows the separation of chip and workpiece without using a physical or geometrical criterion, (ii) PFEM reduces the numerical diffusion due to re-meshing (transient mesh adaptivity is used instead of remeshing, (iii) PFEM needs less degree of freedom than used in a numerical simulation using FEM. Furthermore, PFEM predicts similar result to the other software and experiments as shown in Figure 64 and Table 17.

The computing time needed by PFEM under Matlab programming and exploding code vectorization (intuitive, concise and faster programming style) is similar to FEM software. It is expected, that PFEM under high level programming language needs less computing time than standard finite element software.

Chapter 5

5 Concluding remarks

The primary goal of this work was to explore the possibilities of the numerical simulation of chip formation using the particle finite element method (PFEM). A phenomenological approach was adopted to mathematically represent the behavior of the workpiece and the tool. Research effort has been focused on three topics: 1. A stabilized, mixed, displacement-pressure formulation for thermo-elasto-plastic solid media with low order finite elements with equal interpolation order for both displacement and pressure fields 2. A reduction of the computing time of a typical numerical simulation of metal cutting processes based on the correct selection of the time integration scheme of the thermo-mechanical problem, 3. The development of a meshing scheme based on the particle finite element method which includes mesh quality improvement through Delaunay triangulation, an innovative data transfer scheme with minimum numerical diffusion and an efficient strategy to model the separation of the chip and the piece.

The innovative part of our modeling is mainly connected to the numerical simulation of continuous and serrated chip formation.

5.1 On the general features of the proposed solution scheme

In chapter 1 we presented the different numerical strategies available in the literature to model machining processes. As discussed in chapter 1, the numerical modeling of machining process needs of different ingredients including: the spatial discretization of the workpiece and the tool, the time discretization of the balance equations, the contact strategy that allows us to model the transfer of momentum and energy at the tool-chip interface, the contact searching algorithm, the constitutive model of the workpiece and the tool, the friction law at the tool chip face interface and the time integration of the constitutive equations.

The introduction to the vocabulary and the state of the art of the numerical simulation of metal cutting presented in chapter 1 are considered an essential reading for new researchers as well as researchers interested in expanding their knowledge about the numerical simulation of metal cutting. Therefore, the state of art is considered an important contribution of this work.

The state of art presented in chapter 1 identified three ingredients that can be improved to optimize and to increase the robustness of the simulation schemes that currently exists, these are the following: 1) the finite element discretization, 2) the time discretization, and 3) the meshing scheme.

5.1.1 On the mixed displacement-pressure formulation for thermo-elasto-plastic problem.

Workpiece plastic behavior is considered isochoric. This behavior makes necessary the use of finite elements, which are free of volumetric locking. To discretize the workpiece domain we use a stabilized, mixed, displacement-pressure formulation for thermo-elasto-plastic solid media with low order finite elements with equal interpolation order for both displacement and pressure fields which is an extension and validation of the Polynomial Pressure Projection to the field of non-linear solid mechanics. The introduction of the stabilized mixed displacement-pressure finite elements has proved crucial in avoiding the adverse effects of volumetric locking, exhibited typically by standard pure displacement finite elements. The extension of the Polynomial Pressure Projection to the field of non-linear solid mechanics can be considered also an original contribution of this work.

5.1.2 On the time integration scheme of the coupled thermo-mechanical problem

Due to the multiple length scales involved in the numerical simulation of metal cutting processes and therefore the substantial amount of degrees of freedom, the typical implicit and explicit time integration schemes of the balance equations are time consuming. We were thus compelled to develop an alternative, apparently novel, method for dealing with this problem. The proposed global integration procedure has the intuitive flavor of a fractional step method (FSM), since it is based on decoupling of the balance equations and the evolution equations for the internal variables. The algorithmic structure underlying this methodology has been discussed in an in-depth manner, placing special emphasis on the issue of convergence with decreasing the time step towards the implicit/explicit solution. The introduction of the IMPLEX (implicit-explicit) integration scheme has proved crucial in decreasing the computing time up to 9 times in some representative numerical simulations of machining processes in comparison with the standard implicit/explicit schemes. Furthermore, it has become evident that, the IMPLEX procedure offers an efficient solution to the trade-off between robustness and computational time requirements.

5.1.3 On the meshing scheme using the particle finite element method (PFEM)

The meshing scheme in this work is proposed in the framework of the particle finite element (PFEM). In this work, we add to the PFEM two new ingredients: 1) The constrained Delaunay triangulation in order to improve mass conservation and chip shape through the simulation, and 2) The insertion and remotion of particles for resolving fine-scales features in the solution. Also, we proposed a novel transfer operator of the internal variables that allows us to

minimize the error due to numerical diffusion. The meshing scheme developed in this work is considered an original contribution of this work.

5.2 On the simulation technology

The simulation tool developed in this work allowed us to study the sensibility of machining to processes variables like the tool radius, the rake angle, the flank angle, the undeformed chip thickness and tool stiffness. Also, the technology developed allows us to estimate the cutting force and the feed force, the contact length and the deformed chip variables that give us information about how to optimize the cutting process. Likewise, the transition from continuous to segmented chip with increasing cutting speed is predicted by our simulation technology.

5.3 Open lines of research

A point that clearly needs to be improved in future works is the three-dimensional applications. Although the concepts and ideas developed here apply to 3D as well, the contact algorithm and the remeshing described in Chapter 2 become much more complicated.

It is also important to investigate strategies to increase the time step in general (e.g. by integrating the particles along the trajectories), apply parallel computing techniques with domain decomposition methods such that processes like drilling, turning, milling can be simulated in reasonable computing times.

The friction law at the tool-chip interface and the workpiece constitutive law need further research, in such a way that the predicted numerical results fit well the experimental data.

References

[1] M. P. Groover, *Fundamentals of Modern Manufacturing: Materials, Processes, and Systems*, 2006.

[2] E. Trent and P. Wright, *Metal cutting*, Fourth Edition ed., 2000.

[3] M. Heinstein and D. Segalman, "Simulation of Orthogonal Cutting with Smooth Particles Hydrodynamics," Sandia National Laboratories1997.

[4] F. Fleissner, T. Gaugele, and P. Eberhard, "Applications of the discrete element method in mechanical engineering," *Multibody system dynamics* vol. 18, pp. 81-94, 2007.

[5] R. Ambati, X. Pan, H. Yuan, and X. Zhang, "Application of material point methods for cutting process simulations," *Computational Materials Science,* vol. 57, pp. 102-110, 2012.

[6] L. Illoul and P. Lorong, "On some aspects of the CNEM implementation in 3D in order to simulate high speed machining or shearing," *Computer and Structures,* vol. 89, pp. 940–958, 2011.

[7] M. Vaz, D. R. J. Owen, V. Kalhori, M. Lundblad, and L. E. Lindgren, "Modelling and Simulation of Machining Processes," *Archives of Computational Methods in Engineering,* vol. 14, pp. 173-204, 2007.

[8] K. S. Al-Athel and M. S. Gadala, "The Use of Volume of Solid (VOS) in Simulating Metal Cutting with Chamfered and Blunt Tools," *International Journal of Mechanical Sciences,* vol. Vol. 53, pp. 23-30, 2010.

[9] E. Uhlmann, R. Gerstenberger, M. Graf von der Schulenburg, J. Kurnert, and A. Mattes, "The Finite Pointset Method for the Meshfree Numerical Simulation of Chip Formation," presented at the 12 Cirp Conference on Modelling of Machining Operations, San Sebastian, Spain, 2009.

[10] D. J. Benson and S. Okazawa, "Contact in a multi-material Eulerian finite element formulation," *Computer Methods in Applied Mechanics and Engineering,* vol. 193, pp. 4277-4298, 2004.

[11] M. Cremonesi, A. Frangi, and U. Perego, "A Lagrangian finite element approach for the analysis of fluid–structure interaction problems," *International Journal for Numerical Methods in Engineering,* vol. 84, pp. 610-630, 2010.

[12] J. Limido, C. Espinosa, M. Salaün, and J. L. Lacome, "SPH method applied to high speed cutting modelling," *International Journal of Mechanical Sciences,* vol. 49, pp. 898–908, 2007.

[13] C. R. Dohrmann and P. B. Bochev, "A stabilized finite element method for the Stokes problem based on polynomial pressure projections," *International Journal for Numerical Methods in Fluids,* vol. 46, pp. 183–201, 2004.

[14] P. B. Bochev, C. R. Dohrmann, and M. D. Gunzburger, "Stabilization of Low-Order Mixed Finite Elements for the Stokes Equations," *SIAM Journal on Numerical Analysis,* vol. 44, pp. 82-101, 2008.

[15] L. Filice, F. Micari, S. Rizzuti, and D. Umbrello, "A critical analysis on the friction modelling in orthogonal machining," *International Journal of Machine Tools and Manufacture,* vol. 47, pp. 709-714, 2007.

[16] P. J. Arrazola, D. Ugarte, and X. Domínguez, "A new approach for the friction identification during machining through the use of finite element modeling," *International Journal of Machine Tools & Manufacture* vol. 48, pp. 173-183, 2008.

[17] P. J. Arrazola and T. Özel, "Investigations on the effects of friction modeling in finite element simulation of machining," *International Journal of Mechanical Sciences,* vol. 52, pp. 31–42, 2010.

[18] A. J. Haglund, H. A. Kishawy, and R. J. Rogers, "An exploration of friction models for the chip–tool interface using an Arbitrary Lagrangian–Eulerian finite element model," *Wear,* vol. 265, pp. 452–460, 2008.

[19] F. P. Bowden and D. Tabor, *The Friction and Lubrication of Solids*, 1954.

[20] J. F. Archard, "Elastic Deformation and the Laws of Friction," *Proceedings of the Royal Society of London. Series A. Mathematical and Physical Sciences,* vol. 243, pp. 190-205, December 24, 1957 1957.

[21] T. H. C. Childs, K. Maekawa, T. Obikawa, and Y. Yamane, *Metal Machining: Theory and Applications*. Amsterdam, 2000.

[22] M. H. Dirikolu, T. H. C. Childs, and K. Maekawa, "Finite element simulation of chip flow in metal machining," *International Journal of Mechanical Sciences,* vol. 43, pp. 2699-2713, 2001.

[23] T. H. C. Childs, M. I. Mahdi, and G. Barrow, "On the Stress Distribution Between the Chip and Tool During Metal Turning," *CIRP Annals - Manufacturing Technology,* vol. 38, pp. 55-58, 1989.

[24] G. S. Sekhon and J. L. Chenot, "Numerical simulation of continuous chip formation during non-steady orthogonal cutting simulation," *Engineering Computations,* vol. 10, 1993.

[25] T. D. Marusich and M. Ortiz, "Modelling and simulation of high-speed machining," *International Journal for Numerical Methods in Engineering,* vol. 38, pp. 3675–3694, 1995.

[26] D. R. J. Owen and M. Vaz Jr, "Computational techniques applied to high-speed machining under adiabatic strain localization conditions," *Computer Methods in Applied Mechanics and Engineering,* vol. 171, pp. 445–461, 1999.

[27] J. S. Strenkowski and J. T. Carroll, "A Finite Element Model of Orthogonal Metal Cutting," *Journal of Engineering for IndustryTransactions of the Asme* vol. 107, pp. 349-354, 1985.

[28] K. Komvopoulos and S. A. Erpenbeck, " Finite Element Modeling of Orthogonal Metal Cutting," *Journal of Engineering for Industry, ASME Trans,* vol. 113, pp. 253–267, 1991.

[29] A. J. Shih, "Finite element analysis of the rake angle effects in orthogonal metal cutting," *International Journal of Mechanical Sciences,* vol. 38, pp. 1-17, 1995.

[30] A. Raczy, M. Elmadagli, W. J. Altenhof, and A. T. Alpas, "An eulerian finite-element model for determination of deformation state of a copper subjected to orthogonal cutting," *Metalurgical and Materials Transactions A,* vol. 35, pp. 2393-2400, 2004.

[31] M. S. Gadalaa, M. R. Movahhedya, and J. Wangb, "On the mesh motion for ALE modeling of metal forming processes," *Finite Elements in Analysis and Design,* vol. 38, pp. 435–459, 2002.

[32] M. S. Gadala, "Recent trends in ALE formulation and its applications in solid mechanics," *Computer Methods in Applied Mechanics and Engineering,* vol. 193, pp. 4247-4275, 2004.

[33] L. Olovsson, L. Nilsson, and K. Simonsson, "An ALE formulation for the solution of two-dimensional metal cutting problems," *Computers & Structures,* vol. 72, pp. 497–507, 1999.

[34] R. Rakotomalala, P. Joyot, and M. Touratier, "Arbitrary Lagrangian-Eulerian thermomechanical finite-element model of material cutting," *Communications in Numerical Methods in Engineering,* vol. 9, pp. 975–987, 1993.

[35] H. T. Y. Yang, M. Heinstein, and J. M. Shih, "Adaptive 2D finite element simulation of metal forming processes," *International Journal for Numerical Methods in Engineering,* vol. 28, pp. 1409-1428, 1989.

[36] P. O. D. Micheli and K. Mocellin, "Explicit F.E. formulation with modified linear tetrahedral elements applied to high speed forming processes," *International Journal Of Material Forming,* vol. 1, pp. 1411-1414, 2008.

[37] F. Auricchio, L. Beirão da Veiga, C. Lovadina, and A. Reali, "An analysis of some mixed-enhanced finite element for plane linear elasticity," *Computer Methods in Applied Mechanics and Engineering,* vol. 194, pp. 2947-2968, 2005.

[38] A. J. Chorin, "A Numerical Method for Solving Incompressible Viscous Flow Problems," *Journal of Computational Physics,* vol. 135, pp. 118-125, 1997.

[39] E. Oñate, J. Rojek, R. L. Taylor, and O. C. Zienkiewicz, "Finite calculus formulation for incompressible solids using linear triangles and tetrahedra," *International Journal for Numerical Methods in Engineering,* vol. 59, pp. 1473–1500, 2004.

[40] C. Agelet de Saracibar, M. Chiumenti, Q. Valverde, and M. Cervera, "On the orthogonal subgrid scale pressure stabilization of finite

deformation J2 plasticity," *Computer Methods in Applied Mechanics and Engineering,* vol. 195, pp. 1224–1251, 2006.

[41] M. Chiumenti, Q. Valverde, C. Agelet de Saracibar, and M. Cervera, "A stabilized formulation for incompressible elasticity using linear displacement and pressure interpolations," *Computer Methods in Applied Mechanics and Engineering,* vol. 191, pp. 5253–5264, 2002.

[42] M. Chiumenti, Q. Valverde, C. Agelet de Saracibar, and M. Cervera, "A stabilized formulation for incompressible plasticity using linear triangles and tetrahedra," *International Journal of Plasticity,* vol. 20, pp. 1487–1504, 2003.

[43] M. Cervera, M. Chiumenti, Q. Valverde, and C. Agelet de Saracibar, "Mixed linear/linear simplicial elements for incompressible elasticity and plasticity," *Computer Methods in Applied Mechanics and Engineering,* vol. 192, pp. 5249–5263, 2003.

[44] F. M. Andrade Pires, E. A. de Souza Neto, and D. R. J. Owen, "On the finite element prediction of damage growth and fracture initiation in finitely deforming ductile materials," *Computer Methods in Applied Mechanics and Engineering,* vol. 193, pp. 5223–5256, 2004.

[45] E. A. de Souza Neto, F. M. Andrade Pires, and D. R. J. Owen, "F-bar-based linear triangles and tetrahedra for finite strain analysis of nearly incompressible solids. Part I: formulation and benchmarking," *International Journal for Numerical Methods in Engineering,* vol. 62, pp. 353–383, 2005.

[46] G. T. Camacho and M. Ortiz, "Computational modelling of impact damage in brittle materials," *International Journal of Solids and Structures,* vol. 33, pp. 2899-2938, 1996.

[47] Y. Guo, M. Ortiz, T. Belytschko, and E. A. Repetto, "Triangular composite finite elements," *International Journal for Numerical Methods in Engineering,* vol. 47, pp. 287-316, 2000.

[48] J. Bonet and A. J. Burton, "A simple average nodal pressure tetrahedral element for incompressible and nearly incompressible dynamic explicit applications," *Communications in Numerical Methods in Engineering,* vol. 14, pp. 437-449, 1998.

[49] J. Bonet, H. Marriott, and O. Hassan, "Stability and comparison of different linear tetrahedral formulations for nearly incompressible explicit dynamic applications," *International Journal for Numerical Methods in Engineering,* vol. 50, pp. 119-133, 2001.

[50] F. M. Andrade Pires, E. A. de Souza Neto, and J. L. de la Cuesta Padilla, "An assessment of the average nodal volume formulation for the analysis of nearly incompressible solids under finite strains," *Communications in Numerical Methods in Engineering,* vol. 20, pp. 569-583, 2004.

[51] M. A. Puso and J. Solberg, "A stabilized nodally integrated tetrahedral," *International Journal for Numerical Methods in Engineering,* vol. 67, pp. 841-867, 2006.

[52] P. O. D. Micheli and K. Mocellin, "2D high speed machining simulations using a new explicit formulation with linear triangular elements," *International Journal of Machining and Machinability of Materials,* vol. 9, pp. 266 - 281, 2011.

[53] C. R. Dohrmann, M. W. Heinstein, J. Jung, S. W. Key, and W. R. Witkowski, "Node-based uniform strain elements for three-node triangular and four-node tetrahedral meshes," *International Journal for Numerical Methods in Engineering,* vol. 47, pp. 1549-1568, 2000.

[54] J. Bonet, H. Marriott, and O. Hassan, "An averaged nodal deformation gradient linear tetrahedral element for large strain explicit dynamic applications," *Communications in Numerical Methods in Engineering,* vol. 17, pp. 551-561, 2001.

[55] F. Greco, D. Umbrello, S. D. Renzo, L. Filice, I. Alfaro, and E. Cueto, "Application of the nodal integrated finite element method to cutting: a preliminary comparison with the "traditional" FEM approach," *Advanced Materials Research,* pp. 172-181, 2011.

[56] J. Marti and P. Cundall, "Mixed discretization procedure for accurate modelling of plastic collapse," *International Journal for Numerical and Analytical Methods in Geomechanics,* vol. 6, pp. 129-139, 1982.

[57] C. Detournay and E. Dzik, "Nodal Mixed Discretization for tetrahedral elements," presented at the 4th International FLAC Symposium on Numerical Modeling in Geomechanics, Minneapolis, 2006.

[58] M. Bäker, J. Rösler, and C. Siemers, "A finite element model of high speed metal cutting with adiabatic shearing," *Computers & Structures,* vol. 80, pp. 495–513, 2002.

[59] J. Rojek, E. Oñate, and R. L. Taylor, "CBS-based stabilization in explicit solid dynamics," *International Journal for Numerical Methods in Engineering,* vol. 66, pp. 1547-1568, 2006.

[60] A. Curnier and P. Alart, "A Generalized Newton Method for Contact Problems with Friction," *Journal De Mecanique Theorique Et Appliquee,* vol. 7, pp. 67-82, 1988.

[61] J. O. Hallquist, G. L. Goudreau, and D. J. Benson, "Sliding interfaces with contact-impact in large-scale Lagrangian computations," *Computer Methods in Applied Mechanics and Engineering,* vol. 51, pp. 107-137, 1985.

[62] J. H. Heegaard and A. Curnier, "An augmented Lagrangian method for discrete large-slip contact problems," *International Journal for Numerical Methods in Engineering,* vol. 36, pp. 569-593, 1993.

[63] R. Michalowski and Z. Mroz, "Associated and non-associated sliding rules in contact friction problems," *Archiwum Mechaniki Stosowanej,* vol. 30, pp. 259-276, 1978.

[64] D. Perić and D. R. J. Owen, "Computational model for 3-D contact problems with friction based on the penalty method," *International Journal for Numerical Methods in Engineering,* vol. 35, pp. 1289-1309, 1992.

[65] P. Wriggers and J. C. Simo, "A note on tangent stiffness for fully nonlinear contact problems," *Communications in Applied Numerical Methods,* vol. 1, pp. 199-203, 1985.

[66] P. Papadopoulos and R. L. Taylor, "A mixed formulation for the finite element solution of contact problems," *Computer Methods in Applied Mechanics and Engineering,* vol. 94, pp. 373-389, 1992.

[67] J. C. Simo and T. A. Laursen, "An augmented lagrangian treatment of contact problems involving friction," *Computers & Structures,* vol. 42, pp. 97-116, 1992.

[68] P. Wriggers and G. Zavarise, "Thermomechanical contact—a rigorous but simple numerical approach," *Computers & Structures,* vol. 46, pp. 47-53, 1993.

[69] P. Wriggers and C. Miehe, "Contact constraints within coupled thermomechanical analysis—A finite element model," *Computer Methods in Applied Mechanics and Engineering,* vol. 113, pp. 301-319, 1994.

[70] G. Zavarise, P. Wriggers, and B. A. Schrefler, "On augmented Lagrangian algorithms for thermomechanical contact problems with friction," *International Journal for Numerical Methods in Engineering,* vol. 38, pp. 2929-2949, 1995.

[71] K. A. Fischer and P. Wriggers, "Frictionless 2D Contact formulations for finite deformations based on the mortar method," *Computational Mechanics,* vol. 36, pp. 226-244, 2005.

[72] M. Tur, F. J. Fuenmayor, and P. Wriggers, "A mortar-based frictional contact formulation for large deformations using Lagrange multipliers," *Computer Methods in Applied Mechanics and Engineering,* vol. 198, pp. 2860-2873, 2009.

[73] S. Hüeber and B. I. Wohlmuth, "Thermo-mechanical contact problems on non-matching meshes," *Computer Methods in Applied Mechanics and Engineering,* vol. 198, pp. 1338-1350, 2009.

[74] J. Oliver, S. Hartmann, J. C. Cante, R. Weyler, and J. A. Hernández, "A contact domain method for large deformation frictional contact problems. Part 1: Theoretical basis," *Computer Methods in Applied Mechanics and Engineering,* vol. 198, pp. 2591-2606, 2009.

[75] S. Hartmann, J. Oliver, R. Weyler, J. C. Cante, and J. A. Hernández, "A contact domain method for large deformation frictional contact problems. Part 2: Numerical aspects," *Computer Methods in Applied Mechanics and Engineering,* vol. 198, pp. 2607-2631, 2009.

[76] T. Belytschko and M. O. Neal, "Contact-impact by the pinball algorithm with penalty and Lagrangian methods," *International Journal for Numerical Methods in Engineering,* vol. 31, pp. 547-572, 1991.

[77] J. Bruchon, H. Digonnet, and T. Coupez, "Using a signed distance function for the simulation of metal forming processes: Formulation of the contact condition and mesh adaptation. From a Lagrangian approach to an Eulerian approach," *International Journal for Numerical Methods in Engineering,* vol. 78, pp. 980-1008, 2009.

[78] K. Komvopoulos and S. A. Erpenbeck, "Finite Element Modeling of Orthogonal Metal Cutting," *Journal of Engineering for Industry,* vol. 113, pp. 253-267, 1991.

[79] O. C. Zienkiewicz and J. Z. Zhu, "The superconvergent patch recovery and a posteriori error estimates. Part 2: Error estimates and adaptivity," *International Journal for Numerical Methods in Engineering,* vol. 33, pp. 1365-1382, 1992.

[80] M. Ortiz and J. J. Quigley IV, "Adaptive mesh refinement in strain localization problems," *Computer Methods in Applied Mechanics and Engineering,* vol. 90, pp. 781-804, 1991.

[81] N.-S. Lee and K.-J. Bathe, "Error indicators and adaptive remeshing in large deformation finite element analysis," *Finite Elements in Analysis and Design,* vol. 16, pp. 99-139, 1994.

[82] D. Perić, M. Vaz Jr, and D. R. J. Owen, "On adaptive strategies for large deformations of elasto-plastic solids at finite strains: computational issues and industrial applications," *Computer Methods in Applied Mechanics and Engineering,* vol. 176, pp. 279-312, 1999.

[83] D. Perić, C. Hochard, M. Dutko, and D. R. J. Owen, "Transfer operators for evolving meshes in small strain elasto-plasticity," *Computer Methods in Applied Mechanics and Engineering,* vol. 137, pp. 331–344, 1996.

[84] C. Shet and X. Deng, "Finite element analysis of the orthogonal metal cutting process," *Journal of Materials Processing Technology,* vol. 105, pp. 95-109, 2000.

[85] G. Chen, C. Ren, X. Yang, X. Jin, and T. Guo, "Finite element simulation of high-speed machining of titanium alloy (Ti–6Al–4V) based on ductile failure model," *The International Journal Of Advanced Manufacturing Technology* vol. 56, pp. 1027-1038, 2011.

[86] D. Umbrello, "Finite element simulation of conventional and high speed machining of Ti6Al4V alloy," *Journal of Materials Processing Technology,* vol. 196, pp. 79-87, 2008.

[87] E. Ceretti, M. Lucchi, and T. Altan, "FEM simulation of orthogonal cutting: serrated chip formation," *Journal of Materials Processing Technology,* vol. 95, pp. 17-26, 1999.

[88] H. Borouchaki, P. Laug, A. Cherouat, and K. Saanouni, "Adaptive remeshing in large plastic strain with damage," *International Journal for Numerical Methods in Engineering,* vol. 63, pp. 1-36, 2005.

[89] D. Umbrello, S. Rizzuti, J. C. Outeiro, R. Shivpuri, and R. M'Saoubi, "Hardness-based flow stress for numerical simulation of hard machining

AISI H13 tool steel," *Journal of Materials Processing Technology,* vol. 199, pp. 64-73, 2008.

[90] D. Umbrello, J. Hua, and R. Shivpuri, "Hardness-based flow stress and fracture models for numerical simulation of hard machining AISI 52100 bearing steel," *Materials Science and Engineering: A,* vol. 374, pp. 90-100, 2004.

[91] E. Uhlmann, R. Gerstenberger, and J. Kuhnert, "Cutting Simulation with the Meshfree Finite Pointset Method," *Procedia CIRP,* vol. 8, pp. 391-396, 2013.

[92] P. Eberhard and T. Gaugele, "Simulation of cutting processes using mesh-free Lagrangian particle methods," *Computational Mechanics,* pp. 1-18, 2012.

[93] D. J. Benson, "A mixture theory for contact in multi-material Eulerian formulations," *Computer Methods in Applied Mechanics and Engineering,* vol. 140, pp. 59-86, 1997.

[94] E. Vitali and D. J. Benson, "Contact with friction in multi-material arbitrary Lagrangian Eulerian formulations using X-FEM," *Int. J. Numer. Meth. Eng* vol. 76, pp. 893–921, 2008.

[95] F. H. Harlow, M. A. Ellison, and J. H. Reid, "The particle-in-cell computing method in fluid dynamics," *Methods Comput. Phys,* vol. 3, pp. 319–343, 1964.

[96] Z. Więckowski, "The material point method in large strain engineering problems," *Computer Methods in Applied Mechanics and Engineering,* vol. 193, pp. 4417-4438, 2004.

[97] S. R. Idelsohn, E. Oñate, and F. D. Pin, "The particle finite element method: a powerful tool to solve incompressible flows with free-surfaces and breaking waves," *International Journal for Numerical Methods in Engineering,* vol. 61, pp. 964-989, 2004.

[98] E. Oñate, S. R. Idelsohn, M. A. Celigueta, and R. Rossi, "Advances in the particle finite element method for the analysis of fluid–multibody interaction and bed erosion in free surface flows," *Computer Methods in Applied Mechanics and Engineering,* vol. 197, pp. 1777-1800, 2008.

[99] E. Oñate, M. A. Celigueta, and S. R. Idelsohn, "Modeling bed erosion in free surface flows by the particle finite element method," *ACTA GEOTECHNICA,* vol. 1 pp. 237-252, 2006.

[100] J. Oliver, J. C. Cante, R. Weyler, C. González, and J. Hernandez, "Particle Finite Element Methods in Solid Mechanics Problems," *Computational Methods in Applied Sciences,* vol. 7, pp. 87-103, 2007.

[101] N. Calvo, S. R. Idelsohn, and E. Oñate, "The extended Delaunay tessellation," *Engineering Computations: Int J for Computer-Aided Engineering,* vol. 20, pp. 583-600, 2003.

[102] J. C. Simo and C. Miehe, "Associative coupled thermoplasticity at finite strains: Formulation, numerical analysis and implementation," *Computer Methods in Applied Mechanics and Engineering,* vol. 98 pp. 41–104, 1992.

[103] J. Bonet and R. D. Wood, *Nonlinear Continuum Mechanics for Finite Element Analysis*: Cambridge University Press, 1997.
[104] J. C. Simo, "A framework for finite strain elastoplasticity based on maximum plastic dissipation and the multiplicative decomposition: part I. continuum formulation," *Computer Methods in Applied Mechanics and Engineering archive,* vol. 666, pp. 199-219, 1988.
[105] J. C. Simo, "A framework for finite strain elastoplasticity based on maximum plastic dissipation and the multiplicative decomposition. Part II: Computational aspects," *Computer Methods in Applied Mechanics and Engineering,* vol. 68, pp. 1-31, 1988.
[106] E. Voce, "A practical strain hardening function.," *Metallurgia,* 1955.
[107] J. C. Simo and T. J. R. Hughes., *Computational Inelasticity*. New York: Springer-Verlag, 1998.
[108] G. H. Johnson and W. H. Cook, "A constitutive model and data for metals subjected to large strains high strain rates and high temperatures," *Proceedings of the 7th symposium on ballistics,* 1983.
[109] M. Bäker, "Finite element simulation of high-speed cutting forces " *Journal of Materials Processing Technology,* vol. 176, pp. 117–126, 2006.
[110] T. Belytschko, W. K. Liu, and B. Moran, *Nonlinear Finite Element for Continua and Structures.*: Wiley, 2000.
[111] M. Čanađija and J. Brnić, "Associative coupled thermoplasticity at finite strain with temperature-dependent material parameters," *International Journal of Plasticity,* vol. 20, pp. 1851-1874, 2004.
[112] J. Lubliner, *Plasticity Theory*: Dover Publications, 2008.
[113] W. D. Callister and D. G. Rethwisch, *Materials Science and Engineering: An Introduction*: Wiley, 2010.
[114] F. Armero and J. C. Simo, "A new unconditionally stable fractional step method for non-linear coupled thermomechanical problems," *International Journal for Numerical Methods in Engineering,* vol. 35, pp. 737-766, 1992.
[115] J. Oliver, A. E. Huespe, and J. C. Cante, "An implicit/explicit integration scheme to increase computability of non-linear material and contact/friction problems," *Computer Methods in Applied Mechanics and Engineering,* vol. 197, pp. 1865-1889, 2008.
[116] O. C. Zienkiewicz and J. Z. Zhu, "The superconvergent patch recovery and a posteriori error estimates. Part 1: The recovery technique," *International Journal for Numerical Methods in Engineering,* vol. 33, pp. 1331-1364, 1992.
[117] J. M. Carbonell, "Modeling of Ground Excavation with the Particle Finite Element Method," 2010.
[118] P. O. De Micheli and K. Mocellin, "A new efficient explicit formulation for linear tetrahedral elements non-sensitive to volumetric locking for infinitesimal elasticity and inelasticity," *International Journal for Numerical Methods in Engineering,* vol. 79, pp. 45-68, 2009.

[119] A. Ibrahimbegovic and L. Chorfi, "Covariant principal axis formulation of associated coupled thermoplasticity at finite strains and its numerical implementation," *International Journal of Solids and Structures,* vol. 39, pp. 499-528, 2002.

[120] Y. Tadi Beni and M. R. Movahhedy, "Consistent arbitrary Lagrangian Eulerian formulation for large deformation thermo-mechanical analysis," *Materials & Design,* vol. 31, pp. 3690-3702, 2010.

[121] P. J. Arrazola, "Modelisation numerique de la coupe: etude de sensibilite des parametres d'entree et identification du frottement entre outil-copeau," Doctoral Thesis, L'École Centrale de Nantes, l'Université de Nantes, France, 2003.

[122] P. M. Dixit and U. S. Dixit, *Modeling of Metal Forming and Machining Processes: by Finite Element and Soft Computing Methods*, 2008.